GULF
PUBLISHING COMPANY

ADVANCED NATURAL GAS ENGINEERING

Xiuli Wang and
Michael Economides

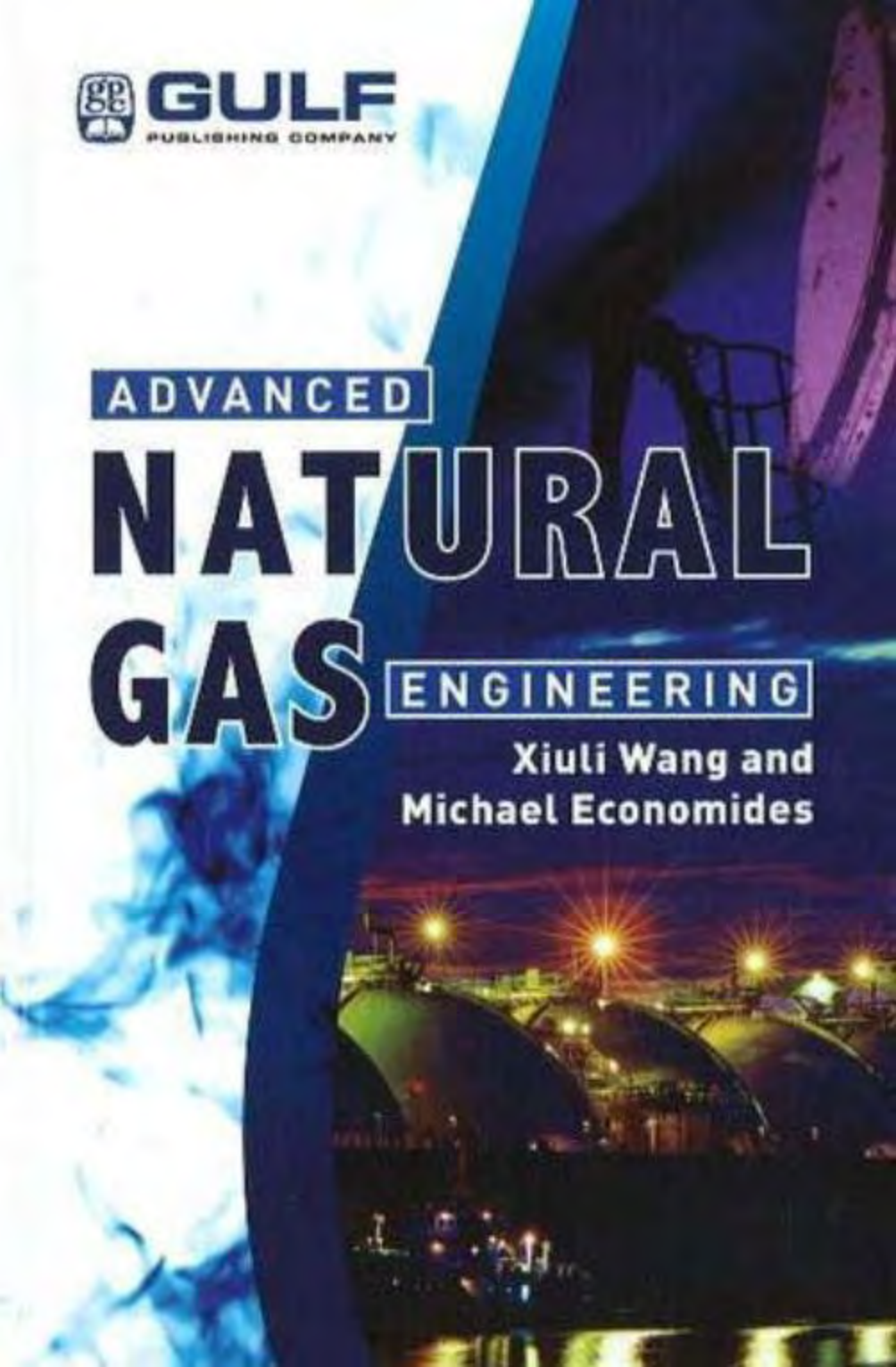

Advanced Natural Gas Engineering

Xiuli Wang
XGAS

Michael Economides
University of Houston

Gulf Publishing Company
Houston, Texas

Advanced Natural Gas Engineering

Gulf Publishing Company
2 Greenway Plaza, Suite 1020
Houston, TX 77046

10 9 8 7 6 5 4 3 2 1

Library of Congress Cataloging-in-Publication Data forthcoming

Printed in the United States of America
Printed on acid-free paper. ∞
Editing, design and composition by TIPS Technical Publishing, Inc

List of Figures

List of Tables

List of Examples

Preface

The role of natural gas in meeting the world energy demand has been increasing because of its abundance, versatility, and clean burning nature. As a result, new gas exploration, field development, and production activities are under way. This is especially true in places where natural gas was (until recently) labeled as "stranded." Because a significant portion of natural gas reserves worldwide are located across bodies of water, gas transportation becomes an issue. We are dealing with many unique issues and facing many challenges in the entire "food chain" (upstream to midstream and downstream) of natural gas engineering.

This necessitates a bridge of the technology gaps in a number of important areas:

- The unique new technologies such as different interpretations of 3-D seismic in natural gas exploration.
- The specific requirements in gas well drilling.
- The need for the hydraulically fracturing of high permeability gas well to bypass the damage but most importantly to reduce turbulence due to high well deliverability.
- Natural gas sea-going transportation such as liquefied natural gas (LNG) and compressed natural gas (CNG).
- Gas conversion and storage.
- Alternative and competing energy sources.

None of these new issues and challenges have not been addressed in depth in any existing books.

Another reason why we put this book together is based on our observations of young professionals and graduate students. With the power of current computing technology, many companies are offering different software to solve engineering problems. Many young engineers and students are good at running programs and plotting beautiful graphs without knowing what the numbers and figures mean. Somehow people have lost their fundamental abilities to tackle problems without using a computer. Here, besides addressing the advanced engineering issues related to natural gas, we also provide equations along with examples and detailed calculation procedures of fundamental chemical and petroleum engineering problems.

This book can serve as a reference book for all engineers in the energy business as well as a textbook for students in petroleum and chemical engineering curricula and in the training departments of a large group of companies.

A book like this, due to its multidisciplinary nature, requires input from a number of friends and colleagues. The authors wish to thank Profs. Russell D. Ostermann, Michael Nikolaou, Ali Ghalambor, and James Richardson for their contributions.

Thanks to Profs. Russell D. Ostermann, Shari Dunn-Norman, Victor Nikolaevskiy, Dr. Iskander Diyashev, Dr. David Wood, and Mr. Tony Martin for reviewing this book.

Special thanks go to Lindsay Fraser and Phil Lewis for providing valuable information and critiques.

Finally the authors would like to recognize the assistance of George Song, Seth Myers, Matteo Marongiu-Porcu, and Wenbo Liu.

—Dr. Xiuli Wang and Prof. Michael J. Economides
Houston, August 2009

Table of Contents

CHAPTER 1

Natural Gas Basics

1.1 Introduction

At the time of the writing of this book, natural gas provided about 23% of the total world energy supply, and that share would certainly increase. While coal is a solid and oil is a liquid, natural gas is a gaseous-phase fossil fuel. It is colorless, odorless, shapeless, and lighter than air. When burned, it gives off about 1,000 Btu (British thermal unit) per scf (standard cubic foot) and is used for domestic applications such as space heating, cooking and, increasingly, to generate electricity. It only ignites when the air-and-gas mixture is between 5 and 15 percent natural gas.

When compared with coal and oil, it burns cleaner, more efficiently, and with lower levels of potentially harmful byproducts that are released into the atmosphere. More important, there are very large deposits of natural gas in the world—far more than oil—Because this resource is difficult to transport, a lot of it has been labeled as "stranded." For these reasons, there has been a considerable increase in new gas exploration, field development, and production activities. To develop a natural gas field, one of the first important steps is to understand the fundamentals of natural gas. What follows is a summary of basic petroleum geology, natural gas origins, resources, and properties.

1.2 Geological Settings

Petroleum reservoirs, both oil and gas, are the result of sedimentary processes that happened over an extensive geological history. Figures 1–1 and 1–2 show artistic cutaways of two reservoirs, one

onshore and another offshore. It is important for the reader to conceptualize how petroleum reservoirs are configured underground, at great depths and, at times, also under many thousands of feet of water.

Figure 1–1 *Artist's rendition of onshore petroleum reservoir* (Graphics by John Perez Graphics & Design, LLC)

Figure 1–2 *Artist's rendition of offshore petroleum reservoir* (Graphics by John Perez Graphics & Design, LLC)

Different geological settings have led to sandstone, carbonate, or conglomerate lithologies. Figure 1–3 represents an artist's rendition of one common type of sedimentary settings with features that eventually would evolve into different types of reservoirs.

Petroleum geology not only attempts to reconstruct these ancient settings through the use of observations, well information, and seismic measurements, but also to apply logical inferences in searching for better quality reservoirs. This happens even within well-established sedimentary environments. For example, consider the detail in Figure 1–3 of a meandering channel. Identifying the channel may indicate the desired site of a well, whether a horizontal well is drilled (perpendicular or longitudinal) or, if complex well architecture is indicated, such as a "fishbone" configuration. Well architecture must take into account the shape of the geological units to be produced.

The second detail in Figure 1–3 shows how sediments are likely to be deposited, even inside a channel. Depending on the bending of the channel, one side will be conducive to deposition and the other conducive to erosion. Clearly, one would be looking for a petroleum accumulation at the likely depositional side.

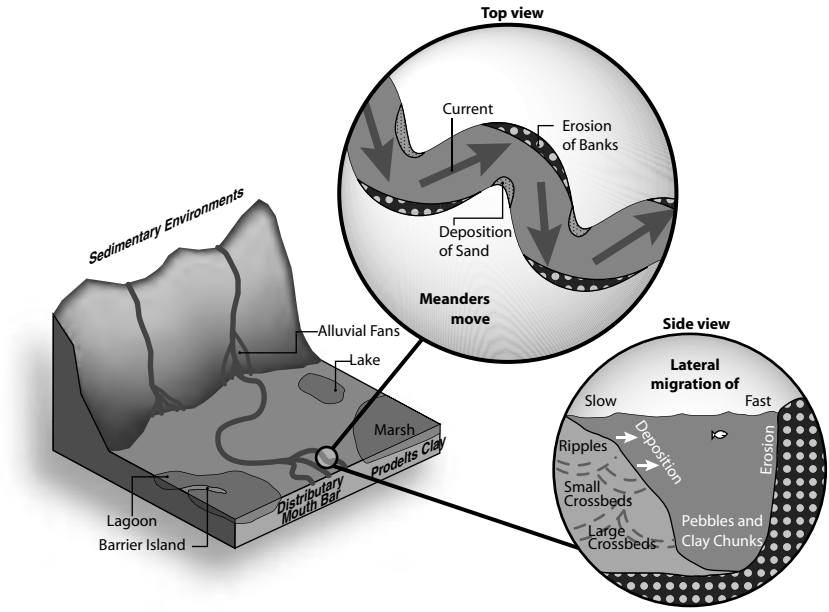

Figure 1–3 *Sedimentary environment*

The depth of a structure becomes critical for a number of important properties. The deeper the formation, the more likely it will be compacted as the grains are finer and consolidated. Secondary cementation processes are usually responsible for rock consolidation as cementing materials have percolated through the rock over geologic time. Shallow reservoirs are likely to consist of coarser materials and are likely to be unconsolidated.

There is gradation between deep highly consolidated rocks at, e.g., 20,000 ft depth and highly unconsolidated rocks at 1,000 ft. Figure 1–4 shows grain sizes from the upper left, which are likely to be encountered in shallow formations, to grain sizes on the lower right, which are likely to be encountered in very deep formations.

Depth also implies a gradation in *permeability* and *porosity*. Deeper reservoirs are far less permeable than shallow reservoirs. At 20,000 ft, permeability of 0.1 md or even less is quite common, whereas at 3,000 ft, permeability may exceed 10,000 md. At 10,000 ft, where some of the most prolific reservoirs in the world are found, permeability is likely to fluctuate between 10 and 100 md.

While porosity does not have such large fluctuations, is still likely to reflect depth. At 20,000 ft, porosity may be 10% or less, whereas at shallow depths it can be 30% or even larger, in some extreme cases.

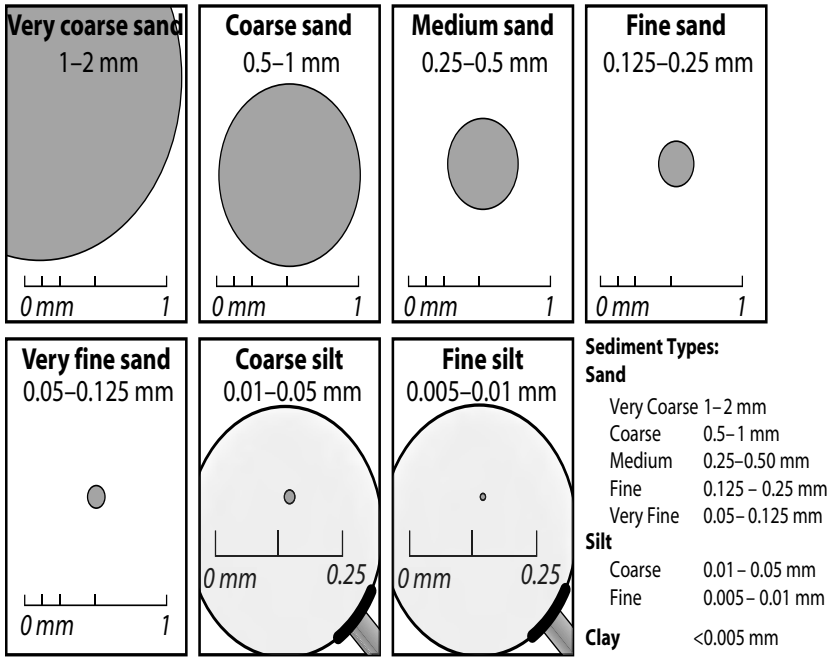

Figure 1–4 *Grain sizes of sediments*

The above applies generally to sandstone reservoirs. Carbonate reservoirs, in some areas, may follow similar trends; but elsewhere they may exhibit unique features, where very large porosities may be found in reservoirs with very small permeabilities.

1.3 Natural Gas Origins and Accumulations

It is commonly accepted that natural gas, like oil, has been generated from organic debris that have been deposited in geologic time and have been embedded along with inorganic matter at a considerable depth below today's surface. Over time (tens to hundreds of millions of years), because of compaction, high pressure, and temperature, the organic material gradually became coal, oil, or natural gas.

Because natural gas and oil are found with water, and because they are less dense, they would rise vertically, including all the way to the atmosphere. Much has escaped over time and continues to this day. However, if a vertical barrier is encountered (cap rock), it stops the migration and confines gas-in-place. Therefore, for natural gas to accumulate, three things have to be present: the source rock (compacted organic materials) for the creation of natural gas; the porous media

(reservoir) to accommodate the created gas; and the impermeable rock on top to trap the gas inside the porous rock-reservoir. Different types of trapping mechanisms are shown in Figure 1–5.

1.4 Natural Gas Resources

As will be discussed in Section 1.4, the presence of gas in a mixture of hydrocarbons depends on their phase behavior, which in turn, depends greatly on the pressure and temperature of the mixture. While a chemical engineer or a chemist would be interested to know the actual composition of the hydrocarbon mixture, petroleum engineers have traditionally opted to discuss it in terms of oil and gas. This of course suggests that what part is oil and what part is gas depends on the vantage point that pressure and temperature provide. Furthermore, the same mixture of hydrocarbons will have a different character in the reservoir than on the surface.

Pressure and temperature do not just play a role today in whether or not a mixture of hydrocarbons is liquid or gas or both. Their history has been critical to the evolution and the nature of the specific reservoir.

While it is not always quite that simple—and certainly with lots of unique and local features—it is generally true that the same organic matter could have evolved into coal, heavy oil with virtually no gas, light oil with lots of dissolved gas, and, finally, to just gas. The difference is the age of the reservoir, its depositional history, and most certainly its history of pressure and temperature, which both increase with depth. The resident hydrocarbons underwent millions of years of natural cracking not unlike what happens in a modern refinery, only in a small fraction of time.

There are exceptions to the following, but depths of 3,000 ft or less are likely to contain heavy oil with virtually no gas. Oil becomes lighter as the depth increases, which means that gas coexists with oil. Gas can be in the form of a gas-cap on top of the oil zone, as shown in Figure 1–6, or it can be dissolved in the oil. As depth increases, more gas is present. Around 10,000 to 12,000 ft depth are some of the most prolific oil reservoirs in the world and almost all of them contain oil of API gravity between 28 and 32. They also coexist with substantial quantities of gas, which, when separated from oil at the surface, will evolve into 500 to 1,000 scf/stb (standard cubic feet per stock tank barrel). This will be addressed in detail in Sections 1.4 and 1.5.

At greater depths, e.g., 17,000 ft and certainly over 20,000 ft, reservoirs contain almost exclusively natural gas. Below, we offer some brief definitions of terms used in the petroleum industry to describe natural gas reservoirs.

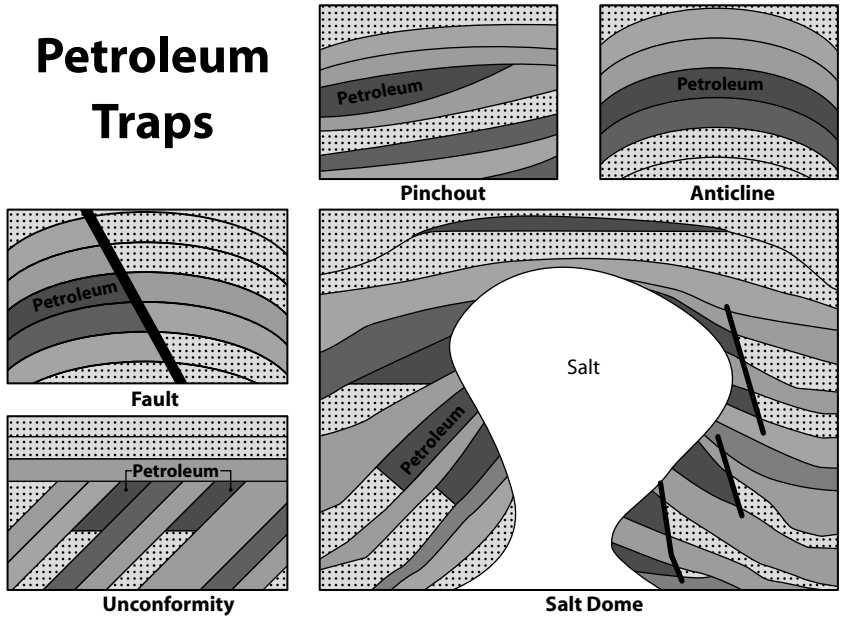

Figure 1–5 *Natural gas reservoirs and trapping mechanisms*

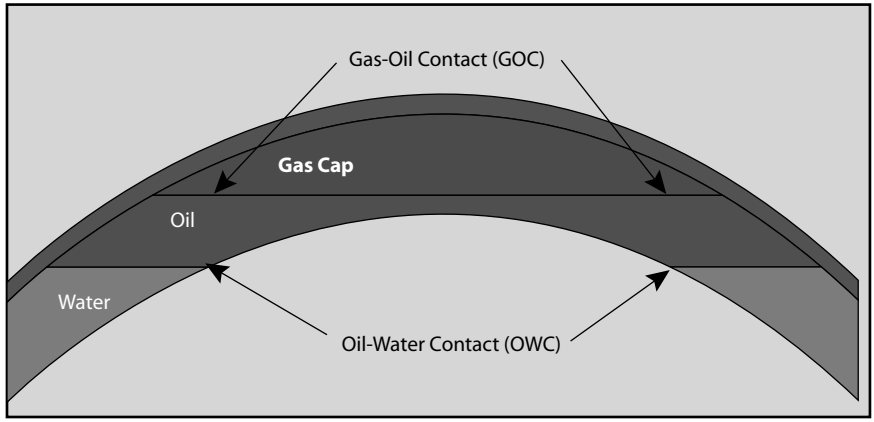

Figure 1–6 *Gas cap*

1.4.1 Nonassociated Gas

These are reservoirs that contain almost entirely natural gas at reservoir conditions. They are generally found at greater depth. If the fluid at the surface still remains gas, then it is called "dry gas." If the surface

pressures cause some liquid hydrocarbons to evolve, it is called a "wet gas" reservoir. It must be emphasized that while nonassociated gas reservoirs are likely to be found at greater depths, upward migration from the source rock, in geologic time, can result in shallow gas reservoirs, and in some cases, such as the Arctic, the cap rock may be the permafrost.

1.4.2 Associated Gas

Almost all oil reservoirs except those classified as extra heavy or tars will produce some natural gas at the surface. Oil will not be shipped in a commercial pipeline or a tanker with gas still in the solution. The term stock tank oil, which is used both as a measure for oil well performance and in commercial pricing of oil, means that all associated gas has been stripped from the liquid at one atmosphere pressure. The gas thus liberated is known as "associated gas."

1.4.3 Unconventional Gas

The term unconventional gas is widely used, but it refers more to the geological setting and rock type rather than to the gas itself, which is nearly all methane. When the term was coined, it implied that these reservoirs presented operational or economic challenges, or both, which would not be ordinarily found in conventional reservoirs.

The most common, "tight gas," formed in sandstones or carbonates, refers to low-permeability formations with permeabilities less than 1 md and often as low as 0.001 md. In such "tight" reservoirs, it is essentially not possible for much of the gas to flow naturally. Massive hydraulic fracturing (which will be addressed in Chapter 3), a widely practiced technique in the petroleum industry, was greatly expanded in the 1970s and 1980s and targeted these reservoirs. In the United States and Canada, tight gas occupies a sizeable part of the natural gas industry. In 2007, about 30% of US natural gas was produced from tight gas reservoirs.

Coalbed methane (CBM) refers to methane gas that is found adsorbed in many buried coalbed deposits. Wells drilled in these deposits are hydraulically fractured and allow for the production of desorbed methane. In 2007, about 9% of US natural gas was produced from CBM.

Finally, shale gas is gas found in organic shale rocks, which exist in relative abundance in the United States. Shale gas has seen increased activity between 2000 and 2008. Because these reservoirs have virtually no permeability, the choice of well completions has been horizontal wells with multiple hydraulic fractures.

1.5 Natural Gas Composition and Phase Behavior

Depending on where and from what type of reservoir the natural gas is produced, its composition can vary widely. Generally, it contains primarily methane (CH_4) with decreasing quantities of ethane (C_2H_6), propane (C_3H_8), butane (C_4H_{10}), and pentane (C_5H_{12}). Some natural gas mixtures can also contain nonhydrocarbon gases such as carbon dioxide (CO_2), oxygen (O_2), nitrogen (N_2), hydrogen sulphide (H_2S), and traces of rare gases (Ar, He, Ne, Xe). No matter what the natural composition of gas is, the product delivered and finally used by the consumers is almost pure methane. This will be discussed in depth in Chapter 5 (Natural Gas Transportation).

Natural gas phase behavior is a function of pressure, temperature, and volume. Therefore it is very often illustrated by the "PVT diagram" or phase behavior envelope. Understanding phase behavior is critical to the hydrocarbon recovery mechanism and production prediction. Certain concepts, demonstrated in Figure 1–7, associated with phase envelopes are worth introducing before we discuss different types of natural gas behaviors.

- **Bubble Point Curve**—the curve that separates the pure liquid (oil) phase from the two-phase (natural gas and oil) region. This means that at a given temperature, when pressure decreases and below the bubble point curve, gas will be emitted from the liquid phase to the two-phase region.

- **Dew Point Curve**—the curve that separates the pure gas phase from the two-phase region. It is the connected points of pressure and temperature at which the first liquid droplet is formed out of the gas phase.

- **Critical Point**—the point on the phase envelope where the bubble point curve meets the dew point curve. At that given pressure and temperature, gas properties are identical to liquid properties. The pressure and temperature at the critical point are called critical pressure and temperature, respectively.

- **Cricondentherm**—the highest temperature at which liquid and vapor can coexist. That means the mixture will be gas irrespective of pressure when the temperature is larger than cricondentherm.

- **Cricondenbar**—the highest pressure at which a liquid and vapor can coexist.

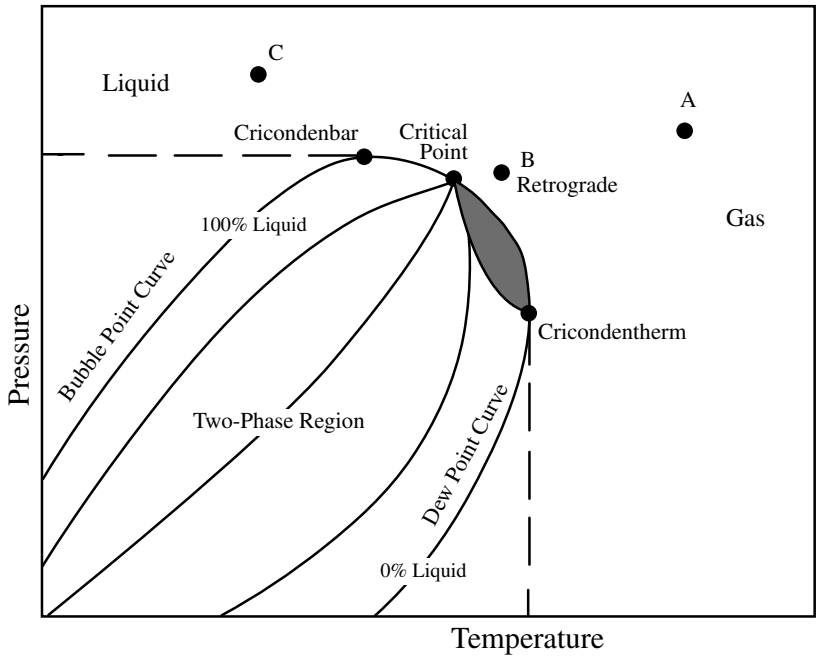

Figure 1–7 *Phase diagram*

Clearly, the natural gas phase envelope can be very different depending on its source.

1.5.1 Dry- and Wet-Gas Phase Behaviors

As discussed earlier in this chapter, dry gas is in the gaseous phase under reservoir conditions, as marked by point A in Figure 1–7. It contains primarily methane with small amounts of ethane, propane, and butane, with little or no heavier compounds. When it is produced to the surface, it is maintained in the gaseous phase with surface temperature falling outside the two-phase envelope. Therefore it will not form any liquids, which are at times referred to as NGL (natural gas liquids).

Wet gas, on the other hand, will have liquid dropped out once it reaches the surface, which means that the surface conditions of pressure and temperature will fall inside the two-phase region.

1.5.2 Retrograde-Condensate-Gas Phase Behavior

Retrograde condensate systems and reservoirs are a unique phenomenon that appears only among hydrocarbon mixtures. No other mix-

tures of gases exhibit such behavior. As pressure decreases from point B to the two-phase shaded area in Figure 1–7, the amount of liquid in the reservoir increases. As pressure decreases further, liquid starts to revaporize. Between the dew point and the point where liquid revaporizes is the region (shaded area in Figure 1–7) of retrograde condensation (McCain, 1973). Many natural gas reservoirs behave in this manner. During production from such reservoirs, the pressure gradient formed between the reservoir pressure and the flowing bottomhole pressure may result in liquid condensation and form a condensate bank around the wellbore, reduce gas relative permeability and remain unrecoverable. Sometimes it could seize production (Wang, 2000).

One way to prevent the formation of condensate is to maintain the flowing well bottomhole pressure above the dew point pressure. This is often not satisfactory because the drawdown (reservoir pressure minus flowing bottomhole pressure) may not be sufficient enough for the economic production rate. An alternative technique is to allow the formation of condensate, but occasionally to inject methane gas into the production well. The gas dissolves and sweeps the liquid condensate into the reservoir. The well is then put back in production. This approach is repeated several times in the life of the well. It is known as gas cycling. Another way is to inject both nitrogen and methane, which develops a miscible displacement process and results in high condensate recoveries (Sanger and Hagoort, 1998).

Removing the bank of condensate from the near-wellbore region is still a challenge for the oil and gas industry. Understanding the near-wellbore gas-condensate flow is thus very important to optimize production of gas-condensate reservoirs.

1.5.3 Associated Gas Phase Behavior

Under reservoir conditions, gas is often dissolved in the oil phase as associated gas. As it is produced to the surface under lower pressure and temperature, gas will come out from the oil phase. An oil reservoir whose pressure is above the bubble point (point C in Figure 1–7) is usually referred to as undersaturated. If the pressure is inside the two-phase envelope it is called a saturated, or two-phase, reservoir and may form a gas-cap on top of the oil zone.

1.6 Natural Gas Properties

From the previous section it is clear that the fluid finds itself at different pressures and temperatures during the whole process of natural

gas production. Unlike those of oil, natural gas properties vary significantly with pressure, temperature, and gas composition. Below is an outline of the gas properties that play very important roles in gas production, prediction, and evaluation. These include the gas specific gravity (often compared to air), the gas deviation factor, density, viscosity, isothermal compressibility, and the formation volume factor.

1.6.1 Gas Specific Gravity

Gas specific gravity, γ_g, as commonly used in the petroleum industry, is defined as the ratio of the molecular weight of a particular natural gas to that of air. The molecular weight of a gas mixture is the summation of the products of the individual mole fractions and molecular weights of each individual component. Air itself is a mixture of gases. It contains about 21% oxygen, 78% nitrogen, and the rest are carbon dioxide, water vapor, and some inactive gases. So the molecular weight of air has been calculated as 28.97. Therefore, γ_g of a natural gas can be defined as

$$\gamma_g = \frac{MW_m}{MW_{air}} = \frac{\sum_{i=1}^{n} y_i MW_i}{28.97}, \tag{1.1}$$

where y_i and MW_i are the mole fractions and molecular weights, respectively, of individual components in the gas mixture. n is the total gas components in the gas mixture.

Table 1–1 gives the molecular weights and critical properties for most hydrocarbon and nonhydrocarbon gases likely to be found in a natural gas reservoir. A lean or light gas reservoir contains primarily methane and ethane with small traces of other gases. Pure methane would have a gravity equal to (16.04/28.97 =) 0.55. A rich or heavy gas reservoir may have a gravity equal to 0.75 or, in some rare cases, higher than 0.9.

Example 1–1 Gas gravity

A natural gas consists of the following (molar) composition: $C_1 = 0.871$, $C_2 = 0.084$, $C_3 = 0.023$, $CO_2 = 0.016$ and $H_2S = 0.006$. Calculate the gas gravity to air.

Table 1–1 Molecular Weights and Critical Properties of Pure Components of Natural Gases *(Economides et al., 1994)*

Compound	Chemical Composition	Symbol (for calculations)	Molecular Weight	Critical Pressure (psi)	Critical Temp. (R)
Methane	CH_4	C_1	16.04	673	344
Ethane	C_2H_6	C_2	30.07	709	550
Propane	C_3H_8	C_3	44.09	618	666
iso-Butane	C_4H_{10}	i-C_4	58.12	530	733
n- Butane	C_4H_{10}	n-C_4	58.12	551	766
iso-Pentane	C_5H_{12}	i-C_5	72.15	482	830
n-Pentane	C_5H_{12}	n-C_5	72.15	485	847
n-Hexane	C_6H_{14}	n-C_6	86.17	434	915
n-Heptane	C_7H_{16}	n-C_7	100.2	397	973
n-Octane	C_8H_{18}	n-C_8	114.2	361	1024
Nitrogen	N_2	N_2	28.02	492	227
Carbon Dioxide	CO_2	CO_2	44.01	1,072	548
Hydrogen Sulfide	H_2S	H_2S	34.08	1,306	673

Table 1–2 Results for Example 1–1

Compound	y_i	MW_i	y_iMW_i
C_1	0.871	16.04	13.971
C_2	0.084	30.07	2.526
C_3	0.023	44.09	1.014
CO_2	0.016	44.01	0.704
H_2S	0.006	34.08	0.204
	1		18.419

Solution

With the data in Table 1–1 and the given composition, the contributions to the natural gas molecular weight can be calculated and shown in Table 1–2.

Therefore, the gas gravity is 18.419/28.97 = 0.64.

1.6.2 Gas Deviation Factor

A natural gas mixture under reservoir conditions is nonideal and its behavior can be approximated by the real gas law, a general equation of state for gases:

$$pV = ZnRT, \tag{1.2}$$

where p is pressure in psi, V is the gas volume in ft^3, n is the number of moles of the gas, T is absolute temperature in R, R is the universal gas constant and equals to 10.73 psi ft^3/lb-mol-R. Z is the gas deviation factor or "Z-factor" in some petroleum literature. Chemical engineers have called it the super-compressibility factor. It is defined as the ratio of the real volume (the volume actually occupied by a gas at a given p and T) to the ideal volume (volume it would occupy had it behaved as an ideal gas). It is a measure of how a real gas deviates from ideality.

The gas deviation factor is an important gas property and it is involved in calculating gas properties such as the formation volume factor, density, compressibility, and viscosity. All these properties are necessary in calculating initial gas-in-place (and, thus, reserves), predicting future gas production, and designing production tubing and pipelines (Elsharkawy and Elkamel, 2001).

The Z can be determined in a PVT laboratory. In common practice it is calculated from published charts such as the one shown in Figure 1–8 by Standing and Katz (1942). To use this chart, it is necessary to calculate the pseudoreduced properties (pressure and temperature).

Pseudoreduced Properties

For gas mixtures, the gas critical pressure and temperature are called pseudocritical pressure and temperature to be distinguished from those of pure components, and can be calculated as

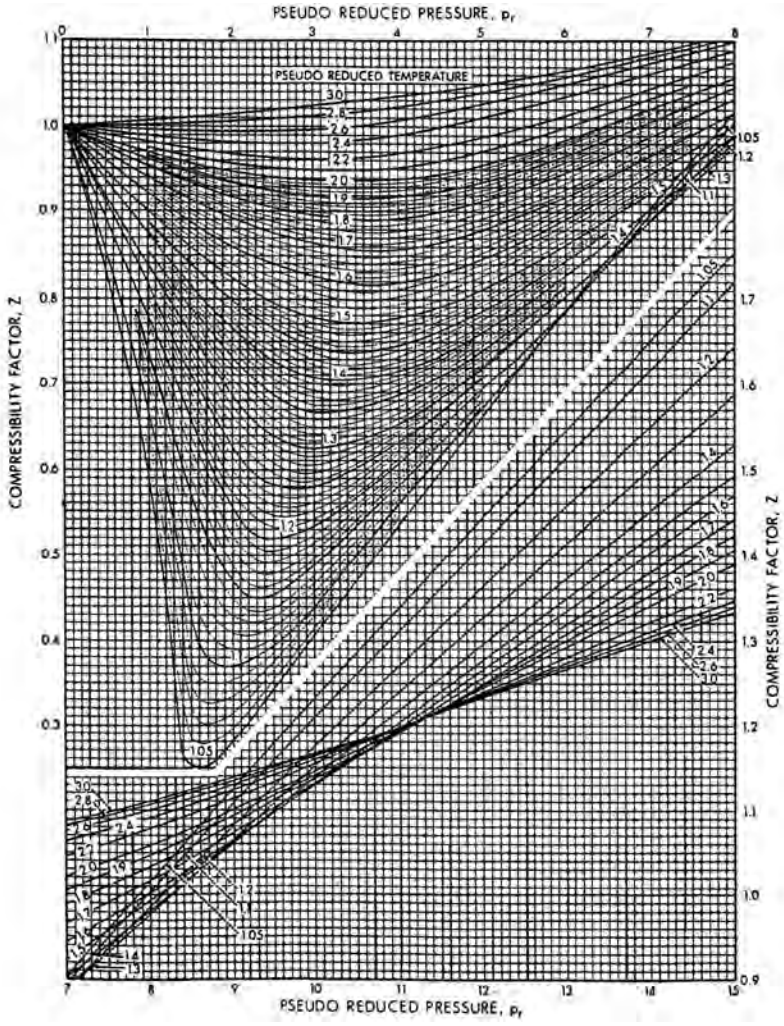

Figure 1–8 *The gas deviation factor for natural gases* (Standing and Katz, 1942)

$$p_{pc} = \sum_{i=1}^{n} y_i p_{ci}, \tag{1.3}$$

$$T_{pc} = \sum_{i=1}^{n} y_i T_{ci}, \tag{1.4}$$

where p_{ci} and T_{ci} are critical pressures and temperatures of individual components, respectively. The temperature must be absolute (R or K), which is simply °F + 460 or °C + 273. The pseudoreduced pressure and temperature of the mixture are simply

$$p_{pr} = \frac{p}{p_{pc}}, \tag{1.5}$$

$$T_{pr} = \frac{T}{T_{pc}}. \tag{1.6}$$

As can be seen from Figure 1–8, at the standard conditions of p_{sc} = 14.7 psi and T_{sc} = 60°F = 520 R, the gas deviation factor, Z_{sc}, can be taken as equal to 1.

Pseudocritical properties of gas mixtures can be estimated from the given gas specific gravity if gas composition is not known. Figure 1–9 relates the gas specific gravity (to air) with the pseudocritical properties of gas mixtures. This chart can be used as an approximation when only the gas specific gravity is known or when a quick calculation is indicated.

Example 1–2 Calculations with real gas law

Given the natural gas gravity to air γ_g = 0.75, the pseudocritical pressure, p_{pc} and temperature, T_{pc} are 667 psi and 405 R, respectively. If the pressure and temperature are 1,500 psi and 20°F, respectively, calculate how many lb of gas can fit in 1,000 ft^3 of space? At what pressure increase would the mass increase by 50%, if the temperature remains constant?

Solution

For T = 20°F = 480 R, T_{pr} = 480/405 = 1.19 (which will remain constant). For p = 1,500 psi, p_{pr} = 1,500/667 = 2.25. From Figure 1–8, Z is obtained as 0.51. By using the real gas law and gas gravity definition, the mass of gas that can fit in 1,000 ft^3 of space is:

$$m = \frac{pV\gamma_g MW_{air}}{ZRT} = \frac{1{,}500 \times 1{,}000 \times 0.75 \times 28.97}{0.51 \times 10.73 \times 480} = 12{,}408 \text{ lb}.$$

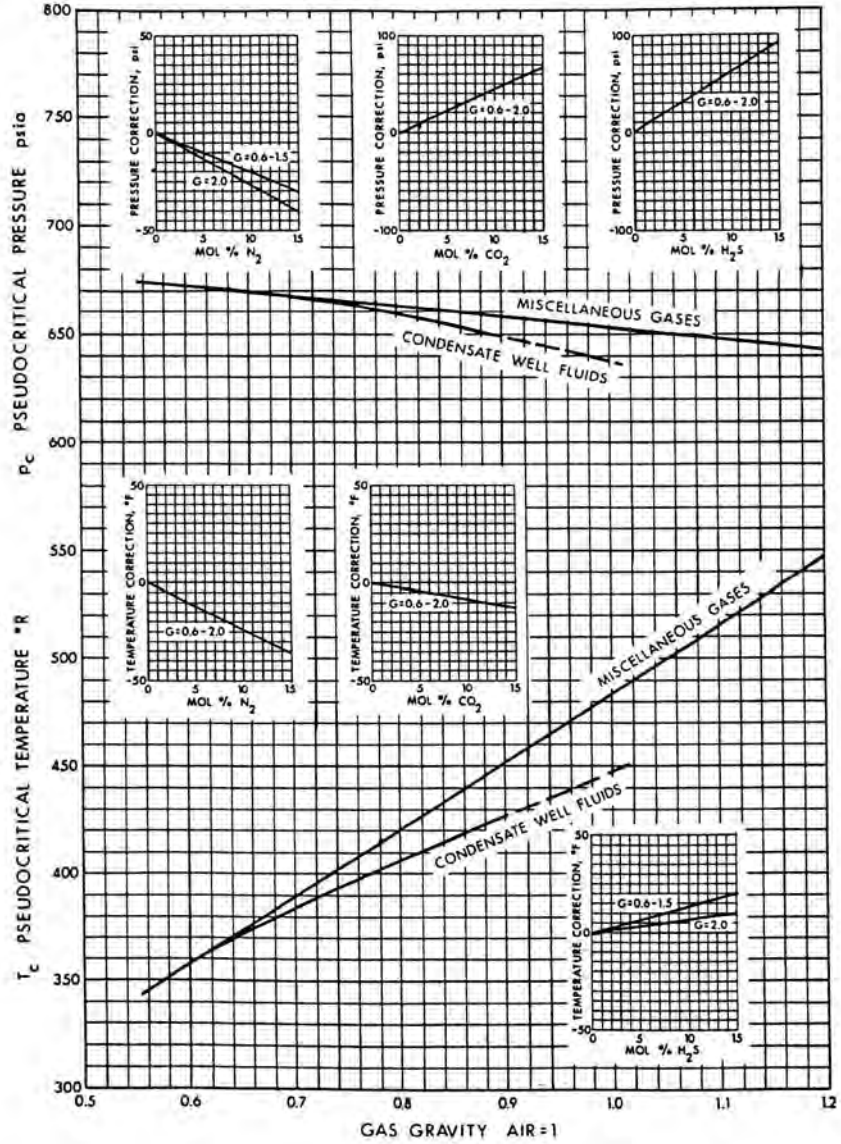

Figure 1–9 *Pseudocritical properties of natural gases* (Brown et al., 1948; inserts from Carr et al., 1954)

The idea then is for p/Z to become 1.5 times the current p/Z, that is $(1.5 \times 1{,}500)/(0.51) = 4{,}412$. It requires trial and error but using the same T_{pr} curve. For each assumed pressure the p_{pr} must be calculated, then a Z must be obtained and the ratio p/Z must be checked against

the 4,412 value. Answer: p = 2,600 psi (a 73% increase) with p_{pr} = 3.9 and Z = 0.59.

Example 1–3 Calculation of gas reservoir volume

Use the real gas law to calculate the volume of 5 lb-mol of a gas mixture at reservoir conditions of T = 180°F and p = 4,000 psi. Assume that this natural gas has the following molar composition: C_1 = 0.874, C_2 = 0.083, C_3 = 0.022, i-C_4 = 0.006, n-C_4 = 0.002, i-C_5 = 0.008, n-C_5 = 0.003, n-C_6 = 0.001 and C_7+ = 0.001.

Solution

OPTION 1—Calculate the pseudocritical properties of the mixture. These properties are simply the summation of the individual contributions of the component gases, weighted by their molar fractions. This is based on the classical thermodynamics law for ideal mixtures and Dalton's law of partial pressures. Table 1–3 gives the results of this calculation.

Table 1–3 Calculated Results for Example 1–3

Compound	y_i	MW_i	y_iMW_i	p_{ci}	y_ip_{ci}	T_{ci}	y_iT_{ci}
C_1	0.874	16.04	14.019	673	588.20	344	300.66
C_2	0.083	30.07	2.496	709	58.85	550	45.65
C_3	0.022	44.09	0.970	618	13.60	666	14.65
i-C_4	0.006	58.12	0.349	530	3.18	733	4.40
n-C_4	0.002	58.12	0.116	551	1.10	766	1.53
i-C_5	0.008	72.15	0.577	482	3.86	830	6.64
n-C_5	0.003	72.15	0.216	485	1.46	847	2.54
n-C_6	0.001	86.17	0.086	434	0.43	915	0.92
C_7+	0.001	114.2*	0.114	361*	0.36	1,024*	1.02
	1		18.94		p_{pc}=671		T_{pc}=378

* Use the properties of *n*-octane.

The pseudoreduced properties are, p_{pr} = 4,000/671 = 5.96 and T_{pr} = (180 + 460)/378 = 1.69. From Figure 1–8, Z = 0.855.

Then, from Eq. (1.2) and rearrangement,

$$V = \frac{0.855 \times 5 \times 10.73 \times 640}{4,000} = 7.34\,\text{ft}^3.$$

OPTION 2—Obtain p_{pc} and T_{pc} from gas specific gravity. Based on Table 1–3, the calculated molecular weight is 18.94. That leads to γ_g = 18.92/28.97 = 0.65.

From Figure 1–9, p_{pc} = 670 psi and T_{pc} = 375 R, which compare with 671 psi and 378 R calculated above.

OPTION 3—Use published correlation to calculate p_{pc} and T_{pc}, which will be discussed in a later section of this chapter.

Presence of Nonhydrocarbon Gases

It is worth noting that the well known graph in Figure 1–8 was constructed for only hydrocarbon gas mixtures. In the presence of large amounts of nonhydrocarbon gases, the gas deviation factor must be adjusted. In the absence of complete natural gas composition but knowing the gas gravity and the composition of nonhydrocarbon gases, the inserts in Figure 1–9 can be used to adjust the pseudocritical properties of a gas mixture to account for the presence of nonhydrocarbon gases.

Wichert and Aziz (1972) have presented a correlation that allows the use of the Standing-Katz graph (Figure 1–8) in the presence of nonhydrocarbon gases. The pseudocritical properties, T_{pc} and p_{pc}, can be corrected by

$$T'_{pc} = T_{pc} - \varepsilon_3, \tag{1.7}$$

$$p'_{pc} = \frac{p_{pc} T'_{pc}}{T_{pc} + y_{H_2S}(1 - y_{H_2S})\varepsilon_3}, \tag{1.8}$$

where y_{H_2S} is the mole fraction of hydrogen sulfide (natural gas with a high content of H_2S is often referred to as a "sour" gas) and the term ε_3 is a function of the H_2S and CO_2 concentrations, which can be obtained from Figure 1–10.

Example 1–4 Calculation of the *Z*-factor for a sour gas

Calculate the gas deviation factor, *Z*, of a sour gas at 190°F and 4,000 psi. Gas composition is given below:

C_1	C_2	C_3	i-C_4	n-C_4	i-C_5	n-C_5	C_6+	N_2	CO_2	H_2S
0.784	0.028	0.007	0.0008	0.0005	0.0008	0.0003	0.0006	0.005	0.021	0.152

Solution

OPTION 1—From Figure 1–10 and using the compositions of CO_2 and H_2S, the adjustment factor ε_3 = 23.5 R. The pseudocritical properties are calculated as shown in Table 1–4. Therefore, from Eq. (1.7)

$$T'_{pc} = 407 - 23.5 = 383.5\,\text{R},$$

and from Eq. (1.8),

$$p'_{pc} = \frac{777 \times 383.5}{407 + [0.152 \times (1 - 0.152) \times 23.5]} = 726.7\,\text{psi}.$$

The pseudoreduced properties are then, T_{pr} = (190 + 460)/383.5 = 1.70 and p_{pr} = 4,000/726.7=5.5, respectively. From Figure 1–8, Z = 0.9.

OPTION 2—Calculate the pseudocritical properties from Figure 1–9. The molecular weight is 20.19, so γ_g = 20.19/28.97 = 0.697. Therefore, from Figure 1–9, T_{pc} = 390 R and p_{pc} = 668 psi. These must be corrected by the inserts in Figure 1–9. Thus,

$$T_{pc} = 390 - 2 - 2 + 20 = 406\ \text{R}$$

$$p_{pc} = 668 - 2 + 9 + 92 = 767\ \text{psi}.$$

After adjusted for N_2, CO_2, and H_2S, respectively, the values of T_{pc} and p_{pc} are 406 R and 767 psi, compared with 407 R and 777 psi, as calculated explicitly in Table 1–4. To use the Z graph, these values must be adjusted again using Eqs. (1.7 and 1.8).

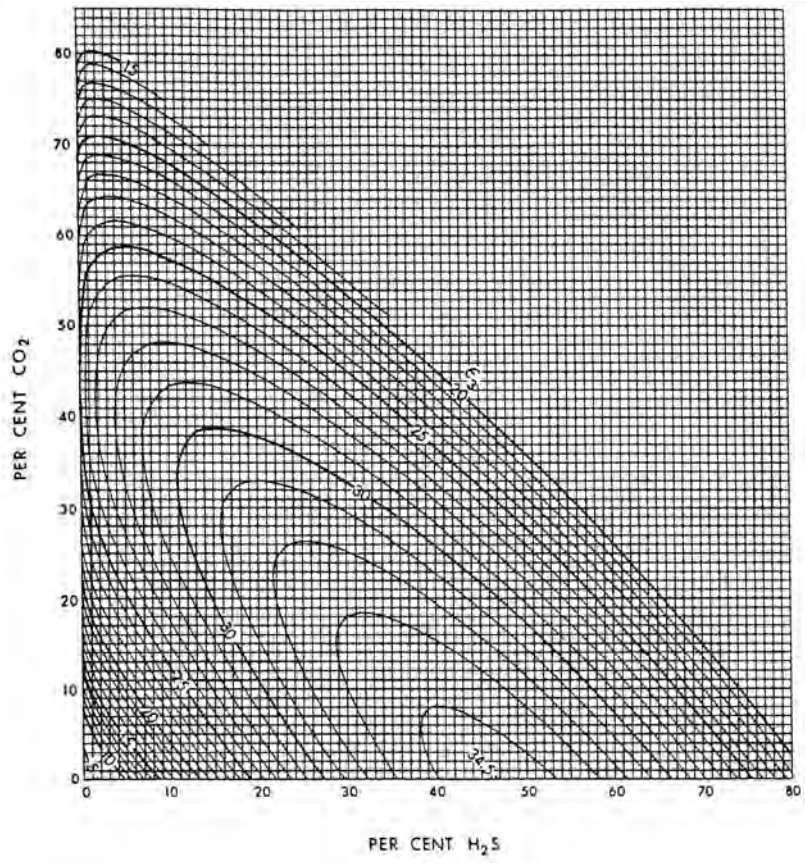

Figure 1–10 *Pseudocritical temperature adjustment factor, ε_3* (Wichert and Aziz, 1972)

1.6.3 Gas Density

The gas density is defined as mass (m) per unit volume (V). It can be calculated from the real gas law

$$\rho_g = \frac{m}{V} = \frac{pMW_m}{ZRT}, \tag{1.9}$$

In field unit, R is 10.73 psi-ft^3/lb-mol-R, ρ_g is in lb/ft^3, and p and T are in psi and R, respectively. In SI unit, R is 8.314 m^3-Pa/K-mol, ρ_g is in kg/m^3, and p and T are in Pa and K, respectively.

Table 1–4 PseudoCritical Properties for Example 1–4

Compound	y_i	MW_i	y_iMW_i	p_{ci}	y_ip_{ci}	T_{ci}	y_iT_{ci}
C_1	0.784	16.04	12.575	673	527.63	344	269.70
C_2	0.028	30.07	0.842	709	19.85	550	15.40
C_3	0.007	44.09	0.309	618	4.33	666	4.66
i-C_4	0.0008	58.12	0.046	530	0.42	733	0.59
n-C_4	0.0005	58.12	0.029	551	0.28	766	0.38
i-C_5	0.0008	72.15	0.058	482	0.39	830	0.66
n-C_5	0.0003	72.15	0.022	485	0.15	847	0.25
C_6+	0.0006	100.2	0.060	397	0.24	973	0.58
N_2	0.005	28.02	0.140	492	2.46	227	1.14
CO_2	0.021	44.01	0.924	1072	22.51	548	11.51
H_2S	0.152	34.08	5.180	1306	198.51	673	102.30
	1.000		20.19		p_{pc}= 777		T_{pc}= 407

Based on the gas specific gravity definition listed in Eq. (1.1), the molecular weight of the gas mixture (MW_m) in Eq. (1.9) can be replaced by γ_g. That gives the correlation between ρ_g and γ_g:

$$\rho_g = 2.7\frac{p\gamma_g}{ZT}. \tag{1.10}$$

Eq. (1.10) is in field unit where ρ_g is in lbm/ft^3, p and T are in psi and R, respectively.

1.6.4 Gas Formation Volume Factor

The formation volume factor relates the reservoir volume to the volume at standard conditions of any hydrocarbon mixture. In the case of a natural gas, the formation volume factor, B_g, can be related with the application of the real gas law for reservoir conditions and for standard conditions. Thus,

$$B_g = \frac{V}{V_{sc}} = \frac{ZnRT / p}{Z_{sc}nRT_{sc} / p_{sc}}. \tag{1.11}$$

For the same mass, nR can be cancelled out and, after substitution of $Z_{sc} \approx 1, T_{sc} = 60 + 460 = 520$ R, and $p_{sc} = 14.7$ psi, Eq. (1.11) becomes

$$B_g = 0.0283\frac{ZT}{p}(\text{res ft}^3 / \text{scf}). \tag{1.12}$$

If the initial formation volume factor of the gas, B_{gi}, is known, then the initial gas-in-place, G_i, can be calculated as

$$G_i = 43{,}560\frac{Ah\varphi S_g}{B_{gi}}(\text{scf}), \tag{1.13}$$

where A is the reservoir area in acres, h is reservoir net thickness in ft, ϕ is reservoir porosity, and S_g is gas saturation.

Example 1–5 Relating downhole rate with the rate at standard conditions

For a production rate of 10 MMscf/d (million cubic feet per day), calculate the downhole rate if downhole $p = 1{,}500$ psi, $T = 180$°F, and gas gravity is 0.64 (assume there are no non-hydrocarbon gases).

Solution

Gas gravity is 0.64, from Figure 1–9, $p_{pc} = 670$ psia and $T_{pc} = 370$ R. If $p = 1{,}500$ psi and $T = 180$°F, then $p_{pr} = 1{,}500/670 = 2.25$ and $T_{pr} = (180 + 460)/370 = 1.73$. From Figure 1–8, $Z = 0.89$.

Using Eq. (1.12) gives

$$B_g = 0.0283\frac{ZT}{p} = 0.0283 \times \frac{0.89 \times 640}{1{,}500} = 0.0107\frac{\text{res ft}^3}{\text{scf}}.$$

At a surface flow rate of 10 MMscf/d, the downhole flow rate is:

$$q = 10\ (\text{MMscf/d}) \times 0.0107 = 107\ \text{Mresft}^3/\text{d}.$$

Example 1–6 Calculation of the initial gas-in-place, G_i

The reservoir is about 2,100 acres in area and 70 ft thick, reservoir porosity is 18%, and gas saturation is 80%. Reservoir pressure and temperature are 4,000 psi and 180°F, respectively. The gas composition is the same as that in Example 1–3.

Solution

The gas deviation factor was calculated in Example 1–3 as 0.855. The initial formation volume factor, B_{gi}, is given by Eq. (1.12) and therefore,

$$B_{gi} = \frac{0.0283 \times 0.855 \times (180 + 460)}{4{,}000} = 3.87 \times 10^{-3} \text{ res ft}^3 / \text{scf}.$$

The initial gas-in-place then can be calculated by Eq. (1.13)

$$G_i = \frac{43{,}560 \times 2{,}100 \times 70 \times 0.18 \times 0.8}{3.87 \times 10^{-3}} = 2.38 \times 10^{11} \text{ scf}.$$

1.6.5 Gas Compressibility

The gas compressibility, c_g, often referred to as isothermal compressibility, has an exact thermodynamic expression:

$$c_g = -\frac{1}{V}\left(\frac{\partial V}{\partial p}\right)_T. \tag{1.14}$$

For an ideal gas, it can be shown that c_g is exactly equal to $1/p$. For a real gas, c_g is neither small nor constant. By using real gas law, the derivative $\partial V/\partial p$ can be evaluated:

$$\frac{\partial V}{\partial p} = -\frac{ZnRT}{p^2} + \frac{nRT}{p}\left(\frac{\partial Z}{\partial p}\right)_T. \tag{1.15}$$

Substitution of the volume, V, by its equivalent from real gas law and the derivative $\partial V/\partial p$ from Eq. (1.15) into Eq. (1.14) results in

$$c_g = \frac{1}{p} - \frac{1}{Z}\left(\frac{\partial V}{\partial p}\right)_T, \tag{1.16}$$

or, more conveniently,

$$c_g = \frac{1}{p} - \frac{1}{Z\,p_{pc}}\left(\frac{\partial Z}{\partial p_{pr}}\right)_T. \tag{1.17}$$

Eq. (1.17) is useful because it allows for the calculation of the compressibility of a real gas at any temperature and pressure. The gas deviation factor Z and the slope of the Standing-Katz correlation, $\partial Z/\partial p_{pr}$, at the corresponding temperature (i.e., the associated pseudoreduced temperature curve) are needed. The derivative can be calculated numerically with existing correlations, which will be discussed in a later section of this chapter.

1.6.6 Gas Viscosity

Viscosity is a measure of a fluid's internal resistance to flow. The viscosity of a natural gas, expected to increase with both pressure and temperature, is usually several orders of magnitude smaller than that of oil or water; and therefore, gas is much more mobile in the reservoir than either oil or water.

Gas viscosity correlations have been presented by a number of authors. However, the Carr, Kobayashi, and Burrows (1954) correlation presented in Figures 1–11 and 1–12, has been the most popular. Figure 1–11 allows the calculation of the viscosity at any temperature and at a pressure of 1 atm. Figure 1–12 provides the estimation of $\mu/\mu_{1\text{atm}}$, which is the ratio of the viscosity at an elevated pressure to the viscosity at 1 atm.

If the composition of the natural gas mixture is known, then the viscosity of the mixture at given temperature and 1 atm pressure can be calculated by

$$\mu_g = \frac{\sum \mu_{gi} y_i MW_i^{1/2}}{\sum y_i MW_i^{1/2}}, \tag{1.18}$$

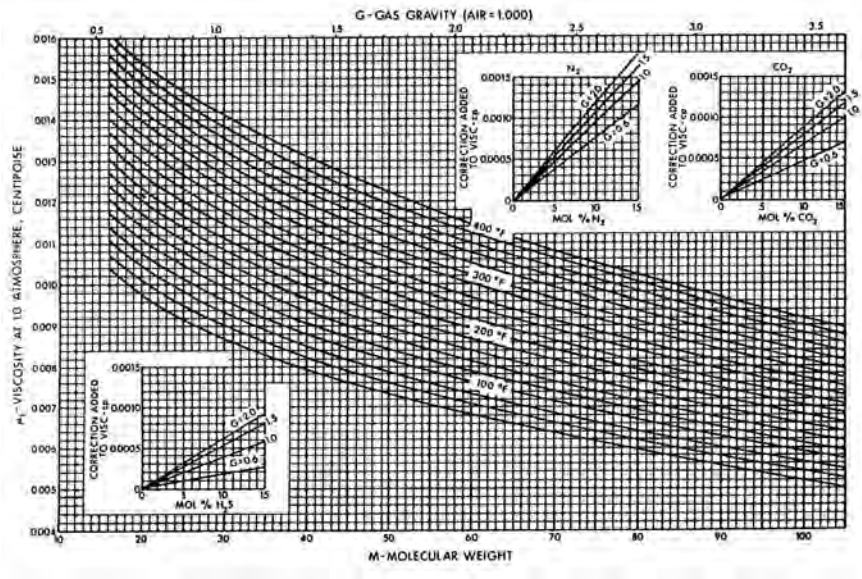

Figure 1–11 *Viscosity of natural gases at 1 atm* (Carr et al., 1954)

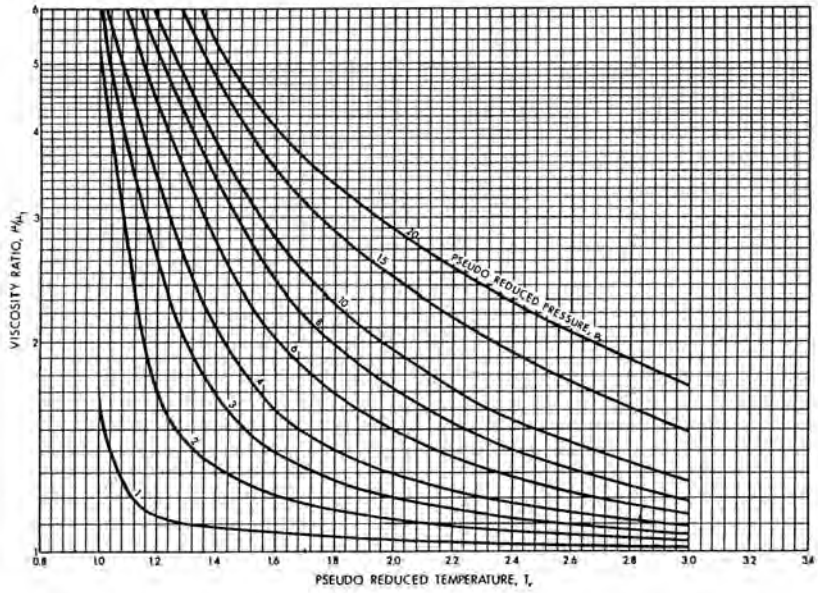

Figure 1–12 *Viscosity ratio at elevated pressures and temperatures* (Carr et al., 1954)

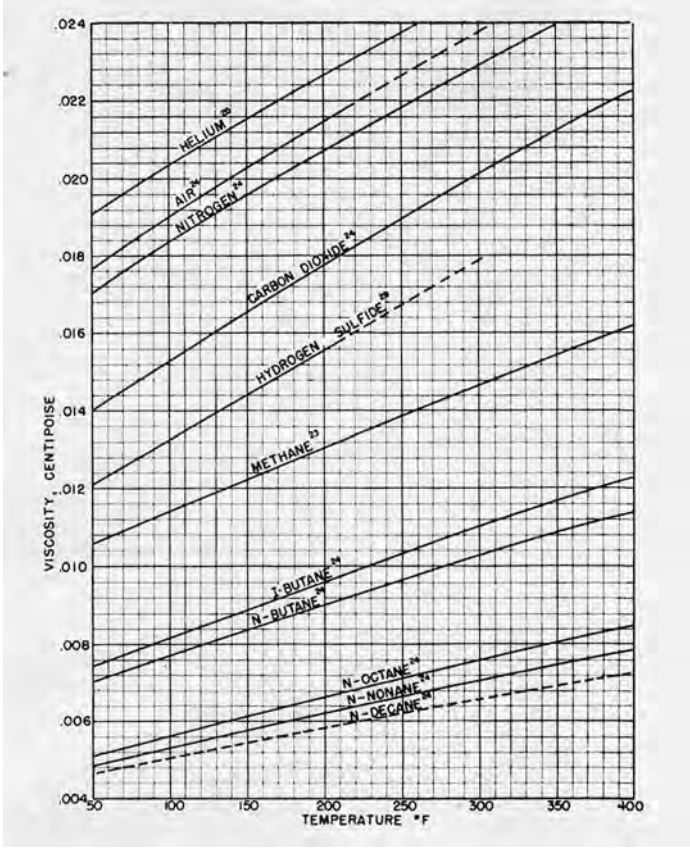

Figure 1–13 *Viscosity of gases at 1 atm* (Carr et al., 1954)

where μ_{gi} is the viscosity of the individual component in the gas mixture at given temperature and 1 atm which can be obtained from Figure 1–13. With the estimation of μ/μ_{1atm} from Figure 1–12, the viscosity at an elevated pressure and given temperature can be calculated. The most commonly used unit of viscosity is the centipoises (cp). 1 cp is 0.01poise (p), or 0.000672 lbm/ft-s, or 0.001 Pa-s.

Example 1–7 Calculation of gas viscosity

Calculate the natural gas viscosity at given conditions described in Examples 1–3 and 1–4.

Solution

For the natural gas in Example 1–3, the gas gravity is 0.65, and therefore, from Figure 1–11 and at T = 180°F, μ_{1atm} = 0.0122 cp. Since the pseudoreduced properties are p_{pr} = 5.96 and T_{pr} = 1.69, then from Figure 1–12, μ/μ_{1atm} = 1.85, therefore $\mu = 1.85 \times 0.0122 = 0.0226$ cp.

For the sour gas in Example 1–4, the gas gravity is 0.70, which results (from Figure 1–11) in μ_{1atm} = 0.0121 cp. However, the presence of nonhydrocarbon gases requires the adjustments given in the insets in Figure 1–11. These adjustments are to be added to the viscosity value and are 0.00005, 0.0001, and 0.0004 cp for the compositions of N_2, CO_2, and H_2S (in Example 1–3), respectively. Therefore, μ_{1atm} = 0.0127 cp. Since p_{pc} and T_{pc} are 777 psi and 407 R, respectively, then p_{pr} = 4,000/777 = 5.15 and T_{pr} = (190 + 460)/397.4 = 1.60. From Figure 1–12, μ/μ_{1atm} = 1.84, resulting in $\mu = 0.0127 \times 1.84 = 0.0234$ cp.

1.6.7 Useful Correlations

So far we have introduced the natural gas properties, such as gas specific gravity, gas deviation factor, gas viscosity, compressibility, and density. While these properties can be measured in the laboratory, it is usually expensive and time consuming. Data and graphical representations have been developed and are referred to in this chapter. Early calculations of properties, using graphs, were generally done by hand as shown in this chapter. Some of these graphs date back to early 1940s. With the advent of computers, many correlations have been developed based on the published data. Thus, properties can be computerized and numerically solved. Below is a summary of some useful correlations.

Correlations to Calculate Pseudocritical Properties

Some useful correlations to calculate pseudocritical properties from gas specific gravity are summarized in Table 1–5.

Example 1–8 Determination of pseudocritical properties

Calculate pseudocritical properties by using the Standing (1981) correlations listed in Table 1–5 and by using the properties given in Example 1–3.

Table 1–5 Correlations to Calculate Pseudocritical Properties from γ_g

Sutton (1985)

$$p_{pc} = 756.8 - 131.07\gamma_g - 3.6\gamma_g^2$$

$$T_{pc} = 169.2 + 349.5\gamma_g - 74.0\gamma_g^2$$

The gases used in developing Sutton correlation are high molecular weight gases, which are rich in heptanes plus with minor amount of carbon dioxide and nitrogen, and no hydrogen sulfide. It is valid when $0.57 < \gamma_g < 1.68$.

Guo and Ghalambor (2005)

$$p_{pc} = 709.604 - 58.718\gamma_g$$

$$T_{pc} = 170.491 + 307.344\gamma_g$$

These are valid for $H_2S < 3\%$, $N_2 < 5\%$, and total content of inorganic compounds less than 7%.

Standing (1981)

$$p_{pc} = 706 - 51.7\gamma_g - 11.1\gamma_g^2$$

$$T_{pc} = 187 + 330\gamma_g - 71.5\gamma_g^2$$

These correlations are developed based on low molecular weight California natural gases. They work only for natural gases without nonhydrocarbon gases.

Elsharkawy et al. (2000)

$$p_{pc} = 787.06 - 147.34\gamma_g - 7.916\gamma_g^2$$

$$T_{pc} = 149.18 + 358.14\gamma_g - 66.976\gamma_g^2$$

These are developed based on retrograde gases and suitable for gas condensate.

Ahmed (1989)

$$p_{pc} = 678 - 50(\gamma_g - 0.5) - 206.7y_{N_2} + 440y_{CO_2} + 606.7y_{H_2S}$$

$$T_{pc} = 326 + 315.7(\gamma_g - 0.5) - 240y_{N_2} - 83.3y_{CO_2} + 133.3y_{H_2S}$$

These correlations are applicable for mixture with impurities such as N_2, CO_2, H_2S.

Solution

From Example 1–3, the gas specific gravity is calculated as 0.65, therefore pseudocritical properties are

$$p_{pc} = 706 - 51.7 \times 0.65 - 11.1 \times 0.65^2 = 668 \text{ psi}$$

$$T_{pc} = 187 + 330 \times 0.65 - 71.5 \times 0.65^2 = 371 \text{ R}$$

Correlations to Calculate Gas Viscosity

One of the commonly used correlations to calculate gas viscosity is the correlation developed by Lee et al. (1966):

$$\mu_g = K \exp(X \rho_g^Y), \tag{1.19}$$

where

$$K = \frac{(9.4 + 0.02MW_g)T^{1.5}}{209 + 19MW_g + T}, \tag{1.20}$$

$$Y = 2.4 - 0.2X, \tag{1.21}$$

$$X = 3.5 + \frac{986}{T} + 0.01MW_g. \tag{1.22}$$

This correlation is quite accurate for typical natural gas mixtures with low nonhydrocarbon content. Here temperature (T) is in R, the density (ρ_g) is in gm/cm^3 (calculated at the pressure and temperature of the system), which can be predicted by using Kay's method (1936), and the resulting viscosity is expressed in centipoises (cp). Experimental viscosity data used to develop this correlation were presented for temperatures from 100 to 340°F and pressures from 100 to 8,000 psia. Other correlations to calculate gas viscosity include Dempsey (1965) and Dean and Stiel (1958).

Correlations to Calculate Gas Deviation Factor and Compressibility

Gas Deviation Factor Correlation by Dranchuk et al. (1974) is introduced below:

$$Z = 1 + (A_1 + A_2 / T_r + A_3 / T_r^3)\rho_r + (A_4 + A_5 / T_r)\rho_r^2 + A_5 A_6 \rho_r^5 / T_r + A_7 \rho_r^2 / T_r^3 (1 + A_8 \rho_r^2) \exp(-A_8 \rho_r^2), \quad (1.23)$$

where

$$\rho_r = 0.27(\frac{p_r}{ZT_r}), \quad (1.24)$$

$$\begin{aligned} A_1 &= 0.31506237 \\ A_2 &= -1.04670990 \\ A_3 &= -0.57832729 \\ A_4 &= 0.53530771 \\ A_5 &= -0.61232032 \\ A_6 &= -0.10488813 \\ A_7 &= 0.68157001 \\ A_8 &= 0.68446549 \end{aligned} \quad (1.25)$$

The Newton-Raphson iteration method can be used as Z-factor appears on both side of the equation:

$$Z_{n+1} = Z_n - (f_Z / f_Z'), \quad (1.26)$$

where Z_{n+1} and Z_n are the new and old values of Z-factor, f_Z is the function Z described in Dranchuk et al. (1974) correlation, and f_Z' is its derivative. This correlation is valid when the pseudoreduced temperature is between 1.05 and 3.0 and pseudoreduced pressure is between 0 and 30.

Other correlations for gas deviation factor include Brill and Beggs (1974), Hall and Yarborough (1973), and Takacs (1976). For sour gas, gas deviation factor can be calculated by using correlations developed by Piper (1993), Wichert and Aziz (1972), and Elsharkawy and Elkamel (2001).

With gas deviation correlations, the gas isothermal compressibility, c_g, can be calculated by using Eq. (1.17). Detailed calculation procedure can be found in Mattar et al. (1975), Trube (1957), Meehan and Lyons (1979), and Abou-Kassem et al. (1990). The range of validity will be the same as Z-factor.

1.7 Units and Conversions

We have used "oilfield" units throughout the text, even though this system of units is inherently inconsistent. We chose this system because more petroleum engineers "think" in Mscf/d (thousand standard cubic feet per day) for gas rate and psi for pressure than in terms of m^3/s (cubic meter per second) and Pa. All equations presented include the constant or constants needed with oilfield units. To employ these equations with SI units, it will be easier to first convert the SI units to oilfield units, calculate the desired results in oilfield units, and then convert the results to SI units. However, if an equation is to be used repeatedly with the input known in SI units, it will be more convenient to convert the constant or constants in the equation of interest. Conversion factors between oilfield and SI units are given in Table 1–6.

Example 1–9 Equations for the gas formation volume factor

Develop expressions for the gas formation volume factor and density in SI units, in terms of p, T and Z. Note: the standard conditions are: p_{sc}= 14.7 psia and T_{sc} = 520 R.

Solution

The standard conditions for SI units are as follows: SI: p = 101,325 Pa, T = 288.7 K, R = 8.314 J/mol-K.

Thus, the formation volume factor in SI units is:

$$B_g = \frac{V_{res}}{V_{sc}} = \frac{\left(\frac{ZnRT}{p}\right)_{res}}{\left(\frac{ZnRT}{p}\right)_{sc}} = \frac{\left(\frac{ZT}{p}\right)_{res}}{\left(\frac{(1)(288.7)}{(101{,}325)}\right)_{sc}} = 350.7\frac{ZT}{p}\left(\frac{\mathrm{m}^3}{\mathrm{sm}^3}\right), \tag{1.27}$$

while in oilfield units it is $0.0282\frac{ZT}{p}\left(\frac{\mathrm{res\,ft}^3}{\mathrm{scf}}\right)$.

For gas density:

$$\rho_g = \frac{p\left(MW_g\right)}{RTZ} = \frac{p\left(MW_g\right)}{(8.314)TZ} = \frac{0.1203p\left(MW_g\right)}{TZ}(\mathrm{kg/m}^3), \tag{1.28}$$

whereas, in oilfield units it is $\frac{0.0932p\left(MW_g\right)}{TZ}(\mathrm{lbm/ft}^3)$.

Table 1–6 Typical Units for Reservoir and Production Engineering Calculations *(Earlougher, 1977)*

Variable	Oilfield Units	SI	Conversion (Multiply Oilfield Unit)
Area	acre	m^2	4.04×10^3
Compressibility	psi^{-1}	Pa^{-1}	1.45×10^{-4}
Length	ft	m	3.05×10^{-1}
Permeability	md	m^2	9.9×10^{-16}
Pressure	psi	Pa	6.9×10^3
Rate (oil)	stb/d	m^3/s	1.84×10^{-6}
Rate (gas)	Mscf/d	m^3/s	3.28×10^{-4}
Viscosity	cp	Pa-s	1×10^{-3}

1.8 References

Abou-Kassem, J.H., L. Mattar, and P.M. Dranchuk. 1990. Computer calculations of compressibility of natural gas. *JCPT* 29 (Sept.–Oct.): 105.

Ahmed, T. 1989. *Hydrocarbon Phase Behavior*. Houston, TX: Gulf Publishing Co.

Brill, J.P. and H.D. Beggs. 1974. Two-phase flow in pipes. Intercomp Course, The Hague.

Brown, G.G., D. L Katz, C.G. Oberfell, and R.C. Alden. 1948. Natural gasoline and the volatile hydrocarbons. NGAA, Tulsa, OK.

Carr, N.L., R. Kobayashi, and D.B. Burrows. 1954. Viscosity of hydrocarbon gases under pressure. *Trans. AIME* 201: 264–272.

Dean, D.E. and L.I. Stiel. 1958. The viscosity of non-polar gas mixtures at moderate and high pressures. *AICHE J.* 4: 430–6.

Dempsey, J.R. 1965. Computer routine treats gas viscosity as a variable. *Oil & Gas J.* (August): 141.

Dranchuk, P.M., R.A. Purvis, and D.B. Robinson. 1974. Computer calculations of natural gas compressibility factors using the Standing and Katz correlation. *Institute of Petroleum Technical Series* IP 74-008.

Earlougher, R.C., Jr. 1977. *Advances in Well Test Analysis*. SPE monograph, SPE 5, Richardson, TX.

Economides, M.J., A.D. Hill, and C.A. Ehlig-Economides. 1994. *Petroleum Production Systems*. New York: Prentice Hall.

Elsharkawy, A.M., Y. Kh. Hashem, and A.A. Alikhan. 2000. Compressibility factor for gas condensate reservoirs. Paper SPE 59702.

Elsharkawy, A.M. and A. Elkamel. 2001. The accuracy of predicting compressibility factor for sour natural gases. *Petroleum Science and Technology* 19 (5&6): 711–731.

Guo, B. and A. Ghalambor. 2005. *Natural Gas Engineering Handbook*. Houston TX: Gulf Publishing Company.

Hall, K.R. and L. Yarborough. 1973. A new equation of state for Z-Factor calculations. *Oil & Gas* (June): 82.

Kay, W.B. 1936. Density of hydrocarbon gases and vapors at high temperature and pressure. *Ind. Eng. Chem:* 1014–1019.

Lee, A.L., M.H. Gonzalez, and B.E. Eakin. 1966. The viscosity of natural gases. *JPT* (August): 997–1000.

Mattar, L., G.S. Brar, and K. Aziz. 1975. Compressibility of natural gas. *Gas Technology* (October–December): 77.

McCain, W.D. Jr. 1973. *The Properties of Petroleum Fluids*. Tulsa, OK: Petroleum Publishing Company.

Meehan, D.N. and W.K. Lyons. 1979. Calculations programmable for gas compressibility. *Oil & Gas* (October): 74–78.

Piper, L.D., Jr. McCain, and J.H. Corredor. 1993. Compressibility factors for naturally occurring petroleum gases. Paper SPE 26668.

Sanger, P.J. and J. Hagoort. 1998. Recovery of gas condensate by nitrogen injection compared with methane injection. *SPE J* 3 (1): 26.

Standing, M.B. and D.L. Katz. 1942. Density of natural gases. *Trans. AIME* 146: 140–149.

Standing, M.B. 1981. *Volumetric and Phase Behavior of Oil Field Hydrocarbon Systems*. 9th printing. Dallas, TX: Society of Petroleum Engineers of AIME.

Sutton, R.P. 1985. Compressibility factors for high molecular weight reservoir gases. Paper SPE 14265.

Takacs, G. 1976. Comparisons made for computer Z-factor calculations. *Oil and Gas Journal* (December 20): 64–66.

Trube, A.S. 1957. Compressibility of natural gases. *J. of Petroleum Technology* (January): 69.

Wang, X. 2000. Pore-level modeling of gas-condensate flow in porous media. PhD diss., University of Houston.

Wang, X. and M.J. Economides. 2004. Aggressive fracture slashes turbulence in high-permeability gas well. *World Oil* (July).

Wichert, E. and K. Aziz. 1972. Calculation of Z's for sour gases. *Hydrocarbon Processing* 51 (5).

CHAPTER 2

Unique Issues in Natural Gas Exploration, Drilling, and Well Completion

2.1 Introduction

This chapter provides a fairly general and rudimentary exposure to problems in the exploration, drilling, and completion of natural gas wells. The chapter is by no means intended to be comprehensive but instead it provides an engineer, new to natural gas, insight about some of the challenges in accessing these reservoirs. For a petroleum engineer with experience in oil wells, the chapter provides a taste of those unique problems that are different from oil wells. The examples and calculations are also intended to showcase the idiosyncrasies of gas wells, as they differentiate from oils wells.

2.2 Exploration

Until the late 1970s, successful drilling was a hit-and-miss operation. New wells, even in presumably prolific areas, were termed "wildcat," and a rate of 10% (i.e. one good well and nine dry holes for every ten drilled) was considered attractive.

Few technologies in the history of the petroleum industry can match the importance of 3D seismic measurements and the impact they had on exploration and, today, production (Greenlee et al., 1994).

Aylor (1998) in an extensive study suggested that in the crucial period between 1990 and 1996, the time when 3D seismic measurements became commonplace, the overall success rate in identifying commercial wells increased from 14% to 49%. Also during the same period, wells covered by 3D seismic measurements increased from 1% to 44%. Equally important was the better identification of bad versus

good reservoir prospects. He found that 3D "reliably condemns 1.4 of the average 3.4 previously defined prospects, and discovers two new, previously unknown prospects per (3D) survey."

Modern seismic surveys allow a considerable improvement in a number of important exploration areas:

- Geologic structure delineation.
- By-passed zone identification.
- Well targeting, and especially avoiding bad ones.
- Reduction of previously required minimum reserves to exploit reservoirs.

Seismic measurements involve the generation of a seismic event, a mini-earthquake that is transmitted downwards from the surface. In the early days of the technology, several thousand pounds of chemical explosives were used. Today, heavy-duty thumper trucks (vibroseis) create vibrations by hammering the ground. The trucks produce a repeatable and reliable range of frequencies and are a preferred source compared with dynamite. In offshore locations, a specially designed vessel with airguns shoots highly pressurized air into the water, which creates a concussion that hits and locally vibrates the sea floor. This seismic energy transmits through the earth's crust, and as it encounters layers of rock with different acoustic properties, the energy bounces back as reflection (Dobrin, 1976). It is then recorded by an array of sensors called geophones or hydrophones. Figure 2–1 shows the seismic data collection process.

The product of density and velocity (ρv) is called acoustic impedance, Z. The amount of energy that is reflected depends on the contrast in acoustic impedance between the rocks. This can be expressed by a simple equation where the reflection coefficient R_c is defined as:

$$R_c = \frac{Z_2 - Z_1}{Z_2 + Z_1}, \tag{2.1}$$

where the subscripts 1 and 2 refer to layers 1 and 2, respectively.

Seismic signals, like all acoustic waves passing through media, separate into compressional (P-wave) and shear (S-wave) waves. The latter are converted from compressional waves. Compressional waves move along the direction of propagation but shear waves move perpendicular to the direction of propagation.

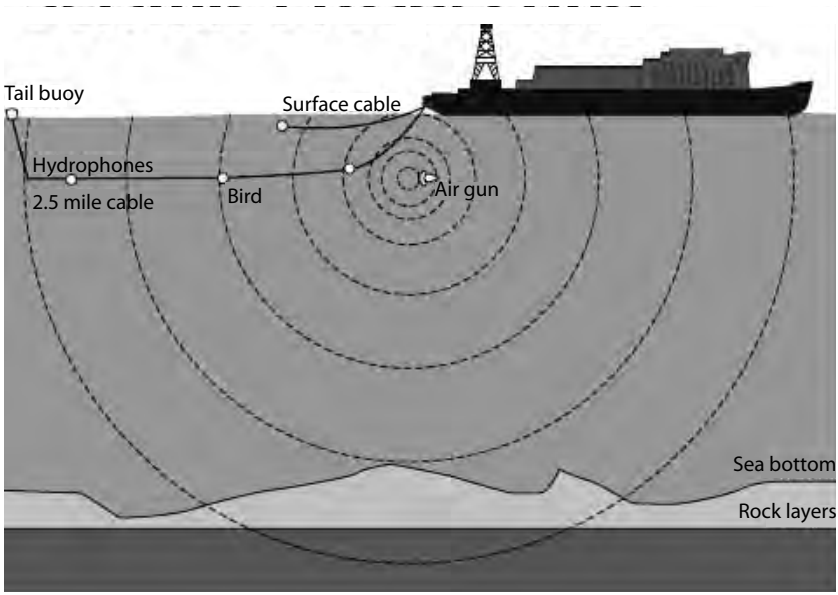

Figure 2–1 *Offshore seismic data acquisition*

The velocities of the two waves are given, respectively, by

$$v_c = \left(\frac{E + \frac{4\mu}{3}}{\rho} \right), \tag{2.2}$$

$$v_s = \left(\frac{\mu}{\rho} \right), \tag{2.3}$$

where E is the elastic modulus, μ is rigidity and ρ is density.

The reflection and arrival back to the surface of shear and compressional waves, and especially the knowledge that shear waves do not propagate through fluid, allows the identification of zones that are likely to contain fluids versus those that do not.

The degree to which seismic energy is converted to shear wave depends on the angle of incidence between layers and the contrast in the Poisson ratio between the two layers. Such contrast is related to lithology, porosity, pore pressure, and fluid content. The conversion of compressional to shear waves is the basis of, what in the seismic

discipline, has been labeled the amplitude versus offset effect (AVO), and it is instrumental in detecting natural gas. The term offset is the distance between the seismic source and the receiver.

In all cases, a seismic wave travels into the ground, traversing layers (strata) to considerable depth. Different geologic strata provide different reflection effects as the seismic wave traverses them.

An example of the type of seismic data and their interpretation is shown in Figures 2–2 and 2–3 from Mallick (2001). Figure 2–2 shows the S-wave impedance as plotted from an inversion of the AVO. It shows how distinct layers and their undulations can be differentiated in the visualization. The boxed region is the zone of interest where the Poisson ratio of layers is calculated. Specifically, this example is from an offshore natural gas deposit marking the bottom-simulating reflector (BSR), which represents the boundary between solid gas hydrates and free gas below it.

Figure 2–3 is a blowup of the zone of interest, showing the calculated Poisson ratios around the BSR. The illustration clearly shows zones of small values of the Poisson ratio denoting gas bearing formations. Poisson ratios between 0.3 and 0.4 denote shales. Water-bearing sands have Poisson ratios between 0.22 and 0.3, whereas gas bearing sands have Poisson ratios between 0.1 and 0.15.

The use of seismic "attributes" is a major advance in seismic data interpretation. As many as 20 different combinations of the character of seismic data have been used to further hone the analysis. An example is shown in Figure 2–4 from Alsos et al. (2002). The ratio of the compressional-reflection to shear-reflection amplitude reveals both lithology and fluid content. In such case the representation shows both the sand deposition and hydrocarbon accumulations inside the area of interest.

It is considerably outside the scope of this book to provide expert analysis and interpretation of seismic signals, and especially, seismic attributes (which are even more advanced). However, for natural gas engineers who use seismic information and the identification of natural gas bearing formations, it is easy to see why natural gas reservoirs are far more readily identifiable than both formations without fluids and those containing mostly liquids (water and oil).

Eqs. (2.1 to 2.3) which form the basis of all seismic analyses contain the density of a layer as one of the prominent variables.

The composite density of a layer would be

$$\rho = (1 - \phi)\rho_f + \phi(1 - S_W)\rho_{o,g} + \phi S_W \rho_W \,, \tag{2.4}$$

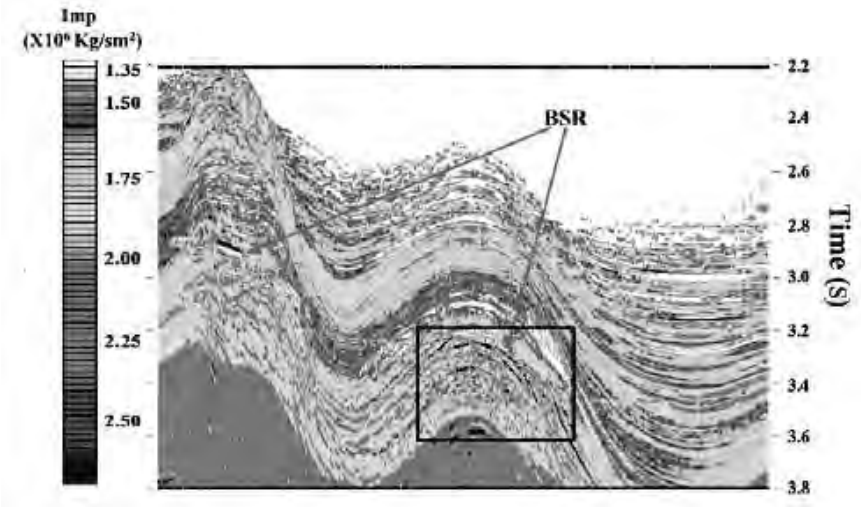

Figure 2–2 *S-wave impedance from AVO inversion for an offshore natural gas bearing structure. The boxed region is the area of interest below the BSR* (Mallick, 2001)

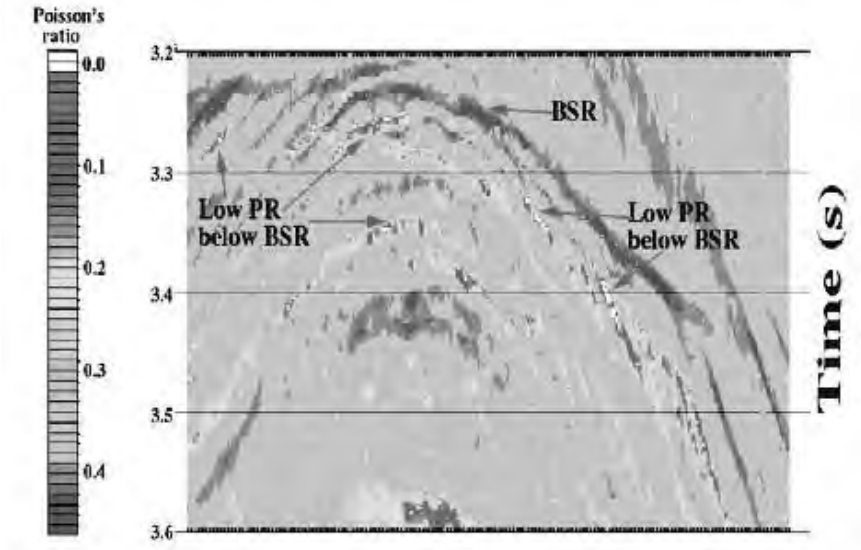

Figure 2–3 *Calculated Poisson ratios for the zone of interest in Figure 2–2* (Mallick, 2001)

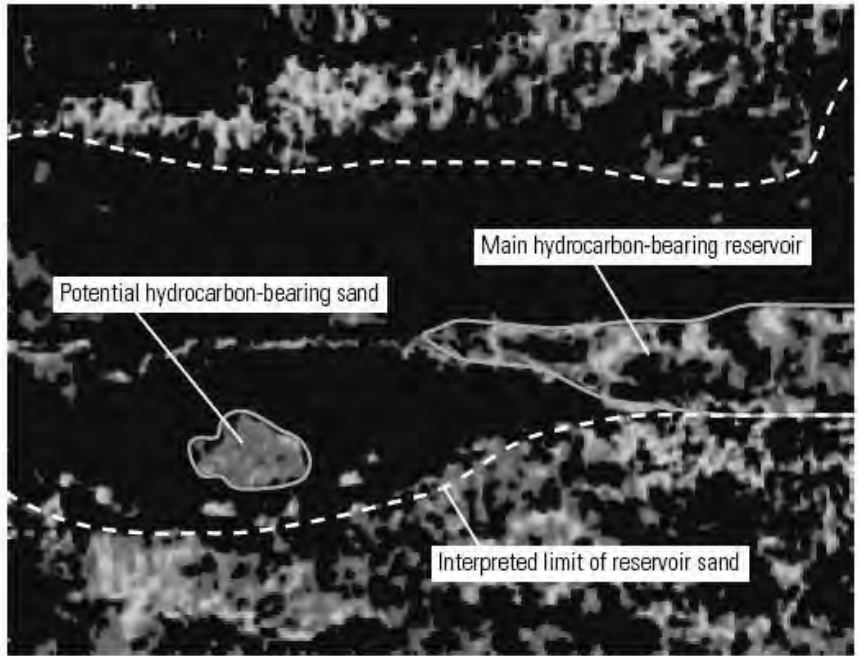

Figure 2–4 *Seismic attribute of a structure: Ratios of compressional-reflection to shear-reflection amplitudes* (Alsos et al., 2002)

where ϕ is porosity, S_w is the water saturation, and ρ_f, ρ_w and $\rho_{o,g}$ are the densities of the formation rock, water and oil or gas, respectively. It is worthwhile to see the difference in the respective composite densities for a dry, oil bearing, and gas bearing formations as in the following Example 2–1.

Example 2–1 Calculation of the composite densities of a dry, an oil bearing, and a gas bearing formation

For both fluids charged formation use $\phi = 0.25$ and $S_w = 0.25$. Densities are $\rho_f = 165$ lb/ft^3, $\rho_w = 65$ lb/ft^3, and $\rho_o = 55$ lb/ft^3. For the gas use $\gamma_g = 0.67$, $T = 180$°F, and $p = 3{,}000$ psi.

Solution

Using Eq. (2.4) for the oil case

$$\rho = (1-0.25)\times 165 + 0.25\times(1-0.25)\times 55 + 0.25\times 0.25\times 65 = 138 \text{ lb/ft}^3.$$

If there is no oil and therefore the formation has only brine, i.e., $S_w = 1$, then the total density, $\rho = 140$ lb/ft^3, which shows a small difference between an oil bearing and a water bearing formation.

For the gas though, using the Dranchuk (1974) correlation, the Z-factor is calculated as 0.871. Using Eq. (1.10) and the procedure outlined in Chapter 1, the gas density at the given conditions is 9.8 lb/ft^3. Eq. (2.4) gives then $\rho = 129$ lb/ft^3, a considerable difference in the composite density and the reason why seismic measurements are so much more definitive in the identification of the presence of gas.

2.3 Drilling

Drilling is one of the most important and complex operations in the oil and gas industry. It involves a lot of equipment (drill bits and pipes/strings, casings), fluids (drilling fluids/muds, completion fluids, cement slurries, formation fluid), and movements (equipment movement, fluids and solids/rock cutting movement, and circulation). The drilling process can be operated in a drilling rig that contains all the necessary equipment. A typical drilling method is the well-known rotary drilling, shown in Figure 2–5, where a roller-bit is attached to a drilling pipe or string. While rotating the drill string, the drill bit breaks into the earth and reaches different depths, and eventually hits the targeted pay zone. At the same time, drilling fluid or mud is pumped down through the drilling pipe to provide hydraulic impact, control the pressure, stabilize exposed formation, prevent fluid loss, and bring the rock cuttings to the surface through the annulus formed between the drill pipe and the created hole.

During this process, different types and sizes of bits might be needed depending on the formation rock hardness and borehole size requirements (usually the bit size is smaller when the drilling depth is deeper). Similarly, mud weight has to be changed along with the drilling depth, because at different depth and geologic layers, the formation pressure and permeability are different (the higher the pressure, the heavier the mud weight).

During the drilling process, different types of casing (conductor, surface casing, intermediate casing, etc) are placed in the hole. Cement is usually placed between the outside of the casing and the borehole to provide structural integrity and isolation between different zones (an example of a gas well wellbore is shown in Figure 2–8 in the Section 2.4 “Well Completions”).

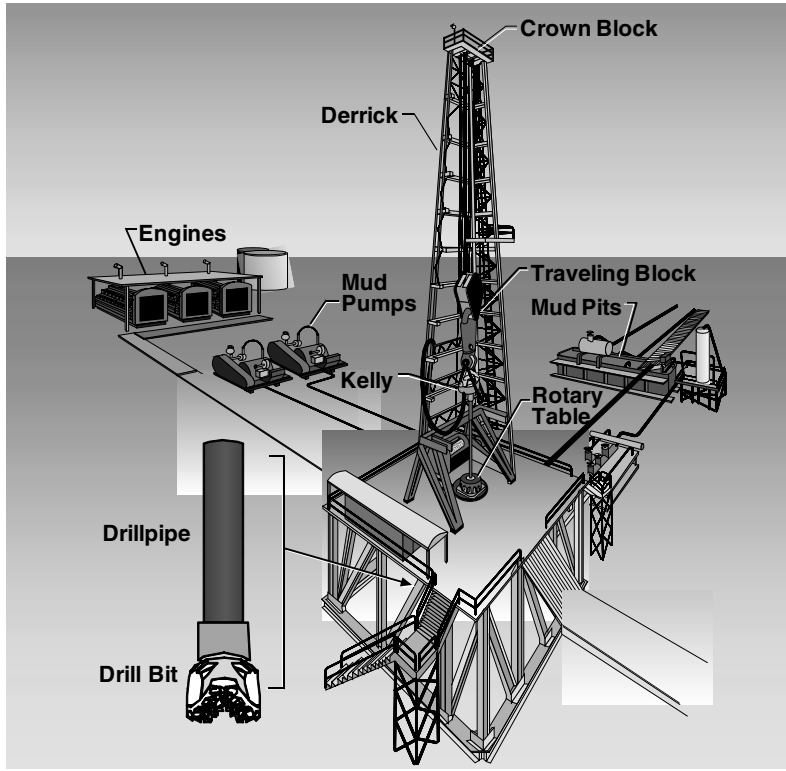

Figure 2–5 *Drilling rig components*

The objectives of drilling are to reach the target zone with minimum cost and time, to deliver a usable and stable borehole for further completion and production, to minimize pay zone damage and fluid invasion; and, of course, to ensure all personnel are safe, no contamination to the fresh water, and no (or minimum) damage to the environment.

2.3.1 Natural Gas Well Drilling

There are several unique problems that affect the drilling of natural gas wells. While this chapter and this section are not intended to provide a comprehensive description of drilling, below a number of engineering calculations and considerations dealing with the drilling of gas wells are mentioned.

In addition to the issues covered below, there are certain concerns that, while not unique to natural gas wells, may require increased attention (Prof. Ali Ghalambor, Personal Communication, 2009):

- There could be a need for higher grade casing because of the occasional need for higher burst rating in gas wells.
- When using oil based drilling fluids, gas solubility could be a problem. Oil based systems can partially mask the existence of a gas kick, thereby creating well control situations in gas wells.
- Although not exclusive to gas wells, but more likely to occur, when the reservoir fluid is associated with corrosive gases, such as H_2S and CO_2, there would be increase demands from the casing selection, using corrosion resistant alloys.
- Although all industry well control schools stress that to handle well control issues in gas wells is similar to oil wells, the wellhead equipment (blowout preventer or BOP, flanges, connections, etc.) could require higher premium products on some gas wells because of higher wellhead pressures and leak potential.

The reservoir pressure is of crucial importance to drilling and it can lead to a series of problems from lost circulation to blowouts and stuck pipes. There are some differences between oil and gas reservoirs. Oil reservoirs, as discussed in Chapter 1, are likely to be found at far shallower depths than gas reservoirs. The latter may be found beneath impermeable barriers of considerable thickness. Thus, the encountered pressure upon entering a gas reservoir may be quite large, a combination of both hydrostatic pressure and the weight of impermeable overburden. Anticipation of such large pressure is essential for both blowout prevention, and the eventuality of a "gas kick," a sudden influx of reservoir gas into the drilling fluid column.

Pressure is measured in psi but also, in traditional drilling units, it is measured in EMW (equivalent mud weight) and the unit is lb/gal. In the oil and gas industry lb/gal is often referred to as ppg. Water density of 1 g/cc or 1,000 kg/m^3 or 62.4 lb/ft^3 is equal to (62.4/7.48=) 8.34 lb/gal.

The hydrostatic pressure in psi with density, ρ in lb/ft^3 is given by

$$p = \frac{\rho H}{144}, \tag{2.5}$$

where H is the depth in ft.

If the density is 62.4 lb/ft^3 (water) then the hydrostatic pressure gradient is the well known 0.433 psi/ft. Similarly, the lithostatic or overburden gradient can be calculated. Using ρ = 160 lb/ft^3 (sandstone) then the gradient is 1.1 psi/ft. For many reservoir brines the pressure gradient is often equal to 0.465 psi/ft.

Predicting reservoir pressure ahead of entering a layer of interest is important. Assuming that a barrier is at a depth H_a and the depth below the barrier is H_b then the expected pressure upon entering the formation just below the barrier would be:

$$p = 0.465H_a + 1.1(H_b - H_a), \tag{2.6}$$

where 0.465 psi/ft is the reservoir fluid gradient and 1.1 psi/ft is the lithostatic or overburden gradient.

Example 2–2 Calculation of the expected pressure at the target zone and required mud weight

An onshore well is drilled to a depth of 25,000 ft. At 21,000 ft, there is a barrier that extends to the target. Repeat the same calculation for an offshore well with the same depth below the mudline with water depth of 5,000 ft.

Solution

1. Onshore: Using Eq. (2.6), the expected pressure is calculated as

$$p = 0.465 \times 21{,}000 + 1.1 \times (25{,}000 - 21{,}000) = 14{,}165 \text{ psi}.$$

Rearranging Eq. (2.5) at 25,000 ft depth with pressure of 14,165 psi, the fluid density is

$$\rho = \frac{144 \times 14{,}165}{25{,}000} = 81.6 \text{ lb/ft}^3.$$

The required mud weight is 81.6 lb/ft^3/7.48 = 10.9 lb/gal.

2. Offshore: Using a modification of Eq. (2.6)

$$p = 0.465 \times 26{,}000 + 1.1 \times (30{,}000 - 26{,}000) = 16{,}400 \text{ psi}$$

The equivalent mud weight is 10.5 lb/gal, at a total depth of 30,000 ft.

2.3.2 Drilling Deep Wells

Drilling for gas at depths of more than 15,000 ft below the mudline, especially offshore, where total depth from the surface may exceed 30,000 ft, is likely to encounter temperatures surpassing 600°F and pressures over 40,000 psi. At those conditions, MWD/LWD (measurements while drilling and logging while drilling) tools cannot function, and thus, pressure management during the drilling operation must be made through mathematical models. These models use surface measurements and then extrapolate downhole pressures using fluid density and viscosity (Bland et al., 2005). Pressure and temperature driven compression and expansion of fluids become considerable at the ranges of conditions that are encountered. Figure 2–6 shows actual laboratory measurements of fluid density at 30,000 psi versus extrapolated density based on correlations valid up to 20,000 psi. The departure is significant. Assuming a total depth of 30,000 ft, a depth that is likely to be encountered only in modern offshore applications, the difference in density (0.09 g/cc) could result in 1,200 psi difference between the extrapolated and actual pressures exercised by the drilling fluid column at that depth.

It seems that an inflection point for base drilling fluid density happens at about 7,500 ft for commonly encountered pressures and temperatures. Measured values are shown in Figure 2–7.

2.3.3 Drilling Damage

Aqueous phase trapping is an important consideration in selecting drilling fluids, and while this is true in all wells, it is especially true for low-permeability, low-pressure gas wells. After fitting numerous experimental data, Bennion et al. (1996) presented correlations that allow for the determination of the "index of aqueous phase trap," I_{APT}, whose value denotes the potential severity of Aqueous Phase Trapping. I_{APT} is given by:

$$I_{APT} = 0.25\log(k_a) + 2.2S_{wi}, \tag{2.7}$$

where k_a is the formation absolute permeability to air and S_{wi} is the initial water saturation, which in certain cases, may not be the interstitial saturation.

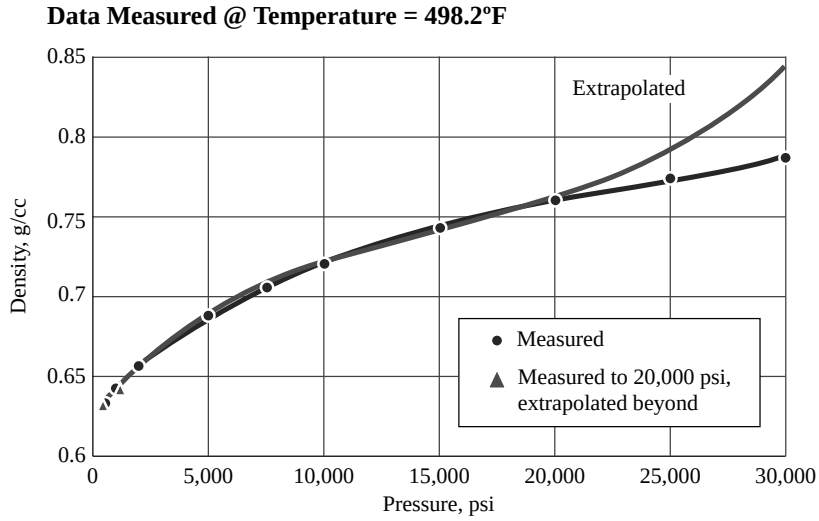

Figure 2–6 *Measured versus extrapolated from correlations drilling fluid densities at high pressures* (Bland et al., 2005)

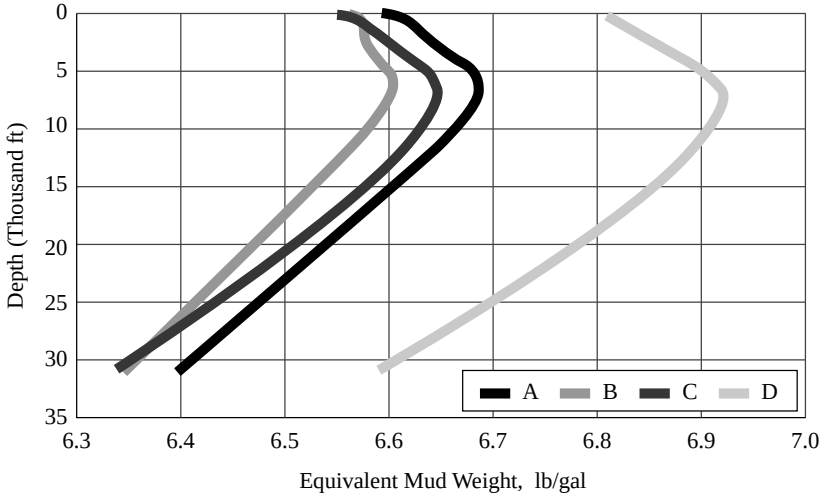

Figure 2–7 *Measured drilling fluid densities of four fluids at depth and at predicted temperatures and pressures* (Bland et al., 2005)

For $I_{APT} > 1$ aqueous phase trap is not likely to happen, for $0.8 > I_{APT} > 1$ the formation may exhibit sensitivity to phase trapping, and for $I_{APT} < 0.8$ the formation is likely to undergo significant phase trapping.

The I_{APT} can be adjusted by three factors: the relative permeability adjustment (I_{RPA}), the invasion profile adjustment (I_{IPA}), and the reservoir pressure adjustment (I_{PA}).

Thus,

$$I_{APT} = 0.25\log(k_a) + 2.2S_{wi} - I_{RPA} - I_{IPA} + I_{PA}. \tag{2.8}$$

The three factors are given by

$$I_{RPA} = 0.26\log(x - 0.5)\ , \tag{2.9}$$

$$I_{IPA} = 0.08\log(r_p + 0.4)\ , \tag{2.10}$$

$$I_{PA} = 0.15\log(p) - 0.175\ , \tag{2.11}$$

where x is the shape factor of the relative permeability curve (ranges between 1 and 8), r_p is the fluid invasion in cm and p is the reservoir pressure in MPa.

Example 2–3 Determination of the index of aqueous phase trapping

Assume k_a = 100 md, S_{wi} = 0.3, x = 2, r_p = 100 cm, and p = 30 MPa. Repeat the calculation for k_a = 1 md, r_p = 10 cm, and p = 15 MPa.

Solution

Using Eqs. (2.9, 2.10, and 2.11) with the first set of variables, I_{RPA} = 0.046, I_{IPA} = 0.16, and I_{PA} = 0, respectively. Thus,

$$I_{APT} = 0.25 \times \log(100) + 2.2 \times 0.3 - 0.046 - 0.16 + 0.046 = 1,$$

which suggests no aqueous trapping.

Repeating with the second set of variables from Eqs. (2.9, 2.10, and 2.11), I_{RPA} = 0.046, I_{IPA} = 0.08, and I_{PA} = 0.046, respectively, and thus,

$$I_{APT} = 0.25\log(1) + 2.2 \times 0.3 - 0.046 - 0.08 + 0 = 0.53,$$

which suggests significant aqueous trapping in this low-permeability, under-pressured formation.

2.3.4 Gas Kick

A sudden influx of reservoir fluids into the drilling fluid column, often happening in gas wells and known as a "gas kick," is an unwanted event, and results in the increase in the annular pressure compared with the shut-in drill pipe pressure. This would require weighing the drilling mud further in order to circulate the gas kick out and also to prevent further gas influx.

The initial shut-in pressure in the drill pipe, $p_{dp,i}$ is given

$$p_{dp,i} = \left[(dp/dH)_r - (dp/dH)_{df}\right]H, \tag{2.12}$$

where $(dp/dH)_r$ and $(dp/dH)_{df}$ are the gradients of the reservoir and drilling fluids, respectively in psi/ft and H is the vertical depth. After a kick the stabilized pressure at the annulus head will be

$$p_{dp,i} = (dp/dH)_r H - (dp/dH)_k \Delta H_k - (dp/dH)_{df}(H - \Delta H_k), \tag{2.13}$$

where $(dp/dH)_k$ is the gradient of the kick and ΔH_k is the kick height.

The following example shows the expected pressure increase in two reservoirs, one shallow, one deep, as a result of a gas kick. The example shows the considerable difference between shallow and deep formations and the inherent danger involved in the latter because of the subtlety of gas kick which may not be detected (Schöffmann and Economides, 1991).

Example 2–4 Calculation of the expected increase in pressure at the top of the annulus

Two reservoirs, one shallow (H = 5,000 ft, T = 150°F, p = 2,500 psi) and one deep (H = 25,000 ft, T = 450°F, p = 12,000 psi) experience kicks, each of 20,000 scf of 0.6 gravity gas. The hole diameter is 9 5/8 in. and the drill pipe diameter is 5 in. The reservoir pressure and the drilling fluid gradients are 0.5 and 0.45 psi/ft, respectively.

Solution

Using the hole and the drill pipe diameters, the cross-sectional area of the annulus is 0.37 ft^2.

For the shallow well, using the physical property calculations of Chapter 1 at the given pressure and temperature, the formation volume factor, $B_g = 5.94 \times 10^{-3}$ $resft^3/scf$ and the density, $\rho = 7.68$ lb/ft^3. For the deep well, the corresponding values are $B_g = 3.1 \times 10^{-3}$ $resft^3/scf$

and the density, ρ = 14.74 lb/ft^3. The kick gradients are the densities in lb/ft^3 divided by 144 and they would be 0.053 psi/ft and 0.102 psi/ft, respectively.

Multiplying the 20,000 scf by the respective formation volume factors, the kick volumes are 119 and 62 ft^3, respectively. Dividing by the annular area of 0.37 ft^2 provides the initial heights of the two kicks: 321 and 167 ft, respectively.

Using Eq. (2.12), the shut-in pressure for the shallow well is 250 psi. Using Eq. (2.13) the annulus head pressure is 378 psi, 51% larger than the static shut-in pressure.

For the deep well, the shut-in pressure is 1,250 psi but the annulus head pressure is 1,308 psi, less than 5% increase over the static pressure. Such small increase may mask a kick in deep gas wells. It is essential that, during drilling, such eventuality is anticipated and measures are taken to control it.

2.4 Well Completions

Once the well is drilled to the designated depth and the gas reservoir is evaluated to be economically attractive, the well is then ready to be completed. The completion is very important as it is the channel to connect the wellbore and the reservoir. It is a multi-disciplinary exercise that requires the completion, drilling, reservoir, and production engineers and rock mechanics specialists to work together to make it successful.

As discussed in the drilling section, a wellbore, shown in Figure 2–8, usually contains several casing strings: drive pipe, conductor pipe, surface casing, and production casing. Some of them contain intermediate casing and liner(s). All of these pipes are cemented in place to either protect fresh water (surface pipe), or prevent loose shale, sand, and gravel (if gravel is used in the completion) from coming into the wellbore causing near wellbore damage. Inside these casing strings, the production tubing, where the reservoir fluid will be produced from the reservoir, enter through the well completion, and get to the surface. Between the production tubing and casing, annular fluid is filled in to prevent tubing burst due to the pressure inside of the tubing. Details inside the tubing such as safety valve and nipples are not shown.

Several completion types (shown in Figure 2–9) can be chosen. A "barefoot" or open completion consists of a packer and tubing above the interval of interest. Slotted liners or gravel packed wells with screens often in association with cemented, cased, and perforated

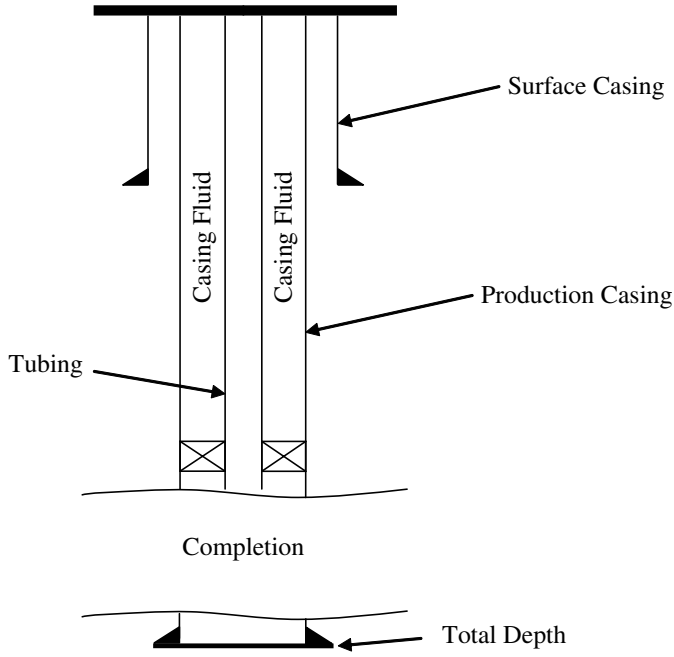

Figure 2–8a *Onshore wellbore example*

wells is another family of completions. Finally, fully automated completions with measurement and control systems optimize well and reservoir performance and reservoir economics without human intervention (an "intelligent" completion) (Schlumberger, 2009). How to choose the proper completion type is an important question. It usually depends on the reservoir rock properties to determine if sand control is needed, well life expectancy, and the cost. One thing that has not been taken into account in gas well completion and is critical in the gas well production is turbulent flow. This will be discussed in depth in Chapter 3 when dealing with natural gas production.

Again, as with other sections of this chapter, the intention here is not to dwell on the general issues related to well completion, but to discuss some of the unique aspects or those with more serious impact for gas wells.

2.4.1 Liquid Loading in Gas Wells

Liquid loading in gas wells is not a new subject. It has been known for many years (Turner et al., 1969; Lea and Nickens, 2004; Gool and Currie, 2008; Solomon et al., 2008). It happens when the gas velocity

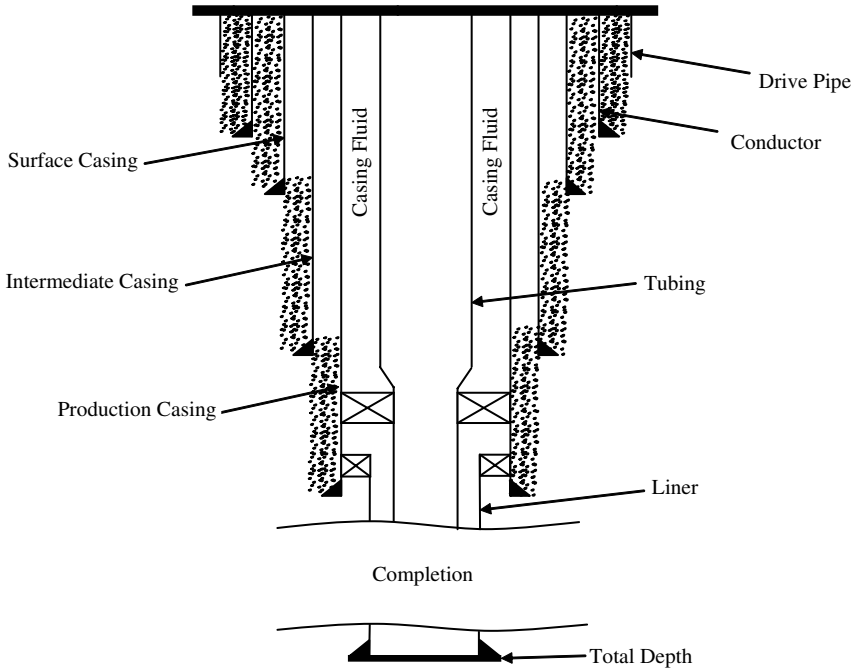

Figure 2–8b *Offshore wellbore example*

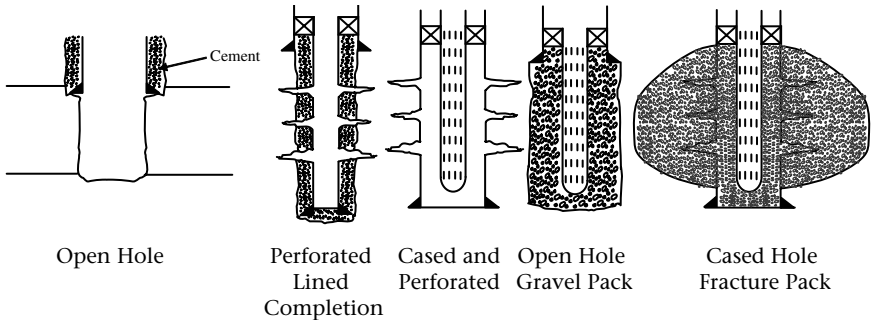

Figure 2–9 *Selected completion types*

drops below a certain "gas critical velocity," and the gas can no longer lift the liquids (hydrocarbon condensate liquid or reservoir water) up to the surface. The liquids will fall back and accumulate at the bottom of the well, reduce gas production, or even "kill" the well.

There are several models (Turner et al., 1969; Coleman et al., 1991; Nosseir et al., 1997) to calculate the gas critical velocity, v_{gc} in ft/s. One of the most commonly used is Turner et als (1969) "droplet model":

$$v_{gc} = 17.6 \frac{\left[\sigma\left(\rho_l - \rho_g\right)\right]^{0.25}}{\rho_g^{0.5}}, \tag{2.14}$$

where σ is the surface tension in dynes/cm (g-cm/s^2) or lbm-ft/s^2 depending on the units of the gas and liquid densities. The assumption is the Reynolds number is in the range of 10^4 to 2×10^5, the drag coefficient is about 0.44, and the Weber number, a dimensionless number in fluid mechanics to analyze fluid flows where there is an interface between two different fluids, is between 20–30 (Turner et al., 1969).

Once the tubing size is known, the tubing cross-sectional area, A, can be calculated. Further, the gas critical flow rate can be obtained as Av_{gc} in ft^3/s. By using gas law, the gas critical flow rate in MMscf/d can be calculated

$$q_{gc} = \frac{3.06 p v_{gc} A}{ZT}. \tag{2.15}$$

The constant 3.06 equals to $60 \times 60 \times 24 \times 520/(14.7 \times 10^6)$.

Eqs. (2.14 and 2.15) are valid at any given well depth but for convenience, the gas critical velocity is usually evaluated at the wellhead. It is clear that if there is no liquid in the wellbore or the gas rate is high enough to lift the liquid upwards, then liquid loading problem can be prevented or alleviated. Therefore several approaches can be used to reduce liquid loading in gas wells (Lea and Nickens, 2004):

- Prevent liquids formation in the downhole.
- Use smaller tubing.
- Lower wellhead pressure.
- Use pump or gas lift.
- Foam the liquids.

Sizing production tubing to eliminate liquid loading is not a trivial task in gas well completions. A brand new gas well with high reservoir pressure might need a big tubing to ensure maximum productivity. When the well is produced for a while and the reservoir pressure declines or the well produces a lot of liquid, a smaller diameter tubing might be better.

Example 2–5 Determination of the gas critical velocity to prevent liquid loading

A gas well with tubing OD = 3.5 in. has tubing weight and grade of 9.3 lbm/ft and H-40, respectively. Important variables are: σ = 65 dynes/cm, ρ_l = 62.4 lbm/ft^3, T = 190°F, γ_g = 0.61. Assume there is neither H_2S nor CO_2. Determine the gas critical velocity and flow rate at flowing tubing pressures p_{ft} = 500, 750, 1,000, 1,250, and 1,500 psi, respectively.

Solution

Using the Schlumberger handbook, the tubing ID is obtained as 2.992 in. Then A = 3.14 × (0.5 × 2.992/12)^2 = 0.488 ft^2.

The following calculation demonstration is based on p_{ft} = 500 psi. Use correlation discussed in Chapter 1, calculate Z = 0.962. Calculate gas density, ρ_g, by Eq. (1.10):

$$\rho_g = 2.7\frac{500\times 0.61}{(190+460)\times 0.962} = 1.32 \text{ lbm/ft}^3.$$

The gas critical gas velocity can be calculated by Eq. (2.14)

$$v_{gc} = 17.6\times\frac{(65/13825)^{0.25}\times(62.4-1.32)^{0.25}}{1.32^{0.5}} = 11.2 \text{ ft/s}.$$

The gas critical flow rate can be calculated by Eq. (2.15)

$$q_{gc} = \frac{3.06\times 500\times 11.2\times 0.0488}{(190+460)\times 0.962} = 1.34 \text{ MMscf/d}.$$

Similar calculation can be conducted at different flowing tubing pressure for the same well. The results are summarized in Table 2–1. Results show that the higher the flowing tubing pressure is, the higher the critical flow rate has to be to prevent liquid loading.

If changing the tubing to ID = 3.548 in. (OD = 4 in., weight = 9.5 lbm/ft, grade = J-55), similar calculations can be performed. The gas critical flow rates are also summarized in Table 2–1 (the last

Table 2–1 Results from Example 2–5

p psia	Z	ρ_g lbm/ft^3	v_{gc} ft/s	q_{gc}(3.5") MMscf/d	q_{gc} (4.0") MMscf/d
250	0.98	0.65	16.1	0.94	1.32
500	0.962	1.32	11.2	1.34	1.88
750	0.945	2.01	9.06	1.65	2.32
1,000	0.930	2.72	7.76	1.92	2.69
1,250	0.917	3.45	6.87	2.15	3.02
1,500	0.907	4.19	6.22	2.36	3.32

column, all other results are the same as those from 3.5 in. tubing). The gas critical flow rate versus the flowing tubing pressure for both 3.5 and 4 in. tubings is plotted in Figure 2–10. Results show that, at the same flowing tubing pressure, bigger tubing requires higher gas flow rate to lift the liquid.

It is worth noting that some of the later studies (Nosseir et al., 1997, Solomon et al., 2008) have indicated the results from the Turner et al. model should be adjusted by 20% to fit field data with wellhead pressure of 800 psia or above. That means the gas critical flow rate should be 20% higher than those calculated from the Turner et al. model (see dashed lines in Figure 2–10).

Completion can be very expensive, especially offshore. Before installing smaller diameter tubing, several factors should be taken into account (Lea and Nickens, 2004):

- Is a smaller tubing indicated for the long-term or, is existing tubing adequate with simple modifications, such as plunger lift?
- After installing smaller tubing, will the flow be above critical velocity at all depths including the bottom of the tubing?

At the same time, the tubing should be extended near the perforations to eliminate casing flow.

2.4.2 Casinghead Pressure

Casinghead or casing pressure is another challenging issue especially in gas wells. Theoretically, the casing pressure in the annulus should

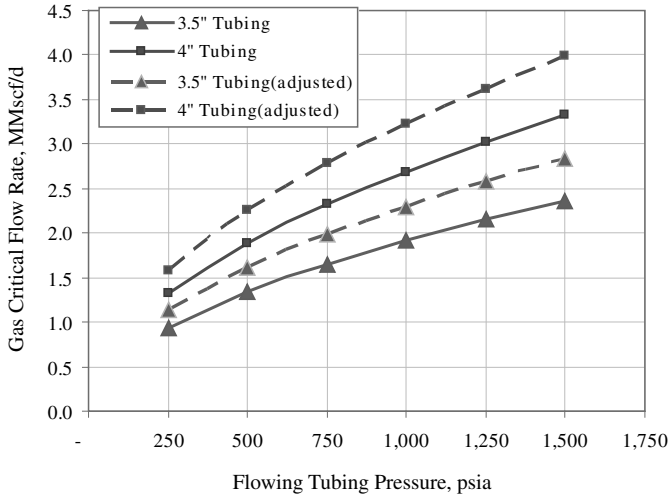

Figure 2–10 *Gas critical flow rate versus flowing tubing pressure for Example 2–5*

be zero as the casing annulus is either cemented or filled with fluid as shown in Figure 2–8. In reality, very often the casinghead pressure is not zero. The possible reasons are hole(s) in the tubing caused tubing-casing communication; packer seal leak; or poor cementing job.

The US Minerals Management Service (MMS) has strict and detailed policies regarding wells with sustained casing pressure. For instance, according to a letter by MMS (Bourgeois, 1994), for wells operated in the Gulf of Mexico (GoM) Outer Continental Shelf (OCS), all casinghead pressures, excluding drive or structural casing, need to be reported to the District Supervisor in a timely manner either in writing or by telephone. Below are the detailed requirements and are taken directly from the same source mentioned above: If the sustained casinghead pressure is less than 20% of the minimum internal yield pressure (MIYP) of the affected casing and can be bled to zero pressure through a ½-inch needle valve within 24 hours or less, the well with sustained casing pressure may continue producing hydrocarbons from the present completion, at the same time, the operators need to monitor and evaluate the well by performing the diagnostic tests required by MMS.

Here the MIYP of the casing is also called burst resistance. It is a function of the specified minimum yield strength, the outside diameter and wall thickness of the casing. It can be found from vendors' handbooks, as shown in Table 2–2. For example, assume the production

Table 2–2 API Recommended Performance Casing *(Schlumberger i-Handbook)*

OD (in.)	Weight (lbm/ft)	Grade	ID (in.)	Collapse Resistance (psi)	Pipe Body Yield (lbm)	Pipe Body Internal Yield (psi)
7.000	23.00	L-80	6.366	3830	532000	6340
7.000	23.00	N-80	6.366	3830	532000	6340
7.000	23.00	C-90	6.366	4030	599000	7130
7.000	23.00	C-95	6.366	4140	632000	7530
7.000	23.00	C/T-95	6.366	4140	632000	7530
7.000	26.00	J-55	6.276	4330	415000	4980
7.000	26.00	K-55	6.276	4330	415000	4980
7.000	26.00	M-65	6.276	4810	492000	5880
7.000	26.00	L-80	6.276	5410	604000	7240
7.000	26.00	N-80	6.276	5410	604000	7240

casing shown in Figure 2–8b has an OD of 7 in. with weight of 23 lbm/ft and grade of N-80, then from Table 2–2 the MIYP can be found as 6,340 psi, so the 20% of MIYP would be 1,268 psi.

According to the same source, if the well has casings with sustained pressure greater than 20% of the MIYP of the affected casing or pressure, and the pressure cannot be bled to zero through a ½-inch needle valve, it must be submitted to the regional MMS office for approval of continuous operations. If the request for a departure from the policy (concerning sustained casing pressure) is denied by the MMS, the operator of the well will have 30 days to respond to the MMS District Office with a plan to eliminate the sustained casinghead pressure. Based on well conditions, certain denials may specify a shorter time period for corrections. In this case, most likely a well workover or recompletion (pulling tubing, reset packer, cementing job, etc) will be needed depending on what is the root cause. It can be very costly especially when the water is deep. For unmanned platforms, a liftboat sometimes fitted with a drilling rig will be needed.

If unsustained casinghead pressure is deliberately applied, such as the result of thermal expansion, gas-lift, backup for packers, or for

reducing the pressure differential across a packoff in the tubing string, the operator does not need to submit a letter to the regional MMS office reporting the unsustained casinghead pressure. However, if the pressure due to the thermal expansion is greater than 20% of the MIYP of the affected casing, or does not bleed to zero through a ½-inch needle valve, then a report must be made.

In summary, gas well drilling and completion are very important in ensuring gas well productivity, and they are very expensive operations. Since most of the new discoveries are in deepwater offshore locations with high pressure and high temperature (HPHT), some of them with high contents of H_2S and CO_2, drilling and well completions become more challenging and costly. New wells will have higher requirements on the drilling and completion fluids, equipments, tubular metallurgy, and sand control means if the formation sand is unconsolidated. Because of environmental and regulatory concerns, we must do it right the first time.

2.5 References

Alsos, T. et al. 2002. Seismic applications throughout the life of the reservoir. *Oilfield Review* (Summer): 48–65.

Aylor, W.K. 1998. The role of 3-D seismic in a world-class turnaround. *The Leading Edge* (December): 1678–1681.

Bennion, D.B., F.B. Thomas, R.F. Bietz, and D.W. Bennion. 1996. Water and hydrocarbon phase trapping in porous media—diagnosis, prevention and treatment. *JCPT* (December): 29–36.

Bland, R., G. Mullen, Y. Gonzalez, F. Harvey, and M. Pless. 2005. Drilling fluid meets deep gas drilling challenges. *Drilling Contractor* (May/June): 50–54.

Bourgeois, D.J. 1994. Policy concerning sustained casing pressure. MMS website: http://www.gomr.mms.gov/homepg/regulate/regs/ltls/940113.html.

Coleman, S.B., H.B. Clay, D.G. McCurdy, and L.H. Norris III. 1991. A new look at predicting gas-well load-up. *JPT* (March): 329–333.

Dobrin, M.B. 1976. *Introduction to Geophysical Prospecting*. New York: McGraw-Hill.

Gool, F.V. and P.K. Currie. 2008. An improved model for the liquid-loading process in gas wells. Paper SPE 106699. *Journal SPE Production & Operations* 23 (November).

Greenlee, S.M., G.M. Gaskins, and M.G. Johnson. 1994. 3-D seismic benefits from exploration through development: An Exxon perspective. *The Leading Edge* 13 (July): 730–734.

Lea, J.F. and H. Nickens. 2004. Solving gas-well liquid-loading problems. Paper SPE 72092, *JPT* 56 (April): 30–36.

Mallick, S. 2001. AVO and elastic impedance. *The Leading Edge* (October) 1094–1104.

Nosseir, M.A., T.A. Darwich, M.H. Sayyouh, and M. El Sallaly. 1997. A new approach for accurate prediction of loading in gas wells under different flowing conditions. Paper SPE 37408.

Schöffmann, F. and M.J. Economides. 1991. Controlling kicks in ultradeep wells and comparison with shallow wells. Paper SPE 22561.

Schlumberger. 2009. Oilfield Glossary.

Solomon, F., G. Falcone, and C. Teodoriu. 2008. Critical review of existing solutions to predict and model liquid loading in gas wells. Paper SPE 115933.

Turner, R.G., M.G. Hubbard, and A.E. Dukler. 1969. Analysis and prediction of minimum flow rate for the continuous removal of liquids from gas wells. *JPT* (November).

CHAPTER 3

Natural Gas Production

3.1 Introduction

Once the well is drilled and completed successfully, it is ready to produce fluids (assuming the oil and gas-in-place are there and it is economical to operate the well). The produced hydrocarbons in the gaseous phase are from two main sources of natural gas (as discussed in Chapter 1).

First, gas is found in association with oil. Almost all oil reservoirs, even those that are insitu above their bubble point pressure, will shed some natural gas, which is produced at the surface with oil and then separated in appropriate surface facilities. The relative proportions of produced gas and oil depend on the physical and thermodynamic properties of the specific crude oil system, the operating pressure downhole, and the pressure and temperature of the surface separators.

The second type of gas is produced from reservoirs that contain primarily gas (dry gas or gas condensate). Usually such reservoirs are considerably deeper and hotter than oil reservoirs. We will deal with the production characteristics of these reservoirs in this chapter.

There are other unconventional sources of natural gas, one of which is coalbed methane desorbed from coal formations, and already in commercial use. The process is described in Chapter 11 of Economides and Martin (2007). In the far future, production from massive deposits of natural gas hydrates is likely, but such eventuality is outside the scope of this book.

In this chapter, gas well performance and deliverability at different flow conditions—steady state, pseudosteady state, and transient flow—under Darcy and non-Darcy flow with and without hydraulic fractures will be discussed.

3.2 Darcy and non-Darcy Flow in Porous Media

To perform natural gas well deliverability calculations, it is essential to understand the fundamentals of gas flow in porous media. Fluid flow is affected by the competing inertial and viscous effects, combined by the well-known Reynolds number, whose value delineates laminar from turbulent flow. In porous media, the limiting Reynolds number is equal to 1 based on the average grain diameter (Wang and Economides, 2004).

Because permeability and grain diameter are well connected (Yao and Holditch, 1993), for small permeability values (e.g., less than 0.1 md) the production rate is generally small; flow is laminar near the crucial sandface and it is controlled by Darcy's law:

$$-\frac{dp}{dx} = \frac{\mu_g}{k_g} v_g, \tag{3.1}$$

where x represents the distance, p the pressure, v_g the gas velocity, μ_g the gas viscosity and k_g the effective permeability to gas. An amount of connate water is always present with the gas. Such water saturation is immobile and, therefore, k_g equals the effective permeability to gas and can be treated as the single-phase permeability. It is often denoted simply as k.

Non-Darcy flow occurs in the near-wellbore region of high-capacity gas and condensate reservoirs: As the flow area is reduced substantially, the velocity increases, inertial effects become important, and the gas flow becomes non-Darcy. The relation between pressure gradient and velocity can be described by the Forchheimer (1914) equation

$$-\frac{dp}{dx} = \frac{\mu_g}{k_g} v_g + \rho_g \beta_g v_g^2, \tag{3.2}$$

where ρ_g is the gas density. β_g is the effective non-Darcy coefficient to gas. It can be calculated by using published theoretical or empirical correlations. Table 3–1 is a summary of some of the correlations. These correlations are valid for single-phase gas flow (subscript "g" is dropped for simplicity).

It is worth noting that condensate liquid may flow if its saturation is above the critical condensate saturation (S_{cc}) (Wang and Mohanty, 1999a). Additional condensate drops out because the further reduced

Table 3–1 Correlations for non-Darcy Coefficient

Reference	Correlation	Unit for β	Unit for k
Cooke (1973)	$\beta = \frac{b}{k^a}$ a and b: experimentally determined constants	atm.s^2/g	darcy
Thauvin & Mohanty (1998)	$\beta = \frac{3.1\times10^4\tau^3}{k}$	1/cm	darcy
Geerstma (1974)	$\beta = \frac{0.005}{k^{0.5}\phi^{5.5}}$	1/cm	cm^2
Tek et al. (1962)	$\beta = \frac{5.5\times10^9}{k^{1.25}\phi^{0.75}}$	1/ft	md
Liu et al. (1995)	$\beta = \frac{8.91\times10^8\tau}{k\phi}$	1/ft	md
Ergun (1952)	$\beta = \frac{a}{b^{0.5}(10^{-8}k)^{0.5}\phi^{1.5}}$ $a = 1.75$, $b = 150$	1/cm	darcy
Janicek & Katz (1955)	$\beta = \frac{1.82\times10^8}{k^{1.25}\phi^{0.75}}$	1/cm	md
Pascal et al. (1980)	$\beta = \frac{4.8\times10^{12}}{k^{1.176}}$	1/m	md
Jones (1987)	$\beta = \frac{6.15\times10^{10}}{k^{1.55}}$	1/ft	md
Coles & Hartman (1998)	$\beta = \frac{1.07\times10^{12}\times\phi^{0.449}}{k^{1.88}}$	1/ft	md
Coles & Hartman (1998)	$\beta = \frac{2.49\times10^{11}\phi^{0.537}}{k^{1.79}}$	1/ft	md
Li et al. (2001)	$\beta = \frac{11500}{k\phi}$	1/cm	darcy
Wang et al. (1999) Wang (2000)	$\beta = \frac{(10)^{-3.25}\tau^{1.943}}{k^{1.023}}$ τ is tortuosity	1/cm	cm^2

pressure will aggravate the situation. Therefore, two phenomena emerge: non-Darcy effects and a substantial reduction in the relative permeability to gas. Because of the radial nature of flow, the near-wellbore region is critical to the productivity of a well. This is true in all wells, but it becomes particularly serious in gas-condensate reservoirs.

Forchheimer's equation describes high-velocity, single-phase flow in isotropic media. Many reservoirs are, however, anisotropic (Wang et al., 1999; Wang, 2000). Wang (2000) used a pore-level model and developed a correlation to calculate the non-Darcy coefficient in an anisotropic medium for single-phase flow (see Table 3–1). Cooper et al. (1998) studied the non-Darcy coefficient by performing experimental tests with carbonate and Berea sandstone cores. Their experimental data gave good agreement with the correlation described by Wang (2000).

A direct understanding of multiphase non-Darcy flow behavior in porous media that are anisotropic at the pore-scale is studied elsewhere (Wang, 2000; Wang and Mohanty, 1999b).

3.3 Gas Well Inflow under Darcy Flow

Well inflow means the fluid flow from the reservoir into the sandface, takes into account the reservoir characteristics, the well geometry (vertical, horizontal, complex architecture), the near-wellbore zone or other features such as hydraulic or natural fractures and the pressure drawdown. Different flow regimes that take into account boundary effects such as steady state, pseudosteady state and transient behavior are considered.

Natural gas well performance will be discussed in the following sections, based on its flow characteristics under different flow regimes.

3.3.1 Steady State and Pseudosteady State Flow

Steady state flow is defined as the behavior when the pressure (wellhead or bottomhole) and flow rates are constant. This behavior usually happens when there is pressure support, either naturally through an aquifer, or through water injection. The well performance under steady state flow can be derived from Darcy's law.

Starting with a well in the center of a drainage, as shown in Figure 3–1, with r_w the wellbore radius, p_{wf} the flowing bottomhole pressure, p the pressure at any given distance r, and with the net reservoir thickness h, the cross-sectional flow area can be calculated as $2\pi rh$. In radial coordinates, Eq. (3.1) becomes

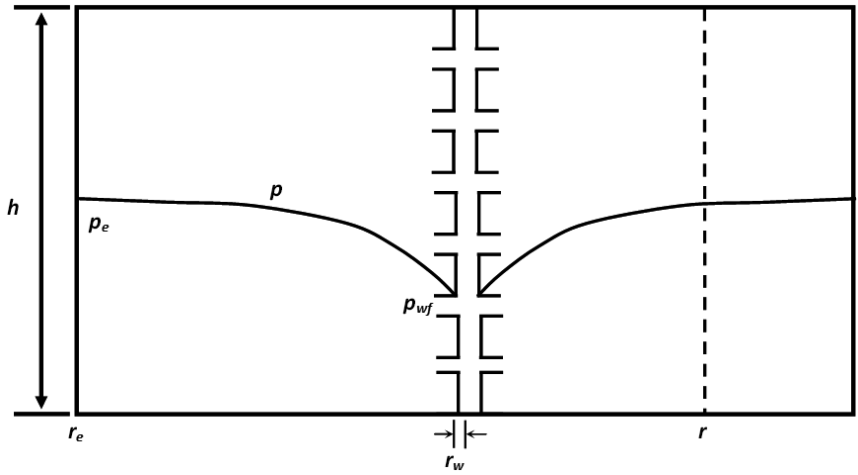

Figure 3–1 *Steady-state flow*

$$q = \frac{kA}{\mu}\frac{dp}{dr} = \frac{2\pi krh}{\mu}\frac{dp}{dr} \,. \tag{3.3}$$

The flow rate q is constant as the flow is under steady state. Eq. (3.3) can be integrated by separating the variables and setting at the outer boundary r_e, a constant pressure p_e:

$$p_e - p_{wf} = \frac{q\mu}{2\pi kh}\ln\frac{r_e}{r_w} \,. \tag{3.4}$$

Van Everdingen and Hurst (1949) quantified the condition of the near-wellbore region with the introduction of the concept of the skin effect. This is analogous to the film coefficient in heat transfer. This skin effect results in an additional steady-state pressure drop, given by

$$\Delta p_s = \frac{q\mu}{2\pi kh}s \,. \tag{3.5}$$

Thus, Eq. (3.4) can provide the total pressure difference including both the reservoir and the near-wellbore zone and becomes

$$p_e - p_{wf} = \frac{q\mu}{2\pi kh}\left(\ln\frac{r_e}{r_w} + s\right). \tag{3.6}$$

In oilfield units, where p_e and p_{wf} are in psi, q is in stb/d, μ is in cp, k is in md, h is in ft, s is dimensionless, and B is the formation volume factor to convert reservoir barrel (res bbl) into stock tank barrel (stb), Eq. (3.6) yields

$$p_e - p_{wf} = \frac{141.2qB\mu}{kh}\left(\ln\frac{r_e}{r_w} + s\right). \tag{3.7}$$

Eq. (3.7) is valid for largely incompressible (i.e., oil) flow under steady state. For highly compressible gas, the formation volume factor, B_g, varies greatly with pressure. Therefore an average expression can be obtained from Eq. (1.12),

$$\overline{B_g} = \frac{0.0283\overline{Z}T}{(p_e + p_{wf})/2}. \tag{3.8}$$

Introducing the gas rate in Mscf/d (thousand standard cubic feet per day), with relatively simple algebra, Eq. (3.7) yields

$$p_e - p_{wf} = \frac{141.2(1{,}000/5.615)q(0.0283)\overline{Z}\,T\overline{\mu}}{[(p_e + p_{wf})/2]kh}[\ln(\frac{r_e}{r_w}) + s], \tag{3.9}$$

and finally

$$p_e^2 - p_{wf}^2 = \frac{1{,}424q\overline{\mu}\overline{Z}T}{kh}[\ln(\frac{r_e}{r_w}) + s], \tag{3.10}$$

which, re-arranged, provides the steady-state approximation for natural gas flow, showing a pressure-squared difference dependency

$$q = \frac{kh(p_e^2 - p_{wf}^2)}{1{,}424\overline{\mu}\overline{Z}T[\ln(\frac{r_e}{r_w}) + s]}, \tag{3.11}$$

where the properties $\overline{\mu}$ and $\overline{Z}$ are average properties between p_e and p_{wf}. (henceforth the bars will be dropped for simplicity).

Eq. (3.11) is valid for gas flow under steady state (with a constant-pressure outer boundary). More commonly, wells eventually feel their

assigned boundary. Drainage areas can either be described by natural limits such as faults, and pinchouts (no-flow boundary), or can be artificially induced by the production of adjoining wells. This condition is often referred to as "pseudosteady state". The pressure at the outer boundary is not constant but instead declines at a constant rate with time, that is, $\partial p_e / \partial t$ = const. Therefore, a more useful expression for the pseudosteady-state equation would be one using the average reservoir pressure, $\bar{p}$. It is defined as a volumetrically weighted pressure (Economides et al., 1994) and in practice can be obtained from periodic pressure buildup tests.

The production rate expression for a gas well can be written for pseudosteady state,

$$q = \frac{kh(\bar{p}^2 - p_{wf}^2)}{1,424\mu ZT[\ln(\frac{0.472r_e}{r_w}) + s]} . \tag{3.12}$$

Eqs. (3.11 and 3.12) suggest a number of interesting conclusions: the flow rate is large if the pressure-squared difference is large, if the permeability and reservoir net thickness are large or the gas deviation factor, the viscosity of the flowing fluid, and the skin damage are small. It is clear that a positive skin means the well is damaged and this will cause additional pressure drop in the near wellbore region. A negative skin means the well is stimulated (through matrix acidizing and removing near-wellbore damage, or through hydraulic fracturing by bypassing the damage zone and changing flow paths).

In summary, Eq. (3.12) (or Eq. (3.11)) is an analytical approximation of gas well rate under pseudosteady (or steady) state and Darcy flow conditions in the reservoir. It is valid when gas flow rate is small. It can be presented in a common form

$$q = C(\bar{p}^2 - p_{wf}^2) . \tag{3.13}$$

A log-log plot of q versus $(\bar{p}^2 - p_{wf}^2)$ would yield a straight line with slope equal to one and intercept C. For large flow rates, non-Darcy flow will be present in the reservoir. This will be addressed in a later section of this chapter.

Example 3–1 Rate versus pressure

Consider a gas reservoir whose pressure is 3,000 psi. Assess the impact of the flowing bottomhole pressure on flow rate. Assume a steady-state relationship and use p_{wf} = 2,500, 2,000, 1,500, 1,000, and 500 psi, respectively. Given,

p_e	3,000	psi
r_e	660	ft
r_w	0.359	ft
k	0.1	md
h	50	ft
T	250	°F
γ_g	0.7	
N_2	0	
CO_2	0	
H_2S	0	
s	0	

Solution

Eq. (3.10) after substitution of variables becomes

$$9\times10^6 - p_{wf}^2 = (1.52\times10^6)q\bar{\mu}\bar{Z} \ .$$

Gas viscosity and Z-factor at different flowing bottom pressures are calculated by using Lee et al. (1966) and Dranchuk et al. (1974) correlations (presented in Chapter 1), respectively. The average properties are the arithmetic average with properties at p_e of 3,000 psi. Results are summarized in Table 3–2.

As an example calculation, for p_{wf} = 1,000 psi, the above equation yields

$$q = \frac{9\times10^6 - 1{,}000^2}{1.52\times10^6\times0.0176\times0.923} = 324 \text{ Mscf/d} \ .$$

Figure 3–2 is a graph of p_{wf} versus q for this example. It shows the flow rate increases when the p_{wf} decreases as the driving force $(p_e^2 - p_{wf}^2)$ increases. If the initial μ_i and Z_i were used (i.e., not averages) the flow rate would be 369 Mscf/d, a deviation of 14%.

Table 3–2 Results for Example 3–1

p_e (psi)	μ, cp	Z			
3,000	0.0199	0.9115			
p_{wf} (psi)	μ, cp	$\bar{\mu}$, cp	Z	$\bar{Z}$	q, Mscf/d
500	0.0146	0.0173	0.963	0.937	356
1,000	0.0153	0.0176	0.934	0.923	324
1,500	0.0162	0.0181	0.913	0.912	270
2,000	0.0173	0.0186	0.902	0.907	195
2,500	0.0186	0.0193	0.9019	0.907	104

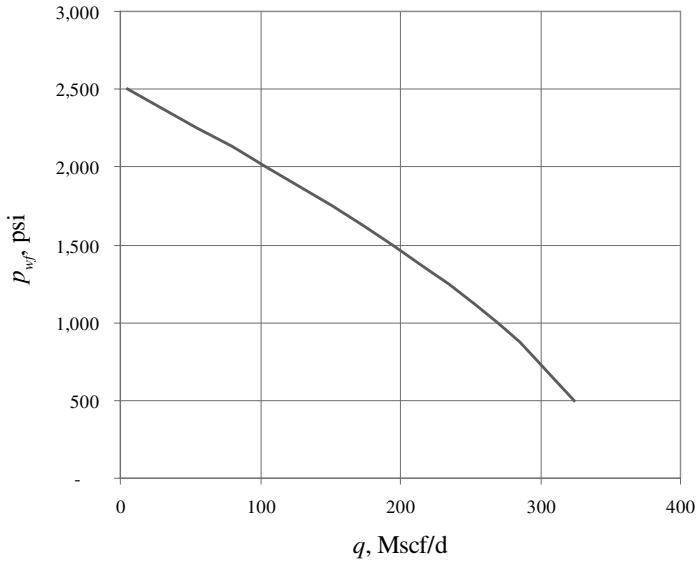

Figure 3–2 *Production versus flowing bottomhole pressure for Example 3–1*

3.3.2 Transient Flow

At early time the flowing bottomhole pressure of a producing well is a function of time if the rate is held largely constant. This type of flow condition is called transient flow and is used deliberately during a pressure transient test. In practice, the well is usually operated under the same wellhead pressure (which is imposed by the well hardware such as chokes, etc.), the resulting flowing bottomhole pressure is also largely constant, and the flow rate will vary with time. To characterize gas flow in a reservoir under transient conditions, the combination of the generalized Darcy's law (rate equation), and the continuity equation can be used (in radial coordinates)

$$\phi \frac{\partial \rho}{\partial t} = \frac{1}{r} \frac{\partial}{\partial r} \left(\rho \frac{k}{\mu} r \frac{\partial p}{\partial r} \right), \tag{3.14}$$

where ϕ is the porosity. Because gas density is a strong function of pressure (in contrast to oil, which is considered incompressible), the real gas law can be employed, and as shown in Eq. (1.9) in Chapter 1.

Therefore,

$$\phi \frac{\partial}{\partial t} \left(\frac{p}{Z} \right) = \frac{1}{r} \frac{\partial}{\partial r} \left(\frac{k}{\overline{\mu Z}} rp \frac{\partial p}{\partial r} \right). \tag{3.15}$$

In an isotropic reservoir with constant permeability, Eq. (3.15) can be simplified to

$$\frac{\phi}{k} \frac{\partial}{\partial t} \left(\frac{p}{Z} \right) = \frac{1}{r} \frac{\partial}{\partial r} \left(\frac{p}{\mu Z} r \frac{\partial p}{\partial r} \right). \tag{3.16}$$

Performing the differentiation on the right-hand side of Eq. (3.16), assuming that the viscosity and gas deviation factor are small functions of pressure, and rearranging, it gives

$$\frac{\phi \mu}{kp} \frac{\partial p^2}{\partial t} = \frac{\partial^2 p^2}{\partial r^2} + \frac{1}{r} \frac{\partial p^2}{\partial r}. \tag{3.17}$$

For an ideal gas, $c_g = 1/p$, and as a result, Eq. (3.17) leads to

$$\frac{\partial^2 p^2}{\partial r^2} + \frac{1}{r} \frac{\partial p^2}{\partial r} = \frac{\phi \mu c}{k} \frac{\partial p^2}{\partial t}. \tag{3.18}$$

This approximation looks exactly like the classic diffusivity equation for oil. Its solution would look exactly like the solutions of the equation for oil, but instead of p, the pressure squared, p^2, should be used as a reasonable approximation.

Al-Hussainy and Ramey (1966) used a far more appropriate and exact solution by employing the real gas pseudopressure function, defined as

$$m(p) = 2\int_{p_o}^{p} \frac{p}{\mu Z} dp \ , \tag{3.19}$$

where p_o is some arbitrary reference pressure (usually zero). The differential pseudopressure, $\Delta m(p)$, defined as $m(p) - m(p_{wf})$, is then the driving force in the reservoir.

Using Eq. (3.19) and the chain rule

$$\frac{\partial m(p)}{\partial t} = \frac{\partial m(p)}{\partial p}\frac{\partial p}{\partial t} = \frac{2p}{\mu Z}\frac{\partial p}{\partial t}. \tag{3.20}$$

Similarly,

$$\frac{\partial m(p)}{\partial r} = \frac{2p}{\mu Z}\frac{\partial p}{\partial r}. \tag{3.21}$$

Therefore, Eq. (3.16) becomes

$$\frac{\partial^2 m(p)}{\partial r^2} + \frac{1}{r}\frac{\partial m(p)}{\partial r} = \frac{\phi \mu c_t}{k}\frac{\partial m(p)}{\partial t}. \tag{3.22}$$

The solution of Eq. (3.22) would look exactly like the solution to the diffusivity equation cast in terms of pressure. Dimensionless time is (in oilfield units):

$$t_D = \frac{0.000264kt}{\phi(\mu c_t)_i r_w^2}, \tag{3.23}$$

and dimensionless pressure is

$$p_D = \frac{kh[m(p_i) - m(p_{wf})]}{1,424qT} \ . \tag{3.24}$$

Equations (3.22) to (3.24) suggest solutions to natural gas problems (e.g., well testing) that are exactly analogous to those for an oil well, except now it is the real gas pseudopressure function that needs to be employed. This function is essentially a physical property of natural gas, dependent on viscosity and the gas deviation function. Thus, it can be readily calculated for any pressure and temperature by using standard physical property correlations.

By analogy with oil, transient rate solution under radial infinite acting conditions can be written as:

$$q = \frac{kh[m(p_i) - m(p_{wf})]}{1{,}638T}\left[\log t + \log\frac{k}{\phi(\mu c_t)_i r_w^2} - 3.23 + 0.87s\right]^{-1}, \quad (3.25)$$

where q is gas flow rate in Mscf/d and c_t is the total compressibility of the system. As usual Eq. (3.25) can be cast in terms of pressure squared difference

$$q = \frac{kh[p_i^2 - p_{wf}^2]}{1{,}638\overline{\mu}\overline{Z}T}\left[\log t + \log\frac{k}{\phi(\mu c_t)_i r_w^2} - 3.23 + 0.87s\right]^{-1}. \quad (3.25a)$$

Equations (3.25) or (3.25a) can be used to generate transient IPR (Inflow Performance Relationship) curves for a gas well. Transient behavior ends when boundaries are felt. A commonly accepted expression for the time in hours when pseudosteady state begins is

$$t_{pss} \approx 1{,}200\frac{\phi\mu c_t r_e^2}{k}. \quad (3.26)$$

Example 3–2 Rate at the onset of pseudosteady state

Use the well in Example 3–1 and calculate the production rate at the time when pseudosteady begins and also at one tenth the time. Use a flowing bottomhole pressure of 1,500 psi. The gas saturation in the reservoir is about 0.75 and the porosity is 0.25.

Solution

First, estimate the time to pseudosteady state using the expression given above. The gas compressibility at initial conditions can be cal-

culated from Eq. (1.17) but at a relatively low pressure of 3,000 psi it can be approximated by

$$c_g \approx \frac{1}{3{,}000} \approx 3.33 \times 10^{-4} \text{ psi}^{-1} .$$

Therefore the total compressibility is approximately equal to

$$c_t \approx S_g c_g \approx 0.75 \times 3.33 \times 10^{-4} = 2.5 \times 10^{-4} \text{ psi}^{-1} .$$

The time to pseudosteady state, using Eq. (3.26) and the data of Example 3–1 and Table 3–2 is then

$$t_{\text{pss}} = 1{,}200 \times \frac{0.25 \times 0.0199 \times 2.5 \times 10^{-4} \times 660^2}{0.1} = 6{,}500 \text{ hr} .$$

Then using Eq. (3.25a) for 6,500 hours

$$q = \frac{0.1 \times 50 \times [3{,}000^2 - 1{,}500^2]}{1{,}638 \times 0.0181 \times 0.913 \times 710} \left[\log 6{,}500 + \log \frac{0.1}{0.25 \times 0.0199 \times 2.5 \times 10^{-4} \times 0.359^2} - 3.23 \right]^{-1}$$
$$= 276 \text{ Mscf/d.}$$

After 650 hours the rate would be 328 Mscf/d.

3.4 Gas Well Inflow under non-Darcy Flow

All expressions given thus far in this chapter have ignored one of the most important effects in natural gas flow: turbulence. For very low permeability reservoirs in mature environments such as the United States and continental Europe, it is sufficient to assume that gas flow in the reservoir obeys Darcy's law as we did in the previous section. Newly found reservoirs are primarily offshore, in developing nations, and are of moderate to high permeability, i.e., 1 to 100 md.

As well deliverability increases, turbulence becomes increasingly dominant in the production of gas wells. For reservoirs whose permeability is more than 5 md, turbulence effects may account for a 20 to

60% reduction in the production rate of an openhole well (when laminar flow is assumed). Turbulence in such cases practically overwhelms all other factors, including damage (Wang and Economides, 2004). In this section, turbulence effects in a vertical well will be discussed.

3.4.1 Turbulent Flow in Gas Wells

As mentioned earlier in this chapter, turbulent flow has been studied since the 1900s (Forchheimer, 1914). Pioneering and prominent among a number of investigators in the petroleum literature have been Katz and co-workers (Katz et al., 1959; Firoozabadi and Katz, 1979; Tek et al., 1962). They suggested that turbulence plays a considerable role in well performance, showing that the production rate is affected by itself; the larger the potential rate, the larger the relative detrimental impact would be. Since most turbulent flow takes place near the wellbore region, the effect of turbulence provides an extra pressure drop as given by

$$p_e^2 - p_{wf}^2 = \frac{1,424\mu ZT}{kh}[\ln(\frac{r_e}{r_w}) + s]q + \frac{1,424\mu ZTD}{kh}q^2 , \tag{3.27}$$

where D is the turbulence coefficient with units of reciprocal rate. Eq. (3.27) can be rearranged and turbulence can be accounted for by a rate-dependent skin effect as described by (Swift and Kiel, 1962)

$$q = \frac{kh(p_e^2 - p_{wf}^2)}{1,424\mu ZT[\ln(r_e/r_w) + s + Dq]} . \tag{3.28}$$

Similarly, the same turbulence coefficient can be employed to the more rigorous expressions using the real-gas pseudopressure. As an example, for pseudosteady state with q in Mscf/d

$$q = \frac{kh(\overline{p}^2 - p_{wf}^2)}{1,424\mu ZT[\ln(0.472 r_e/r_w) + s + Dq]}, \tag{3.28a}$$

or

$$q = \frac{kh[m(\overline{p}) - m(p_{wf})]}{1,424T[\ln(0.472 r_e / r_w) + s + Dq]} . \tag{3.28b}$$

D is usually determined by analysis of multi-rate pressure tests (Economides et al., 1994; Kakar et al., 2004), or from correlations when well test data is not available. In the absence of field measurements, an empirical relation is proposed (Economides et al., 1994)

$$D = \frac{6 \times 10^{-5} \gamma k_s^{-0.1} h}{\mu r_w h_{perf}^2}, \tag{3.29}$$

where h_{perf} is the perforated section length in ft and k_s is the near-wellbore permeability in md.

Example 3–3 Gas well rate with non-Darcy effects

A gas well produces from a reservoir whose pressure is 3,150 psi, and the reservoir temperature is 148°F. Gas specific gravity is 0.61 with no sour gases. The net pay is 50 ft. The damage skin factor is equal to 5 and the reservoir permeability is 20 md. The non-Darcy coefficient D is 1.5E-3 $(\text{Mscf/d})^{-1}$. Calculate the rate of the well at p_{wf} =1,200 psi assuming pseudosteady state. Also assume that: ln $(0.472r_e/r_w)$ = 7. What is the apparent skin at that rate? What would be the miscalculated rate if the non-Darcy effects were ignored?

Solution

Use Lee et al. (1966) and Dranchuk et al. (1974) correlations (described in Chapter 1) to calculate viscosity, Z-factor, and $m(p)$. The calculated PVT data is summarized in Table 3–3.

Using Eq. (3.28b), the gas well production rate would be

$$m(3{,}150) - m(1{,}200) = \frac{1{,}424 \times 608}{20 \times 50}(7+5)q + \frac{1{,}424 \times 608 \times 0.0015}{20 \times 50} q^2 .$$

Substituting the values of the real-gas pseudopressure from Table 3–3 and simplifying, the following quadratic equation is obtained

$$q^2 + 8{,}000q - 4.41 \times 10^8 = 0 .$$

The solution is 17,380 Mscf/d. The apparent skin equals

$$s + Dq = 5 + (1.5E-3) \times 17{,}380 = 31.$$

Table 3–3 PVT Table for Example 3–3

p (psia)	Z	μ (cp)	$p/(\mu Z)$	$p/(\overline{\mu Z})$ Interval	Δp	$p/(\overline{\mu Z}) \times \Delta p$	$2\times(p/(\overline{\mu Z}) \times \Delta p)$	$m(p)$
0			0					
14.7	0.998	0.0127	1,159.80	5.80E+02	14.7	8.52E+03	1.70E+04	1.70E+04
400	0.960	0.0130	32,051.28	1.66E+04	385.3	6.40E+06	1.28E+07	1.28E+07
8,00	0.925	0.0135	64,064.06	4.81E+04	400	1.92E+07	3.84E+07	5.13E+07
1,200	0.895	0.0143	93,760.99	7.89E+04	400	3.16E+07	6.31E+07	1.14E+08
1,600	0.873	0.0152	120,576.40	1.07E+05	400	4.29E+07	8.57E+07	2.00E+08
2,000	0.860	0.0162	143,554.40	1.32E+05	400	5.28E+07	1.06E+08	3.06E+08
2,250	0.856	0.0169	155,532.80	1.50E+05	250	3.74E+07	7.48E+07	3.81E+08
2,500	0.857	0.0177	164,810.90	1.60E+05	250	4.00E+07	8.01E+07	4.61E+08
2,750	0.860	0.0185	172,847.30	1.69E+05	250	4.22E+07	8.44E+07	5.45E+08
3,000	0.867	0.0193	179,285.40	1.76E+05	250	4.40E+07	8.80E+07	6.33E+08
3,150	0.872	0.0197	183,369.80	1.81E+05	150	2.72E+07	5.44E+07	6.87E+08

For a skin equal to 5 the rate would be more than 55,000 Mscf/d, if non-Darcy effects are ignored (i.e. $D = 0$).

3.4.2 Correlations for Turbulence in Vertical Gas Well

Figure 3–3 is a sketch of a vertical gas well and its cross section. It is obvious that when the flow is far away from the wellbore, the flow velocity is small, and the flow can be assumed as laminar. In the near wellbore area, fluid converges to the small diameter production tubing. Turbulence occurs especially when the permeability is high and the well deliverability increases.

In radial gas flow wells, well performance can be described by (Katz et al., 1959)

$$p_e^2 - p_{wf}^2 = \frac{1,424\mu ZT}{kh}[\ln(\frac{r_e}{r_w}) + s]q + \frac{3.16\times 10^{-12}\beta\gamma_g ZT(\frac{1}{r_w} - \frac{1}{r_e})}{h^2}q^2 \text{ , (3.30)}$$

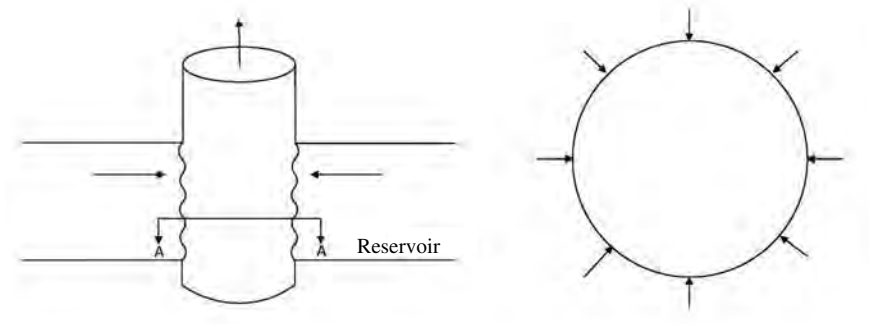

Figure 3–3 *A sketch of an openhole vertical well and its cross section*

where k equals the horizontal permeability, k_H. β is the Katz et al. version of non-Darcy coefficient, and can be calculated by using the Tek et al. (1962) correlation listed in Table 3–1.

The discussion above is for openhole vertical well radial flow. Turbulent flow in perforated cased wells has been addressed elsewhere (Wang and Economodies, 2004; Karakas and Tariq, 1988; Ichara, 1987).

In summary, for higher-permeability natural gas reservoirs, turbulence may become the dominant influence on production. For vertical wells, the accounting for turbulence is relatively well understood and inflow equations have been adjusted to account for the phenomenon. Furthermore, field-testing techniques have been established to obtain the non-Darcy coefficient. Surprisingly, similar work has not yet been done for horizontal wells. This will be detailed in the following section.

3.5 Horizontal Gas Well Inflow

Horizontal wells outside of the former Soviet Union started in the 1980s, and eventually, were widely introduced in the early 1990s. Since then, they have proliferated and have become essential in oil and gas production (Economides and Martin, 2007). The main advantages of horizontal wells are (Joshi, 1991; Cho and Shah, 2001):

- To increase productivity as the wellbore is longer than that of vertical well.
- To reduce water or gas coning.

- *To reduce turbulence in gas wells* (emphasis ours).
- To intersect fractures in naturally fractured reservoirs and drain reservoirs more effectively.
- To improve drainage area per well and reduce the number of vertical wells in low permeability reservoirs.
- To increase injectivity of an injection well and enhance sweep efficiency.

There are quite a few important publications related to horizontal well performance (Celier et al., 1989; Dikken, 1990; Joshi, 1991; Norris et al., 1991; Ozkan et al., 1999; Economides et al., 1994; Cho and Shah, 2001), but few have addressed turbulence effects on well performance. Of those that discussed turbulence, most assumed that turbulence is small and can be neglected. Their assumption is that the horizontal well length (L) is much longer compared to the vertical well height (h), and therefore, they concluded that turbulence is smaller in horizontal wells compared to vertical wells and could be ignored. This is true when the reservoir is isotropic and the permeability is small. But when permeability increases, well deliverability increases, and turbulence effects can no longer be neglected. Based on a recent study, the production loss due to turbulence could account for 30% in horizontal wells. When the reservoir is anisotropic, it is much worse (Wang and Economides, 2009).

Joshi (1991) whose contributions in the understanding of horizontal well performance have been seminal also attempted to quantify turbulence effects in natural gas horizontal wells. He developed (for a pseudosteady state) a horizontal well equation using a vertical well analog

$$q = \frac{k_H h(p^2 - p_{wf}^2)}{1,424\mu ZT\left(\ln(r_e / r_w) - 0.75 + s + s_m + s_{CA} + Dq - c'\right)}, \qquad (3.31)$$

where s is the horizontal well equivalent skin effect that would be imposed on a vertical well, s_m is mechanical (damage) skin, s_{CA} is shape related skin, and c' is a shape constant.

Eq. (3.31) is correct for oil but not for gas where turbulence is important. In fact, it is quite wrong. It uses horizontal well equivalent skins that can only be correct under reservoir flow, such as a pseudo-radial into a vertical well. Then the turbulence effects are presumed to influence flow far away from the well. Indeed the equivalent horizontal well skin under turbulent gas conditions cannot be

the same as for oil wells. By assuming so, and with such skins invariably of large negative values, it is no wonder that the effects of turbulence have been underestimated by Joshi and others who have used his solution.

Diyashev and Economides (2006) calculated vertical well equivalent skins for horizontal wells by using an expression derived from Joshi's own horizontal well equation

$$s = -\ln\left[\frac{L}{4r_w}\frac{1}{\left[I_{ani}\,h/r_w\left(I_{ani}+1\right)\right]^{I_{ani}h/L}}\right]. \tag{3.32}$$

Using Eq. (3.32), negative values of the skin can be as much as –8 for long horizontal wells in favorite anisotropy settings. Introducing such number in the denominator of Eq. (3.31) would certainly underestimate the impact of turbulence. In reality, the expression inside the bracket in Eq. (3.32) should have the Dq term added, which would change the equivalent skin by 30 to 50%.

Wang and Economides (2009) conducted a study to investigate properly the turbulence effects in horizontal wells. They presented appropriate correlations to account for turbulence effects on horizontal well performance, and offered a large range of parametric studies that involve reservoir thickness, permeability anisotropy, porosity, and horizontal well length. Their approach follows.

Analogs to Eq. (3.11) (for steady state), the inflow performance relationships (IPR) for a nonfractured horizontal well in a gas reservoir follows (Joshi, 1991; Economides et al., 1994).

For steady state:

$$q = \frac{k_H h(p_e^2 - p_{wf}^2)}{1{,}424\mu ZT\left(\ln\left\{\frac{a+\sqrt{a^2-(L/2)^2}}{L/2}\right\}+\frac{I_{ani}h}{L}\left\{\ln\frac{I_{ani}h}{r_w(I_{ani}+1)}+Dq\right\}\right)}. \tag{3.33}$$

For pseudosteady state:

$$q = \frac{k_H h(\bar{p}^2 - p_{wf}^2)}{1{,}424\mu ZT\left(\ln\left\{\frac{a+\sqrt{a^2-(L/2)^2}}{L/2}\right\}+\frac{I_{ani}h}{L}\left\{\ln\frac{I_{ani}h}{r_w(I_{ani}+1)}-\frac{3}{4}+Dq\right\}\right)}. \tag{3.34}$$

Or, replacing the approximation $(\bar{p}^2 - p_{wf}^2)/\mu Z$ by the real-gas pseudopressure difference

$$q = \frac{k_H h(m(\bar{p}) - m(p_{wf}))}{1,424T\left(\ln\left\{\frac{a+\sqrt{a^2-(L/2)^2}}{L/2}\right\} + \frac{I_{ani}h}{L}\left\{\ln\frac{I_{ani}h}{r_w(I_{ani}+1)} - \frac{3}{4} + Dq\right\}\right)}, \quad (3.35)$$

where k_H is the horizontal permeability and L is the horizontal well length. I_{ani} is a measurement of vertical-to-horizontal permeability anisotropy and is given by

$$I_{ani} = \sqrt{\frac{k_H}{k_V}}, \quad (3.36)$$

where k_H is defined as $\sqrt{k_x k_y}$ and k_V equals to k_z. a is the large half-axis of the drainage ellipsoid formed by a horizontal well length, L. The expression for this ellipsoid is

$$a = \frac{L}{2}\left\{0.5 + \left[0.25 + \left(\frac{r_{eH}}{L/2}\right)^4\right]^{0.5}\right\}^{0.5} \quad \text{for } \frac{L}{2} < 0.9r_{eH}, \quad (3.37)$$

where r_{eH} is the drainage radius in the horizontal wells.

The correlation of the non-Darcy coefficient, developed by Tek et al. (1962) and listed in Table 3–1, is valid for natural gas flow through porous media. Therefore, it can be used in a horizontal well by making the following adjustment

$$k = \sqrt[3]{k_x k_y k_z} = \sqrt[3]{k_H^2 k_V}. \quad (3.38)$$

So the turbulence factor in a horizontal well is

$$\beta_H = \frac{5.5\times 10^9}{(k_x k_y k_z)^{5/12}\phi^{3/4}}. \quad (3.39)$$

The turbulence coefficient for a horizontal well is

$$D_H = \frac{2.22 \times 10^{-15} (k_x k_y k_z)^{1/3} \gamma_g}{\mu h r_{wH}} \beta_H \,, \tag{3.40}$$

where r_{wH} is the effective wellbore radius of the horizontal wells and is equal to

$$r_{wH} = \frac{r_w (1 + I_{ani})}{2 I_{ani}}. \tag{3.41}$$

With the correlations developed above, the well inflow for horizontal wells with turbulence can be examined.

Example 3–4 Gas horizontal well performance with turbulence

Calculate turbulence effects in the horizontal well and compare the results with those from the vertical well. The input parameters are given in Table 3–4. Assume skin is zero. Reservoir permeability is 0.1, 1, 10, and 100 md, respectively.

Table 3–4 Well and Reservoir Characteristics for Example 3–4

p_e	3,000 psi
p_{wf}	1,500 psi
r_e	2,978 ft
r_w	0.359 ft
h	50 ft
L	1,000 ft
T	710 R
ϕ	18%
μ	0.0162 cp
Z	0.91
γ_g	0.7

Solution

With the procedure outlined above, the flow rates from both horizontal and vertical gas wells with (actual) and without (ideal) turbulence can be calculated. Results are summarized in Table 3–5.

Results show that the production in the ideal openhole horizontal well is about 3.4 times higher than that in the vertical well (assuming no turbulence effects). At the same drawdown, it is obvious that the productivity in the horizontal well is higher than that in the vertical well, as the horizontal well has a longer wellbore.

When turbulence is taken into account, production in both horizontal and vertical wells drops especially when the permeability is high. When permeability is less than 1 md, the impact of turbulence in the horizontal well is less than 2% while it is less than 5% in the vertical well. When permeability increases there is a greater reduction in the production rate. When the permeability is 100 md, as shown in Figure 3–4, the production loss due to turbulence effect climbs to 30% and 40% for the horizontal and vertical wells, respectively. Even with turbulence effect, the horizontal well still performs better than the ideal vertical well. At 100 md permeability, the production from the actual horizontal well (with turbulence) is 2.4 times higher than that from the ideal openhole vertical well (without turbulence).

When comparing the performance between the actual horizontal and vertical wells, the results are even more promising. The horizontal well production is 3.4 times the vertical well at 1 md and this climbs to 3.9 at 100 md, which is higher than the ideal productivity ratio between the horizontal and vertical wells (3.3 at 1 md and 3.4 at 100 md). This shows that, at the given parameters, the horizontal well is the desirable option over the vertical well in terms of reducing turbulence and increasing production, but the effects of turbulence are clearly not negligible.

This effect is even more profound when the formation is anisotropic. Assume the horizontal permeability is 10 md, the vertical permeability is 10, 1, and 0.1 respectively. These values give the index of permeability anisotropy, I_{ani} (= $\sqrt{k_H / k_V}$) as 10, 3, and 1, respectively. All other parameters are the same as those given in Table 3–4. Repeating the same calculation as done in Example 3–4, results are summarized in Table 3–6. The actual rates are not that interesting but the ratios are more profound, and are plotted in Figure 3–5.

It is obvious that horizontal well deliverability is very sensitive to the reservoir anisotropy when compared with the performance of the

Table 3–5 Results for Example 3–4

Δp = 1,500 psi (p_{wf} = 1,500 psi)				
k, md	Vertical Ideal $q_{Ideal\ OH}$, MMscf/d ($\beta = 0$, $s = 0$)	Vertical Actual $q_{Radial\ Flow}$, MMscf/d ($\beta > 0$, $s = 0$)	Horizontal Ideal $q_{Ideal\ OH}$, MMscf/d ($\beta = 0$, $s = 0$)	Horizontal Actual $q_{Radial\ Flow}$, MMscf/d ($\beta > 0$, $s = 0$)
0.1	0.3	0.3	0.8	0.8
1	2.5	2.4	8.4	8.3
10	25.1	21.9	84.2	77.5
100	250.9	158.0	841.2	609.6

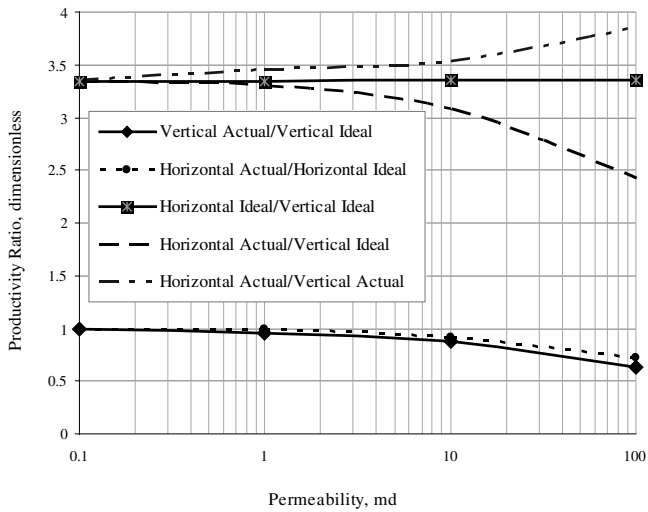

Figure 3–4 *Turbulence effects in both horizontal and vertical wells*

vertical well. This is because the controlling permeability in the horizontal well is a function of the horizontal and vertical permeabilities as shown in Eq. (3.33), while the vertical well performance depends only on the horizontal permeability. Thus, when the horizontal permeability is kept constant (here it is 10 md), the vertical well production is constant (shown in Table 3–6), and the reduction due to turbulence is about 13% (Figure 3–5).

Table 3–6 Effects of Index of Permeability Anisotropy

I_{ani}	Vertical Ideal $q_{Ideal\ OH,}$ MMscf/d ($\beta = 0$, $s = 0$)	Vertical Actual $q_{Radial\ Flow,}$ MMscf/d ($\beta > 0$, $s = 0$)	Horizontal Ideal $q_{Ideal\ OH,}$ MMscf/d ($\beta = 0$, $s = 0$)	Horizontal Actual $q_{Radial\ Flow,}$ MMscf/d ($\beta > 0$, $s = 0$)
1	25.1	21.9	84.2	77.5
3	25.1	21.9	70.4	54.4
10	25.1	21.9	46.2	30.8

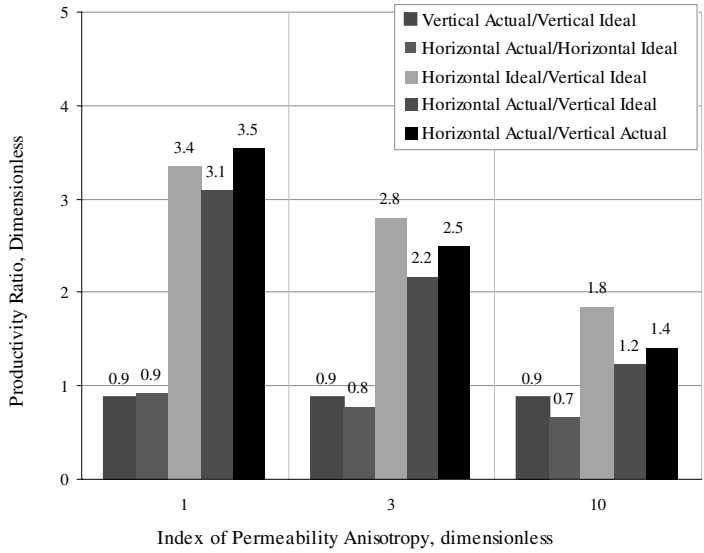

Figure 3–5 *Effects of index of permeability anisotropy*

The production reduction in the horizontal well due to turbulence, on the other hand, changes significantly when the reservoir becomes more anisotropic (from 0.9 to 0.7 shown in Figure 3–5). The production ratio between horizontal and vertical wells is 3.4, 2.8, and 1.8 for the ideal case, and 3.1, 2.2, and 1.2 for the actual horizontal over ideal vertical case at I_{ani} of 1, 3, and 10, respectively. When comparing the production between the actual horizontal and vertical wells, it shows the ratio changes from 3.5 to 2.5 and 1.4 when I_{ani} varies from 1 to 3 and 10, respectively. Important conclusions can be

drawn by comparing the results. For isotropic formations, horizontal wells alleviate turbulence more effectively than vertical wells, showing a larger productivity index ratio than the ideal cases (3.5 versus 3.4). However, as anisotropy increases (e.g., $I_{ani} = 10$) horizontal wells become less efficient to reduce turbulence effects (real versus ideal productivity ratios of 1.4 versus 1.8). In this particular case, turbulence can reduce production in horizontal wells by 30% when permeability is anisotropic.

Turbulence effect in the horizontal well is also a function of reservoir thickness, porosity, and horizontal well length. Detailed discussion can be found in Wang and Economides (2009).

In summary, turbulence effects are the dominant features in the production of high (>5 md) permeability gas wells. Turbulence may account for a 25 to 50% reduction in the expected openhole production rate from such vertical gas wells (Wang and Economides, 2004). In a horizontal well, turbulence effect cannot be neglected as many people have proposed in the past. On the contrary, turbulence effects dominate horizontal well flow in higher permeability reservoirs. In fact, in permeability anisotropic formations they reduce the flow rate by a larger fraction than in vertical wells. Porosity, which was part of the original turbulence correlations, mysteriously disappears from more recently published correlations. It is reintroduced in the correlations in this chapter, as its impact is considerable especially when the permeability is anisotropic (Wang and Economides, 2009).

There are several ways to reduce turbulence in high rate gas wells. One way is to perforate wellbores with long penetrating perforation tunnels and large perforation densities (e.g., 8 to 12 SPF). However, nothing can compete with hydraulic fracturing. In higher permeability gas wells, the incremental benefits greatly exceed those of comparable permeability oil wells. This is because of the dramatic impact on reducing the turbulence effects beyond the mere imposition of a negative skin. It is fair to say that any gas well above 5 md will be greatly handicapped if not hydraulically fractured. In fact, pushing the limits of hydraulic fracturing by using large quantities of premium proppants will lead to extraordinary production rate increases.

3.6 Hydraulic Fracturing

A widely used technique for production enhancement is hydraulic fracturing, which involves the creation of a crack in the reservoir by injecting highly pressurized fluids at a very high rate. The fluids are solutions of polymers, which are used to thicken the carrier fluid, often water, for the purpose of increasing its viscosity and allowing it

to carry particles, called proppants. The hydraulically created fracture is held open (propped) with tens of thousands to millions of pounds of clean, uniform natural sand or synthetic materials, and can have a permeability that is orders of magnitude larger than the surrounding reservoir, creating something equivalent to a super highway.

3.6.1 Hydraulic Fracturing Overview

Hydraulic fracturing started in the late 1940s and has evolved into the second largest investment (after drilling) of the oil and gas industry. From right before 2000 to 2008, the fracturing industry grew from $2.8 billion to $12.8 billion, representing an average increase of ±21% per year. No other petroleum activity showed such increase (Energy Tribune, 2008).

During the first 40 years, hydraulic fracturing was applied almost exclusively to low permeability reservoirs. However, starting in the late 1980s and increasingly in the 1990s, it encompassed any permeability reservoirs, including ones of extremely high permeability such as 200 to as high as 2,000 md. The important development was the ability to perform a tip screenout (TSO). Since unrestricted fracturing would generate both unwanted length and cause inordinate leakoff, a TSO arrests the fracture growth and inflates the fracture to the desired width. As seen below, far shorter but wider fractures are indicated for higher permeability reservoirs and such geometry can be accomplished only through a TSO.

In many writings, we have defined low and high permeability reservoirs for hydraulic fracturing as those where the design of the treatment execution would require TSO or not, respectively. For oil reservoirs below 5 md, the execution can be as an unrestricted fracture, hence they are low permeability. For 50 md and higher a TSO is necessary. For intermediate permeability, a TSO may not be necessary but often is used.

For natural gas wells, these permeability values are an order of magnitude smaller. Low permeability reservoirs are below 0.5 md and those above 5 md should be considered as high permeability formations (Economides et al. 2002a). (Note to the reader: Since the authors have been involved with a recent book specifically dealing with hydraulic fracturing of natural gas wells, the text below will be only an anthology of important concepts, emphasizing production related issues. A far more in-depth analysis can be found in Economides and Martin, 2007.)

Before delving into hydraulic fracturing, it is necessary to review the concept of dimensionless productivity index, as it will be used extensively later in this chapter.

3.6.2 The Concept of Dimensionless Productivity Index

The dimensionless productivity index, J_D, warrants some definition. The relationship between the dimensioned productivity index (PI) and the dimensionless J_D of an oil well is simply

$$\frac{q}{p - p_{wf}} = \frac{kh}{\alpha_r B\mu} J_D \,, \tag{3.42}$$

where the constant α_r is the familiar 141.2 in the traditional oilfield units or 18.4 if q (m^3/d), p (atm) and h (m).

For natural gas wells the analogous expression is

$$\frac{q}{p^2 - p_{wf}^{\ 2}} = \frac{kh}{\alpha_r \mu ZT} J_D \,, \tag{3.43}$$

where the constant α_r is the familiar 1,424 for oilfield units.

In Eqs. (3.42 and 3.43), the reservoir pressure, p, is either the constant outer boundary pressure, p_e, for steady state, or the average (and declining) reservoir pressure, $\bar{p}$, for pseudosteady state. The J_D is well known by familiar expressions for steady state radial flow in a vertical well

$$J_D = \frac{1}{\ln(r_e / r_w) + s} \,, \tag{3.44}$$

or, for pseudosteady-state flow

$$J_D = \frac{1}{\ln(r_e / r_w) - 0.75 + s} \,. \tag{3.45}$$

For a nondamaged well, the J_D would range between 0.11 and 0.13 for almost all drainage and wellbore radii combinations in both steady state and pseudosteady state. Thus, J_D values around 0.1 denote undamaged wells. Smaller values denote damage; larger values denote stimulation such as hydraulic fracturing, or more favorable geometry such as horizontal or complex well architecture (Diyashev and Economides, 2006).

3.6.3 Unified Fracture Design (UFD)

Valkó, Economides, and coworkers such as Romero et al. (2002), introduced a physical optimization technique to maximize the productivity index of a hydraulically fractured well that they have called the Unified Fracture Design (UFD) approach.

Central to the UFD is the Proppant Number, N_{prop}, given by

$$N_{prop} = I_x^2 C_{fD} = \frac{4k_f x_f w}{kx_e^2} = \frac{4k_f x_f w h_p}{kx_e^2 h_p} = \frac{2k_f V_p}{kV_r}, \tag{3.46}$$

where I_x is the penetration ratio and C_{fD} is the dimensionless fracture conductivity, V_r is the reservoir drainage volume, and V_p is the volume of the proppant *in the pay*. It is equal to the total volume injected times the ratio of the net height to the fracture height. k_f is the proppant pack permeability and k is the reservoir permeability.

For gas wells, the nominal proppant pack permeability is reduced to an effective permeability because of turbulence effects in the fracture. How this adjustment is done will be shown in a later section.

The idea of UFD is that fracturing transcends permeability, and for a given value of N_{prop}, there exists a unique geometry involving the fracture length and width (and therefore an optimum fracture conductivity) that would maximize well performance. Any other fracture conductivity, and therefore any other design, would lead to a lower well performance.

As shown by Economides et al. (2002a), at Proppant Numbers less than 0.1 the optimal conductivity, $C_{fD} = 1.6$. At larger Proppant Numbers, the optimum conductivity increases and the absolute maximum for the dimensionless productivity index, J_D is $6/\pi = 1.909$.

While graphical representations of these concepts can be found in the previously mentioned references, Valkó and Economides (1996) also presented correlations for the maximum achievable dimensionless productivity index as a function of the Proppant Number

$$J_{D\max}\left(N_{prop}\right) = \begin{cases} \dfrac{1}{0.990 - 0.5\ln N_{prop}} & \text{if } N_{prop} \le 0.1 \\ \dfrac{6}{\pi} - \exp\left[\dfrac{0.423 - 0.311N_{prop} - 0.089(N_{prop})^2}{1 + 0.667N_{prop} + 0.015(N_{prop})^2}\right] & \text{if } N_{prop} > 0.1 \end{cases}. \tag{3.47}$$

The optimal dimensionless fracture conductivity for the entire range of Proppant Numbers is given by

$$C_{fDopt}\left(N_{prop}\right)=\begin{cases}1.6 & \text{if } N_{prop}<0.1\\ 1.6+\exp\left[\dfrac{-0.583+1.48\ln N_{prop}}{1+0.142\ln N_{prop}}\right] & \text{if } 0.1\le N_{prop}\le 10\\ N_{prop} & \text{if } N_{prop}>10\end{cases}. \tag{3.48}$$

With the optimal dimensionless fracture conductivity determined, then the optimal fracture length and width are set, and they represent the only ones for which the fracture must be designed

$$x_{fopt}=\left(\frac{k_f V_f}{C_{fDopt}kh}\right)^{0.5} \quad \text{and} \quad w_{opt}=\left(\frac{C_{fDopt}kV_f}{k_f h}\right)^{0.5}, \tag{3.49}$$

where V_f is the volume of one propped wing, $V_f = V_p/2$.

UFD is an essential means to optimize fractured well performance and post-treatment evaluation can be made against design expectations. More to the point is that improvements in design, increasing proppant volumes, and using higher quality materials can be accomplished through the employment of these techniques. They can "push the limits" of hydraulic fracturing to levels unthinkable earlier (Demarchos et al., 2004).

Using a set of constraints such as a limit of 1,000 psi net pressure during execution (affecting directly the resulting fracture width), a minimum hydraulic fracture width of at least 3 times the proppant diameter to prevent proppant bridging, and an injection time of no more than 24 hours; Economides et al. (2004) developed a benchmarking graph for the maximum attainable J_D for oil wells for a range of permeabilities, shown in Figure 3–6. This representation is significant because it suggests what extraordinary results can be achieved by pushing the limits of design and using large volumes of higher quality proppant, while still respecting operational and logistical constraints.

One of the most striking conclusions of UFD Pand pushing the limits of fracturing is: If better proppants are used with higher k_f, the indicated propped width of the fracture is smaller, allowing longer

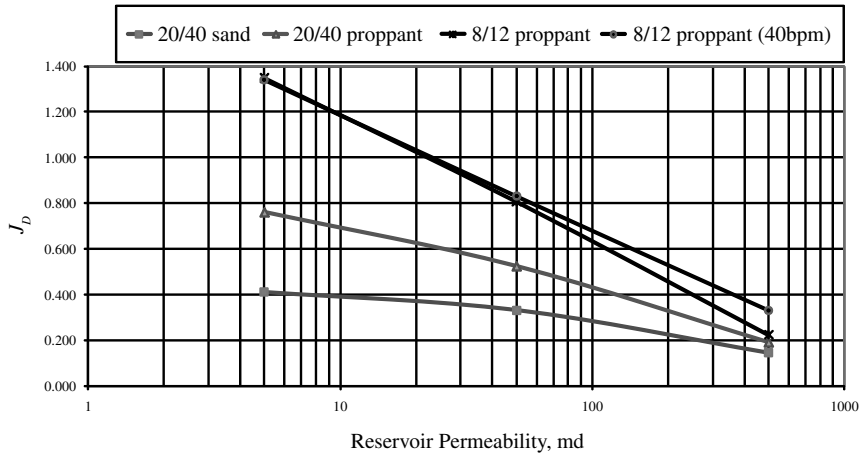

Figure 3–6 *Pushing the limits: maximum J_D with constraints* (Economides et al., 2004)

fractures for a given mass of proppant. Thus, much larger treatments can be executed before a net pressure constraint is in effect. This is counter to conventional practices, where better proppants have been sold to perform smaller treatments, and achieve similar results as those using lower quality proppants such as natural sand, resulting in the saving of a miniscule amount of money, while foregoing huge increases in production.

Example 3–5 Optimized fractured well performance

Use the following well, reservoir, and fracture treatment data. Calculate maximum J_D, optimum C_{fD}, and indicated fracture geometry (length and width). Apply to two different permeabilities: 1 and 100 md. In this example ignore the effects of turbulence. What would be the folds of increase between fractured and nonfractured wells?

Drainage area (square) = 4.0E + 6 ft^2 (equivalent drainage radius for radial flow = 1,130 ft)

Mass of proppant = 200,000 lb

Proppant specific gravity = 2.65

Porosity of proppant = 0.38

Proppant permeability = 220,000 md (20/40 ceramic)

Net thickness = 50 ft

Fracture height = 100 ft

Solution

First, the volume of the proppant in the pay is [200,000 × (50/100)/(2.65 × 62.4 × (1 – 0.38))] = 975 ft.

Then for k = 1 md from Eq. (3.46)

$$N_{prop} = \frac{2 \times 220{,}000 \times 975}{1 \times 2 \times 10^8} = 2.1.$$

Using the lower part of Eq. (3.47), J_D maximum is then 1.1. From Eq. (3.48) $C_{fD,opt}$ = 2.5.

Therefore from Eq. (3.49)

$$x_{fopt} = \left(\frac{220{,}000 \times 975/2}{2.5 \times 1 \times 50} \right)^{0.5} = 920 \text{ ft},$$

and

$$w_{opt} = \left(\frac{2.5 \times 1 \times 975/2}{220{,}000 \times 50} \right)^{0.5} = 0.0105 \text{ ft} = 0.13 \text{ in.}$$

For k = 100 md from Eq. (3.46), the PProppant Number is 100 times smaller (0.021), and as should be expected, $C_{fD,opt}$ = 1.6. (No need to calculate). From Eq. (3.47), maximum J_D is then 0.34. From Eq. (3.49) x_{fopt} and w_{opt} are 115 ft and 1 in., respectively.

Given that the J_D of a nonfractured well would be 0.135 (from Eq. (3.44) and using r_w = 0.328 ft). The folds of increase for the two wells would be 8.2 and 2.5, respectively.

3.6.4 Performance of a Hydraulically Fractured Well with Turbulence

Economides et al. (2002b) presented an iterative procedure combining the UFD method with the Gidley (1990) adjustment to the

proppant pack permeability, and the Cooke (1993) correlations for flow in fractures, to account for the enhanced turbulence effects in fracture flow. It must be emphasized that while turbulence in the fracture reduces the would-be performance, the overall improvement in well production is very large when compared to that of a nonfractured well because of the enhanced turbulence effects in high permeability radial flow (Marongiu-Porcu et al., 2008).

The nominal proppant pack permeability is corrected to an effective value using the Reynolds number in the fracture by

$$k_{f,e} = \frac{k_{f,n}}{1 + N_{\mathrm{Re}}}, \tag{3.50}$$

where $k_{f,n}$ is the nominal fracture permeability.

There is an indicated iterative procedure and it starts by assuming a Reynolds number. An obvious first value for the Reynolds number is zero, which means that the nominal proppant pack permeability is not affected by turbulence and is equal to the effective permeability. Then, after adjusting with Eq. (3.50), the Proppant Number is calculated from Eq. (3.46), and the maximum J_D (Eq. (3.47) and the optimum dimensionless conductivity (Eq. (3.48) are calculated. The latter allows the determination of the indicated fracture dimensions using Eq. (3.49).

For the rest of this calculation, there are additional needed variables compared to designing fractures for oil wells or for low permeability gas wells. The determined dimensionless productivity index and the well drawdown allow the determination of the expected production rate, which in turn is used to calculate the velocity in the fracture and to obtain the Reynolds number. The procedure ends when the assumed and calculated Reynolds numbers are close enough.

The Reynolds number for non-Darcy flow is given by

$$N_{\mathrm{Re}} = \frac{\beta k_{f,n} v \rho}{\mu}, \tag{3.51}$$

where $k_{f,n}$ is the nominal permeability (under Darcy flow conditions) in m^2, β is in 1/m, v is the fluid velocity at reservoir conditions in the fracture in m/s, μ is the viscosity in Pa.s, and ρ is the density in kg/m^3. The value of β is obtained from

$$\beta = (1 \times 10^{8)} \frac{b}{(k_{f,ne})^a}, \tag{3.52}$$

where a and b are obtained from Cooke (1993). The values of a and b for common proppant sizes are given in Table 3–7.

Table 3–7 Constants a and b

Prop Size	a	b
8 to 12	1.24	17,423
10 to 20	1.34	27,539
20 to 40	1.54	110,470
40 to 60	1.6	69,405

Example 3–6 Optimized fractured well performance with turbulence

Repeat Example 3–5 for the 100 md case, but now consider the effects of turbulence in both the nonfractured and fractured wells. Calculate the folds of increase under pseudosteady-state conditions.

Additional variables are:

$\overline{p}$ = 3,000 psi

p_{wf} = 1,500 psi

T = 250°F = 710 R

γ = 0.7

and thus at 1,500 psi, Z = 0.91, and μ = 0.0162 cp,

and at 3,000 psi, Z = 0.91, and μ = 0.02 cp

$D = 3.3 \times 10^{-5}$ (Mscf/d)$^{-1}$ for radial flow.

Solution

Applying the pseudosteady version of Eq. (3.28) and substituting variables

$$q^2 + 2.23 \times 10^5 q = 6.15 \times 10^{10}$$

and thus, q = 160,000 Mscf/d. Ignoring turbulence effects this flow rate would be 276,000 Mscf/d.

For the fractured well and without correcting for turbulence effects, using J_D = 0.34 from Example 3–5 (i.e., N_{Re} = 0),

$$q = \frac{kh(\bar{p}^2 - p_{wf}{}^2)}{1,424\mu ZT} J_D = \frac{100 \times 50 \times (3,000^2 - 1,500^2)}{1,424 \times 0.018 \times 0.91 \times 710} \times 0.34 = 693,000 \text{ Mcf/d}.$$

This rate is 2.5 times the rate for radial flow uncorrected for turbulence (276,000 Mscf/d) as found in Example 3–5. However, turbulence cannot be ignored and the procedure outlined in the earlier section must be followed.

The formation volume factor can be obtained from Eq. (1.12) and is calculated at the flowing bottomhole condition

$$B_g = 0.0283 \times \frac{0.91 \times 710}{1,500} = 0.012(\text{res ft}^3 / \text{scf}).$$

The density can be calculated using Eq. (1.10)

$$\rho_g = 2.7 \times \frac{1,500 \times 0.7}{0.91 \times 710} = 4.83 \text{ lb/ft}^3 = 77.4 \text{ kg/m}^3.$$

And finally, the velocity can be determined by (using 1 in. width as calculated in Example 3–5 and dividing by 2 for the two wings of the fracture):

$$v = (0.012 \times 693,000 \times 1,000)/[24 \times 3,600 \times 100 \times (1/12) \times 2]$$
$$= 5.8 \text{ ft/sec} = 1.77 \text{ m/s}.$$

From Eq. (3.52) and using a = 1.54 and b = 110,470 for 20/40 mesh proppant (from Cooke correlation, Table 3–7)

$$\beta = (1 \times 10^8) \times \frac{110,470}{(220,000)^{1.54}} = 6.54 \times 10^4 1/m .$$

And finally, from Eq. (3.51)

$$N_{\text{Re}} = \frac{6.54 \times 10^4 \times 2.17 \times 10^{-10} \times 1.77 \times 77.4}{0.0162 \times 10^{-3}} = 120 .$$

Clearly, the assumed (zero) and calculated Reynolds numbers are quite different.

An instructive second iteration would be for N_{Re} = 9, which would reduce the effective permeability by a factor of ten as per Eq. (3.50), in this Example to 22,000 md. The Proppant Number becomes ten times smaller than the one calculated in Example 3–5 (0.0021), and again, $C_{fD,opt}$ = 1.6. From Eq. (3.47), J_D maximum is then 0.25. From Eq. (3.49), x_{fopt} and w_{opt} are 36 ft and 3.2 in., respectively. (Note in practice such large width may be unrealistic but is used here for illustration purposes.)

With the new J_D, the rate is 510,000 Mscf/d and the new velocity is now 0.41 m/s. From Eq. (3.51), N_{Re} = 27.8. It is still different from the assumed value of nine.

Convergence occurs at N_{Re} = 18 with maximum J_D = 0.23, new rate = 470,000 Mscf/d. The effective proppant pack permeability is 11,600 md, and x_{fopt} and w_{opt} are 26 ft and 4.5 in., respectively.

Some very important lessons are learned from this Example. The reduction in effective permeability results in a demand for a much larger width (and in this case, one that may not be able to be achieved in the field, but very aggressive designs may approach these widths). More important, is that the ratio of the productivity indexes between the fractured and the nonfractured wells, when considering turbulence effects, is now 470,000/160,000 = 3 (versus. 2.5); showing the considerable impact of fracturing in remedying turbulence.

Marongiu-Porcu et al. (2008) presented an important study comparing the folds of productivity index increase between fractured and nonfractured wells for both oil and gas. Figure 3–7 is the comparison, and the results show the major impact of turbulence in gas wells. First, for oil wells, the folds of increase are predictable. As the reservoir permeability increases, the folds of PI increase are reduced. For example, while at 0.1 md, the folds of increase are over 10, and at 100 md they are only 2. For gas wells at small reservoir permeabilities, the trends are similar to oil, but as the reservoir permeability increases, the folds of PI increase take an upward trend. This is because of the enhanced turbulence effects in radial flow and the considerable reduction of turbulence in the fractured wells. Figure 3–7 is one of the most important indicators that while for oil wells one may make the case that fracturing in high permeability wells may not be compelling (i.e. in some cases horizontal wells may be better than fractured vertical wells); however, for gas wells hydraulic fracturing is absolutely essential in any range of permeabilities. (Note: In Figure 3–7 the fracture width is as wide as determined from the optimum values of J_D and C_{fD}.)

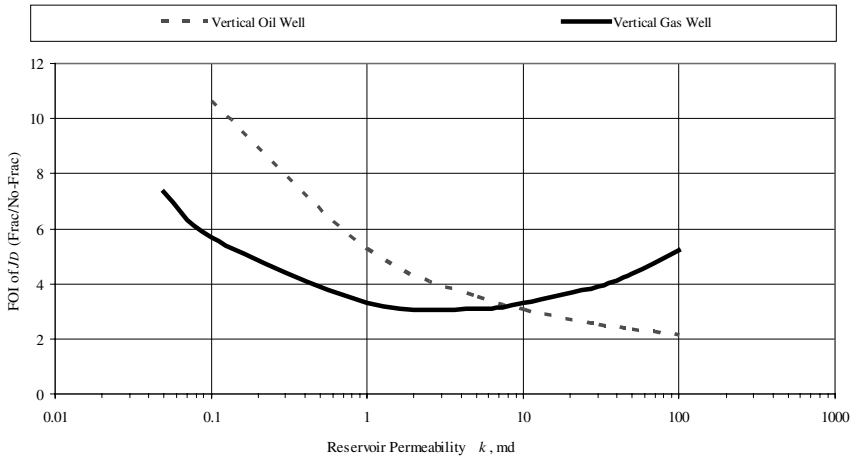

Figure 3–7 *Folds of increase between fractured and unfractured wells* (Marongiu-Porcu et al., 2008)

3.6.5 Fracturing Horizontal Gas Wells

In anticipation of hydraulic fracturing, horizontal wells can be drilled either along the maximum or the minimum horizontal stress orientations, thus, executed fractures will be longitudinal or transverse, respectively. The performance of a longitudinally fractured horizontal well is almost identical to a fractured vertical well when both have equal fracture length and equal conductivity. Therefore, existing solutions for vertical well fractures can be applied to a longitudinally fractured horizontal well (Valkó and Economides, 1996; Soliman et al., 1999; Economides and Martin, 2007).

The interesting new element is the ability to perform multiple transverse fracturing treatments with proper zonal isolation and spacing. The vast majority of applications of fractured horizontal wells are for transverse fractures. The configuration of a transversely fractured horizontal well is demonstrated in Figure 3–8, and it provides a visualization of the process and challenges. The cross section of the contact between a transverse fracture and a horizontal well is $2\pi r_w w$ where w is the width of the fracture (which can be obtained by using a design procedure such as the Unified Fracture Design approach) and r_w is the radius of the horizontal well. Figure 3–8 shows the flow from the reservoir into the fracture is linear while the flow inside the fracture is converging radial. This combination of flows results in an additional pressure drop which can be accounted for by a skin effect, denoted as s_c (Mukherjee and Economides, 1991).

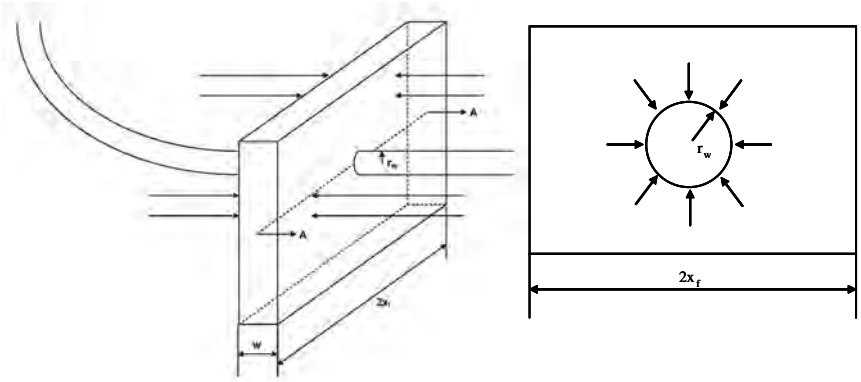

Side View Top View

Figure 3–8 *Fluid flow from reservoir to a transverse fracture*

$$s_c = \frac{kh}{k_f w}\left[\ln\left(\frac{h}{2r_w}\right) - \frac{\pi}{2}\right] . \tag{3.53}$$

Therefore, the design procedure for each transverse fracture employs the UFD, which allows for the calculation of $J_{D,max}$ and s_c. This in turn leads to the dimensionless productivity index of each transverse fracture (neglecting for now turbulence effects), J_{DTH}:

$$J_{DTH} = \frac{1}{\left(\frac{1}{J_{DV}}\right) + s_c} , \tag{3.54}$$

where J_{DV} is the $J_{D,max}$ of the fractured vertical well.

With J_{DTH} and drawdown, the actual production rate can be obtained using

$$q = \frac{kh(\bar{p}^2 - p_{wf}^2)}{1,424\mu ZT} J_{DTH} . \tag{3.55}$$

For gas wells, the iterative procedure outlined in the previous subsection for the performance of fractured vertical wells also applies to transversely fractured horizontal wells. The obvious difference is that turbulence effects will be more pronounced because of the far reduced contact between well and fracture and the cross-sectional

area of flow. For a vertical well the flow area would be $2wh_f$, whereas for a transversely fractured horizontal well, it would be $2\pi r_w w$. For the same width the cross-sectional area of flow of a vertical well would be 100 to 200 times larger ($h_f / \pi r_w$).

Turbulence effects have a great impact on transversely fractured horizontal gas wells due to the small cross section of the contact between the well and the fracture. Because of the impact of turbulence effects, the results for the permeability range of 1 md to 100 md, which performs very well in vertical fractured gas wells, are unacceptable in transversely fractured horizontal gas wells. Marongiu-Porcu et al. (2009) have demonstrated that only a very small range of reservoir permeabilities in gas wells lends itself to the transverse fracture configuration, i.e., $0.1 < k < 0.5$. The conclusion is based on both physical and economic considerations. For larger permeability values, turbulence effects reduce fracture performance (even with multiple fractures such as ten treatments) to unacceptable production rates and vertical wells become preferable. For the lower permeability range, outside of North America, where treatment costs are significantly lower than the rest of the world, the expected production rates are not sufficient to warrant the drilling of horizontal wells and their subsequent well completion and fracturing.

Example 3–7 Performance of transversely fractured horizontal well

Calculate the flow rate in a transversely fractured horizontal well (with one transverse fracture) for formation permeability of 0.1, 1, 10, and 100 md. Relevant well data are given as below:

Nominal proppant permeability = 600,000 md

Mass of proppant = 400,000 lbm

Porosity of proppant pack = 0.3

Specific gravity of proppant = 3.27

Net thickness = 50 ft

Well radius = 0.359 ft

Well drainage radius = 660 ft

Pretreatment skin factor = 0

Fracture height = 100 ft

Gas specific gravity (air = 1) = 0.7

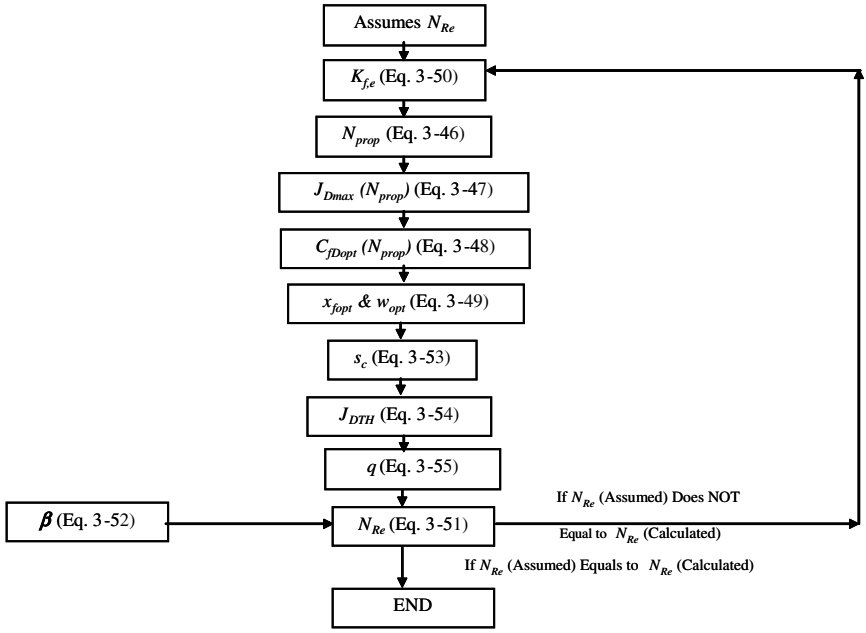

Figure 3–9 *Chart of iterative calculation procedure*

$\overline{p}$ = 3,000 psi

p_{wf} = 1,500 psi

T = 250°F = 710 R

Solution

The calculation procedure is outlined in Figure 3–9. In calculating the Reynolds number with Eq. (3.51) in this Example, the velocity is determined by dividing the downhole volumetric flow rate by the cross-sectional area of flow as explained in the subsection above. This greatly increases turbulence effects in a transverse fracture at any permeability but particularly at higher permeability (see results in Figure 3–10).

For comparison purposes, the flow rate from the ideal openhole vertical well (without turbulence), radial vertical well (actual with turbulence), and vertical fractured well are also calculated. The productivity ratio (against the ideal openhole vertical well) is plotted in Figure 3–10.

Results show that when permeability is 0.1, turbulence is negligible. The fold of increase (FoI) from a single transversely fractured

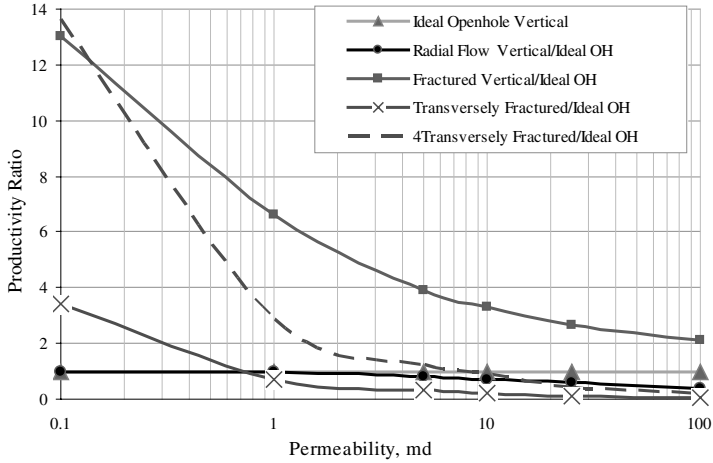

Figure 3–10 *Productivity comparison among vertical and horizontal wells with and without fracture*

horizontal well is about 3.4. FoI from a fractured vertical well is ~13. That is almost four times higher than in the transversely fractured horizontal well, which means that four or more treatments in a horizontal well would result in higher performance than a vertical well/vertical fracture configuration.

Once the permeability is higher than 1 md, the choke and turbulence effects in the transversely fractured horizontal well become dominating. The skin, s_c (described in Eq. (3.53), increases from 0.6 at 0.1 md to 6.7 at 1 md and 137 at 100 md (shown in Figure 3–11). This causes the FoI from the single transversely fractured horizontal well to be less than 1, which means its performance is worse than that in an ideal vertical openhole well ($\beta = 0$, $s = 0$). When permeability is 100 md the FoI drops to 0.05. The FoI from the vertical fractured well is over 2. It would take 40 transverse treatments (2/0.05) in a horizontal well to equal the performance of one vertical well/vertical fracture.

This example suggests that transversely fractured horizontal wells, even with a large number of treatments (and ignoring the economic cost), simply cannot compete physically with vertical fractured wells when the permeability is higher than, e.g., 0.5 md (even when premium proppant such as 600,000 md) is used.

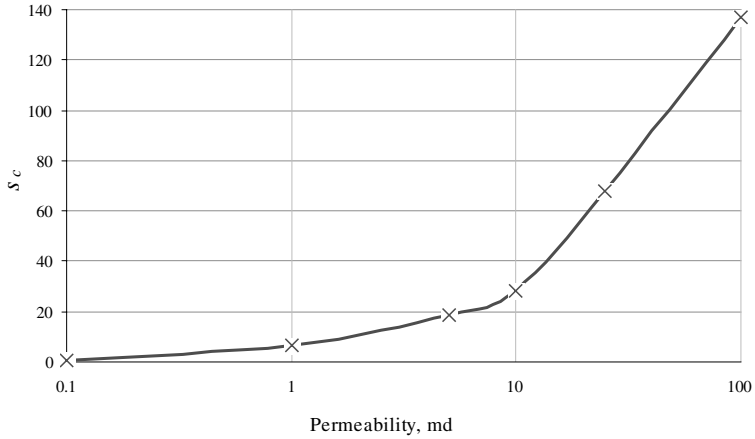

Figure 3–11 *Skin versus permeability in the single transversely fractured horizontal well*

3.7 Well Deliverability

"Deliverability" of a gas well is defined as a production rate into the wellbore, and subsequently, along the production tubing to the surface facilities. In underground storage or enhanced recovery, deliverability also relates to the rate at which gas can be injected from a well into the reservoir (Lee et al., 1984). The flow rate from a drainage area into a wellbore is a function of the properties of both the formation and the fluids, as well as the prevailing gradients of driving forces (Lee et al., 1987).

To perform well deliverability calculations, the pressure drop in a gas well must be determined. The unique aspect is that the fluid is compressible and the fluid density and fluid velocity vary along the pipe. These variations must be included when integrating the mechanical energy balance equation which, with no shaft work and neglecting kinetic energy changes, is

$$\frac{dp}{\rho} + \frac{g}{g_c} dz + \frac{2 f_f u^2 dL}{g_c D} = 0, \tag{3.56}$$

where f_f is the Fanning friction factor. It can be obtained from the Moody friction chart (Moody, 1944) or the Chen equation (Chen, 1979)

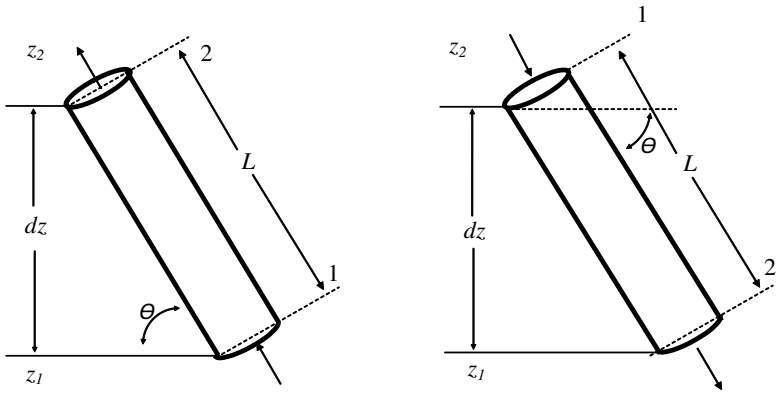

a) Upward Flow b) Downward Flow

Figure 3–12 *Flow geometry in pipe*

$$\frac{1}{\sqrt{f_f}} = -4\log\left\{\frac{\varepsilon}{3.7065} - \frac{5.0452}{N_{\mathrm{Re}}}\log\left[\frac{\varepsilon^{1.1098}}{2.8257} + \left(\frac{7.149}{N_{\mathrm{Re}}}\right)^{0.8981}\right]\right\}, \qquad (3.57)$$

where ε is the relative pipe roughness. N_{Re} is the Reynolds number and its calculation is discussed later in this section.

Since dz in Eq. (3.56) is $\sin\theta dL$ (see demonstration in Figure 3–12), the last two terms can be combined as

$$\frac{dp}{\rho} + \left(\frac{g}{g_c}\sin\theta + \frac{2f_f u^2}{g_c D}\right)dL = 0. \qquad (3.58)$$

Replacing ρ by Eq. (1.10), the fluid velocity can be determined using the real gas law and be related to the well flow rate given in standard conditions, q,

$$u = \frac{4}{\pi D^2} qZ\left(\frac{T}{T_{\mathrm{sc}}}\right)\left(\frac{p_{sc}}{p}\right). \qquad (3.59)$$

Thus, Eq. (3.58) yields

$$\frac{ZRT}{28.97\gamma_g p}dp + \left\{\frac{g}{g_c}\sin\theta + \frac{32f_f}{\pi^2 g_c D^5}\left[\left(\frac{T}{T_{\mathrm{sc}}}\right)\left(\frac{p_{\mathrm{sc}}}{p}\right)qZ\right]^2\right\}dL = 0. \qquad (3.60)$$

Eq. (3.60) requires numerical integration to be solved properly. However, if an average temperature is used in an interval and if, also, an average value of the gas deviation factor, Z, for the interval is used then Eq. (3.60) can be integrated for nonhorizontal flow to yield

$$p_2^2 = e^s p_1^2 + \frac{32 f_f}{\pi^2 D^5 g_c \sin\theta}\left(\frac{\bar{Z}\bar{T} q p_{sc}}{T_{sc}}\right)^2 (e^s - 1), \tag{3.61}$$

where s is defined as

$$s = \frac{-2 \times 28.97 \gamma_g (g / g_c) \sin\theta L}{\bar{Z} R \bar{T}}. \tag{3.62}$$

For horizontal flow, sin θ and s are zero; integration of Eq. (3.60) gives

$$p_1^2 - p_2^2 = \frac{64 \times 28.97 \gamma_g f_f \bar{Z}\bar{T}}{\pi^2 g_c D^5 R}\left(\frac{p_{sc} q}{T_{sc}}\right)^2 L. \tag{3.63}$$

For each interval, an estimate of the average $\bar{Z}$ can be obtained as a function of the average temperature, $\bar{T}$, and the known pressure, p_1. After the pressure, p_2, is calculated, the assumed $\bar{Z}$ can be compared with the calculated value using $\bar{T}$ and the average pressure, $(p_1 + p_2)/2$. Iteration may be necessary in some cases.

To complete the calculation, the friction factor must be obtained from the Reynolds number and the pipe roughness. Since the product, $\rho\mu$, is a constant for flow of a compressible fluid, N_{Re} can be calculated based on standard conditions as

$$N_{Re} = \frac{4 \times 28.97 \gamma_g q p_{sc}}{\pi D \bar{\mu} R \bar{T}_{sc}}. \tag{3.64}$$

The viscosity should be evaluated at the average temperature and pressure as was the compressibility factor, $\bar{Z}$.

Eq. (3.60) for vertical flow and in oilfield units becomes

$$p_2^2 = e^s p_1^2 + 2.685 \times 10^{-3} \frac{f_f (\bar{Z}\bar{T} q)^2}{\sin\theta\ D^5}(e^s - 1), \tag{3.65}$$

or

$$p_1^2 = e^{-s} p_2^2 - 2.685 \times 10^{-3} \frac{f_f (\bar{Z}\bar{T}q)^2}{\sin\theta \; D^5} (1 - e^{-s}), \tag{3.66}$$

if the flowing bottomhole pressure (p_1) is the unknown and will be calculated from the surface pressure of p_2. In Eqs. (3.65 and 3.66), s is defined as

$$s = \frac{-0.0375 \gamma_g \sin\theta L}{\bar{Z}\bar{T}}. \tag{3.67}$$

Eq. (3.62) for horizontal flow becomes

$$p_1^2 - p_2^2 = 1.007 \times 10^{-4} \frac{\gamma_g f_f \bar{Z}\bar{T} q^2 L}{D^5}. \tag{3.68}$$

Finally the Reynolds number becomes

$$N_{\text{Re}} = 20.09 \frac{\gamma_g q}{D\mu}. \tag{3.69}$$

In Eqs. (3.65 to 3.69), p is in psia, q is in Mscf/d, D is in inches, L is in ft, μ is in cp, and T is in R.

Example 3–8 Wellbore hydraulics and pressure calculations

A well flows 10 MMscf/d of natural gas from a depth of 13,000 ft with a 3-in. tubing in a vertical well. At the surface, the temperature is 150°F and the pressure is 650 psia; the bottomhole temperature is 230°F. The gas gravity is 0.7 and the relative roughness of the tubing is 0.0006. Calculate the flowing bottomhole pressure at the given rate. Repeat the calculation for 20 MMscf/d and show what tubing diameter would be required to produce the same flowing bottomhole pressure.

What would the rate be for a 3-in. pipe if the wellhead pressure is 650 psia and the flowing bottomhole pressure cannot exceed 2,000 psi?

Solution

Eqs. (3.66, 3.67, and 3.69) are needed to solve this problem.

Using the average temperature, 650 R, and using the known pressure at the surface as the average pressure (for now), 650 psia, with the given gas gravity, and the assumption of zero percent of sour gases; the average *Z*-factor and gas viscosity can be obtained from the correlations in Chapter 1 as $\overline{Z} = 0.936$ and $\overline{\mu} = 0.0137$ cp.

From Eq. (3.69), the Reynolds number is,

$$N_{\mathrm{Re}} = 20.09 \times \frac{0.7 \times 10{,}000}{3 \times 0.0137} = 3.42 \times 10^{6},$$

and with roughness of 0.0006, using the Chen equation (Eq. (3.57)) leads to $f_f = 0.0044$. Since the flow direction is vertical upward, $\theta = +90°$.

Now using Eq. (3.67),

$$s = \frac{-0.0375 \times 0.7 \times \sin(90^{0}) \times 130{,}000}{0.936 \times 650} = -0.56.$$

The bottomhole pressure is calculated from Eq. (3.66)

$$p_1^2 = e^{-(-0.602)} \times 650^2 - 2.685 \times 10^{-3} \times \frac{0.0044 \times (0.875 \times 650 \times 10{,}000)^2}{\sin(90^{0}) \times 3^5}(1 - e^{-(-0.602)})$$

and thus, $p_1 = p_{wf} = 1{,}445$ psia.

Readjusting the average pressure to (1,445 + 640)/2 = 1,048 psi, new $\overline{Z}$ and $\overline{\mu}$ are obtained and the above calculation is repeated. The final results are $\overline{Z} = 0.90$, $\overline{\mu} = 0.014$, $N_{Re} = 3.25 \times 10^6$, $f_f = 0.044$, $s = -0.58$, and the flowing bottomhole pressure at 10 MMscf/d is $p_1 = p_{wf} = 1{,}440$ psia.

Doubling the rate to 20 MMscf/d would require a flowing bottomhole pressure equal to 2,431 psi.

For a flow rate of 20 MMscf/d, a wellhead pressure of 650 psi, and a bottomhole pressure of 1,440 psi, the required tubing diameter would be 4 in.

For the 3-in. pipe with two pressure constraints (650 and 2,000), the flow rate is 15.8 MMscf/d.

Example 3–9 Gas well deliverability

A natural gas well produces from a depth of 13,000 ft with a 3-in. tubing in a vertical well. The surface temperature is 150°F and the pressure is 650 psia; the bottomhole temperature is 230°F. The gas gravity is 0.7 and the relative roughness of the tubing is 0.0006 (this information is the same as for Example 3–8).

If the reservoir permeability is 1 md, the pay thickness is 75 ft, and the reservoir pressure is 6,000 psi:

1. Determine the well deliverability.
2. Repeat the calculation for a ten-fold larger permeability of 10 md.
3. Determine what tubing diameter would be required to produce the same flowing bottomhole pressure in the second reservoir as for the first.

Solution

Using the same procedure outlined in Example 3–8, for the first question the flowing rate is about 12 MMscf/d at the corresponding flowing bottomhole pressure of 1,650 psi. By using the same procedure, the tubing performance curve is generated for a range of potential rates.

The IPR curve was obtained from the Swift and Kiel (1962) pseudosteady-state model Eq. (3.28), while the non-Darcy coefficient D has been estimated to be approximately equal to 10^{-4} $(\text{Mscf/d})^{-1}$ by using the correlation given by Eq. (3.29). Graphical solution of this case is presented in Figure 3–13.

For a permeability of 10 md and all other input data unchanged, a flowing rate of about 38.5 MMscf/d is obtained at the corresponding flowing bottomhole pressure of 4,530 psi. Graphical solution of this case is presented in Figure 3–14.

The results of Figure 3–14 are significant. First, it is clear that the production rate is not even close to a ten-fold increase over the 1 md reservoir case. The reasons are the much large turbulence effects in the reservoir, and as important, the pressure drops in the tubing. Note the almost 3-fold increase in the required flowing bottomhole pressure. Clearly this well is tubing limited.

For the same inflow condition determined in Question 2, the tubing diameter required to produce the same flowing bottomhole pressure of Question 1 (1,650 psi) is 6.3 in., which also produces a new flowing rate of about 79 MMscf/d. These results show the importance of proper tubular designs in high rate natural gas wells. (Note:

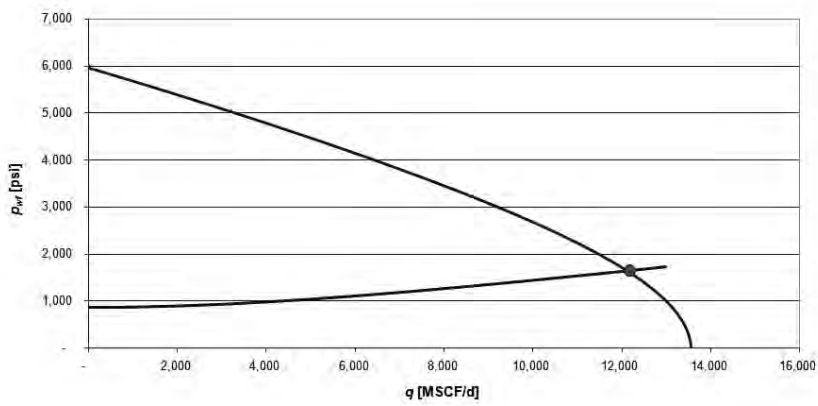

Figure 3–13 *Well deliverability for Example 3–9, k =1 md, D_{tbg} = 3 in.*

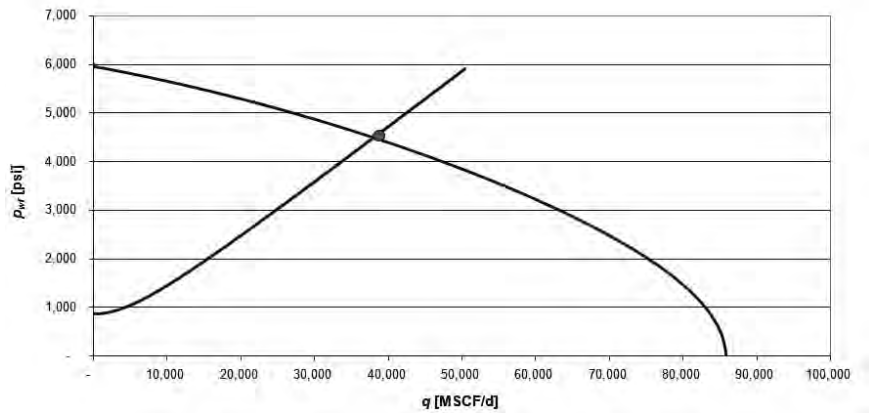

Figure 3–14 *Well deliverability for Example 3–9, k =10 md, D_{tbg} = 3 in.*

the calculated tubing diameter is theoretical. In practice, a standard tubing size would be used, e.g., 6 in.) Graphical solution of this case is presented in Figure 3–15.

3.8 Forecast of Well Performance and Material Balance

Forecast of well performance is intended to predict well deliverability, adding the very important variable of time. Production under steady state is simple. Assuming that a well can be maintained at roughly

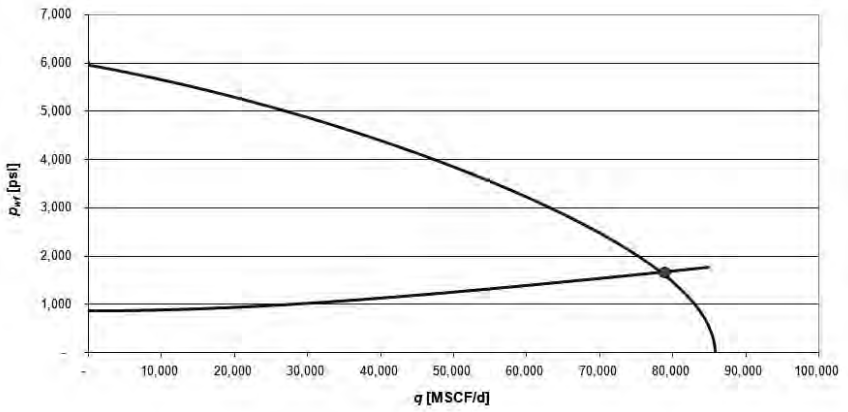

Figure 3–15 *Well deliverability for Example 3–9, k =10 md, D_{tbg} = 6.3 in.*

steady state because of e.g., strong bottom water drive, then the production rate will remain largely constant for as long as the condition is maintained. Under transient conditions, forecast of well performance is also relatively easy. The intersection of transient IPR's with the well vertical lift performance curve will provide the expected production rates versus time. Transient well performance will be in force if the reservoir permeability is quite low and, thus boundary effects will take time to appear.

Of unique interest is the forecast of well performance under pseudosteady state conditions for which material balance is necessary.

If G_i and G are the initial and current gas-in-place in standard conditions within a drainage area, the difference between the two of them is the cumulative production from a gas reservoir, as a result of fluid expansion and, thus

$$G_p = G_i - G = G_i - G_i \frac{B_{gi}}{B_g} \tag{3.70}$$

where B_{gi} and B_g are the initial and current formation volume factors, respectively.

Eq. (1.12) in Chapter 1 provides B_g in terms of pressure, temperature, and the gas deviation factor. Substitution in Eq. (3.70) for isothermal conditions, which is a reasonable assumption, and rearrangement results in

$$G_p = G_i \left(1 - \frac{\bar{p} / Z}{p_i / Z_i} \right). \tag{3.71}$$

Eq. (3.71) is one of the best known expressions in reservoir and production engineering, and it suggests that a plot of G_p, the cumulative production, in the abscissa, $\overline{p}/Z$ and in the ordinate, should form a straight line. At G_p=0, $\overline{p}/Z = p_i/Z_i$, and at $\overline{p}/Z = 0$, $G_p = G_i$. For any value of the reservoir pressure (and associated Z), there exists a corresponding G_p.

The indicated well performance forecast procedure follows.

First, a reservoir pressure decline increment is assumed, e.g., 500 psi. The resulting average pressure (and the easy to calculate $\overline{p}/Z$) would lead to the cumulative recovery for the interval. Next, the production rate for the interval can be determined, using the pseudosteady state relationships presented earlier in this chapter (Eq. (3.14) without turbulence effects and Eq. (3.29) with turbulence effects), employing the average reservoir pressure of the interval and the well deliverability methods outlined in the last section. The time for each interval would then be simply $\Delta G_p/q$.

Example 3–10 Forecast of gas well performance under pseudosteady state

Present a forecast of production, reservoir pressure, and cumulative recovery as a function of time. The same natural gas well that was used in Examples 3–8 and 3–9 (depth 13,000 ft, with 3-in. tubing ID, surface temperature 150°F, surface pressure 650 psia, reservoir temperature 230°F, gas gravity 0.7) drains 160 acres with porosity equal to 0.2, and water saturation equal to 0.3. The reservoir permeability is 1 md, the pay thickness is 75 ft, and the initial reservoir pressure is 6,000 psi.

Abandonment reservoir pressure is 2,000 psi.

Solution

The first step is to calculate the initial Z-factor, which is equal to 1.08, and therefore p_i/Z_i = 5,560 psi.

Then, the initial gas-in-place is calculated

$$G_i = 160 \times 43{,}560 \times 75 \times 0.2 \times (1 - 0.3) / 3.5 \times 10^{-3} = 20.9 \times 10^9 \text{ scf} = 20.9 \text{ Bcf},$$

where the initial formation volume factor, $B_{gi} = 3.5 \times 10^{-3}$ res ft^3/scf.

Figure 3–16 is the graphical depiction of the material balance whose algebraic expression in Bcf is $G_p = 20.9 - 0.00375\ \overline{p}/Z$.

One round of calculations is shown next.

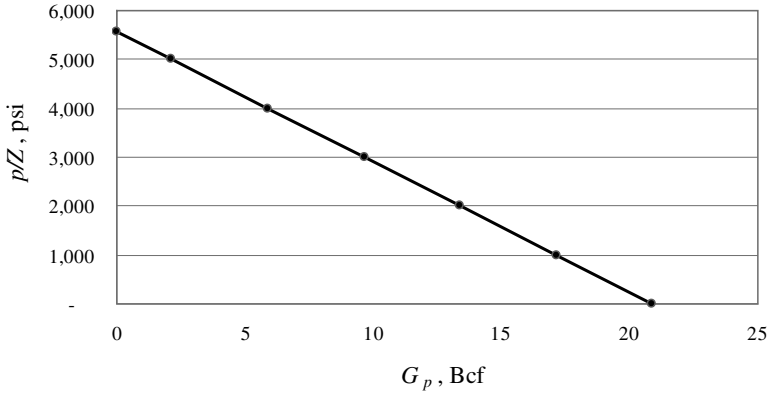

Figure 3–16 *Material balance for Example 3–10*

Assume the reservoir pressure declines to 5,500 psi. Then $Z = 1.04$ and $\overline{p}/Z = 5{,}290$ psi. The cumulative recovery, G_p is then (from Figure 3–16) 1.06 Bcf.

Then, using a deliverability calculation as shown in Example 3–9, ignoring turbulence, and with an average reservoir pressure of (6,000 + 5,500)/2 = 5,750 psi, the flow rate q = 13.5 MMcf/d. Therefore G_p/q = 79 days.

Table 3–8 contains all the calculations for this exercise. The production rate, reservoir pressure, and cumulative production versus time are plotted in Figure 3–17.

The material balance, depicted in Figure 3–16, can be constructed before production starts. It can be based on the initial pressure build up test, from which the initial reservoir pressure will be determined, and on geological information of drainage area, reservoir net thickness, porosity, and water saturation.

During production, if the original assumption was correct, then a plot of actual cumulative production versus p/Z (also determined from successive pressure build up tests) should fall exactly on the original material balance curve. Otherwise, if the points are to the left of the initial curve, they would extrapolate to a lower G_p, suggesting smaller drainage area or smaller reservoir net thickness.

Conversely, if the actual data are to the right of the initial curve, this would invariably suggest strong bottom water drive, in which case the entire construction is not really valid.

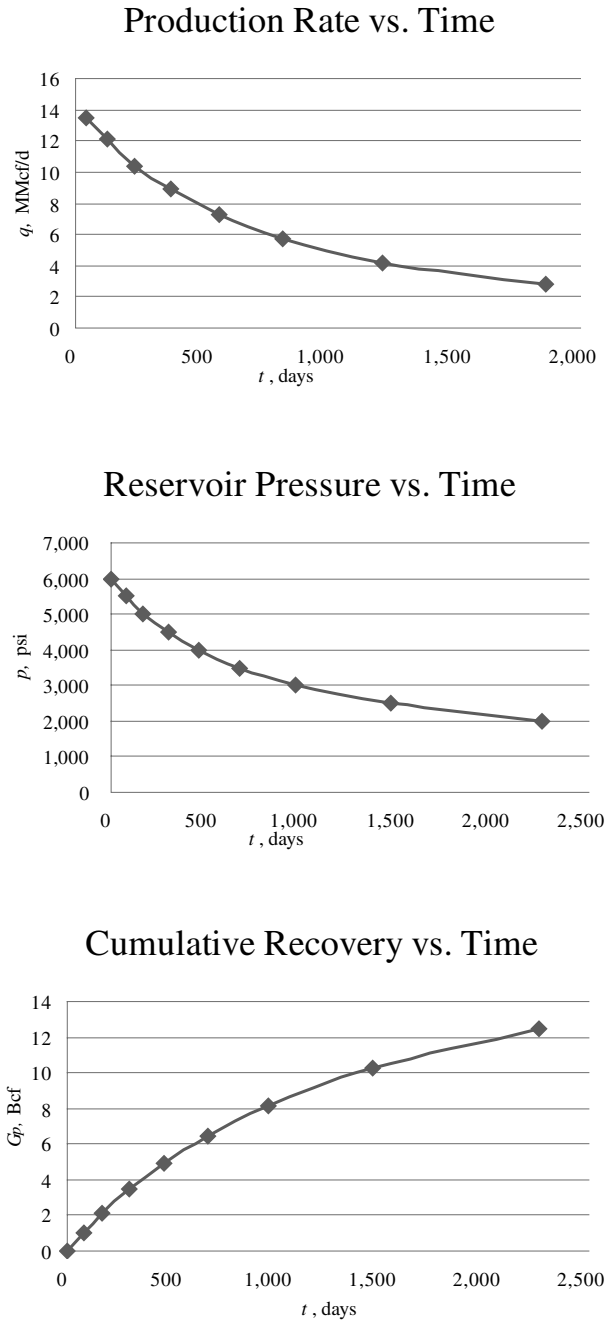

Figure 3–17 *Production rate, reservoir pressure, and cumulative recovery for Example 3–10*

Table 3–8 Material Balance Calculations for Example 3–10

p, psi	Z	p/Z, psi	G_p, Bcf	ΔG_p, Bcf	q, MMcf/d	Δt,days	t,days
6000	1.08	5,560					
				1.06	13.5	79	
5,500	1.04	5,288	1.06				79
				1.09	12.1	90	
5,000	1	5,000	2.15				169
				1.35	10.4	130	
4,500	0.97	4,639	3.5				299
				1.44	8.9	162	
4,000	0.94	4,255	4.94				461
				1.54	7.3	211	
3,500	0.91	3,846	6.48				672
				1.68	5.7	295	
3,000	0.89	3,371	8.16				967
				2.09	4.2	498	
2,500	0.88	2,841	10.25				1465
				2.22	2.8	793	
2,000	0.89	2,247	12.47				2258

3.9 References

Al-Hussainy, R., and H.J. Ramey Jr. 1966. Application of real gas theory to well testing and deliverability forecasting. *JPT* (May): 637–642.

Celier, G.C.M.R., P. Jouault, and O.A.M.C. de Montigny. 1989. Zuidwal: A gas field development with horizontal wells. Paper SPE 19826.

Chen, N.H. 1979. An Explicit Equation for Friction Factor in Pipe. *Ind. Eng. Chem. Fund.* 18: 296.

Cho, H. and S. Shah. 2001. Prediction of specific productivity index for long horizontal wells. Paper SPE 67237.

Coles, M.E. and K.J. Hartman. 1998. Non-Darcy measurements in dry core and effect of immobile liquid. Paper presented at SPE Gas technology Symposium, Calgary, Alberta, March 15–18.

Cooke, C.E., Jr. 1973. Conductivity of proppants in multiple layers. *JPT* (September): 1101–1107.

Cooper, J., X. Wang, and K.K. Mohanty. 1999. Non-Darcy flow experiment in anisotropic porous media. *SPE J.* 4 (December): 334–341.

Demarchos, A.S., A.S. Chomatas, M.J. Economides, J.M. Mach, and D.S. Wolcott. 2004. Pushing the limits in hydraulic fracture design. Paper SPE 86483.

Dikken, B. 1990. Pressure drop in horizontal wells and its effect on production performance. *JPT* (November) 1426–1433.

Diyashev, I. and M.J. Economides. 2006. A general approach to well evaluation. *SPEPO* (August): 394–401.

Dranchuk, P.M., R.A. Purvis, and D.B. Robinson. 1974. Computer Calculations of Natural Gas Compressibility Factors Using the Standing and Katz Correlation. *Institute of Petroleum Technical Series* IP 74-008.

Economides, M.J., A.D. Hill, and C.A. Ehlig-Economides. 1994. *Petroleum Production Systems*. Prentice Hall, NY.

Economides, M.J., R.E. Oligney, and P.P Valkó. 2002a. *Unified Fracture Design*. Houston: Orsa Press.

Economides, M.J., R.E. Oligney, and P.P. Valkó. 2002b. Applying unified fracture design to natural gas wells. *World Oil* (October): 52–62.

Economides, M.J., A.S. Demarchos, J.M. Mach, J. Rueda, and D.S. Wolcott. 2004. Pushing the limits of hydraulic fracturing in Russia. Paper SPE 90357.

Economides, M.J. and T. Martin. 2007. Eds. *Modern Fracturing: Enhancing Natural Gas Production*. Houston: Energy Tribune Publishing.

Energy Tribune. December 2008. The international state of hydraulic fracturing. Houston: Energry Tribune Publishing.

Ergun, S. 1952. Fluid flow through packed column. *Chemical Engineering Progress* 48: 89.

Firoozabadi, A. and D.L. Katz. 1979. An analysis of high-velocity gas flow through porous media. *JPT* (February): 211–216.

Forchheimer, P. 1914. Hydraulik, Teubner, Leipzig and Berlin 116–118.

Geertsma, J. 1974. Estimating the coefficient of inertial resistance in fluid flow through porous media. *SPE J.* 14: 445.

Gidley, J.L. 1990. A method for correcting dimensionless fracture conductivity for non-Darcy flow effects. Paper SPE 20710.

Ichara, M.J. 1987. The performance of perforated completions in gas reservoirs. Paper SPE 16384.

Janicek, J.D. and D.L. Katz. 1955. Applications of unsteady state gas flow calculations. Paper presented at the University of Michigan Research Conference, June 20.

Jones, S.C. 1987. Using the inertial coefficient, β, to characterize heterogeneity in reservoir rock. Paper SPE 16949.

Joshi, S. 1991. *Horizontal Well Technology*. PennWell.

Kakar, A.M., S. Zheng, and G. Stewart. 2004. Well test analysis of hydraulically fractured gas wells for non-Darcy flow effects. Paper presented in 2004 Annual Technical Conference, Islamabad, Pakistan, October 8–9.

Karakas, M. and S. Tariq. 1988. Semi-analytical production models for perforated completions. Paper SPE 18247.

Katz, D.L., D. Cornell, R. Kobayashi, F.H. Poettmann, J.A. Vary, J.R. Ellenbaas, and C.F. Weinang. 1959. *Handbook of Natural Gas Engineering*. New York: McGraw-Hill.

Lee, A.L., M.H. Gonzalez, and B.E. Eakin. 1966. The Viscosity of Natural Gases. *JPT* (August): 997–1000.

Lee, R.L., R.W. Logan, and M.R. Tek. 1984. Deliverability of natural gas. Proceedings of the Eight Doha Technical Symposium (November): 41–47.

Lee, R.L., R.W. Logan, and M.R. Tek. 1987. Effect of turbulence on transient flow of real gas through porous media. Paper SPE 14205, 1987.

Li, D. and T.W. Engler. 2001. Literature review on correlations of the non-Darcy coefficient. Paper SPE 70015.

Liu, X., F. Civan, F., R.D. Evans. 1995. Correlation of the non-Darcy flow coefficient. *JCPT* 43: 50.

Marongiu-Porcu, M., M.J. Economides, and S.A. Holditch. 2008. Economic and physical optimization of hydraulic fracturing. Paper SPE 111793.

Marongiu-Porcu, M., X. Wang, and M.J. Economides. 2009. Delineation of application: Physical and economic optimization of fractured gas wells. Paper SPE 120114.

Moody, L. F. 1944. Friction factors for pipe flow. *Trans. ASME* 66: 671.

Mukherjee, H., M.J. Economides. 1991. A parametric comparison of horizontal and vertical well performance. Paper SPE 18303.

Norris, S.O., J.L. Hunt, M.Y. Soliman, and S.K. Puthigal. 1991. Predicting horizontal well performance: A review of current technology. SPE 21793.

Ozkan, E., C. Sarica, and M. Haci. 1999. Influence of pressure drop along the wellbore on horizontal-well productivity. *SPEJ* (September): 288–301.

Pascal, H. and R.G. Quillian. 1980. Analysis of vertical fracture length and non-Darcy flow coefficient using variable rate tests. Paper SPE 9348.

Romero, D.J., P.P. Valkó, and M.J. Economides. Optimization of the productivity index and the fracture geometry of a stimulated well with fracture face and choke skins. Paper SPE 73758.

Soliman, M.Y., J.L Hunt, and M. Azari. 1999. Fracturing horizontal wells in gas reservoirs. *SPE Prod. & Facilities* 14 (November).

Swift, G.W. and O.G. Kiel. 1962. The prediction of gas-well performance including the effects of non-Darcy flow. *JPT* (July): 791–798.

Tek, M.R., K.H. Coats, and D.L. Katz. 1962. The effect of turbulence on flow of natural gas through porous reservoir. *JPT* (July): 799.

Thauvin, F. and K.K. Mohanty. 1998. Network modeling of non-Darcy flow through porous media. *Transport in Porous Media* 31 (1): 19.

Valkó, P. and M.J. Economides. Performance of a longitudinally fractured horizontal well. *SPEJ* (March): 11–19.

Van Everdingen, A.F. and W. Hurst. 1949. The application of the laplace transformation to flow problems in resevoirs. *Trans. AIME* 186: 305–324.

Wang, X. 2000. Pore-level modeling of gas-condensate flow in porous media. PhD diss., University of Houston.

Wang, X., and M.J. Economides. 2004. Aggressive fracture slashes turbulence in high-permeability gas well. *World Oil* (July).

Wang, X., and K.K. Mohanty. 1999a. Critical condensate saturation in porous media. *J. Coll. & Interf. Sci.* 214: 416.

Wang, X., and K.K. Mohanty. 1999b. Multiphase non-Darcy flow in gas-condensate reservoirs. Paper SPE 56486.

Wang, X., F. Thauvin, and K.K. Mohanty. 1999. Non-Darcy flow through anisotropic porous media. *Chem. Eng. Sci.* 54: 1859.

Wang, X. and M.J. Economides. 2009. Horizontal well deliverability with turbulence effects. Paper SPE 121382.

Yao, C. Y. and S.A. Holditch. 1993. Estimating permeability profiles using core and log data. Paper SPE 26921.

CHAPTER 4

Natural Gas Processing

4.1 Introduction

As discussed in Chapter 1, natural gas produced from either an oil or gas reservoir is a complex mixture with different compounds of hydrocarbons (primarily methane and varying amounts of ethane, propane, butane, and even higher molecular weight hydrocarbons), an amount of water vapor, small amounts of nonhydrocarbon gases (hydrogen sulfide, carbon dioxide, and mercaptans such as methanethiol and ethanethiol), and even neutral gases such as nitrogen and helium, etc. The gas composition depends on the geological area, as well as the underground deposit type, depth, and location. The gas that is finally transported in pipelines (discussed in Chapter 5), on the other hand, must meet the quality standards specified by pipeline companies. Those quality standards vary from pipeline to pipeline and are usually a function of a pipeline system's design, its downstream interconnecting pipelines, and its customer base. In general, these standards specify how a commercially acceptable natural gas should be (EIA, 2006):

- It must be within a specific Btu content range. For example, in the United States, it should be about 1,035 ±50 Btu per standard cubic foot (at 1 atmosphere and 60°F).
- It should be delivered at a specified hydrocarbon dew point temperature level. This would prevent liquids to condense and form liquid slugs which could be very damaging to the pipeline.

- The gas should not contain more than trace amounts of compounds or elements such as hydrogen sulfide, carbon dioxide, mercaptans, nitrogen, water vapor, and oxygen.
- The water vapor must be removed (i.e., dehydrate the gas) sufficiently to prevent corrosion and the formation of gas hydrates in the processing plant or the pipelines.
- All particulates must be removed.

The above suggest that the natural gas produced from wells must be processed and treated, i.e., cleaned, before it can be delivered to the pipelines. Natural gas that is not within certain specific gravities, pressures, Btu content range, or water content levels will cause operational problems, pipeline deterioration such as corrosion and fouling, or even pipeline rupture (EIA, 2006).

So the purpose of gas processing is to produce a gas stream that meets sales requirements and specifications including heating value and the recovery of maximum amount of NGLs (Natural Gas Liquids).

The processing of wellhead natural gas into pipeline-quality natural gas (e.g., 99.9% methane) can be quite complex and usually involves several processes. A generalized gas processing schematic is shown in Figure 4–1. In addition to those four processes (to remove oil, water, compounds, or elements such as sulfur, helium, carbon dioxide, and natural gas liquids), it is often necessary to install scrubbers and heaters at or near the wellhead (EIA, 2006). The scrubbers serve primarily to remove sand and other large particle impurities. The heaters ensure that the temperature of the natural gas does not drop too low to form a hydrate with the water vapor content of the gas stream. Natural gas hydrates are crystalline solids that block the passage of natural gas through valves and pipes.

In this chapter, we will focus on natural gas and liquid separation, and water and acid gas removal. After that, the pipeline quality natural gas will be ready to be transported, which will be covered in the next chapter (Chapter 5).

4.2 Natural Gas and Liquid Separation

Natural gas and liquid separation is usually performed in the field immediately after the gas is produced. A field separator is intended to remove solids and free liquid from the gas, the entrained liquid mist from the gas, and the entrained gas from the liquid (Ikoku, 1984). In addition, the separated gas and liquid from the vessel must be dis-

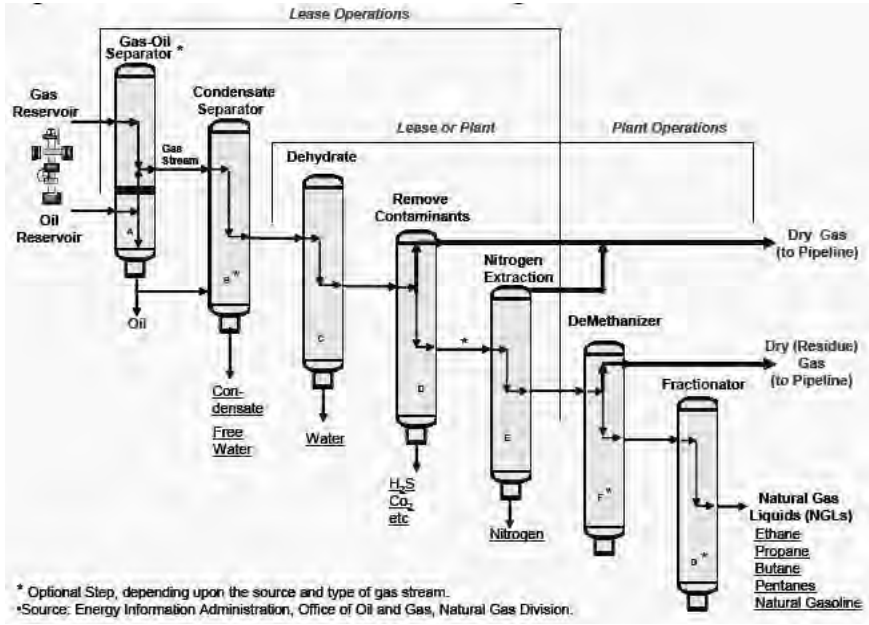

Figure 4–1 *Generalized gas processing schematic* (EIA, 2006)

charged without re-entrainment. Several technologies are available to achieve those goals (Wines and Brown, 1994): gravity separators, centrifugal separators or cyclone separators, filter vane separators, mist eliminator pads, and liquid/gas coalescers. Table 4–1 summarizes each of these technologies and provides guidelines for proper selection.

Common types of separators in gas processing include vertical, horizontal (with single or double tube), and spherical. There are several published sources that have detailed descriptions on these separators in terms of their structures, functions, advantages, disadvantages, and applications (Ikoku, 1984; Leecraft, 1987; Campbell, 1998; Mokhatab et al., 2006; Speight, 2007).

The cyclone separator (utilized for years in other kinds of processing) is a relatively new type of separating device in the gas industry (Young, 2004). It uses only centrifugal force to affect the separation between gas and liquid. This type of separator is used primarily as a scrubber, i.e., for the separation of small volumes of liquid from relatively large volumes of gas. Because a cyclone separator requires a relatively small diameter, it can be constructed very economically (Young, 2004).

The selection of the separator type and its size is dictated by the gas and liquid flow rates, the type of natural gas as denoted by its

Table 4–1 Types of Liquid/Gas Separators *(Wines and Brown, 1994)*

Technology	Droplet Size Removed
Gravity Separator	Down to 300 μm
Centrifugal Separator	Down to 8–10 μm
Mist Eliminator Pad	Down to 10 μm
Vane Separator	Down to 10 μm
High Efficiency L/G Coalescer	Down to 0.1 μm

specific gravity, the specifications of the produced oil and water, the separator operating conditions (pressure and temperature), the presence of solids, the floor space availability such as on an offshore platform, cost, etc. Since vertical and horizontal gravity separators are widely used, the following section will go step by step to design these two types of separators as examples.

4.2.1 Gravity Separation Mechanism

A gravity separator, also called a "knockout drum" or, more formally, gravitational-forces-controlled separator, is typically used as a first stage scrubber. In such a liquid-vapor separation vessel, there are typically three stages of separation (Svrcek and Monnery, 1993; Monnery and Svrcek, 1994 and 2000): The first stage is gas passing through the inlet diverter. This causes the largest liquid droplets to collide on the diverter and then drop out by gravity. Now inlet diverters have evolved and new cyclonic and distribution baffle inlet devices are used (Mokhatab et al., 2006). The next stage is when the gas flows through the vapor disengagement section of the separator where smaller droplets are separated from gas by gravity. The third and final stage is mist elimination where the smallest droplets amalgamate and form larger droplets and separated by gravity.

Gravity Separation of Two Phases (Gas and Liquid)

In separating two phases (gas and liquid) vertically, gravity and flow direction are expected to play a significant role. The droplets of any liquid in a gas flow are acted on by three forces (shown in Figure 4–2): gravity (directed downward), buoyancy (opposite of the gravity force), and drag (opposite of the direction of droplet velocity). As a result, the liquid droplet will move in the direction of the net force.

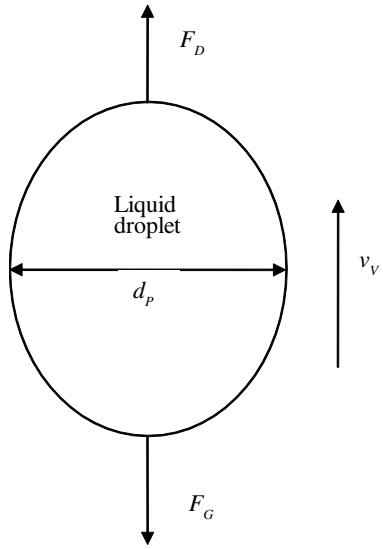

Figure 4–2 *Forces on liquid droplet*

Therefore, the primary design feature of gravity separation is to size the separator so that the drag and buoyancy forces become less than the gravity force. This forces the liquid droplets to separate from the flowing gas.

The net gravity force (gravity minus buoyancy) is

$$F_G = \frac{M_P(\rho_l - \rho_g)g}{\rho_l g_c}, \tag{4.1}$$

where F_G is the gravity force, M_P is droplet mass in lb, ρ_l is liquid density in lb/ft^3, ρ_g is gas density in lb/ft^3, g is gravity acceleration (32.17 ft/s^2), and g_c is dimension proportionality constant equal to 32.2 lbf/lbm-ft/s^2. The drag force F_D is

$$F_D = \frac{(\pi / 8)C_D d_P^2 v_V^2 \rho_g}{g_c}, \tag{4.2}$$

where C_D is the drag coefficient, d_P is droplet diameter in ft, and v_V is vertical velocity in ft/s. When F_G equals F_D, the liquid droplets will settle at a constant terminal velocity, v_T. Substituting the mass of the droplet and assuming a spherical shape

$$M_P = \frac{4}{3}\pi\left(\frac{d_p}{2}\right)^3 \rho_l \,.$$

Eqs. (4.1 and 4.2) result in

$$v_T = \sqrt{\frac{4g d_p(\rho_l - \rho_g)}{3C_D \rho_g}} \,. \tag{4.3}$$

Hence, as long as the vapor velocity, v_V, is less than v_T, the liquid droplets will settle out. Eq. (4.3) can be rewritten as Eq. (4.4), in the well-known Souders-Brown (1934) form

$$v_T = K\sqrt{\frac{(\rho_l - \rho_g)}{\rho_g}} \,, \tag{4.4}$$

where

$$K = \sqrt{\frac{4g d_P}{3C_D}} \,. \tag{4.5}$$

Here K is the terminal velocity constant in ft/s for vertical gravity settling. d_P is the liquid droplet diameter in ft (microns $\times$ 3.2808 $\times$ 10^{-6}). C_D is the drag coefficient, dimensionless. For a separator without mist eliminator and with the droplet diameter known, the drag coefficient can be calculated by using the following correlation (Svrcek and Monnery, 1993):

$$C_D = \exp(8.4111 - 2.243X + 0.273X^2 - 1.865 \times 10^{-2}X^3 + 5.201 \times 10^{-4}X^4), \tag{4.6}$$

where

$$X = \ln\left(\frac{0.95 \times 10^8 \; d_P^3 \, \rho_g \, (\rho_l - \rho_g)}{\mu_g{}^2}\right). \tag{4.7}$$

Here densities are in lb/ft^3 and viscosity is in cp.

For very small droplets, it is not practical to separate them from the main flow stream by gravity alone (Svrcek and Monnery, 1993). A coalescing device such as a mist eliminator is required. The complication is that the droplet diameter changes as the droplets coalesce, and therefore, the K factor for coalescing devices is usually an empirical value, determined from experiments, published data, or vendors (for their particular coalescing devices). A commonly used source of empirical K factors for mist eliminators is the GPSA (Gas Processors Suppliers Association engineering Data Book, 1987). Some typical K values are given in Table 4–2.

Horizontal separators have an additional complication because the liquid droplets to be separated are subjected to a horizontal drag force, which is perpendicular to gravity, and therefore, different from the case of vertical separators (Monnery and Svrcek, 1994). In analogy to e.g., proppant transport in hydraulic fracturing, the time that it takes for the droplet to travel from the inlet to the outlet of the horizontal separator must be greater than the time it takes for the droplet to travel the vertical distance to the liquid surface. This design requirement implies that the vertical K values listed in Table 4–2 have to be modified (GPSA, 1987; Watkins, 1967; Gerunda, 1981; Monnery and Svrcek, 2000). Later in this chapter, we will use the "droplet settling approach" (Monnery and Svrcek, 1994) that will allow the use of K values for vertical settlers directly.

Table 4–2 Separator K Factors *(Monnery and Svrcek, 1994)*

Vendor: Otto H. York Company Inc.	
With Mist Eliminator:	
$1 \le p \le 15$	$K = 0.1821 + 0.0029p + 0.0461 \ln(p)$
$15 \le p \le 40$	$K = 0.35$
$40 \le p \le 5{,}500$	$K = 0.430 - 0.023 \ln(p)$
where p is in psia.	
Gas Processors Suppliers Association	
$0 \le p \le 1{,}500$	$K = 0.35 - 0.0001(p - 100)$
For most vapors under vacuum, $K = 0.20$ For glycol and amine solutions, multiply K by 0.6–0.8 For vertical vessels without demisters, divide K by 2 For compressor suction scrubbers, mole sieve scrubbers and expander inlet separators, mutiply K by 0.7–0.8 where p is in psig.	

Gravity Separation of Three Phases (Gas, Light and Heavy Liquids)

For three-phase separation (Monnery and Svrcek, 1994), while the gas and liquid separation is the same as the one described above, the settling of the heavy liquid droplet in the light liquid is assumed to obey Stoke's law of buoyancy:

$$v_T = \frac{1{,}488 g_c d_P^{\,2} (\rho_{HI} - \rho_{LI})}{18\mu}, \tag{4.8}$$

where 1,488 converts viscosity of the continuous phase from lb/ft-s to cp . ρ_{HI} and ρ_{LI} are heavy and light liquid densities in lb/ft^3, respectively. A simplified version of Eq. (4.8) (and also converting the terminal settling velocity units from ft/s to in./min) is

$$v_T = \frac{k_s (\rho_{HI} - \rho_{LI})}{\mu}, \tag{4.9}$$

where

$$k_s = 2.06151 \times 10^{-5} d_P^{\,2} \tag{4.10}$$

and k_s can be obtained from Table 4–3.

As should be expected, Eq. (4.9) suggests that the terminal settling velocity is inversely proportional to the viscosity of the continuous phase. Therefore the bigger the viscosity of the continuous phase is, as would be the case in heavy crude, the more difficult would be to settle droplets out of the continuous phase. In separator design, v_T is usually limited to 10 in./min (Monnery and Svrcek, 1994).

4.2.2 Three-Phase Separator Design

Three-phase separators can be either vertical or horizontal, but almost invariably are horizontal. As suggested by Monnery and Svrcek (1994), vertical orientation (Figure 4–3) is used when large amounts of gas need to be separated from a relatively small amount of light and heavy liquids (<10–20 wt%). To further facilitate the liquid separation, a baffle is commonly used.

Monnery and Svrcek (1994) also suggested that for horizontal separators (Figure 4–6), different devices can be used to control the interface level such as a boot, a weir, or the combination of a bucket and weir. A boot is used when the volume of heavy liquid is <15–20 wt%, while a weir is used when the volume is much greater. The bucket and

Table 4–3 k_s Values for Some Systems *(Monnery and Svrcek, 1994)*

Light Phase	Heavy Phase	Minimum Droplet Diameter, μm	k_s
Hydrocarbons			
S_G at 60°F < 0.85	Water or caustic	127	0.333
S_G at 60°F < 0.85	Water or caustic	89	0.163
Water	Furfural	89	0.163
Methylethyl ketone	Water	89	0.163
sec-Butyl alcohol	Water	89	0.163
Methyl isobutyl ketone	Water	89	0.163
Nonyl alcohol	Water	89	0.163

weir type design is used when the interface level control may be difficult, such as heavy oil, or when large amounts of emulsions or paraffins are present (Arnold and Stewart, 1986). In designing three-phase separators, it is a good idea to examine both vertical and horizontal configurations for the specific case, and decide on the one that meets the physical requirements, stream specifications, and economic attractiveness.

There are several published sources on gravity separator design (Ikoku, 1984; Kumar, 1987; Campbell, 1992; Arnold and Stewart, 1998; Monnery and Svrcek, 1994; Jekel et al., 2001), but here we will adopt the procedure introduced by Monnery and Svrcek (1994) to design three-phase separators. For brevity, we will not refer to the authors in the following sections (both vertical and horizontal separator design).

Three-Phase Vertical Separator Design Procedure

Figure 4–3 is a schematic of a vertical three-phase separator with the symbols that will be used in the design procedure. Table 4–4 lists the symbols and their definitions as used in Figure 4–3.

Notes on definitions:

- Holdup—the time it takes to reduce the liquid level from normal to empty while maintaining a normal outlet flow without feed makeup. This allows for control and safe operation.

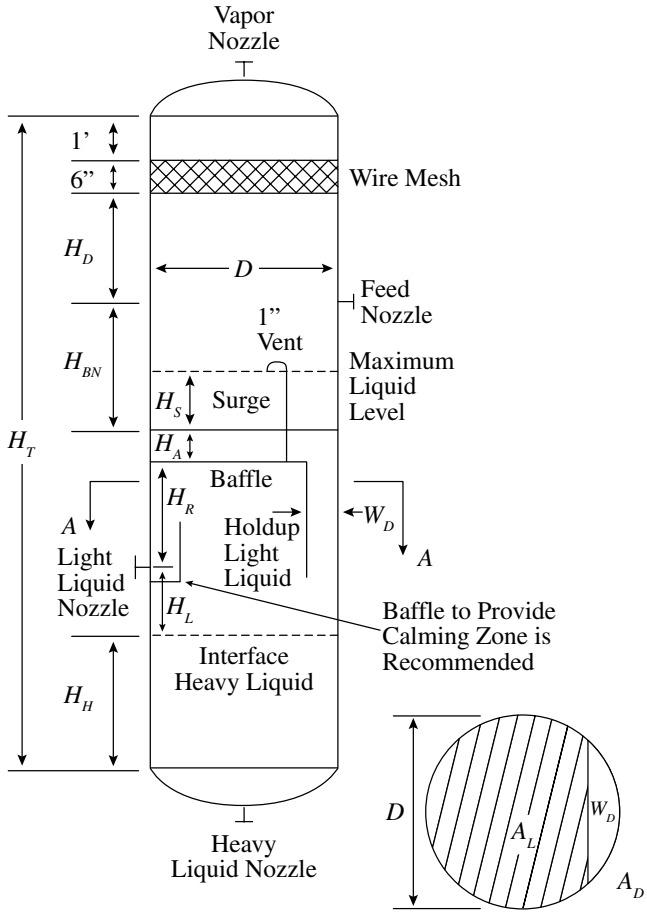

Figure 4–3 *Vertical three-phase separator* (Monnery and Svrcek, 1994)

- Surge time—the time it takes for the liquid level to rise from normal to maximum, while maintaining a normal feed without any outlet flow (i.e., accumulating liquid as result of upstream or downstream variations or an upset, such as a slug).

- In the absence of specific requirements, surge time may be taken as one half of the holdup time. Holdup time can be obtained from experiences or published data (Monnery and Svrcek, 1994). It is usually between 2 to 10 minutes multiplied by a factor of 1.0 to 1.5 depending on the personnel (experienced or inexperienced) and instrumentation (good or poor).

Table 4–4 Symbols used in Figure 4–3

Symbol	Nomenclature
A	Vertical vessel cross-sectional area, ft^2
A_D	Downcomer cross-sectional area, ft^2
A_L	Equals $A - A_D$
D	Vessel diameter, ft or in.
H	Height, ft
H_A	Liquid level above baffle, in. or ft
H_{BN}	Liquid height from above baffle to feed nozzle, ft
H_D	Disengagement height, ft
H_H	Holdup height, ft
H_L	Height from liquid interface to light liquid nozzle, ft
H_R	Height from light liquid nozzle to baffle, ft
H_S	Surge height, ft
H_T	Total vertical separator height, ft
W_D	Downcomer chord width, in.

In the following, the subscript "Hl" is for heavy (H) liquid (l) and "Ll" is for light (capital letter "L") liquid (small letter "l," not one).

1. Calculate the vertical terminal velocity by using Eq. (4.4). Calculate K value by using one of the methods listed in Table 4–2. For a conservative design, set

$$v_V = 0.75 v_T . \tag{4.11}$$

2. Calculate the vapor volumetric flow rate

$$Q_g = \frac{W_g}{3600 \rho_g} . \tag{4.12}$$

3. Calculate the vessel internal diameter, D_i

$$D_i = \left(\frac{4Q_g}{\pi v_V} \right)^{0.5}. \tag{4.13}$$

With a mist eliminator, add 3–6 in. to D_i to accommodate a support ring, and round it up to the next half or whole foot increment to obtain D. Without a mist eliminator, $D = D_i$.

4. Calculate the settling velocity (v_{Hl}) of the heavy liquid out of the light liquid by using Eq. (4.9). Here μ equals the light liquid viscosity, μ_{Ll}.

5. Calculate the rising velocity (v_{Ll}) of the light liquid out of the heavy liquid by using the same Eq. (4.9). Here μ equals the heavy liquid viscosity, μ_{Hl}.

6. Calculate the light /heavy liquid volumetric flow rates, Q_{Ll} and Q_{Hl}.

$$Q_{Ll} = \frac{W_{Ll}}{60\rho_{Ll}}, \tag{4.14}$$

$$Q_{Hl} = \frac{W_{Hl}}{60\rho_{Hl}}. \tag{4.15}$$

7. Calculate the settling times for the heavy liquid droplets to settle through a distance H_L (minimum of 1 ft) and the light liquid droplets to rise through a distance H_H (minimum of 1 ft)

$$t_{s,Hl} = \frac{12H_L}{v_{Hl}}, \tag{4.16}$$

$$t_{s,Ll} = \frac{12H_H}{v_{Ll}}. \tag{4.17}$$

8. If there is a baffle plate, calculate the baffle plate area, which is the settling area for the light liquid

$$A_L = A - A_D \,, \tag{4.18}$$

where A is the vertical vessel cross-sectional area

$$\mathrm{A} = \pi D^2 / 4. \tag{4.19}$$

A_D is the downcomer cross-sectional area. In the design, the larger value calculated from the following two ways is used

(a) $$A_D = \left(\frac{7.48\text{gal}}{\text{ft}^3}\right)\left(\frac{60\,\text{min}}{1\text{hr}}\right)\left(\frac{Q_{Ll} + Q_{Hl}}{G}\right), \tag{4.20}$$

where G is baffle liquid load in gph/ft^2 (gallon per hour per square foot) and can be obtained from Figure 4–4. The "high liquid level above interface" in Figure 4–4 refers to $H_L + H_R$, where the minimum value for H_R is 9 in.

(b) Assume W_D = 4 in., calculate $x = W_D / D$. Then use the following equation to calculate $y = A_D / A$

$$y = \frac{a + cx + ex^2 + gx^3 + ix^4}{1.0 + bx + dx^2 + fx^3 + hx^4} \,, \tag{4.21}$$

where

$a = -4.755930\times10^{-3}$

$b = 3.924091$

$c = 0.174875$

$d = -6.358805$

$e = 5.668973$

$f = 4.018448$

$g = -4.916411$

$h = -1.801705$

$i = -0.145348.$

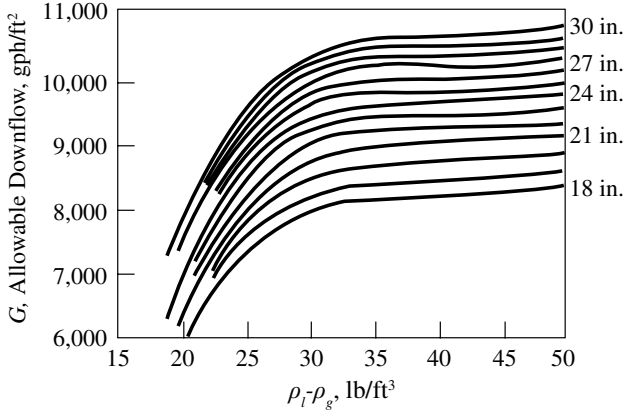

Figure 4–4 *Obtain G from the downcomer allowable flow* (Monnery and Svrcek, 1994)

9. Calculate the residence time of each phase based on the volumes occupied by the light and heavy liquid phases

$$t_{r,Ll} = \frac{H_L A_L}{Q_{Ll}}, \tag{4.22}$$

$$t_{r,Hl} = \frac{H_H A_H}{Q_{Hl}}, \tag{4.23}$$

where $A_H = A$. If $t_{r,Ll} < t_{s,Hl}$ or $t_{r,Hl} < t_{s,Ll}$, which implies the liquid separation is controlling, the diameter needs to be increased, and then the procedure must be repeated from Step 7.

10. Calculate the height of the light liquid above the outlet (holdup height) based on the required holdup time:

$$H_R = \frac{Q_{Ll} t_H}{A_L}. \tag{4.24}$$

- Compare this value with the assumed one in Step 8 and check whether the assumed value is reasonable.
- Calculate the surge height (minimum of 6 in.) based on surge time if surge is not specified:

$$H_S = \frac{t_S(Q_{Ll} + Q_{Hl})}{A} . \tag{4.25}$$

11. Calculate the vessel total height

$$H_T = H_H + H_L + H_R + H_A + H_{BN} + H_D \tag{4.26}$$

with the following design guidelines:

- The minimum value of H_A is assumed to be 6 in.
- $H_{BN} = 0.5d_N$ + greater of (2 ft or H_s + 0.5 ft). Here d_N is the inlet or outlet vapor/liquid nozzle diameter in ft and can be calculated by

$$d_N \geq \left(\frac{4Q_m}{60\pi} \rho_m{}^{1/2} \right)^{1/2} , \tag{4.27}$$

  where Q_m and ρ_m are the inlet mixture volumetric flow rate (ft^3/s) and density (lb/ft^3).

- $H_D = 0.5D$ or minimum of 3 ft + $0.5d_N$ (without mist eliminator), or 2 ft + $0.5d_N$ (with mist eliminator).
- If a mist eliminator pad is used, additional height is added as shown in Figure 4–3.

The last step is to make sure that the ratio of H_T/D is within a reasonable range (1.5–6.0).

The two-phase vertical separator design is very similar to that of the three-phase vertical separator, except it does not need to separate light liquid from heavy liquid as there is only one liquid phase. Details can be found in Svrcek and Monnery (1993) and will be demonstrated later in Example 4–2.

Example 4–1 Three-phase vertical separator design

Size a three-phase vertical separator with baffle plate and wire mesh mist eliminator (shown in Figure 4–3).

A field produces 121 MMscf/d of natural gas ($\gamma_g = 0.7$ with no sour gas). The wellhead pressure and temperature are 105°F and 460 psi,

respectively. At those conditions, the fluid density and formation volume factor can be calculated (by using the correlations introduced in Chapter 1) as: $\rho = 1.72$ lb/ ft^3 and $B_g = 0.0319$ ft^3/scf.

The separator operating pressure and temperature are 165 psi and 100°F, respectively. At separator conditions, assume the mixture contains 1% (weight) of water and 4% (weight) hydrocarbon liquid. The densities and viscosities of hydrocarbon gas, liquid (light liquid or Ll), and water (heavy liquid or Hl) are also calculated by using the correlations in Chapter 1 and are given here: $\rho_g = 0.72$ lb/ ft^3, $\rho_{Ll} = 54.0$ lb/ft^3, and $\rho_{Hl} = 62.1$ lb/ ft^3, $\mu_g = 0.0113$ cp, $\mu_{Ll} = 0.630$ cp, and $\mu_{Hl} = 0.764$ cp.

The hydrocarbon liquid holdup time is 25 minutes and the surge time is assumed to be 5 minutes.

Solution

The fluid mass flow rate at wellhead conditions (105°F and 460 psi) is the product of the standard condition flow rate multiplied by the formation volume factor and multiplied by the density

$$W = 121 \times 10^6 \times 0.0319 \times 1.72/24 = 2.77 \times 10^5 \text{ lb/h}.$$

At separator conditions (165 psi and 100°F), water (heavy liquid), hydrocarbon liquid (light liquid), and hydrocarbon gas (vapor) mass flow rates are

$$W_{Hl} = 2.77 \times 10^5 \times 1\% = 2{,}770 \text{ lb/h},$$

$$W_{Ll} = 2.77 \times 10^5 \times 4\% = 11{,}080 \text{ lb/h},$$

$$W_g = 2.77 \times 10^5 \times 95\% = 263{,}150 \text{ lb/h}.$$

Liquid mixture density at separator operating conditions is

$$\begin{aligned}\rho_l &= 54.0 \times (11{,}080/(11{,}080 + 2{,}770)) \\ &\quad + 62.1 \times (2{,}770/(11{,}080 + 2{,}770)) \\ &= 55.6 \text{ lb/ ft}^3.\end{aligned}$$

Now the separator can be designed using the procedure outlined above:

Step 1. Calculate the vertical terminal velocity by using Eq. (4.4) and a K value by using one of the methods listed in Table 4–2:

$$K = 0.43 - 0.023 \times \ln(165) = 0.313 \text{ ft/s}$$
(Otto H. York Co. in Table 4–2),

or

$$K = 0.35 - 0.0001 \times (165 - 100) = 0.344 \text{ ft/s}$$
(GPSA data in Table 4–2).

The K values calculated from the two different sources are quite close. In the following calculation $K = 0.313$ ft/s is used:

$$v_T = 0.313\sqrt{\frac{(54.0 - 0.72)}{0.72}} = 2.69 \text{ ft/s}.$$

For a conservative design, set

$$v_V = 0.75 \times 2.69 = 2.02 \text{ ft/s}.$$

Step 2. Calculate the vapor volumetric flow rate from Eq. (4.12):

$$Q_g = \frac{263{,}150}{3600 \times 0.72} = 101.5 \text{ ft}^3/\text{s}.$$

Step 3. Calculate the vessel internal diameter, D_i from Eq. (4.13):

$$D_i = \left(\frac{4 \times 101.5}{3.1416 \times 2.02}\right)^{0.5} = 8.01 \text{ ft}.$$

With mist eliminator, add 3–6 in. to D_i to accommodate a support ring and round it up to the next half foot increment to obtain $D = 8.5$ ft.

Step 4. Calculate the settling velocity (v_{Hl}) by using Eq. (4.9):

Choose $k_s = 0.163$ from Table 4–3, then

$$v_{Hl} = \frac{0.163 \times (62.1 - 54)}{0.630} = 2.10 \text{ in./min}.$$

Step 5. Calculate the rising velocity (v_{Ll}) by using the same Eq. (4.9):

$$v_{Ll} = \frac{0.163 \times (62.1 - 54)}{0.764} = 1.73 \text{ in./min.}$$

Step 6. Calculate the light/heavy liquid volumetric flow rate, Q_{Ll} and Q_{Hl} from Eqs. (4.14 and 4.15):

$$Q_{Ll} = \frac{11080}{60 \times 54.0} = 3.42 \text{ ft}^3 / \text{min.},$$

$$Q_{Hl} = \frac{2{,}770}{60 \times 62.1} = 0.74 \text{ ft}^3 / \text{min.}$$

Step 7. Calculate the settling times from Eqs. (4.16 and 4.17):

Assume: H_L = 1 ft and H_H = 1 ft:

$$t_{s,Hl} = \frac{12 \times 1}{2.1} = 5.73 \text{ min},$$

$$t_{s,Ll} = \frac{12 \times 1}{1.73} = 6.94 \text{ min.}$$

Step 8. Calculate the baffle plate area, A_L from Eq. (4.18):

The vertical vessel cross-sectional area A, Eq. (4.19), is

$$\text{A} = 3.1416 \times 8.5^2 / 4 = 56.75 \text{ ft}^2.$$

Calculate the downcomer cross-sectional area, A_D from Eqs. (4.20 and 4.21) and choose the greater value of the two results:

(a) $$A_D = 7.48 \times 60 \times \left(\frac{3.42 + 0.74}{9{,}800} \right) = 0.19 \text{ ft}^2,$$

where G (= 9,800 gph/ft^2) is obtained from Figure 4–4 with the assumption of H_R = 1 ft and $H_R + H_L$ = 24 in.

(b) Assume W_D = 4 in., that gives $x = W_D/D = 0.039$. From Eq. (4.21), $y = A_D/A = 0.013$. Further $A_D = 0.76$ ft^2.

The A_D calculated from (b) is greater than that from (a), therefore choose $A_D = 0.76$ ft^2. From Eq. (4.18)

$$A_L = 56.75 - 0.76 = 55.99 \text{ ft}^2.$$

Step 9. Calculate the residence time from Eqs. (4.22 and 4.23)

$$t_{r,Ll} = \frac{1 \times 55.99}{3.42} = 16.4 \text{ min},$$

$$t_{r,Hl} = \frac{1 \times 55.99}{0.74} = 76.3 \text{ min}.$$

Obviously $t_{r,Ll} > t_{s,Hl}$ and $t_{r,Hl} > t_{s,Ll}$ and we can proceed to the next step.

Step 10. Calculate the height of the light liquid above the outlet (holdup height) from Eq. (4.24) (t_H is given as 25 min)

$$H_R = \frac{3.42 \times 25}{55.99} = 1.5 \text{ ft}.$$

This number is close enough to the assumed value of 1 ft in Step 8(a).

Calculate the surge height from Eq. (4.25) (t_S is given as 5 min)

$$H_S = \frac{5 \times (3.42 + 0.74)}{56.75} = 0.37 \text{ ft}.$$

Use H_s = 0.5 ft.

Step 11. Calculate the vessel total height:

- Calculate d_N from Eq. (4.27)

$$d_N \geq \left(\frac{4 \times 101.6}{60 \times 3.1416} \left(\overline{)0.76} \right) \right)^{1/2} = 1.37 \text{ ft},$$

where Q_m =101.52 + (3.42 + 0.74)/60 = 101.6 ft^3/s, and ρ_m = 0.76. Set d_N = 1.5 ft.

- H_s (which is 0.5 ft from Step 10) + 0.5 is smaller than 2 ft. So H_{BN} = 0.5 × 16.4 + 2 = 2.75 ft. Use H_{BN} = 3.0 ft.
- 0.5D = 4.25 ft is larger than 2 + 0.5d_N = 2.75 ft (with mist eliminator). Choose H_D = 4.5 ft
- Assume H_A = 0.5 ft.
- In summary: H_H = 1.0 ft, H_L = 1.0 ft, H_R = 1.5 ft, H_A = 0.5 ft, H_{BN} = 3.0 ft, and H_D = 4.5 ft. Add another 1.5 ft (see Figure 4–3) for mist eliminator, and that gives H_T (from Eq. (4.26))

$$H_T = 1 + 1 + 1.5 + 0.5 + 3 + 4.5 + 1.5 = 13.0 \text{ ft.}$$

Reality check: H_T/D = 13.0/8.5 = 1.5 which is in the range of 1.5–6.0. So the final dimensions of this separator are H_T = 13 ft and D = 8.5 ft.

Example 4–2 Two-phase vertical separator design

Size a two-phase vertical separator, shown in Figure 4–5, with inlet diverter and wire mesh mist eliminator. Symbols and nomenclatures used in Figure 4–5 are summarized in Table 4–5. Use similar data from Example 4–1 and remove the water. So ρ_g = 0.72 lb/ ft^3, ρ_l = 54.0 lb/ft^3, μ_g = 0.0113 cp, μ_l = 0.630 cp.

$$W_l = 2.77 \times 10^5 \times 5\% = 13{,}850 \text{ lb/h},$$

$$W_g = 2.77 \times 10^5 \times 95\% = 263{,}150 \text{ lb/h}.$$

The separator operating pressure and temperature are 165 psi and 100°F, respectively. The hydrocarbon liquid holdup time, t_H, is 25 minutes and the surge time, t_S, is assumed to be 5 minutes.

Solution

The vapor-liquid separation process in a two-phase separator design is identical to Steps 1–3 of the three-phase separator design.

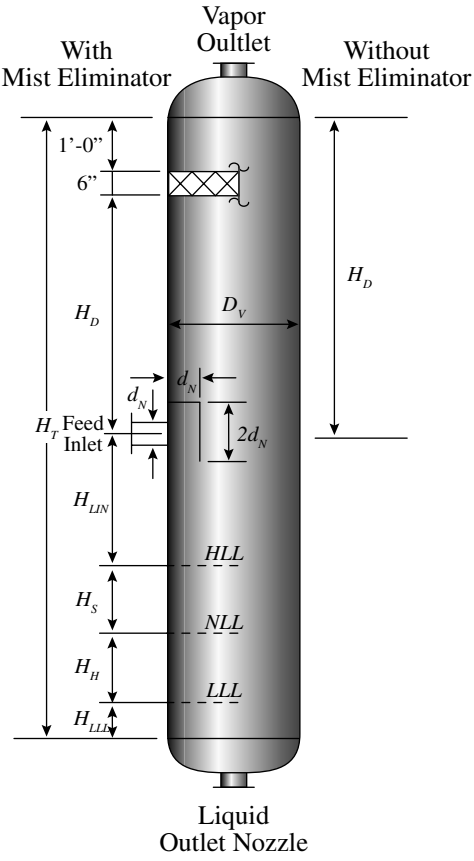

Figure 4–5 *Two-phase vertical separator* (Svrcek and Monnery, 1993)

Since there is no second liquid phase in the two-phase separator, there is no need to calculate anything that is related to liquid-liquid separation. This means Steps 4, 5, 7, 8, and 9 in the three-phase separator design are not needed in the two-phase design. Below is the adjustment of the three-phase design procedure for a two-phase separator.

Step 4. In the two-phase separator design, calculate the liquid volumetric flow rate, Q_l (Eq. (4.14)) and the vessel cross-sectional area, A (Eq. (4.19)).

Step 5. Calculate the holdup and surge volumes.

$$V_H = t_H Q_l \tag{4.28}$$

Table 4–5 Symbols and Nomenclatures used in Figure 4–5

Symbol	Nomenclature
D_V	Vessel diameter, ft or in.
d_N	Inlet or outlet nozzle diameter, ft or in.
H	Height, ft
H_D	Disengagement height, ft
H_H	Holdup height, ft
H_{LIN}	HLL to inlet nozzle centerline height, ft
H_{LLL}	Low Liquid Level (LLL) height, ft
HLL	High Liquid Level
H_S	Surge height, ft
H_T	Total vertical separator height, ft
NLL	Normal Liquid Level

$$V_S = t_S Q_l \tag{4.29}$$

Now the heights of different sections of the separator can be calculated.

Step 6. Obtain low liquid level height, H_{LLL}, from Table 4–6.

Step 7. Calculate the height from low liquid level to normal liquid level, H_H (minimum of 1 ft), and the height from normal liquid level to high liquid level, H_S (or high level alarm, minimum of 0.5 ft)

$$H_H = \frac{V_H}{A}\,, \tag{4.30}$$

$$H_S = \frac{V_S}{A}. \tag{4.31}$$

Step 8. Calculate the height from high liquid level to the centerline of the inlet nozzle

Table 4–6 Low Liquid Level Height *(Svrcek and Monnery, 1993)*

Vessel Diameter, ft	Vertical LLL, in.		Horizontal LLL, in.
	<300 psia	>300 psia	
≤4	15	6	9
6	15	6	10
8	15	6	11
10	6	6	12
12	6	6	13
16	6	6	15

$$H_{LIN} = 1 + d_N, \text{ ft (with inlet diverter)},$$

$$H_{LIN} = 1 + 0.5d_N, \text{ ft (without inlet diverter)}.$$

Step 9. Calculate the disengagement height, from the centerline of the inlet nozzle to

(a) the vessel top tangent line if there is no mist eliminator or,

(b) the bottom of the demister (mist eliminator) pad:

$H_D = 0.5D$ or minimum of

$H_D = 3 + 0.5d_N$, ft (without mist eliminator),

$H_D = 2 + 0.5d_N$, ft (with mist eliminator).

Step 10. Calculate the total height of the two-phase vertical separator:

$$H_T = H_{LLL} + H_H + H_S + H_{LIN} + H_D + H_{ME} \text{ ft}, \tag{4.32}$$

where

- H_{ME} = 1.5 ft if there is a mist eliminator (6 in. for the mist eliminator and 1 ft from the top of the mist eliminator to the top tangent line of the vessel).
- H_{ME} = 0 if there is no mist eliminator.

The results from this particular problem (Example 4–2) are summarized in Table 4–7 with necessary explanations.

H_T/D = 12.5/8.5 = 1.5, which is in the range of 1.5–6.0. So the final dimensions of this separator are H_T = 12.5 ft and D = 8.5 ft.

For this particular case, the diameter of three- and two-phase separators are the same and the height is slightly different. This is because the same input parameters are used with the exception that the three-phase separator has a 1 wt% of water and is a small amount compared to the gas and the hydrocarbon liquid.

Three-Phase Horizontal Separator Design Procedure

Figure 4–6 shows the basic three-phase horizontal separator.

The design procedure for the basic three-phase horizontal separator is outlined below:

1. Calculate the vapor volumetric flow rate, Q_g, using Eq. (4.12).

2. Calculate the light and heavy liquid volumetric flow rates, Q_{Ll} and Q_{Hl}, using Eqs. (4.14 and 4.15).

3. Calculate the vertical terminal velocity, v_T, using Eq. (4.4) (select a K value from Table 4–2) and set $v_V = 0.75v_T$.

4. Select holdup and surge times from experiences or published data, and calculate the holdup and surge volumes, V_H and V_S, (unless surge is otherwise specified, such as a slug volume), using Eqs. (4.28 and 4.29).

5. Obtain an L/D from Table 4–8 and initially calculate the diameter according to

$$D = \left(\frac{4(V_H + V_S)}{0.5\pi(L/D)} \right)^{1/3}. \tag{4.33}$$

   Calculate the total cross-sectional area, A_T, using Eq. (4.19).

6. Set the vapor space height, H_V, to the larger of 0.2D or 2 ft (1 ft if there is no mist eliminator). Using $x = H_V/D$, calculate $y = A_V/A_T$ from Eq. (4.21) and then obtain A_V.

7. Set the heights of the heavy and light liquids, H_{HL} and H_{LL}.

Table 4–7 Results from Example 4–2

Input			Output			Notes
Step 1: Calculate vertical terminal vapor velocity.						
W_l	13,850	lb/h	K	0.313	ft/s	by York in Table 4–2
ρ_l	54.0	lb/ft^3	v_T	2.69	ft/s	Eq. (4.4)
ρ_g	0.72	lb/ft^3	v_V	2.02	ft/s	Eq. (4.11)
p	165	psi				
Step 2: Calculate vapor volumetric flow rate.						
W_g	263,150	lb/h	Q_g	101.52	ft^3/s	Eq. (4.12)
ρ_g	0.72	lb/ft^3				
Step 3: Calculate vessel internal diameter.						
			D_i	8.01	ft	Eq. (4.13)
			Add	3.00	in.	Mist Eliminator
			D	8.26	ft	
			Set D	8.50	ft	
Step 4: Calculate liquid volumetric flow rate and vessel cross-sectional area.						
W_l	13,850	lb/h	Q_l	4.27	ft^3/min	Eq. (4.14)
			A	56.75		Eq. (4.19)
Step 5: Calculate the holdup and surge volumes.						
t_H	25	min	V_H	106.87	ft^3	Eq. (4.28)
t_S	5	min	V_S	21.37	ft^3	Eq. (4.29)
Step 6: Obtain low liquid level height.						
H_{LLL}	15	in.	Set H_{LLL}	1.5	ft	Table 4–6
Step 7: Calculate H_H (minimum of 1 ft) H_S (minimum of 0.5 ft).						
			H_H	1.9	ft	Eq. (4.30)
			Set H_H	2.00	ft	Guideline
			H_S	0.38	ft	Eq. (4.31)
			Set H_s	0.50	ft	Guideline

Table 4–7 Results from Example 4–2 (cont'd)

Input			Output			Notes	
Step 8: Calculate the vessel total height.							
			Q_m	101.6	ft³/s		
			Q_l/Q_m	9.92E-03			
			ρ_m	1.25	lb/ft³		
			$d_N \geq$	1.55	ft	Eq. (4.27)	
Set			$d_N \geq$	18.62	in.		
d_N	1.5	ft	H_{LIN}	2.50	ft	With inlet diverter	Follow the design guidelines outlined in Step 8.
			Use H_{LIN}	2.50	ft		
H_{top}	1	ft	H_D	2.75	ft		
			H_{D2}	4.25	ft		
			Set H_D	4.5	ft	With demistor	
			Set H_{ME}	1.5			
			H_T	12.5	ft	Eq. (4.32)	

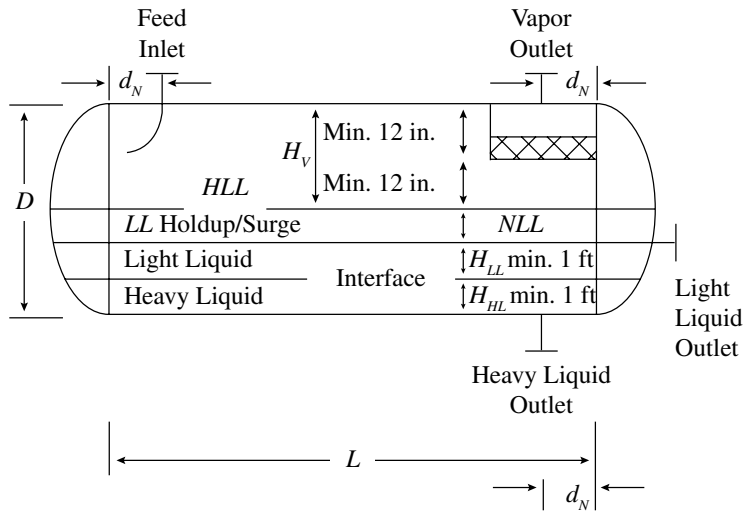

Figure 4–6 *Three-phase horizontal separator* (Monnery and Svrcek, 1994)

Table 4–8 *L/D* Ratio Guidelines *(Monnery and Svrcek, 1994)*

Vessel operating pressure, psig	*L/D*
$0 < p \le 250$	1.5–3.0
$250 < p < 500$	3.0–4.0
$p > 500$	4.0–6.0

8. Find $y = (A_{HL} + A_{LL})/A_T$, using $x = (H_{HL} + H_{LL})/D$ in Eq. (4.21), and calculate $A_{HL} + A_{LL}$.

9. Calculate the minimum length to accommodate the liquid holdup/surge:

$$L = \frac{V_H + V_S}{A_T - A_V - (A_{HL} + A_{LL})}. \tag{4.34}$$

10. Calculate the liquid dropout time:

$$t = H_V / v_V. \tag{4.35}$$

11. Calculate the actual vapor velocity:

$$v_{VA} = Q_g / A_V. \tag{4.36}$$

12. Calculate the minimum length required for vapor/liquid separation:

$$L_{MIN} = v_{VA} t. \tag{4.37}$$

Guidelines:

- If $L > L_{MIN}$, the design is acceptable for vapor/liquid separation.
- If $L < L_{MIN}$, then set $L = L_{MIN}$ (here, vapor/liquid separation controls). This results in some extra holdup and residence time.

- If $L << L_{MIN}$, then increase H_V and recalculate A_V, then repeat from Step 9.

- If $L >> L_{MIN}$ (liquid holdup controls), L can only be reduced and L_{MIN} increased if H_V is reduced. H_V may only be reduced if it is greater than the minimum specified in Step 6. (With reduced H_V, recalculate A_V and repeat the procedure from Step 9.) Note: For this and other calculations, "much less than" (<<) and "much greater than" (>>) mean a variance of greater than 20%.

13. Calculate the settling velocities of the heavy liquid out of the light liquid phase and the light liquid out of the heavy liquid phase, v_{HL} and v_{LH}, using Eq. (4.9) (find k_s from Table 4–3, $\mu = \mu_{Ll}$ for $v_{HL,}$ and $\mu = \mu_{Hl}$ for v_{LL} calculation, respectively).

14. Calculate the settling times of the heavy liquid out of the light liquid phase and the light liquid out of the heavy phase with Eqs. (4.16 and 4.17) by replacing H_L in Eq. (4.16) with D-H_V-H_{HL} and H_H in Eq. (4.17) with H_{HL}.

15. Calculate the residence times of the heavy and light liquids:

$$t_{r,Hl} = \frac{A_{HL}L}{Q_{Hl}}\,, \tag{4.38}$$

$$t_{r,Ll} = \frac{(A_T - A_V - A_{HL})L}{Q_{Ll}}. \tag{4.39}$$

16. If $t_{r,Hl} < t_{s,Hl}$ or $t_{r,Ll} < t_{s,Ll}$, then increase the vessel length (liquid separation controls)

$$L = \max\left(\frac{t_{s,Ll}Q_{Hl}}{A_{HL}}, \frac{t_{s,Hl}Q_{Ll}}{(A_T - A_V - A_{HL})}\right). \tag{4.40}$$

17. Calculate L/D. If $L/D << 1.5$, decrease D (unless it is already at its minimum), and if $L/D >> 6.0$, then increase D; repeat from Step 5.

18. Calculate the thickness of the shell and heads according to Table 4–9.

19. Calculate the surface area of the shell and heads according to Table 4–9.

20. Calculate the approximate vessel weight according to Table 4–9.

21. Increase or decrease the vessel diameter by 6-in. increments and repeat the calculations until the *L/D* ratio ranges from 1.5–6.0 (see guidelines in Table 4–8).

22. Using the optimum vessel size (minimum weight), calculate the normal and high liquid levels:

$$H_{HLL} = D - H_V \,, \tag{4.41}$$

$$A_{NLL} = A_{HL} + A_{LL} + V_H / L. \tag{4.42}$$

Obtain H_{NLL} using the following equation by setting $y = H_{NLL}/D$ and $x = A_{NLL}/A_T$,

$$y = \frac{a + cx + ex^2 + gx^3 + ix^4}{1.0 + bx + dx^2 + fx^3 + hx^4} \,, \tag{4.43}$$

where (note: the expression of Eq. (4.43) is exactly the same as Eq. (4.21), but the constants *a* through *i* are not the same as those listed in Eq. (4.21), because here it is an inverse calculation from area ratio to height and diameter ratio):

a = 0.00153756

b = 26.787101

c = 3.299201

d = –22.923932

e = 24.353518

f = –14.844824

g = –36.999376

h = 10.529572

i = 9.892851

If an additional device (i.e. a boot, a weir, or a bucket and weir) is used to control the interface level, then additional calculation procedures to account for this device will be added to the procedure for the basic horizontal separator design. Below is an example of the design procedure for the three-phase horizontal separator with a weir, as shown in Figure 4–7.

Steps 1 to 4 are the same as those described in the previous procedure for the basic three-phase horizontal separator design (below BTPHSD is used as the acronym).

Step 5. Obtain an *L/D* from Table 4–8 and initially calculate the diameter according to

$$D = \left(\frac{16(V_H + V_S)}{0.6\pi(L/D)} \right)^{1/3}. \tag{4.44}$$

Then calculate the total cross-sectional area, A_T, using Eq. (4.19).

Step 6. Same as BTPHSD.

Step 7. Calculate the low liquid level in the light liquid compartment by reading it from Table 4–6 or using

$$H_{LLL}\ (\text{in.}) = 0.5D\ (\text{ft}) + 7. \tag{4.45}$$

Round H_{LLL} up to the nearest inch. If $D \leq 4.0$ ft, then $H_V = 9$ in. Obtain A_{LLL} by using Eq. (4.21) to calculate $y = A_{LLL}/A_T$ by setting $x = H_{LLL}/D$.

Step 8. Calculate the weir height

$$H_W = D - H_V\ . \tag{4.46}$$

If $H_W < 2$ ft, increase D and repeat the calculation from Step 6.

Step 9. Calculate the minimum length of the light liquid compartment to accommodate the liquid holdup/surge (Figure 4–7)

$$L_2 = \frac{V_H + V_S}{A_T - A_V - A_{LLL}}. \tag{4.47}$$

Table 4–9 Wall Thickness, Surface Area, and Approximate Vessel Weight *(Monnery and Svrcek, 1994)*

Component	Wall Thickness, in.	Surface Area, ft^2
Shell	$\frac{pD}{2SE-1.2p}+w_c$	πDL
2:1 Elliptical Heads	$\frac{pD}{2SE-0.2p}+w_c$	$1.09D^2$
Hemispherical Heads	$\frac{pD}{4SE-0.4p}+w_c$	$1.571D^2$
Dished Heads	$\frac{0.885pD}{SE-0.1p}+w_c$	$0.842D^2$
Approximate Vessel Weight	$W(\frac{490\text{ lb}}{\text{ft}^3})(\frac{w}{12})(A_{Shell}+2A_{Head})$	

Notes for Table 4–9:
- The design pressure, p, is typically either the operating pressure with 15 to 30 psi added to it, or the operating pressure +10%, whichever is greater.
- For the allowable stress, S, see ASME (1986). The joint efficiency, E, ranges from 0.6 to 1; use 0.85 for spot examined joints, and 1 for 100% X-rayed joints.
- The corrosion allowance, w_c, typically ranges from 1/16 to 1/8 in.
- The vessel thickness, w, is the larger of w_S (shell thickness, in.) and w_H (head thickness, in.) up to the nearest 1/8 in.
- The vessel heads are selected based on the criteria listed in Table 4–10.

Table 4–10 Selection of Horizontal Separator Heads *(Monnery and Svrcek, 1994)*

Conditions	Typical Heads Used
D < 15 ft and p < 100 psig	Dished with knuckle radius = 0.06 D
D < 15 ft and p > 100 psig	2:1 Elliptical
D > 15 ft, regardless of pressure	Hemispherical
where: p = design pressure and D = drum diameter	

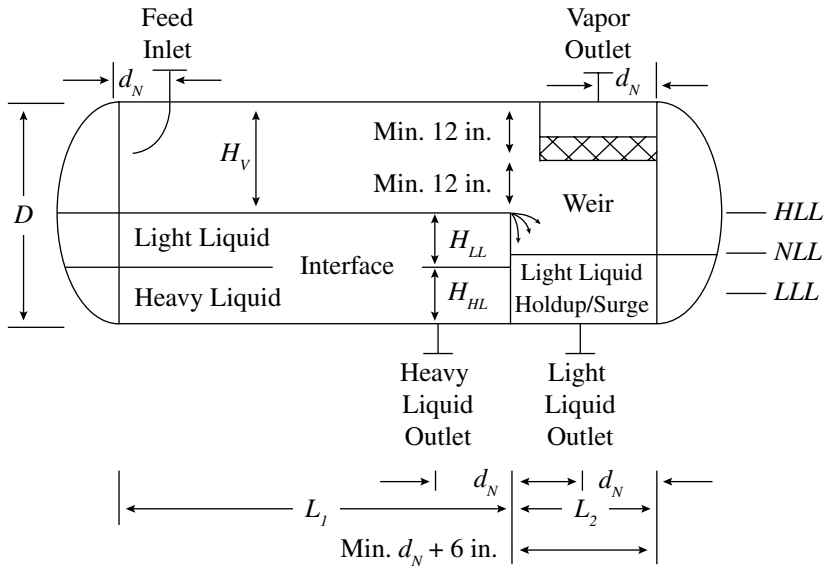

Figure 4–7 *Three-phase horizontal separator with a weir* (Monnery and Svrcek, 1994)

Round it to the nearest 0.5 ft. The minimum for $L_2 = d_N + 1$ (ft).

Step 10. Set the interface at the height of $H_W/2$, which gives the heights of the heavy and light liquids $H_{HL} = H_{LL} = H_W/2$.

Step 11. Calculate the cross-sectional area of the heavy liquid from Eq. (4.21) by setting $x = H_{HL}/D$ and $y = A_{HL}/A_T$. Then calculate the cross-sectional area of the light liquid

$$A_{LL} = A_T - A_V - A_{HL}. \tag{4.48}$$

Step 12. Same as Step 13 in BTPHSD.

Step 13. Same as Step 14 in BTPHSD, and replace H_L in Eq. (4.16) with H_{LL} and H_H in Eq. (4.17) with H_{HL}.

Step 14. Calculate the minimum L_1 (to facilitate liquid-liquid separation) by using Eq. (4.40) and replacing $A_T - A_V - A_{HL}$ with A_{LL}. Round it up to the nearest 0.5 ft.

Step 15. Calculate the total length

$$L = L_1 + L_2. \tag{4.49}$$

Steps 16–18 are the same as Steps 10–12 in BTPHSD.
Steps 19–23 are the same as Steps 17–21 in BTPHSD.

Step 24. With the optimum vessel size (minimum weight); calculate the high liquid level by using Eq. (4.41) and obtain normal liquid level, H_{NLL}, by using Eq. (4.43) and setting $y = H_{NLL}/D$ and $x = A_{NLL}/A_T$, where

$$A_{NLL} = A_{LLL} + v_H / L_2. \tag{4.50}$$

Example 4–3 Three-phase horizontal separator design

Design a three-phase horizontal separator with a weir by using the same input data (rates, separator pressure, and temperature) used in Example 4–1. The holdup and surge time are assumed as 10 and 5 mins, respectively.

Solution

From Example 4–1, we know:

$W_{Hl} = 2.77 \times 10^5 \times 1\% = 2{,}770$ lb/h
$W_{Ll} = 2.77 \times 10^5 \times 4\% = 11{,}080$ lb/h
$W_g = 2.77 \times 10^5 \times 95\% = 263{,}150$ lb/h
$\rho_g = 0.72$ lb/ft^3
$\rho_{Ll} = 54.0$ lb/ft^3
$\rho_{Hl} = 62.1$ lb/ft^3
$\mu_g = 0.0113$ cp
$\mu_{Ll} = 0.630$ cp
$\mu_{Hl} = 0.764$ cp

Using the procedure outlined above, the design results are summarized in Table 4–11.

The final dimensions are: $D = 6.5$ ft, $L_1 = 1.0$ ft, $L_2 = 9.0$ ft, $L = 10.0$ ft, $H_V = 4.5$ ft, $H_{LL} = H_{HL} = 1.0$ ft, $H_{LLL} = 10.5$ in. or 0.875 ft, $H_{NLL} = 1.6$ ft, $H_{HLL} = 2.0$ ft, and $L/D = 1.54$, which is in the range of 1.5–6.0.

Table 4–11 Results from Example 4–3

Input and Assumptions			Output			Note
Step 1: Calculate the vapor volumetric flow						
W_g	263,150	lb/h	Q_g	101.52	ft³/s	Eq. (4.12)
ρ_g	0.72	lb/ft³				
Step 2: Calculate the light and heavy liquid volumetric flow						
W_{LI}	11,080	Q_{LI}	Q_{LI}	3.42	ft³/min	Eq. (4.14)
W_{HI}	2,770	lb/h	Q_{HI}	0.74	ft³/min	Eq. (4.15)
ρ_{LI}	54	lb/ft³				
ρ_{HI}	62.1	lb/ft³				
Step 3: Caculate the vertical terminal velocity						
p	165	psi	K	0.172		GPSA from Table 4–2
p_g	0.19	lb/ft³	v_T	2.89	ft/s	Eq. (4.4)
			v_V	2.17	ft/s	
Step 4: Calculate the holdup and surge volumes						
Holdup & surge time	15	min	t_s	5	min	
Assume	(Table 4–9)		V_H	34.20	ft³	Eq. (4.28)
t_H	10	min	V_S	17.10	ft³	Eq. (4.29)
			$V_H + V_H$	51.30	ft³	
Step 5: Calculate the total, the diameter, and the total cross-sectional area						
Assume	(Table 4–10)		D	6.5	ft	Eq. (4.44)
L/D	1.6		Use D	6.5	ft	manual
			A_T	33.18	ft²	Eq. (4.19)
Step 6: Calculate the A						
Assume			H_V	4.5	ft	Greater than min.
H_V/D	0.7		A_V/A_T	0.741		Eq. (4.21)
Greater than minimum since vapor is ~95%			A_T	24.59	ft²	Eq. (4.19)
Step 7: Calculate the low liquid level in the liquid compartment						
			H_{LLL}	10.3	in.	Eq. (4.45)
			Use H_{LLL}	10.5	in.	manual
			H_{LLL}/D	0.135		
			A_{LLL}/A_T	0.080		Eq. (4.21)
			A_{LLL}	2.66	ft²	

Table 4–11 Results from Example 4–3 (cont'd)

Input and Assumptions			Output			Note
Step 8: Calculate the weir height						
			H_W	2	ft	Eq. (4.46)
Step 9: Calculate the minimum length of the light liquid compartment						
			L_2	8.66	ft	Eq. (4.47)
			Use L_2	9	ft	manual
Step 10: Set the interface						
Set H_{HL}	1	ft	Set H_{HL}	1.00	ft	$H_{HL} = 0.5H_W$
Set H_{LL}	1	ft	Set H_{LL}	1.00	ft	$H_{LL} = 0.5H_W$
Step 11: Calculate the cross-sectional area of the heavy liquid						
			H_{HL}/D	0.1538462		
			A_{HL}/A_T	0.098		Eq. (4.21)
			A_{HL}	3.24	ft^2	
			A_{LL}	5.35	ft^2	Eq. (4.48)
Step 12: Calculate the settling velocities						
k_s	0.333	(Table 4–3)	v_{HL}	11.24	in./min	Eq. (4.9)
μ_{Ll}	0.24	cp	Use v_{HL}	10	in./min	max., manual
μ_{Hl}	0.682	cp	v_{LH}	3.95	in./min	Eq. (4.9)
			Use v_{LH}	3.95	in./min	manual
Step 13: Calculate the settling times						
			$t_{s,Hl}$	1.2	min	Eq. (4.16)
			Use $t_{s,Hl}$	1.5	min	manual
			$t_{s,Ll}$	3.04	min	Eq. (4.17)
			Use $t_{s,Ll}$	3.5	min	manual
			$t_{s,Hl}$	1.2	min	Eq. (4.16)
Step 14 Calculate the minimun *L1*						
			L_1	1.0	ft	Eq. (4.40)
			Use L_1	1.0	ft	
Step 15 Calculate the total length						
			L	10	ft	Eq. (4.49)
Step 16 Calculate the liquid dropout time						
			t	2.08	s	Eq. (4.35)
Step 17 Calculate the actual vapor velocity						
			v_{VA}	4.13	ft/s	Eq. (4.36)

Table 4–11 Results from Example 4–3 (cont'd)

Input and Assumptions			Output			Note
Step 18 Calculate the minimum length required for vapor/liquid separation						
Set			L_{min}	8.6	ft	Guideline: $L > L_{min,}$ acceptable
L_1	1.0	ft	Use L	10.0	ft	
L_2	9.0	ft				
Step 19: Calculate L/D						
			L/D	1.54		
Step 20: Calculate the thickness of the shell and heads.						
Assume 2:1 Elliptical heads		(Table 4–11)	p	195	psi	
E	0.85		w_S	0.58	in.	Table 4–10
			Use w_s	0.58	in.	manual
			w_H	0.57	in.	Table 4–10
From AMSE (1986)			Use w_H	0.57	in.	manual
S	17,500	psi				
w_C	0.0625	in.				
Step 21: Calculate surface area of the shell and heads						
			A_S	204.20	ft^2	Table 4–10
			A_H	46.05	ft^2	Table 4–10
Step 22: Calculate the approximate vessel weight						
			W	6,950	lb	Table 4–10
No need to perform Step 23 as L/D = 1.54, it is in the ranges of 1.5–6.0.						
Step 24: Calculate the high liquid level and normal liquid level						
Given			H_{HLL}	2	ft	Eq. (4.41)
a	0.00153756		A_{NLL}	6.46	ft^2	Eq. (4.50)
b	26.787101		A_{NLL}/A_T	0.19		
c	3.200201		A_{NLL}/D	0.25		Eq. (4.43)
d	–22.923932		H_{NLL}	1.60	ft	
e	24.353518					
f	–14.844824		H_{LLL}	10.5	in.	
g	–36.999376		or	0.875	ft	
h	10.529572					
i	9.892851					

The two-phase horizontal separator design procedure is very similar to that of the three-phase separator design, except there is no liquid-liquid separation; as demonstrated in Example 4–1 and 4–2 for the three-phase versus two-phase vertical separators design.

In summary, the designs of both two-phase and three-phase (either horizontal or vertical) gravitational separators are very straight forward. With current, advanced computerized design tools, it is very easy to program the procedures and design a separator within minutes; however, that does not mean the designed separator is optimized and can do the job. The key issue here is how to subjectively select those design parameters. Using current, advanced visualization tools, the actual fluid flow can be simulated and engineers can further fine-tune the selected design parameters. The purposes of the examples above are to introduce the fundamental theories of separator designs. It is not our intention to present final results/numbers, because each separator has to be case specific.

Other separation techniques (such as multistage, centrifugal, low temperature, mist eliminator pad, vane, high-efficiency liquid-gas coalesce, etc.) are out of the scope of this book and can be found elsewhere (Ikoku, 1984; Wines and Brown, 1994; Guo and Ghalambor, 2005; Mokhatab et al., 2006).

4.3 Natural Gas Dehydration—Water Removal

As discussed in the beginning of this chapter, water with natural gas can generate a great number of problems. One serious problem is that it could form solid hydrates (see Section 4.3.2 "Natural Gas Hydrates" for a definition) at certain pressures and temperatures, which can plug facilities and pipelines. Also, when pressure and temperature drop, water vapor condenses and can cause slug flow and possible erosion and corrosion in the system, especially when acid gases are present. Finally, water vapor increases the total volume and decreases the heating value of gas, which subsequently, cannot meet gas stream specifications. Therefore, water has to be removed from natural gas before it is transported.

Most free water is removed after the gas-liquid separation is at or near the wellhead. However, there are still small amounts of water vapor associated with the main stream of natural gas that requires further treatment to remove (dehydration).

In the following sections, the water content in a natural gas stream will be determined. First, as it impacts the selection of the type of dehydration method and the design procedure of the dehydration

system; then hydrates will be discussed; and finally, the dehydration process is presented.

4.3.1 Water Content Determination

There are quite a few publications for determining water content (measured in lb/MMcf) in pure components such as hydrogen sulfide-water system, carbon dioxide-water system, and hydrocarbon (methane or propane)-water system. Detailed application ranges and limitations of these methods are summarized in the review paper by Carroll (2002).

Natural gas, however, is usually a complex mixture and sometimes contains acid/sour gas that changes the behavior of the natural gas, and causes the deviation of water content calculation.

Several methods are available to estimate the water content of sweet (McKetta and Wehe, 1958; Katz et al., 1959; Ning et al., 2000) and sour (Maddox, 1988; Robinson et al., 1980; Carroll, 2002; Wichert and Wichert, 2003) natural gases. One of the most commonly used is the Mcketta and Wehe (1958) approach. They developed a chart (Figure 4–8) to estimate the water content for sweet natural gas. It is clear (from the general chart of Figure 4–8) that water content or solubility increases, as temperature increases and pressure decreases. Since salts dissolved in the liquid water in equilibrium with natural gas have a tendency to reduce the water content of the gas, an inset chart is provided in Figure 4–8 to correct for the effects of salinity (see below procedure and Example 4–4 for detailed calculation). This approach is applicable for pressure up to 10,000 psi, temperatures from 50 to 300°F, gas gravity in the range of 0.6 to 1.8, and a brine salinity up to 3%.

Figure 4–8 is not applicable to sour natural gas, but based on the Mcketta and Wehe (1958) work and published experimental data on water content of sour gases, Wichert and Wichert (2003) developed an updated chart based (using Figure 4–8 and augmented by Figure 4–9) correlation to calculate the equilibrium water content of a sour gas. This approach is applicable for pressure up to 10,000 psi, temperature from 50 to 350°F, and H_2S content up to 55%.

The calculation procedure using the Wichert and Wichert (2003) approach is outlined below.

1. At given pressure and temperature, determine the water vapor content of sweet gas from Figure 4–8:

    1.1 Get the water content at 14.7 psi and 60°F from the general chart of Figure 4–8, assuming 0.6 gravity gas contacting with pure water, W in lb/MMcf.

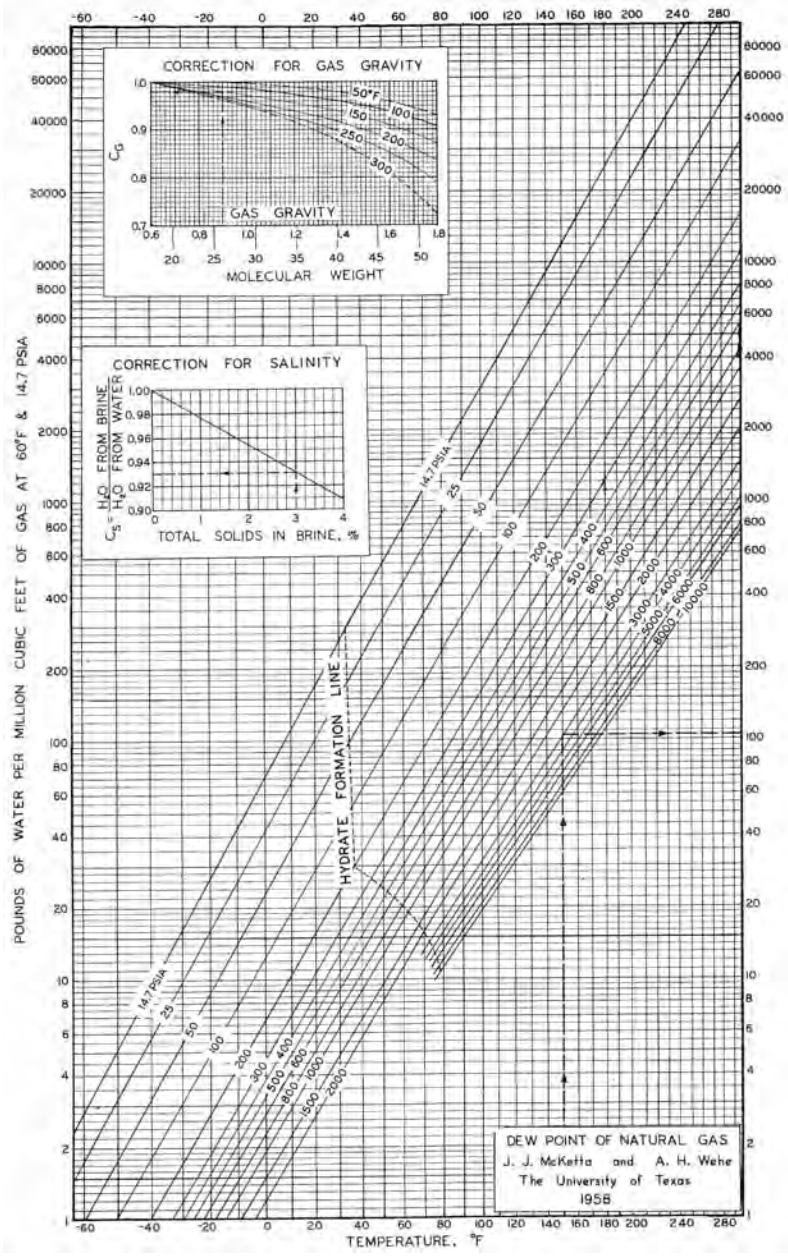

Figure 4–8 *Water content of sweet natural gas* (Mcketta and Wehe, 1958)

1.2 Get the gravity correction factor, C_G, from the inset chart, "Correction for Gravity", where

$$C_G = \frac{\text{lbs. water in gas of gravity, } \gamma_g}{\text{lbs. water in gas of gravity of 0.6}}. \quad (4.51)$$

Note: This is the original definition from Mcketta and Wehe (1958). Wichert and Wichert (2003) used "gas relative density" to obtain C_G in their updated inset chart (not shown here).

1.3 Get the salinity correction factor, C_S, from the inset chart, "Correction for Salinity," where

$$C_S = \frac{\text{lbs. water in gas if gas had been in contact with brine}}{\text{lbs. water in gas if gas had been in contact with water}}. \quad (4.52)$$

1.4 The water content for the sweet natural gas is

$$W_{sweet} = W \times C_G \times C_S. \quad (4.53)$$

2. Determine the mole% of H_2S equivalent concentration of the sour gas by

$$\text{mole\% of } H_2S \text{ equivalent} = \text{mole\% of } H_2S + 0.7 \times (\text{mole\% of } CO_2). \quad (4.54)$$

3. Determine the ratio of water in sour gas to water in sweet gas by using Figure 4–9:

   3.1 Locate the point that represents the "mole% of H_2S equivalent" calculated from Eq. (4.54) and the given temperature in the lower part of Figure 4–9.

   3.2 From this point, move to the upper chart to the given pressure, and move to the left to get the ratio.

4. Determine the saturated water content of the sour gas (W_{sour}) at the given pressure and temperature by multiplying the value from Step 1 (water vapor content of sweet gas) and the ratio from Step 3 (correction).

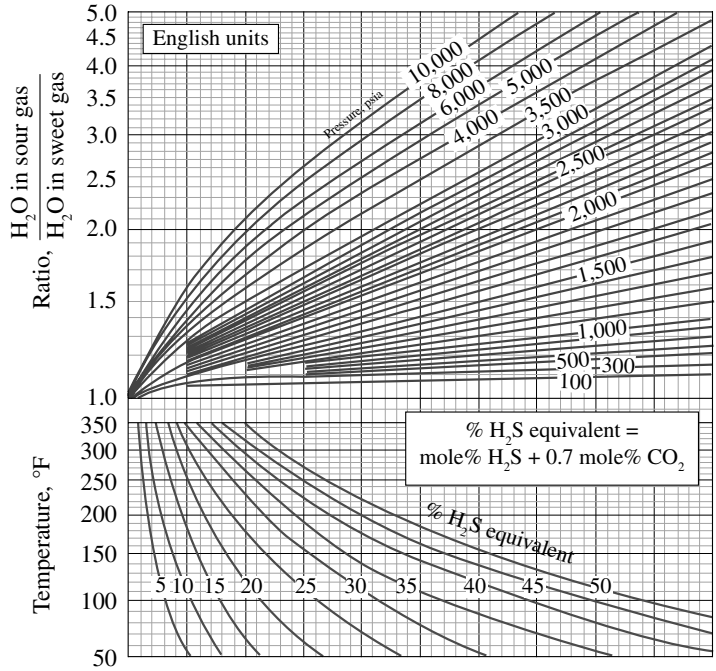

Figure 4–9 *Water content correction for sour natural gas* (Wichert and Wichert, 2003)

Example 4–4 Determination of equilibrium water vapor content in a sour gas

Assume a natural gas mixture with 66% hydrocarbon gas, 21 mole% H_2S, and 13 mole% CO_2 contacting with an aquifer that contains 3% of NaCl. $\gamma_g = 0.86$. The conditions are $p = 2{,}000$ psi and $T = 100°F$.

Solution

Follow the procedure outlined above.

1. Determine water vapor content of sweet gas from Figure 4–8.

   1.1 From general chart: $W = 62$ lb/MMcf.

   1.2 From the inset chart "Correction for Gravity": $C_G = 0.90$.

   1.3 From the inset chart "Correction for Salinity": $C_S = 0.93$.

1.4 The water content for the sweet natural gas is

$$W_{sweet} = 62 \times 0.9 \times 0.93 = 51.9 \text{ lb/MMcf/d.}$$

2. Determine the mole% of H_2S equivalent concentration of the sour gas from Eq. (4.54), mole% of H_2S equivalent = 21 mole% of H_2S + 0.7 × (13 mole% of CO_2) = 30%.

3. Determine the ratio of water in sour gas to water in sweet gas by using Figure 4–9. With 30 mole% H_2S equivalent, p = 2,000 psi and T = 100°F, ratio = 1.53.

4. Determine the saturated water content of the sour gas (W_{sour}) at the given pressure and temperature by multiplying the value from Step 1 (water vapor content of sweet gas) and the ratio from Step 3 (correction):

$$W_{sour} = 51.9 \times 1.53 = 79.4 \text{ lb/MMcf/d.}$$

4.3.2 Natural Gas Hydrates

Natural gas hydrates are solid crystalline compounds formed by the chemical combination of natural gas and water under pressure at temperature considerably above the freezing point of water. The chemical formulae for natural gas hydrates are:

Methane	$CH_4 \bullet 7H_2O$
Ethane	$C_2H_6 \bullet 8H_2O$
Propane	$C_3H_8 \bullet 18H_2O$
Carbon Dioxide	$CO_2 \bullet 7H_2O$

Hydrates tend to form when there is:

- Free water present and temperature decreases below that of hydrate-formation. This usually happens in the flow string or surface line;
- Sudden pressure drop due to expansion. This usually happens when fluids flows through orifices, back pressure regulators, or chokes.

If a small "seed" crystal of hydrate or acid gas (H_2S or CO_2) is in the system and the flow rate is high with agitation, it will definitely promote the formation of natural gas hydrates.

Hydrate formation can be predicted by using Figure 4–8 (for $\gamma_g = 0.6$, hydrates tend to form to the left of the "hydration formation" line) and Figure 4–10 (for first approximations of hydrate formation conditions at different values of gas gravity). The permissible expansion (without hydrate formation) of natural gas at different gas gravity can be found in GPSA (1977) or Ikoku (1984). For example (from Figure 4–10), if a natural gas mixture exists with $\gamma_g = 0.9$ and $T = 60°F$, natural gas hydrate might form when the pressure is above 500 psi; if a natural gas exists with $\gamma_g = 1.0$ and $p = 90$ psi, then natural gas hydrate might form when the temperature is below 40°F. If the natural gas contains acid gases (H_2S or CO_2), the hydrate-formation envelope will expand as acid gases will increase the possibility of hydrate formation.

Figure 4–8 also can reveal one of the greatest potential future resources of natural gas. For example, at the ocean floor at a depth of 7,000 ft the pressure would be over 3,000 psi. This means that if the temperature is less than 72°F (from Figure 4–8) hydrates will form. The temperature is far lower, closer to 32°F. This means that natural gas hydrates will form if natural gas is present. In fact at 40°F, natural gas hydrates will form if the pressure is 250 psi, i.e., a depth of less than 600 ft. There is ample evidence that the bottom of the oceans contain massive quantities of natural gas in the form of hydrates. In some cases, geologists have postulated that the frozen hydrate may be the only caprock to hydrocarbon reservoirs.

From the above examples, it is clear that hydrates can be prevented if the temperature of the natural gas system is kept (such as by heating) above the hydrate temperature at all times; by injecting chemicals into the system that will react with the free water, so that it will no longer be free to form hydrates; or to remove the water altogether, so that there will be no water to form hydrates after cooling. The last option is usually done in the gas processing plant before transporting natural gas to the customers.

There are four ways to dehydrate the natural gas: direct cooling, compression followed by cooling, absorption, and adsorption. The last two approaches are more commonly used, as the first two usually cannot sufficiently dehydrate the gas to pipeline requirements.

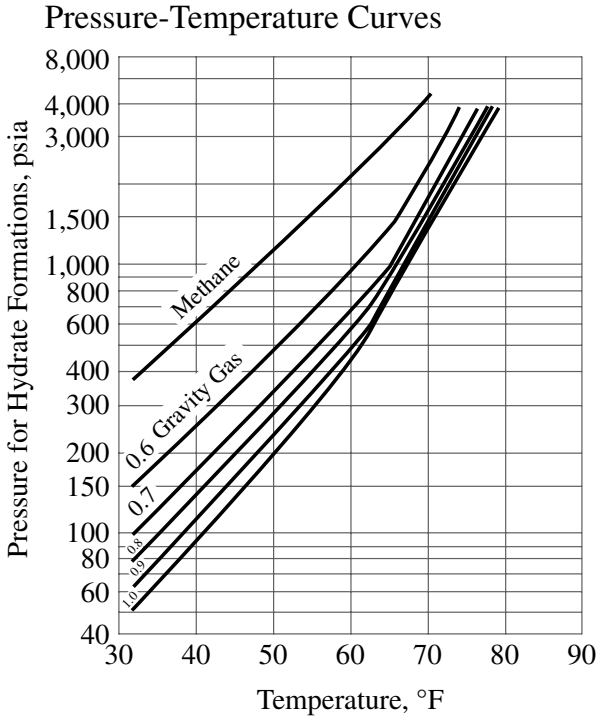

Figure 4–10 *Hydrate formation prediction* (GPSA, 1977)

4.3.3 Adsorption Dehydration

Adsorption dehydration removes water by flowing gas through a granulated solid bed called solid desiccant or adsorbent. Because of the microscopic pores and capillary openings, the solid desiccant has a very large effective surface area per unit weight to retain water on the surface of the solid medium. The adsorption dehydration unit usually contains an inlet gas stream separator for initial separation, two or more adsorption towers (also called adsorbers or contactors) to dehydrate gas, a high temperature heater to dry solid desiccant in the towers, a regeneration gas cooler to condense water from the hot regeneration gas, and a regeneration gas separator to remove water from the regeneration gas stream (Leecraft, 1987). In addition, piping, manifolds, switching valves, and controls are needed to direct and control the flow of gases according to process requirement.

In this book, focus is given to the most popular technique of water removal—counter-current absorption.

4.3.4 Absorption Dehydration

Absorption dehydration is the water removal process by counter-flowing natural gas through a certain liquid solvent that has special attractions or affinities for water. The liquid solvent is called a dehydrating agent or liquid desiccant.

Dehydrating Agents

The most desirable dehydrating agents that can be used for commercial dehydration purposes should possess the following important properties (Campbell, 1998):

- High water absorption efficiency;
- High decomposition temperature;
- Low vaporization losses;
- Easy and economic to be separated and regenerated;
- Non-corrosive and non-toxic to the system.

Glycols such as ethylene glycol (EG), diethylene glycol (DEG), triethylene glycol (TEG), and tetraethylene glycol (T_4EG) fall into this category. Among these four, TEG is the most popularly used as it provides superior dew point depression, is easier to regenerate to ~99%, has higher decomposition temperature with relatively high operation reliability, low operating cost, and low vaporization losses. It can also be used to dehydrate sweet and sour natural gases over the following range of operating conditions: dew point depression of 40–140°F, gas pressure of 25–2,500 psig, and gas temperature of 40–160°F (Ikoku, 1984).

Here the dew point depression is a very important concept. It is used very often to design the water dehydration process and determine the amount of water removed. It is the difference between the dew point temperature of a water-saturated gas stream, and the dew point after the stream has been dehydrated.

Glycol Dehydration Process

Figure 4–11 is a sketch of a typical glycol dehydration process, regardless of what type of glycols are used (Campbell, 1998). Here both the "wet" and "rich" gas means the gas is rich in water and "dry" and "lean" gas means the gas is lean in water. Similarly the "wet" and "rich" glycol means the glycol is rich in water and "dry" and "lean"

glycol means the gas is lean in water. The separator is often referred to as the scrubber, the glycol gas absorber as contactor, the still column as stripper, and glycol regenerator as glycol reconcentrator.

The wet gas first enters a two-phase separator (not shown in Figure 4–11), so that the liquid can be removed from the gas mixture. If free water is present, a three-phase separator must be used. The gas leaving the separator from the top contains a small amount of water vapor despite the mist eliminator on top of the separator. This still "wet" gas then enters the bottom of the glycol gas absorber, flows upwards through the trayed or packed tower with mist eliminator to remove any entrained glycol droplets from the gas stream, and exits on the top of the absorber as dry gas. The dry gas then flows through a glycol cooler to cool the hot regenerated glycol before the glycol enters the absorber.

The dry glycol, on the other hand, flows down the tower, absorbs water from the up flowing gas mixture, and exits at the bottom of the absorber as rich glycol. The rich glycol then flows through a reflux condenser at the top of the still column, and enters a flash tank where most of the entrained, soluble, and volatile components are vaporized. After leaving the flash tank, the rich glycol flows through the glycol filters and the rich-lean glycol exchanger, where it exchanges heat with the hot lean glycol. The rich glycol then enters the glycol regenerator that contains the still column and reboiler, where the water is removed by distillation, and the glycol concentration is increased to meet the lean glycol requirement. For processes requiring gas with very low water dew points, a stripping vapor will most likely be needed to aid the regeneration process (Hernandez-Valencia et al., 1992).

Absorber Design

As shown in the flow diagram of Figure 4–11, the main equipment in the glycol dehydration process is the absorber. A properly designed absorber is critical to achieve the design criteria or desired results, such as glycol to water circulation rate of 2 to 6 gal TEG/lb, H_2O removed for most glycol dehydration requirements, or 2.5 to 4 gal TEG/lb H_2O for most field absorbers; and the lean TEG concentration from glycol regenerator to be 99.0 to 99.9%, or 99.5% lean TEG for most design considerations (Ikoku, 1984). To achieve these goals, it is necessary to know the maximum gas flow rate, gas composition, or gas specific gravity; in addition to the absorber operating and maximum working pressures, gas inlet temperature, and outlet gas water dew point, or water content required (which is the goal needed to be achieved). This will be demonstrated in Example 4–5.

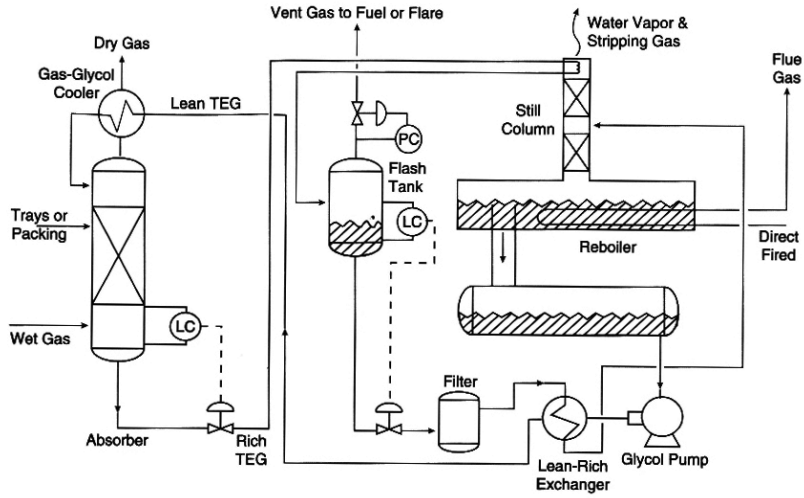

Figure 4–11 *A sketch of a typical glycol dehydration process* (Campbell, 1998)

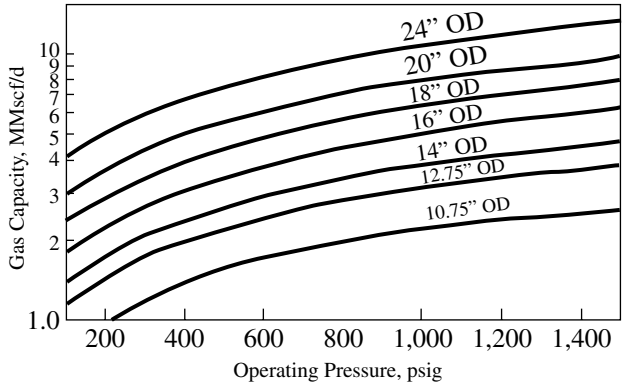

Figure 4–12 *Gas capacity for packed glycol gas absorbers for* $\gamma_g = 0.7$ *at 100°F* (Sivalls, 1977)

The diameter of the absorber depends on both the liquid and the vapor load, and can be determined by using the same approach introduced earlier in this chapter for separator design (Eq. (4.13)). Here, the diameter is plotted as a function of the operating pressure and the approximated gas capacity. An example for packed glycol gas absorbers is shown in Figure 4–12. The gas capacity in this figure is

determined for $\gamma_g = 0.7$ at 100°F, and needs to be corrected to the actual operating gas gravity and temperature:

$$Q_o = Q_s(C_t)(C_g), \tag{4.55}$$

where Q_o and Q_s are gas capacities (MMscf/d) of the absorber at the operating conditions and at $\gamma_g = 0.7$ at 100°F (at operating pressure), respectively. C_t and C_g are correction factors for operating temperature and for gas gravity, respectively. They can be determined by using the following correlations (developed based on the published data by Sivalls, 1977):

$$C_t = 0.601T^{0.1103}, \tag{4.56}$$

$$C_g = 0.6429\gamma_g^2 - 1.6298\gamma_g + 1.829, \tag{4.57}$$

where T is the operating temperature in °F and is in the range of 50 to 120°F, and γ_g is in the range of 0.55 to 0.9. A similar approach can be used to determine the trayed glycol gas absorber.

The water removed from the glycol absorber unit can be calculated by (Ikoku, 1984)

$$W_r = \frac{Q_g(W_i - W_o)}{24}, \tag{4.58}$$

where W_r is the water removed in lbm/hr. W_i and W_o are the water contents of the inlet (wet) and outlet (dry) gas (lb H_2O/MMcf), and can be calculated by using the approach introduced earlier in Section 4.3.1 "Water Content Determination". Q_g is the gas flow rate in MMscf/d.

The height of a packed tower must be sufficient to provide enough contact between the vapor and liquid to give the desired result (Campbell, 1998). The actual packing height, h, is calculated as

$$h = (\text{HETP})(N)\ , \tag{4.59}$$

where N is the number of theoretical stages. HETP stands for Height Equivalent to a Theoretical Plate and can be determined experimentally in laboratory or pilot plant tests. It is a function of packing type, vapor and liquid densities, liquid viscosity and surface tension diffusivity, and vapor and liquid loading. For the glycol dehydration unit, an HETP of 5 ft (1.5 m) can be used to estimate contactors for both random and structured packing. N can be determined by using Figure 4–13. In this figure, the dew point depression (°F) is the differ-

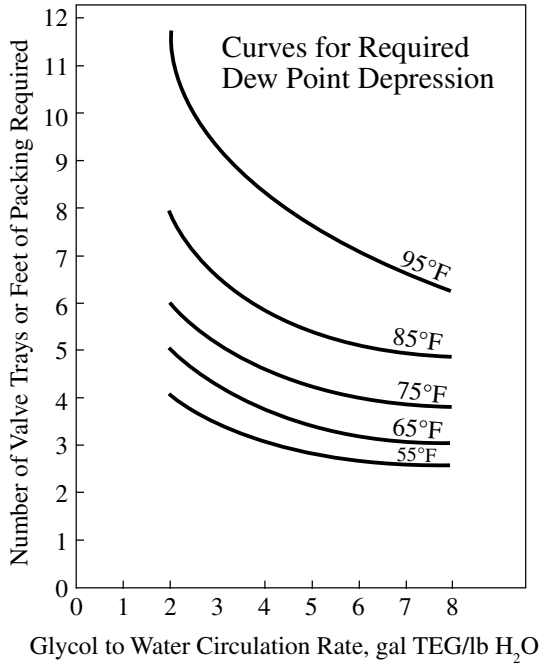

Figure 4–13 *Trays or packing required for glycol dehydrators* (Sivalls, 1977)

ence between the inlet gas temperature and the outlet gas dew point temperature. If a detailed packing depth is required, a modified McCabe-Thiele diagram (McCabe and Smith, 1976) should be used.

Extensive discussion on glycol absorber design can be found in Sivalls (1977), Ikoku (1984), and Campbell (1998). There are other important equipment in the absorption dehydration process, such as the flash tank, glycol regenerator (still column and reboiler), heat exchanger, filter, and pump. Detailed designs and operational discussions of the equipment can also be found from the published literature mentioned above.

Example 4–5 Packed glycol absorber design

Size a packed glycol absorber by using the following parameters:

Gas flow rate Q_o = 9.5 MMScf/d, γ_g = 0.8, Operating pressure p = 1,000 psig, gas inlet temperature T_i = 110°F. Assume there is no sour gas. Requirement: water content in the outlet gas stream W_o= 6.0 lb H_2O/MMscf. Glycol to water circulation rate = 3.0 gal TEG/lb H_2O.

Solution

Step 1. Determine absorber diameter, D:

Determine the correct factors by using Eqs. (4.56 and 4.57) and Q_s by Eq. (4.55),

$C_t = 0.601 \times (110)^{0.1103} = 1.01$,

$C_g = 0.6429 \times (0.8)^2 - 1.6298 \times 0.8 + 1.829 = 0.94$,

$Q_s = Q_o/((C_t)(C_g)) = 9.5/(1.01 \times 0.94) = 10.0$ MMscf/d.

Determine absorber diameter by using Figure 4–12: $D = 24$ inches.

Step 2. Determine the number of stages, N:

Determine outlet dew point temperature by Figure 4–8, $T_o = 28$°F. Then dew point depression = 110 – 28 = 82°F. The number of stages can be determined by Figure 4–13, $N = 6.5$.

Step 3. Determine the water removed:

Under $T_i = 110$°F and $p = 1{,}000$ psig, water content can be determined from the general chart of Figure 4–8, $W = 80$ lb H_2O/MMscf. Correct it for $\gamma_g = 0.8$ by using the insert chart, $C_G = 0.99$. Determine water content of the inlet gas stream by using Eq. (4.53), $W_i = 80 \times 0.99 = 79.2$ H_2O/MMscf. Water removed from the absorber = 79.2 – 6.0 = 73.2 lb/MMscf, or

$$W_r = \frac{9.5 \times (79.2 - 6.0)}{24} = 30 \text{ lb/hr.}$$

Glycol Dehydrators Design Considerations

There is no doubt that the design parameters control the behavior of the absorption system, and play key roles in the amount of the residual water content in the outlet gas stream. Hernandez-Valencia et al. (1992) performed a parametric study.

As expected, their results showed that the equilibrium at the top of the absorber depends on the glycol circulation rate and the

number of trays/stages of packing. The reboiler temperature in the regenerator and the amount of stripping gas used (if it is used) determine the equilibrium water content, because they limit the purity of the lean glycol to the absorber. The operating pressure of the regenerator affects the lean glycol purity as well.

Their study also showed that several other factors affect the residual water content in the gas. They found that the temperature of the inlet gas stream controls the total amount of water to be removed; lower temperatures mean that less water is absorbed by the glycol. Also the lean glycol temperature at the top of the absorber affects the water partial pressure at the top equilibrium stage, which means that high glycol temperatures lead to large water content in the overhead gas. The top temperature is usually at least 10°F above the inlet gas to prevent condensation of hydrocarbons in the feed. This temperature is maintained lower by a gas/glycol exchanger that cools the lean glycol by 10°F, using the dry gas.

Environmental issues include the fact that the plant feed contains small quantities of aromatic hydrocarbons (primarily comprised of benzene, toluene, ethylbenzene, or xylenes) that are very soluble in the TEG (Hernandez-Valencia et al., 1992). These aromatics are carried by the TEG in the flash tank where some are released along with other volatile compounds. The rest are removed in the regenerator, boiled off by heating. Usually these organics and aromatics are vented to the atmosphere, and even in small plants, the aromatic emissions may easily exceed 100 lb/day, causing a serious environmental compliance concern (Fitz and Hubbard, 1987).

Acid gases (such as H_2S and CO_2) are also a concern because as discussed earlier, they absorb water vapor and increase the water content of the gas stream. Acid gases need to be considered in the design of the dehydration units. Large amount of H_2S in the regenerator can accelerate corrosion, and CO_2 can act as a stripping vapor in the regenerator (Kohl and Riesenfeld, 1985).

In summary, the absorption dehydration systems, by using glycols as dehydrate agents, are very effective and have been used widely in practice. Equipment costs are low and the small pressure drop across absorption towers saves power and operating costs.

There are some disadvantages and operational problems such as:

- Glycol solutions may be contaminated by dirt, scale, and iron oxide.
- Overheating of glycol solution may lead to decomposed products and cause some loss of efficiency.

- Glycol losses due to foaming, degradation, inadequate mist extraction, etc.

Some of these problems can be corrected by adding new equipment (such as placing a filter ahead of the solution pump), optimizing the units, and operating the equipment properly.

4.4 Natural Gas Sweetening—Acid Gases Removal

It should be clear by now that CO_2, and especially H_2S, must be removed before the gas is sent to sales. As defined in Chapter 1, sour gas means the amount of H_2S in natural gas is above the acceptable industry limits, while sweet gas means the gas virtually has no H_2S (either it does not have it in the first place or it is treated). The process of removing H_2S is called natural gas sweetening. Based on published information (Ikoku, 1984; Leecraft, 1987; Campbell, 1997; GPSA, 1998; Mokhatab et al., 2006), a summary of some of the natural gas sweetening processes are presented in Table 4–12.

Table 4–12 Summary of the Natural Gas Sweetening Processes

Iron-Sponge Sweetening	
Reaction	$2\ Fe_2O_3 + 6H_2S \rightarrow 2\ Fe_2S_3 + 6\ H_2O$
Regenerating	$2\ Fe_2S_3 + 3\ O_2 \rightarrow 2\ Fe_2O_3 + 6\ S$
Notes	A batch process. Most applicable for small gas volume with low H_2S content. Operating temperature of the vessel <120°F.
Alkanolamine Sweetening	
Reaction	MEA + $H_2S \rightarrow$ MEA hydrosulfide + heat MEA + H_2O + $CO_2 \rightarrow$ MEA carbonate + heat
Regenerating	MEA hydrosulfide + heat $\rightarrow$ MEA + H_2S MEA carbonate + heat $\rightarrow$ MEA + H_2O + CO_2
Notes	Alkanolamine: organic compounds including Monoethanolamine (MEA), Diethanolamine (DEA), and Triethanolamine (TEA). Not selective and have to be designed for total acid-gases removal. Operating p > 125 psi for DEA. Can absorb most of the acid gases and meet the specified pipeline requirement. Reversible equilibrium reactions.

Table 4–12 Summary of the Natural Gas Sweetening Processes (cont'd)

Glycol/Amine Process	
Notes	A solution composed of 10–30 wt% MEA, 45–85% glycol, and 5–25% water for the simultaneous removal of water vapor, H_2S, and CO_2. The process flow scheme is essentially the same as that for MEA. Applicable when low dew point is not required. Disadvantage: MEA losses due to vaporization in regeneration with high temperature.
Sulfinol Process	
Notes	The solvent (composed of sulfolane, diisopropanolamine (DIPA), and water) acts as the physical (sulfolane) and chemical (DIPA) solvent. Advantages: low solvent circulation rates—smaller equipment and lower cost. Disadvantages: absorption of heavy hydrocarbons and aromatics.
Chemsweet and Zinc Oxide Process Process	
Reaction	$ZnAc_2 + H_2S \rightarrow ZnS + 2\ HAc$, $ZnO + H_2S \rightarrow ZnS + H_2O$
Regenerating	$ZnO + 2HAc \rightarrow ZnAc_2 + H_2O$
Notes	Can treat gas with high H_2S concentration. Operating p between 89–1,415 psi. Should not be used when Mercaptan concentration is above 10% of H_2S concentration in gas stream as mercaptans reacts with ZnO and forms Zn(OH)RH which will form a sludge and possibly cause foaming problems.

4.5 References

Arnold, K. and M. Stewart. 1998. *Surface Production Operations. Vol. 1*: *Design of Oil-Handling Systems and Facilities*, 2nd ed. Houston: Gulf Professional Publishing.

American Society of Mechanical Engineers. 1986. ASME Pressure Vessel Code. Sec. VIII, Div. 1, Table UCS-23, ASME, New York, 270–271.

Campbell, J. M. 1998. *Gas Conditioning and Processing*, *Vol. 2*. Norman, OK: Campbell Petroleum Series.

Carroll, J.J. 2002. The Water Content of Acid Gas and Sour Gas from 100° to 220°F and Pressures to 10,000 PSIA. Presented at the 81st Annual GPA Convention, Dallas, TX, March 11–13.

Energy Information Administration (EIA), *Office of Oil and Gas*, January 2006.

Fitz, C. W., and R.A. Hubbard. 1987. Quick, manual calculation estimates amount of benzene absorbed in glycol dehydrator. *Oil & Gas*: 72.

Gas Processors Suppliers Association. 1977. *Engineering Data Book*, 9th ed., 3rd revision.

Gas Processors Suppliers Association. 1987. *Engineering Data Book*, 10th ed. vol. 1, Ch. 7. Tulsa, OK.

Gas Processors Suppliers Association. 1998. *Engineering Data Book*, 11th ed. Tulsa, OK.

Gerunda, A. 1981. How to size liquid vapor separators. *Chem. Eng:* 81–84.

Guo, B. and A. Ghalambor. 2005. *Natural Gas Engineering Handbook*. Houston: Gulf Publishing Company.

Hernandez-Valencia, V. N., M.W. Hlavinka, and J.A. Bullin. 1992. Design Glycol Units for Maximum Efficiency. Proceedings of the Seventy-First Gas Processors Association Annual Convention. Tulsa, OK: 310–317.

Ikoku, C. U. 1984. *Natural Gas Production Engineering*. New York: John Wiley & Sons.

Jekel, T.B., D.T. Reindl, M.J. Fisher. March 2001. Gravity separator fundamentals and design. Paper presented at IIAR 2001 Ammonia Refrigeration Convention & Exhibition, Long Beach, CA.

Katz, D.L., D. Cornell, R. Kobayashi, F.H. Poettmann, J.A. Vary, J.R. Ellenbaas, and C.F. Weinang. 1959. *Handbook of Natural Gas Engineering*. New York: McGraw-Hill.

Kohl, A. and F. Riesenfeld. 1985. *Gas Purification*. Houston: Gulf Publishing Company.

Kumar, S. 1987. *Gas Production Engineering*. Houston: Gulf Publishing Company.

Leecraft, J. 1987. *Field Handling of Natural Gas*, Austin, TX: Petroleum Extension Service.

Mokhatab, S., W.A. Poe, and J. G. Spreight. 2006. *Handbook of Natural Gas Transmission and Processing*. Burlington, MA: Elsevier.

Maddox, R.N., L.L. Lilly, M. Moshfeghian, and E. Elizondo. 1988. Estimating water content of sour natural gas mixtures. Paper presetend at the Laurance Reid Gas Conditioning Conference, Norman, OK.

McCabe, W.L. and J.C. Smith. 1976. *Unit Operations of Chemical Engineering*. 3rd ed. New York: McGraw-Hill.

Mcketta, J.J. and A.H. Wehe. 1958. Use This Chart for Water Content of Natural Gases. *Petroleum Refiner* (August): 153–154.

Monnery, W.D. and W.Y. Svrcek. 1994. Successfully specify three-phase separators. *Chem Eng Prog* (September): 29.

Monnery, W.D. and W.Y. Svrcek. 2000. Analytical Study of Liquid/Vapour Separation Efficiency. In the Alternative Flaring Technologies program sponsored by Environment Canada, CAPP, and PTAC.

Ning, Y., H. Zhang, and G. Zhou. 2000. Mathematical simulation and program for water content chart of natural gas. [In Chinese] *Chem. Eng. Oil Gas* 29: 75–77.

Robinson, J.N., R.G. Moore, R.A. Heidemann, and E. Wichert. 1980. Estimation of the water content of sour natural gas. Paper presented at the Laurance Reid Gas Conditioning Conference, Norman, OK.

Sivalls, C.R. 1977. Fundamentals of oil and gas separation. Proceedings of the Gas Conditioning Conference, University of Oklahoma.

Souders, M. and G.G. Brown. 1934. Design of fractionating columns, entrainment and capacity. *Ind. & Eng. Chem* 38 (1): 98–103.

Speight, J.G. 2007. *Natural Gas: A Basic Handbook*. Houston: Gulf Publishing Company.

Svrcek, W.Y. and W.D. Monnery. 1993. Design two-phase separators within the right limits. *Chem Eng Prog* (October): 53.

Watkins, R.N. 1967. Sizing separators and accumulators. *Hydrocarbon Processing* 46 (11).

Wines, T.H. and R.L. Brown, Jr. 1994. Recent development in liquid/gas separation technology. Paper presented at the Laurance Reid Gas Conditioning Conference, Norman, OK, February 28.

Wichert, G.C. and E. Wichert. 2003. New charts provide accurate estimations for water content of sour natural gas. *Oil & Gas J* (October 27)*:* 64–66.

Young, A.H. 2004. *Natural Gas Processing Principles and Technology—Part II*. University of Calgary.

CHAPTER 5

Natural Gas Transportation—Pipelines and Compressed Natural Gas

5.1 Introduction

As will be discussed in Chapter 9, natural gas has come to the forefront of the international energy debate due to increasing demands in many countries, headed by the United States, China, and India. This has been prompted by a changing worldwide preference in power generation because of environmental concerns. As a result, transport of natural gas over long distances has become very important. Two well established technologies are predominantly used to transport natural gas from sources to consumption markets: pipelines, accounting for 70 percent of transported gas, and liquefied natural gas (LNG), accounting for the remaining 30 percent. Pipelines over land are the cost-effective technology of choice. Underwater pipelines are also feasible, but are quite expensive, as much as ten times the cost of on-land pipelines of same length, and are limited by the underwater terrain they have to traverse. The de facto choice for natural gas transport, when a pipeline cannot be used, is currently LNG. It is a technologically proven and safe method of transport. Also, a number of LNG terminals and ships are available worldwide. However, the investment cost is quite high for LNG facilities, both for the regasification process at the receiving terminal, and particularly, for the liquefaction process at the shipping terminal. Additionally, the energy consumed for LNG liquefaction and transport is high, amounting to as much as the equivalent of one quarter of the gas.

While LNG dominates the market for sea transport of natural gas, a number of recent studies have shown that compressed natural gas (CNG) is economically more attractive than LNG for sea transport of relatively smaller volumes of gas over shorter distances (Wang and

Marongiu-Porcu, 2008; Marongiu-Porcu et al., 2008; Nikolaou et al., 2009). CNG requires minimal investment in facilities at the shipping and receiving sites and wastes far less energy. The main capital cost for CNG is incurred in building the transportation vessels. Although the cost for transportation vessels is higher for CNG than for LNG (stemming from corresponding gas compression ratios of usually 200:1 versus 600:1, respectively), overall economics favor CNG for short distances and small loads, as outlined in Figure 5–1.

Figure 5–1 clearly suggests that CNG offers an economically attractive way to deliver commercial quantities of natural gas by ships to customers within 2,000 km (about 1,200 miles), assuming that underwater pipelines are not feasible. For smaller volumes, such as 1 to 2 Bcm/yr (about 100 MMscf/d to 200 MMscf/d), CNG is the indicated solution to bring natural gas to many markets. It should be emphasized that Figure 5–1 is premised on zero installed base, namely, facilities for each candidate technology would be built from scratch at nominal prices. Clearly, additional factors have to be taken into account when prices are distorted as a result of existing installed base (e.g., LNG terminals or ships), or supply and demand vary drastically as a result of economic growth or downturn.

In this chapter, we focus on natural gas transport via pipeline and CNG, as these two technologies rely on compression only and do not employ conversion of natural gas to a liquid. LNG, relying on conversion of natural gas to its liquid form via deep refrigeration, will be discussed in Chapter 6. Other gas transportation forms, such as gas-to-liquids (GTL), which relies on the conversion of natural gas to liquid products via chemical reactions, will be elaborated upon in Chapter 7.

5.2 Pipelines

A pipeline is a very efficient way to transport natural gas, especially on land. According to the EIA (2008), there were about 210 natural gas pipeline systems in the United States, spanning more than 300,000 miles of interstate and intrastate transmission pipelines. Interstate pipelines, often called “trunklines,” are long-distance and wide-diameter (20–42 in.), and traverse more than one state. There are more than 1,400 compressor stations to maintain pressure on this pipeline network. Intrastate pipelines operate inside a single state.

The basic concepts involved in pipeline capacity design are shown in Figure 5–2 (EIA, 2008). The supply sources of natural gas imported into a pipeline could be from another pipeline, LNG, gas processing plants, and gas gathering systems. Gas then goes through a

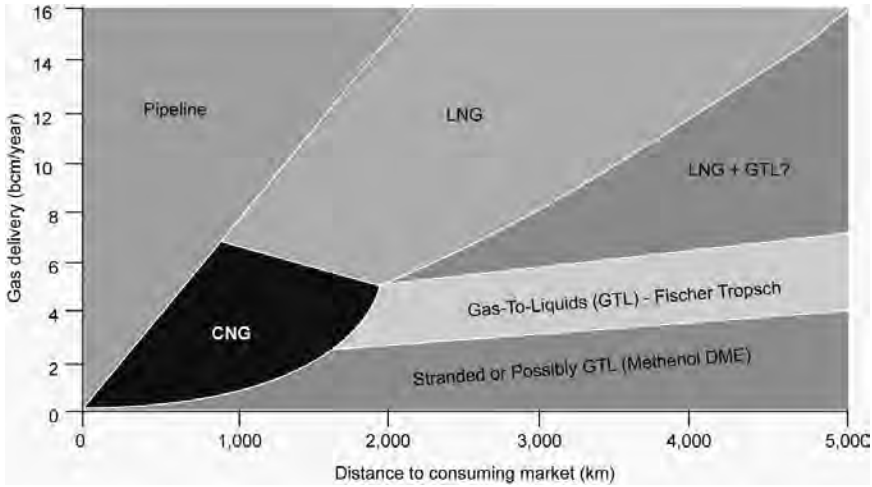

Figure 5–1 *Economically preferred options for monetizing stranded natural gas* (Wood et al., 2008)

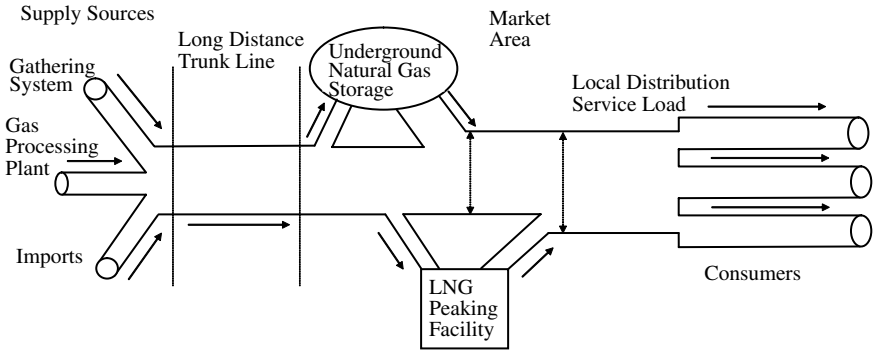

Figure 5–2 *Basic pipeline capacity design concept* (EIA, 2008)

long-distance trunkline and eventually reaches the consuming markets. During the nonheating season (spring–summer), excess gas goes to LNG peaking facilities and underground natural gas storage (which will be discussed in Chapter 8). During the heating season (winter) or peak period, additional gas is supplied into the pipeline transmission system to meet the demand from the customers. This pattern, which has lasted for decades, will be altered in the future because of two new issues: much larger LNG imports and the increasing use of natural gas for electricity generation (air conditioning has its own peaks in the summer).

5.2.1 Pipeline Size

Pipeline design means appropriate size, appropriate distance between compression stations, and adequate compressor sizes that would allow optimum operation and ability to expand in the future. Pipeline throughput depends on pipeline diameter and the operating pressure; taking into account the length of the pipeline and the terrain. Typical onshore pipeline operating pressure is about 700 to 1,100 psi (with some as high 4,000 psi); for offshore pipelines, the operating pressure is typically between 1,400 to 2,100 psi, depending on the material and the age of the pipeline (Speight, 2007).

As discussed in the previous chapter, after the natural gas processing, the gas in the transporting pipelines is purely methane, a single-phase compressible fluid. So the pressure drop in the horizontal pipeline can be calculated by using Eq. (3.68). In that equation, the average values of Z, T, and μ for the entire length of pipe are used. The kinetic energy pressure drop was neglected with the assumption that the flow rate is not very high. In a high rate, low pressure line, however, the change in kinetic energy may be significant and should not be neglected (Economides et al., 1994). In this case, for a horizontal pipeline, the mechanical energy balance is

$$\frac{dp}{\rho} + \frac{u\,du}{g_c} + \frac{2f_f u^2 dL}{g_c D} = 0\,. \tag{5.1}$$

For a real gas, ρ and u are given by Eqs. (1.10 and 3.59), respectively. The differential form of the kinetic energy term is

$$u\,du = -\left(\frac{4qZT}{\pi D^2}\frac{p_{sc}}{T_{sc}}\right)^2 \frac{dp}{p^3}\,. \tag{5.2}$$

Substituting for ρ and $u\,du$ in Eq. (5.1), assuming average values of Z and T over the length of the pipeline, and integrating, we obtain

$$p_1^2 - p_2^2 = \frac{32}{\pi^2}\frac{28.97\gamma_g \bar{Z}\bar{T}}{Rg_c D^4}\left(\frac{p_{sc}q}{T_{sc}}\right)^2\left(\frac{2f_f L}{D} + \ln\frac{p_1}{p_2}\right), \tag{5.3}$$

which for field units is

$$p_1^2 - p_2^2 = (4.195\times10^{-6})\frac{\gamma_g \bar{Z}\bar{T}q^2}{D^4}\left(\frac{24f_f L}{D} + \ln\frac{p_1}{p_2}\right), \tag{5.4}$$

where p_1 and p_2 are in psi, T is in R, q is in Mscf/d, D is in inches, and L is in ft. The friction factor is obtained from Eq. (3.57) as a function of the Reynolds number and pipe roughness. The Reynolds number for field units is given by Eq. (3.69).

Eq. (5.4) is identical to Eq. (3.68) except for the additional ln (p_1/p_2) term, which accounts for the kinetic energy pressure drop. Eq. (5.4) is an implicit equation in p and must be solved iteratively. With a computer program, this should be very easy to do.

Example 5–1 Calculation of pipeline pressures and dimensions

Gas is gathered at point A from gas processing plants B and C (see Figure 5–3), and transported to customers at D. The gas rates from plants B and C are 80 and 50 MMscf/d, respectively.

The distances between BA, CA, and AD are 1,000 ft, 800 ft, and 10 miles, respectively. The diameters of pipelines CA and AD are 5 and 10 in., respectively. The pressure at destination D has to be 500 psi. Assume the temperature is 77°F in the whole process. The pipeline relative roughness is 0.001. All gas is methane.

1. What is the inlet pressure in the AD pipeline?

2. If gas from pipeline BA is injected into the main pipeline AD at the same pressure (BA outlet pressure = AD inlet pressure) and the inlet pressure at B has to be 1,240 psi, what should the diameter of pipeline BA be?

3. If the diameter of pipeline CA is 5 in., pressure at C is 1,000 psi. What is the outlet pressure at CA? To get CA gas stream injected to main stream AD at the same pressure as the inlet pressure of AD, how much pressure has to be boosted by a compressor?

Solution

1. For the total rate of 130 MMscf/d for pipeline AD, assume the Reynolds number is 1.0×10^7, with pipe relative roughness equal to 0.001. Using Eq. (3.57), the Fanning friction factor $f_f = 0.0049$ (will need to check Reynolds number once we get the pressure).

   To calculate the inlet pressure of pipeline AD, the Z-factor is needed, and trial and error is indicated, because the Z-factor

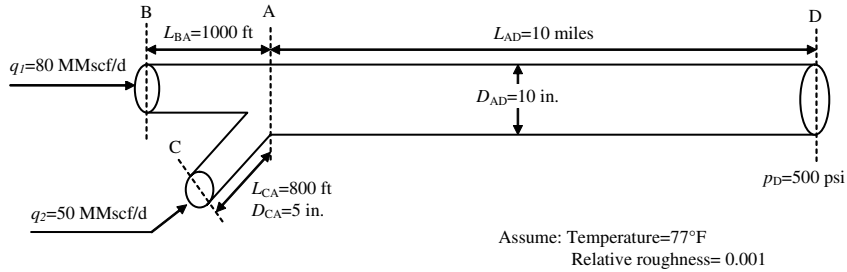

Figure 5–3 *Diagram for Example 5–1*

depends on the pressure. Also, in checking for the Reynolds number, the viscosity must be adjusted by the calculated pressure.

Assume the inlet pressure is 1,000 psi. Since all the gas is methane, then $\gamma_g = 0.56$, $p_{pc} = 673.6$ psi, and $T_{pc} = 346.1$ R. For $p = (1{,}000 + 500)/2 = 750$ psi and $T = 77°$F, $Z = 0.9$ (from Z chart).

The left hand side (LHS) of Eq. (5.4) does not equal the right hand side (RHS). Adjust the inlet pressure and calculate the new Z-factor until the LHS of Eq. (5.4) equals the RHS. That gives an inlet pressure of pipeline AD 1,200 psi with $Z = 0.89$.

Check the Reynolds number: at $(1{,}200 + 500)/2 = 850$ psi and 77°F, viscosity is 0.0126 cp. The calculated Reynolds number (by using Eq. (3.69)) is 1.16×10^7. That gives the $f_f = 0.0049$ (Eq. (3.57)). Therefore the previous assumption of 1.0×10^7 is close enough.

Another option to tackle this problem is to assume that at a short distance from destination D (such as 3,000 ft or less), the pressure drop is small (less than 70 psi in this case). So one can assume in this segment of pipeline, Z is constant and can be calculated under the outlet condition (that is 500 psi). Use Eq. (5.4) to calculate the pressure at 3,000 ft away from destination D. Continue to do so until point A is reached which is 52,800 ft (10 miles) away from D.

2. Use Eq. (5.4), with $p_1 = 1{,}240$, $p_2 = 1{,}200$ psi, $q = 80$ MMscf/d, and $L = 1{,}000$ ft. The pipeline BA diameter is calculated as 6 in. with $Z = 0.85$, $\mu = 0.0134$ cp, $N_{Re} = 1.1 \times 10^7$, and $f_f = 0.0049$.

3. Use Eq. (5.4), with q =50 MMscf/d, L = 800 ft, the calculated pipe CA outlet pressure is 960 psi with Z = 0.88, μ = 0.0128 cp, N_{Re} = 8.8 × 10^6, and f_f = 0.0049. A compressor to pressurize this gas stream to 1,200 psi, i.e., about 240 psi, is needed.

It is worth noting that the Fanning friction factor equals 0.0049 for all three cases, regardless of the differences in the Reynolds number. This is because at high turbulent flow, N_{Re} is a large number and $1/N_{Re}$ in Eq. (3.57) can be assumed to be zero. Therefore, the Fanning friction factor is only a function of the pipe relative roughness. This can be seen clearly from the Moody Diagram (1944), shown in Figure 5–4.

It is also worth noting that there are two "Moody diagrams" in the published literature and they all have the same vertical axis as "friction factor." But the friction factor value is different. The best way to distinguish them is to check the friction factor under laminar flow. If the friction factor equals $16/N_{Re}$, then this Moody diagram (Figure 5–4) gives the Fanning friction factor (f_f), and is the same as that calculated from Eq. (3.57). If the friction factor equals $64/N_{Re}$, then this Moody diagram gives the Darcy-Weisbach friction factor, and it has to be divided by 4 before using Eqs. (3.68 or 5.4) for calculations.

Example 5–2 Determining the number of compressor stations needed along a major pipeline

A 4,000-kilometer gas pipeline in Asia is 1,046 mm in diameter (X70 steel grade, wall thickness ranges from 14.6 to 26.2mm) with designed pressure of 10 MPa. It can deliver 12 to 17 Bcm/yr of natural gas. If the pressure cannot be lower than 1,000 psi, and the compressor discharge pressure is 2,000 psi, how many gas compressor stations will be needed? Assume the pipeline relative roughness is 0.0006 and the temperature is 100°F.

Solution

With the pipeline wall thickness equal to 20 mm, the pipeline diameter, D = (1,046 – 20)/25.4 = 40 in. Assume the inlet pressure of the pipeline equals the discharge pressure of the compressor, and the outlet pressure of the pipeline equals the suction pressure of the compressor at each station, as shown in Figure 5–5. Thus, p_1 = 2,000 psi,

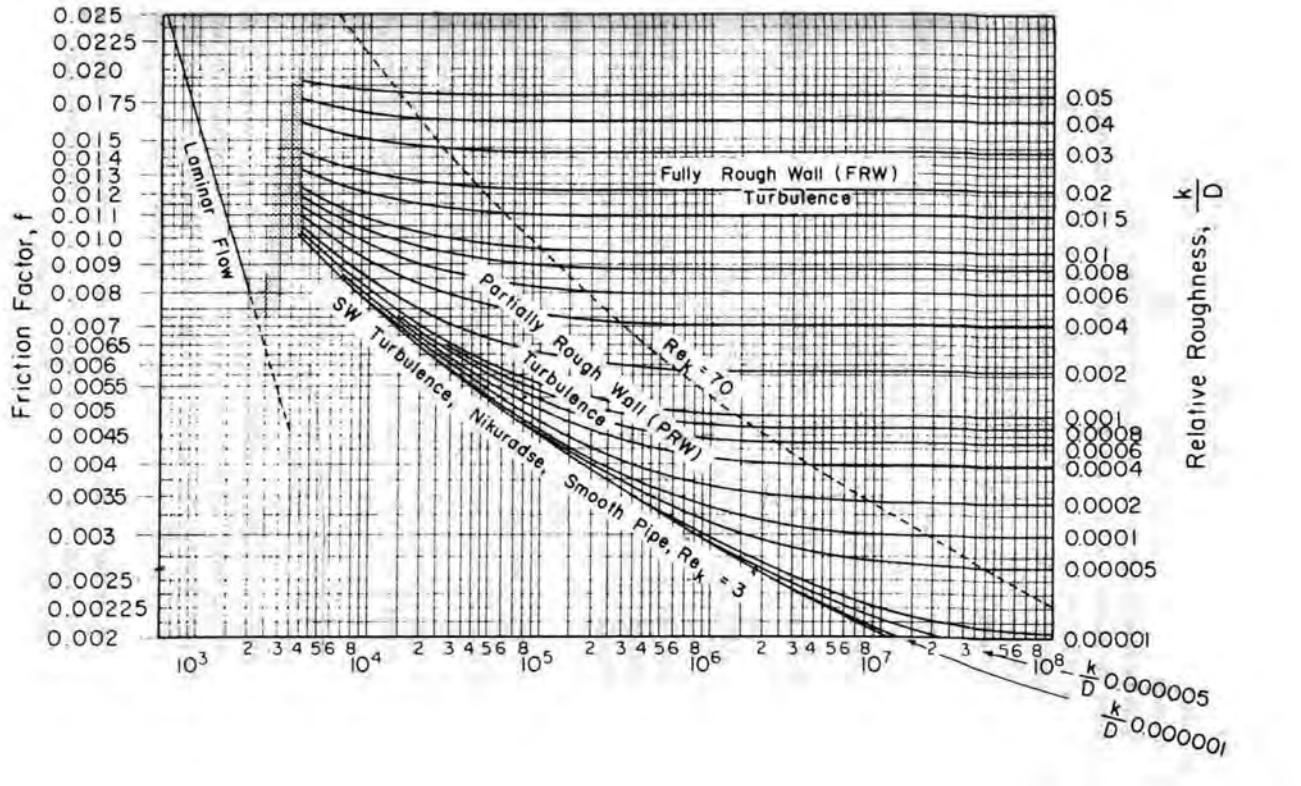

Figure 5–4 *Moody diagram* (Moody, 1944)

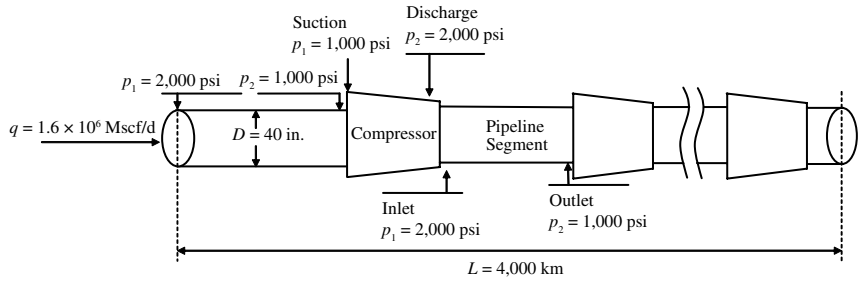

Figure 5–5 *Pipeline and compressor station for Example 5–2*

p_2 = 1,000 psi, from which Z = 0.86, μ = 0.0143 cp, N_{Re} = 3.14 × 10^7 (Eq. (3.69)), and f_f = 0.00435 (Eq. (3.57)).

The designed pipeline gas capacity, q = 16.5 × (1,000,000/365) × 35.31 = 1.6 × 10^6 Mscf/d, and by using Eq. (5.4), the pipeline segment between two compressor stations is calculated as L_1 = 1.0 × 10^6 ft = 310 km. The total length of the pipeline is L = 4,000 km, therefore, the number of compressor stations needed is 4,000/310 – 1 = 12.

5.2.2 Compression

Examples 5–1 and 5–2 clearly show that the pressure of natural gas flowing through a pipeline decreases along the distance because of friction pressure drop. Therefore, compressors are needed to ensure that the natural gas gets to the destination with sufficient pressure along the path and outlet.

According to the EIA (2007), along the interstate pipeline network, compressor stations are usually placed between 50 and 100 miles apart. Most compressor stations are unmanned, and are monitored by an electronic system that manages and coordinates the operations of several compressor stations. In a large-scale trunckline or a mainline, the average horsepower per compression station is about 14,000, and this can move about 700 MMcf/d of natural gas. Some of the largest stations can handle as much as 4.6 Bcf/day.

Two types of compressors are used: reciprocating and turbine engines. Most of them have natural gas-fired and high speed reciprocating engines. Both types of compressors are periodically retrofitted to cope with new emerging technologies, but most of the time, to increase efficiency and safety (EIA, 2007).

Besides compressors, there are other components in a compressor station. These include scrubbers and filters. Although gas is treated

before entering the transportation pipelines, liquid may still condense and accumulate in the pipelines during the transportation process, and particulates may form with the coating materials inside of the pipelines. Thus, liquids and solids have to be removed before entering compressors. Between the parallel or multistage compressors, interstage coolers are needed to cool down the heated gas due to pressurization, further reducing the needed horsepower (hp) of the compressor. The theoretical hp of the compressor required to compress a given amount of natural gas can be obtained from either the analytical solution or an enthalpy-entropy diagram. The enthalpy-entropy diagram approach can be found in Brown (1945). The analytical solution will be elaborated next.

Theoretical Horsepower

Horsepower (hp or HP) is the work done over a period of time. One hp equals 33,000 ft-lb/min, or 746 watts, or 75kg-m/s. It is commonly used in measuring the output of piston engines, turbines, electric motors, and other machinery. The theoretical hp of the compressor required to compress a given amount of natural gas can be calculated by assuming the system to be either isothermal ($\Delta T = 0$) or adiabatic/isentropic ($\Delta H = 0$). Of course, in reality, compression of a gas naturally increases its temperature, and there will always be some heat leaking out of the system.

When the system is assumed to be adiabatic, the calculated theoretical hp gives the maximum required hp while under the assumption of isothermal condition; the calculated theoretical value gives the minimum required hp. Therefore, the actual required hp to compress a given gas, shown in Figure 5–6, is between these upper and lower boundaries.

Assuming the change in kinetic energy, potential energy of position, and that the energy losses are negligible (Katz et al., 1959), the theoretical work required to compress natural gas becomes

$$W = \int_{p_1}^{p_2} V dp, \tag{5.5}$$

where p_1 and p_2 are the suction and discharge absolute pressures of the gas, respectively. Often a negative sign in front of the work (W) is to distinguish between compression and expansion.

For an ideal gas, if the compression process is isothermal, then

$$pV = nRT = \text{constant}. \tag{5.6}$$

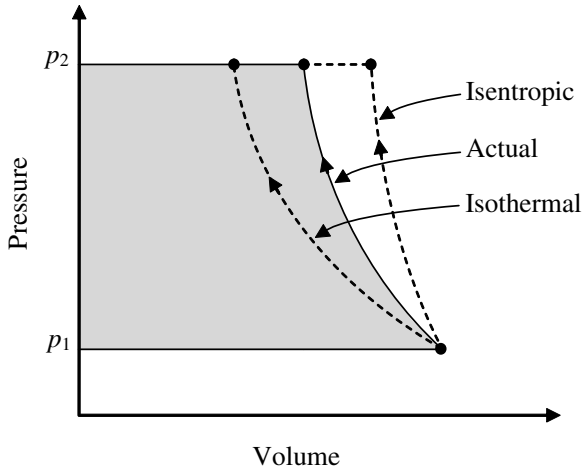

Figure 5–6 *Work needed to compress gas from p_1 to p_2*

Substituting Eq. (5.6) into Eq. (5.5) and integrating, gives the theoretical hp to compress 1 mole of ideal gas as

$$W = RT \ln(p_2 / p_1). \tag{5.7}$$

Similarly, if the compression process is under isentropic condition, then

$$pV^k = \text{constant}, \tag{5.8}$$

where k is evaluated under suction conditions and equals C_p/C_v, the ratio of the ideal-gas specific heats with C_p and C_v at constant pressure and volume, respectively. Thus, using Eq. (5.6) and Eq. (5.8) in Eq. (5.5), the theoretical hp to compress 1 mole ideal gas is (Joffe, 1951)

$$W = \frac{kRT_1}{k-1}[(\frac{p_2}{p_1})^{(k-1)/k} - 1], \tag{5.9}$$

where T_1 is the gas suction temperature in R.

Several efforts have been made to empirically modify the ideal gas behavior to reflect the real gas behavior, and further, to calculate the theoretical hp for real gas (Katz et al., 1959; Edmister and McGarry, 1949; Joffe, 1951). The theoretical work (W in hp) required to

compress q_g MMscf/d real gas at standard conditions (T_{sc} = 60°F, p_{sc} = 14.65 psia) is given as:

$$W = 0.08531 q_g T\left(\int_{0.2}^{p_{r,2}} \frac{Z}{p_r} dp_r - \int_{0.2}^{p_{r,1}} \frac{Z}{p_r} dp_r\right), \tag{5.10}$$

under isothermal conditions (Katz et al., 1959), and under isentropic conditions (Katz et al., 1959)

$$W = 0.08531 \frac{k}{k-1} q_g Z_1 T_1 \left[\left(\frac{p_2}{p_1}\right)^{(k-1)/k} - 1\right]. \tag{5.11}$$

The constant 0.08531 is a unit conversion factor.

Joffe's (1951) study indicated that the actual or polytropic compression process of a real gas should be assumed as

$$pV^n = \text{constant}, \tag{5.12}$$

where n is a constant to be determined from the actual behavior of the gas in the compressor. That gives another empirically modified equation as

$$W = 0.08531 \frac{n}{n-1} q_g Z_1 T_1 \left[\left(\frac{p_2}{p_1}\right)^{(n-1)/n} - 1\right]. \tag{5.13}$$

Replacing $n/(n-1)$ by $k/Z_1(k-1)$, Eq. (5.13) becomes

$$W = 0.08531 \frac{k}{k-1} q_g T_1 \left[\left(\frac{p_2}{p_1}\right)^{Z_1(k-1)/k} - 1\right]. \tag{5.14}$$

Some others (Economides et al., 1994) suggested a simplified empirical expression as

$$W = 2.23 \times 10^2 q_g \left[\left(\frac{p_2}{p_1}\right)^{0.2} - 1\right]. \tag{5.15}$$

The differences among these empirical solutions will be discussed further in Example 5–3.

Once the theoretical hp is obtained, the Brake horsepower (BHP), the actual or useful hp, which is added into the compressor, is then calculated as (Katz et al., 1959)

$$\text{BHP} = \frac{\text{Theoretical HP}}{\text{Efficiency } (E)}. \tag{5.16}$$

The efficiency, E, is the combination of the compression and mechanical efficiencies. It is a function of suction pressure, compression ratio, speed, the physical design of the compressor, and the mechanical condition of the compressor. It can be determined from published data or from vendors directly. In most modern compressors, the compression efficiency is between 83 and 93% while the mechanical efficiency is between 88 and 95%. These give the overall efficiency of 75 to 85% (Guo and Ghalambor, 2005).

The ratio of p_2/p_1 is called compression ratio (R_c). Since compression generates heat, this ratio is usually kept under six. In field practice, this ratio seldom exceeds four (Guo and Ghalambor, 2005) to ensure that the compressor performs at high efficiency. That is why, very often, the natural gas is compressed in stages. In that case, the overall compression ratio is

$$R_o = \left(\frac{p_f}{p_1}\right)^{1/n}, \tag{5.17}$$

where p_f is the final discharge pressure in psia and n is the number of stages.

Heat Removed by Interstage Cooler

According to the work done by Joffe (1951), the discharge temperature can be determined as

$$T_2 = \frac{Z_1}{Z_2} T_1 R_c^{Z_1(k-1)/k}, \tag{5.18}$$

with T_1 and T_2 in °F or R. This equation is not recommended when the discharge temperature of the gas is considerably above its critical temperature.

Once the discharge temperature T_2 is known, the heat removed by the interstage cooler can be calculated as

$$\Delta H = n_g \overline{C_p} \Delta T, \tag{5.19}$$

where n_g is the number of lb-moles of natural gas. $\overline{C_p}$ is the specific heat under constant operating pressure and average temperature of the interstage cooler.

Example 5–3 Calculate the required horsepower needed at each compressor station in Example 5–2. Use $k = 1.28$.

Solution

Given in Example 5–2, the suction and discharge pressures of gas are p_1 = 1,000 psi and p_2 = 2,000 psi. (Note: the pipeline inlet pressure = compressor discharge pressure and the pipeline outlet pressure = compressor suction pressure. See Figure 5–5.) Also T_1 = 100°F and $q = 1.6 \times 10^3$ MMscf/d. So, at suction conditions, Z_1 can be calculated as 0.89.

For the theoretical work needed to compress 1.6×10^3 MMscf/d natural gas from 1,000 to 2,000 psi, use Eq. (5.11),

$$\begin{aligned} W &= 0.08531 \times \frac{1.28}{1.28-1} 1.6 \times 10^3 \times 0.89 \\ &\quad \times (100+460) \times [(\frac{2{,}000}{1{,}000})^{(1.28-1)/1.28} - 1] \\ &= 51{,}189 \text{ hp.} \end{aligned}$$

Use Eq. (5.14),

$$\begin{aligned} W &= 0.08531 \times \frac{1.28}{1.28-1} 1.6 \times 10^3 \times 0.89 \\ &\quad \times (100+460) \times [(\frac{2{,}000}{1{,}000})^{0.89 \times (1.28-1)/1.28} - 1] \\ &= 50{,}773 \text{ hp.} \end{aligned}$$

Use Eq. (5.15),

$$W = 2.23 \times 10^2 \times 1.6 \times 10^6 \times [(\frac{2{,}000}{1{,}000})^{0.2} - 1] = 53{,}056 \text{ hp.}$$

Results show the empirical solution proposed by Economides et al. (1994) is higher and on the more conservative side.

5.3 Marine CNG Transportation[1]

CNG is natural gas compressed at pressures of 2,000 to 3,000 psi (130 to 200 atm) and sometimes chilled (but not liquefied) to temperatures down to –40°F (–40°C) for even higher reduction of its volume. It is a technology proven in many applications, including transport by ship, truck, and barge. It has been used to fuel taxis, private vehicles, and buses worldwide.

CNG transportation over sea requires specifically designed CNG ships, which are, in effect "floating pipelines". While at the time of this writing, there were at least six commercial concepts of marine transport of CNG, none had yet materialized, although there were several signs that the technology was to be deployed soon.

The required onshore facilities for loading and offloading from CNG transport, shown in Figure 5–7, consist of simple jetties or buoys which are minimal compared to LNG. The key differences between these two technologies are summarized in Table 5–1.

The first attempt towards commercial CNG transport by ship was made in the 1960s (Broeker, 1969). Columbia Gas' SIGALPHA (originally named *Liberty Ship*) completed cycles of loading, transport, offloading, and regasification of both CNG and MLG (medium condition liquefied gas) in cargo bottles. The capacity of the SIGALPHA was 820 Mscf of MLG and 1,300 Mscf of CNG. The American Bureau of Shipping (ABS) classified the SIGALPHA for service and the U.S. Coast Guard awarded SIGALPHA a certificate of compliance. The project was eventually aborted, because at that time, it was not economical to proceed as the price of natural gas was extremely low.

There have been three factors which have prevented CNG marine transport. First, most investment have been on LNG, for understandable reasons (see Figure 5–1). Second, the use of CNG was envisioned

1. Section contributed by Michael Nikolaou, based on concepts introduced by Nikolaou et al. (2009) and Nikolaou (2008).

(a). At Source

(b). At Destination

Figure 5–7 *Loading and offloading terminal for LNG and CNG* (XGAS website http://www.xgas.us)

to take market share away from LNG, which, as was explained above, is not necessarily a good approach, because CNG and LNG are suitable for different transportation scenarios (see Figure 5–1). Third, innovative low-cost and high-efficiency designs for CNG vessels have become available in the 2000s.

There are several areas (Figure 5–8) where population centers are separated from natural gas sources by 2,000 km (or 1,200 miles) or less across water. For each of these areas, there exist multiple scenarios for CNG distribution, in terms of number of vessels, vessel capacities, and itineraries. Identification of promising scenarios is necessary to determine project economics, and possibly guide future technological developments, particularly as new CNG vessel technologies become available (Stenning and Cran, 2000; Dunlop and White, 2003).

5.3.1 CNG Carriers

CNG technology is quite simple and can be easily brought into practical applications, assuming the economics are attractive. Creative

Table 5–1 Process and Cargo Differences between CNG and LNG *(Patel et al., 2008)*

	CNG	LNG
Fluid State	Gas	Liquid
Pressure	100–50 bar (1,450 – 3,600 psi)	1 bar (14.5 psi)
Temperature	30°C to –40°C (or 86 to –40°F)	–163°C (or –261°F)
Loading	Dehydrate, compress	Treat, liquefy, store
Terminals	Jetty or buoy	Jetty, or regas offshore
Ships	Simple, like bulk-carrier	Sophisticated, efficient
Receiving	Heat & decompress—untilize energy released	Store, regasify
Loading/Offloading	Gas under pressure	As liquid
Compression Ratio	~200–250:1	~600:1
Containment D/t	~25–60	~1,000
Material	Fine grain normalized C-Mn steel, FRP	Aluminum, stainless, Ni steel

Figure 5–8 *Regions actively investigating CNG projects* (Dunlop and White, 2003)

solutions have been proposed for the choice of materials (e.g., steel, composites), configuration of gas containers (e.g., vertical or horizontal cylinders, coiled pipe), and loading and offloading techniques. There is also flexibility in the choice of transport vessels, which can be ships or barges, depending on a number of factors, as shown in Table 5–2.

The new generation of CNG ships under consideration is optimized to transport large quantities of gas. Such ships can carry approximately one-third the amount of an LNG carrier of the same size. The economic attractiveness of CNG hinges on the far lower capital cost of required land facilities and the considerably lower operating costs compared to LNG. Several companies have developed CNG delivery systems. Some of them have already received approval by classification organizations and are ready for commercialization.

One CNG technology variant employs a high-pressure gas storage and transportation system based on a coil of relatively small diameter pipe (6 to 8 inches, about 15 to 20 cm) sitting in a steel-girder carousel (Figure 5–9). Considering natural gas compressed at 3,000 psi and at ambient temperature, a typical CNG carrier assembled with 108 carousels can offer up to 330 MMscf (about 10 MMscm) capacity.

Another CNG technology variant requires that the compressed gas is also cooled to temperatures generally below 0°F, to achieve a further reduction of the gas specific volume. This high-pressure gas storage and transportation system, is based on horizontal or vertical arrays of 36-meter (about 118 ft), long large diameter pipes (40 in, about 1 m), segregated, and manifolded into a common pressure and flow system in groups of 24, called modules. These modules are then arranged in holds, whose count determines the CNG carrier capacity. The largest model of such a vessel can offer up to 800 MMscf (about 22 MMscm) of capacity. One example of this type of containment is shown in Figure 5–10.

How does chilling help reduce the volume of CNG?

The relationship between volume, V, pressure, p, and temperature T, is given by the real gas law shown in Eq. (1.2), or rearranged as

$$V = \frac{ZnRT}{p}. \tag{5.20}$$

The volume taken by an amount of gas n, is proportional to ZT/p. Consequently, if gas pressure needs to be raised to a certain value, for gas volume to be reduced to a certain amount at ambient temperature, lowering the temperature (chilling) can reduce the compression

Table 5–2 CNG Sea Transport Vessels *(John Dunlop, Personal Communication, 2008)*

	Articulated Tug Barge	Ship
Volume	0.7–2 MMcm (25–75 MMscf)	8–29 MMcm (300–1,000 MMscf)
Loading/unloading rates	0.3–2 MMcm/day (10–75 MMscf/day)	2–14 MMcm/day (75–500 MMscf/day)
Distance	100–1,000 km (50–500 nautical miles)	250–5,000 km (135–2,700 nautical miles)
Speed	<25 km/hr (<14 knots)	<33 km/hr (<18 knots)
Estimated cost	$15–35 million	$150–350 million

Figure 5–9 *Schematic of a CNG vessel* (Courtesy Sea NG Corp., 2008)

requirement for the gas to occupy the same volume. At typical CNG pressure levels (2,000–3,000 psi), the *Z*-factor (calculated as discussed in the note below), may differ significantly from 1 when the temperature varies, as shown in Figure 5–11. Therefore, the *Z*-factor must also be taken into account in related calculations.

Figure 5–10 *Schematic of a CNG vessel* (Courtesy Enersea Transport LLC, 2008)

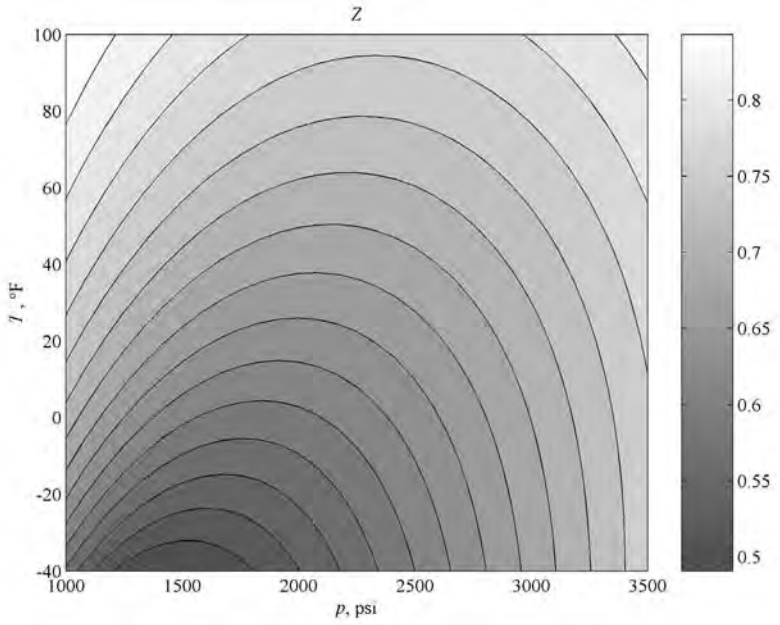

Figure 5–11 *Gas deviation factor Z as function of pressure and temperature for natural gas*

The value of ZT/p is shown in Figure 5–12, suggesting that mild chilling may have a significant effect on CNG volume. For example, as shown in Figure 5–12, the same amount stored at about 3,000 psi and 100°F can be stored at about 2,000 psi and 0°F. To what degree

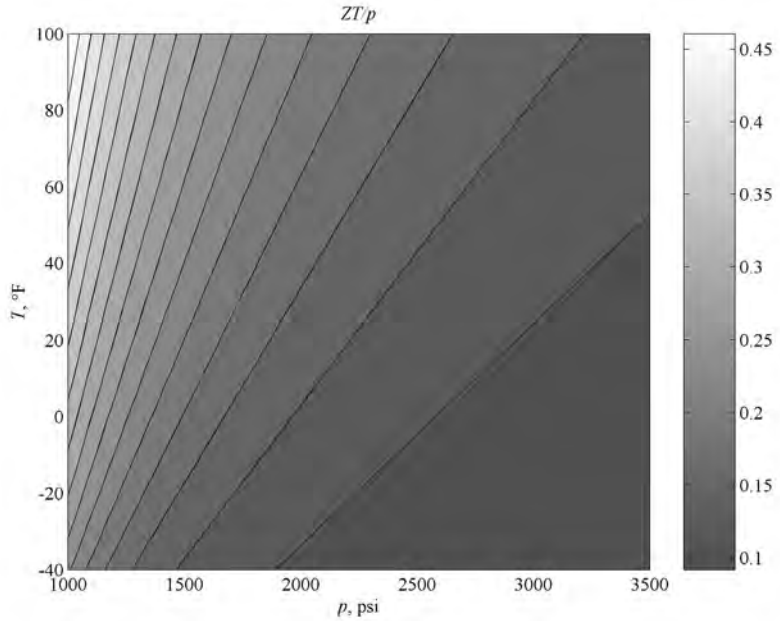

Figure 5–12 *Value of ZT/p as function of pressure and temperature for natural gas*

chilling is used to relax compression is ultimately determined by economics.

For the analysis presented here, it is assumed that ships are suitable for the weather conditions prevailing over sea transportation routes. A typical itinerary for a CNG vessel involves a cycle consisting of the following steps: gas loading at the source, transportation to delivery site(s), offloading, and returning to the source. The number and capacity of these ships, as well as related itineraries, will be the focus of the following analysis. Some economic issues will be discussed as well.

5.3.2 Optimizing Vessel Capacity and Itineraries in CNG Transportation

Optimization of the number of transportation vessels, capacity, and transportation itinerary ultimately depends on economics. However, an all-encompassing economic optimization, comprised of both fixed and operating costs, would be overly complicated and sensitive to a number of factors, such as natural gas price, transportation cost, and others. Even though such optimization is certainly feasible for a

particular project, the generation of merely an optimal solution would provide little insight into the general principles that guide the design of CNG transportation fleets and schedules. Therefore, the objective of this section is to present a physical optimization, namely optimization of the number of vessels required, capacity of each vessel, and itineraries followed.

The rationale for choosing this type of optimization is that the main capital expenditure (more than 80%) for CNG projects is for transportation vessels (as opposed to less than 40% for LNG projects). In the following analysis, simplified assumptions are made. That is, the natural gas has to be delivered to each receiving site at a constant rate throughout the year, without taking seasonal variation into account. An annual average rate is used for each receiving site, although the same analysis could be easily repeated for peak rates as well.

As explained in the following sections, the preferred path for CNG transportation vessels may follow "hub-and-spoke" or "milk-run" patterns depending on consumption rates at receiving sites. For sites with consumption rates high enough to justify using transportation vessels above a minimum reasonable size for each site, a hub-and-spoke pattern is preferred. Each vessel would serve as storage facility while offloading gas to consumption. If consumption is low, then vessels with size above a reasonable minimum will visit multiple sites and offload natural gas to local storage at each site (milk-run pattern). Storage capacity should be high enough for gas to last until the next vessel following the milk-run pattern would visit that site.

A potential mix of hub-and-spoke and milk-run schemes for CNG transportation from the Trinidad area to island countries in the Caribbean are shown in Figure 5–14 and Figure 5–15, respectively (Nikolaou et al., 2009).

Hub-and-Spoke CNG Distribution Pattern

To explain the basis for the hub-and-spoke pattern, assume for now that no storage facilities are available at the site of gas delivery. Rather, each transportation vessel from which gas is offloaded also serves as a floating storage facility during the offloading period. The offloading rate can be adjusted according to market demand. To ensure continuous delivery of gas to a market, at least one vessel must be offloading gas to consumption at any given time. (If the offloading rate cannot meet the consumption rate, multiple vessels will be offloading concurrently.) As soon as gas offloading is completed, a second vessel (already connected to the delivery line) must take over. After being disconnected from the delivery line, the empty first vessel will have to travel back to the nat-

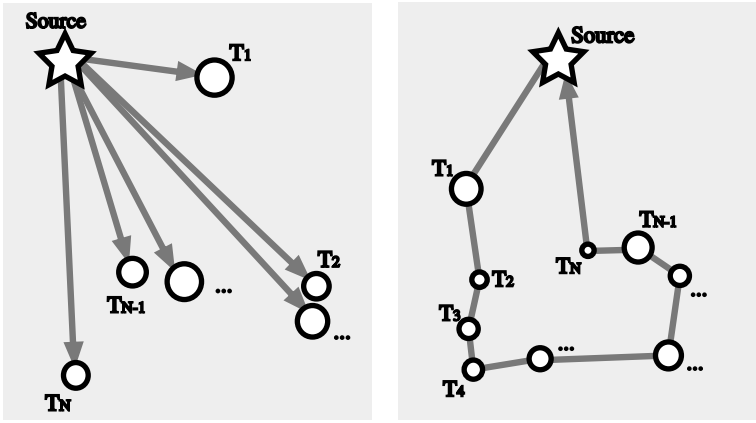

Figure 5–13 *"Hub-and-Spoke" (left) and "Milk-Run" (right) paths for CNG distribution to N receiving sites (terminals T_1,…, T_N)*

ural gas source, be loaded with gas, and return to the delivery point to resume as needed. This cycle can be repeated indefinitely to ensure uninterrupted gas delivery. Assuming that the offloading rate can meet the consumption rate and absence of any storage facility at the delivery site, a minimum of two vessels are required for uninterrupted delivery, as shown in Figure 5–16. After the first vessel offloads the entire amount of gas at the delivery site, it enters a travel-to-source/load/travel-to-sink cycle that involves the following steps:

1. Disconnect from the delivery line (black bar).
2. Travel to the source (white bar).
3. Connect to the loading line (black bar).
4. Load gas (gray bar).
5. Disconnect from the loading line (black bar).
6. Travel to the delivery site (white bar).
7. Connect to the delivery line (black bar) in anticipation of starting gas delivery.

While the first vessel is offloading, the second vessel completes the cycle (1) through (7) described above and is ready to start offloading. At the same time, the first vessel repeats the cycle (1) through (7).

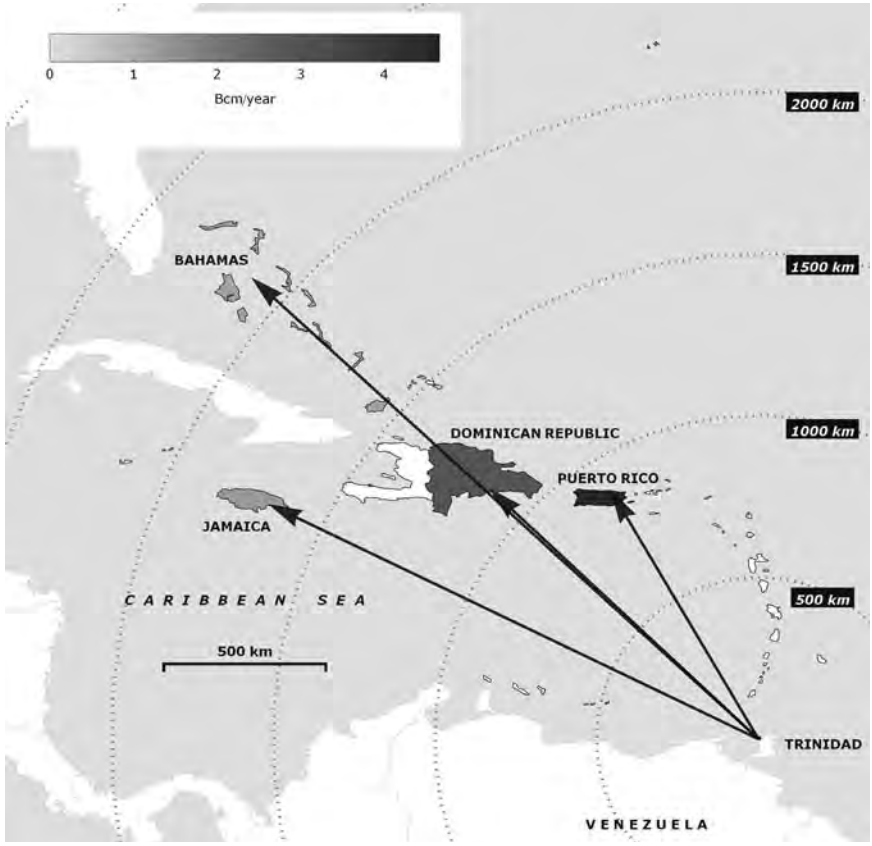

Figure 5–14 *Potential "Hub-and-Spoke" scheme for CNG distribution to island countries in the Caribbean Sea with large consumption of electricity* (Nikolaou et al., 2009)

It is clear that, for uninterrupted gas delivery, the diagram of Figure 5–16 can be extended to three or more vessels. For the case of three vessels, two vessels successively offload, while the third vessel completes the total cycle of the above steps (1) through (7) as shown in Figure 5–17. Extrapolation to n vessels is straightforward (Figure 5–18) under the assumption that the loading site can handle the itineraries of $n - 1$ vessels as they load. The key is to ensure that the next vessel in line is ready to start offloading after the previous one has completed offloading. To accomplish this, while one vessel is completing the cycle of the above steps (1) through (7), the remaining vessels successively offload their entire loads; and each one of them enters the cycle (1) through (7) after finishing offloading.

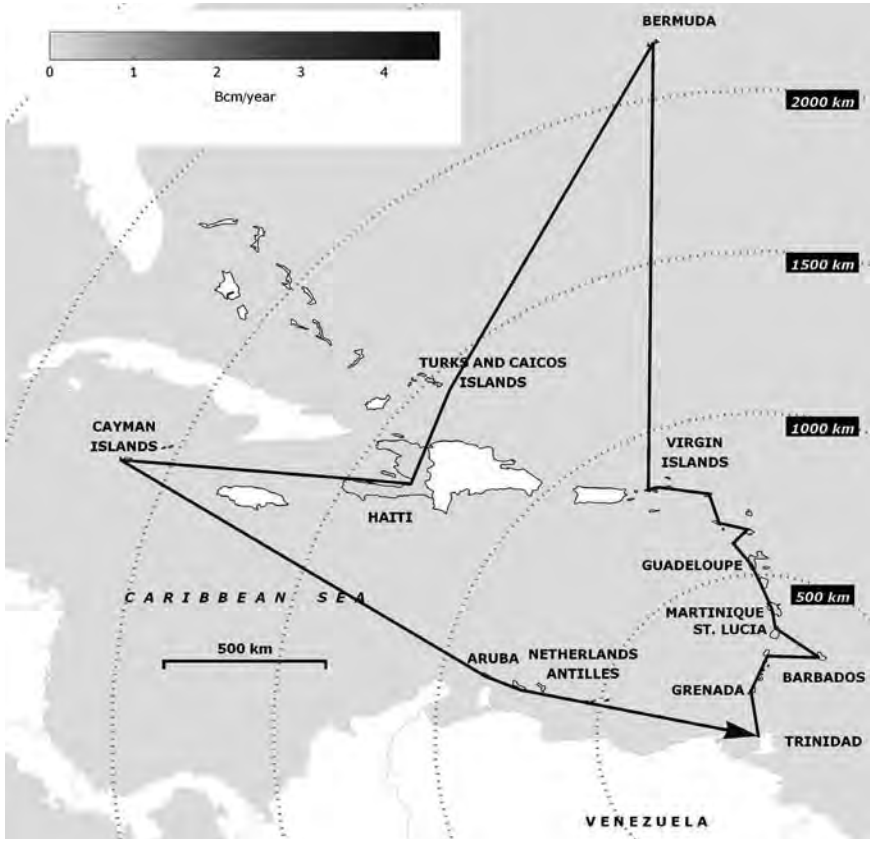

Figure 5–15 *Potential "Milk-Run" scheme for CNG distribution to island countries in the Caribbean Sea with small consumption of electricity* (Nikolaou et al., 2009)

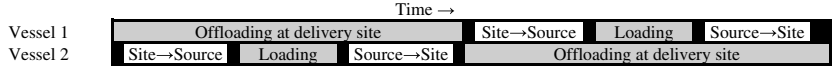

Figure 5–16 *Scheduling of gas delivery from a single source to a single delivery site using two CNG vessels*

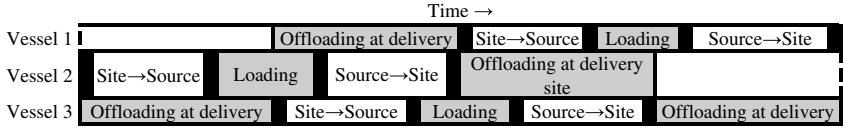

Figure 5–17 *Scheduling of gas delivery from a single source to a single delivery point using three CNG vessels*

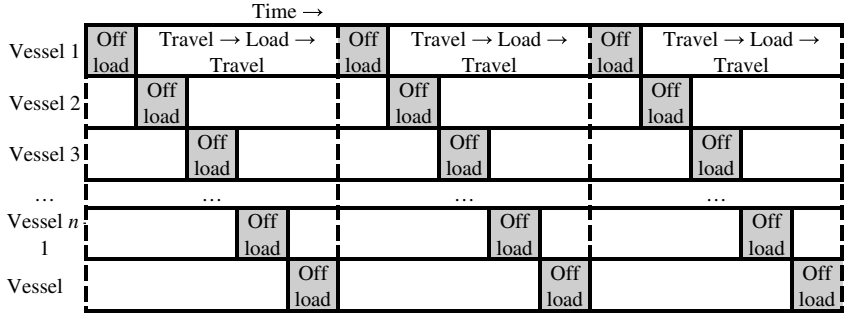

Figure 5–18 *Scheduling of gas delivery from a single source to a single delivery site using n CNG vessels*

The schedules shown in Figure 5–17, Figure 5–18, and Figure 5–19, determine the capacity required for each vessel in order to complete each schedule. Matching the time taken by a vessel to complete the cycle travel/load/travel (above steps (1) through (7)) to the time taken by the remaining $n - 1$ vessels to successively offload at a rate dictated by market demand, implies that the natural gas capacity (volume) of each vessel must be (Nikolaou et al., 2009)

$$G_n = \frac{4t_{connect} + 2\dfrac{L}{v}}{\dfrac{(n-1)(1-f)}{q_{offload}} - \dfrac{1}{q_{load}}}. \tag{5.21}$$

Eq. (5.21) implies that the total capacity G_{total} for a fleet of n vessels *per cycle* is

$$G_{total} = \frac{4t_{connect} + 2\dfrac{L}{v}}{\dfrac{(n-1)(1-f)}{q_{offload}} - \dfrac{1}{q_{load}}}. \tag{5.22}$$

Eq. (5.21) and Eq. (5.22) imply that the (theoretically) minimum total capacity for given $t_{connect}$, L, v, q_c, and q_{load} is

$$G_{total,min} = \frac{4t_{connect} + 2\dfrac{L}{v}}{1-f} q_{offload}, \tag{5.23}$$

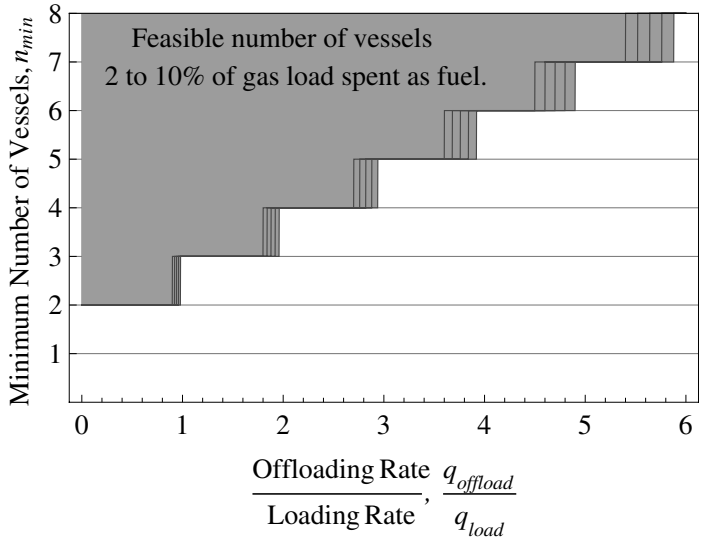

Figure 5–19 *Minimum number of vessels, n_{min}, required to implement a CNG delivery schedule corresponding to various ratios of consumptions rates over loading rates*

attained as $n \to \infty$. The above value for $G_{total,min}$ serves as an order of magnitude estimate only and would never be realized in practice. This is because it would correspond to an inordinately large number of vessels, each of tiny capacity (essentially an approximation of a "floating pipeline" by a series of discrete carriers). Nevertheless, it is interesting to visualize the trend of $G_{total,min}$ as a function of offloading rate, $q_{offload}$, and travel distance, L (Figure 5–19).

Since G_n must be positive, Eq. (5.21) implies a lower bound on the number of vessels, n, required to implement a schedule as

$$n \geq 1 + \frac{q_{offload}}{q_{load}(1-f)} \cdot \tag{5.24}$$

Eq. (5.24) provides the minimum number of vessels required to implement a CNG delivery schedule and it is the smallest integer, n_{min}, that is larger than or equal to

$$1 + \frac{q_c}{q_{load}(1-f)}$$

as shown in Figure 5–19. Here it is assumed that 2 to 10% of loaded gas is spent as fuel during transportation. Obviously, a number of vessels larger than n_{min} could be used, but that would be uneconomical.

Given that the cost of a CNG transportation fleet of n vessels is an increasing function of the total capacity of the fleet, Eq. (5.22) gives a trend of the investment needed to service a market, given a consumption rate, q_c, and distance from the source, L. The following trends emerge from Eq. (5.22):

1. For distances between gas source and delivery point of a few hundred kilometers and for sailing speed of about 25 km/hr (Table 5–2), the total travel time $2(L/v)$ dominates $4t_{connect}$ in Eq. (5.22), which implies that total fleet capacity is roughly proportional to CNG transportation distance as

$$G_{total} \approx \frac{2n\dfrac{L}{v}}{\dfrac{(n-1)(1-f)}{q_{offload}} - \dfrac{1}{q_{load}}} . \tag{5.25}$$

   This observation agrees with Figure 5–1, which indicates that CNG is preferable for relatively short distances (<2,000 km), because most of the capital investment for CNG projects is for transportation vessels.

2. Given a fleet of several vessels ($n >> 1$) and distance L between gas source and delivery point, the total fleet capacity becomes roughly proportional to CNG offloading rate, $q_{offload}$, as

$$G_{total,min} = \frac{4t_{connect} + 2\dfrac{L}{v}}{1-f} q_{offload} . \tag{5.26}$$

   This is also in agreement with an upper limit on the range of distances for CNG shown in Figure 5–1.

Example 5–4 Calculation of the fleet size for a given market by using Hub-and-spoke CNG transportation scheme

Natural gas must be delivered as CNG to a destination located 600 nautical miles away from a shipping point at a rate of 500 MMscf/d.

What CNG fleet should service this market? Assume that the maximum loading and offloading rate is 150 MMscf/d, the time needed to connect or disconnect to facilities is 1 hour, the sailing velocity is 14 knots, and that 4% of natural gas loaded is consumed as fuel.

Solution

Since the offloading rate cannot satisfy the consumption rate, multiple cycles of CNG vessels must be used. Given that q_c = 500 MMscf/d and $q_{offload,max}$ = 150 MMscf/d, there is a need for at least

$$q_c / q_{offload,max} = 500 / 150 = 3.3 , \tag{5.27}$$

or 4 cycles. Each cycle should deliver $q_{offload,max}$ = 500/4 = 125 MMscf/d. From Eq. (5.24), the smallest number of vessels needed for each cycle must be greater than or equal to

$$n \geq 1 + \frac{125}{150 \times (1 - 0.04)} = 1.87 , \tag{5.28}$$

i.e., greater than or equal to 2. Consequently, from Eq. (5.22), the capacity of the total fleet for all 4 cycles would be

$$G_{total,all\ cycles} = 4n \frac{4 \times 1(\text{hr}) + 2 \times \dfrac{600(\text{nm})}{14(\text{nm/hr})}}{\dfrac{(n\text{-}1)(1-0.04)}{125(\text{MMscf/d})} - \dfrac{1}{150(\text{MMscf/d})}} \frac{1(\text{d})}{24(\text{hr})} , \tag{5.29}$$

and from Eq. (5.21), the capacity of each vessel would be

$$G_n = \frac{4 \times 1(\text{hr}) + 2 \times \dfrac{600(\text{nm})}{14(\text{nm/hr})}}{\dfrac{(n\text{-}1)(1-0.04)}{125(\text{MMscf/d})} - \dfrac{1}{150(\text{MMscf/d})}} \frac{1(\text{d})}{24(\text{hr})} . \tag{5.30}$$

The above two equations can be used to visualize the dependence of the total fleet capacity and vessel capacity on the number of vessels, *n,* used per cycle, as shown in Figure 5–20.

From a scheduling viewpoint, it would be possible to service this market with 2 vessels per cycle (a total of 8 vessels for all 4 cycles); but that would require vessel sizes of about 3,689 MMscf each, which is clearly beyond constructability limits. However, using 3 vessels per cycle would reduce that requirement to vessel sizes of 430 MMscf each, which is clearly feasible (cf. Table 5–2). The total fleet size for 3 vessels per cycle would be $3 \times 4 \times 430$ = 5,160 MMscf.

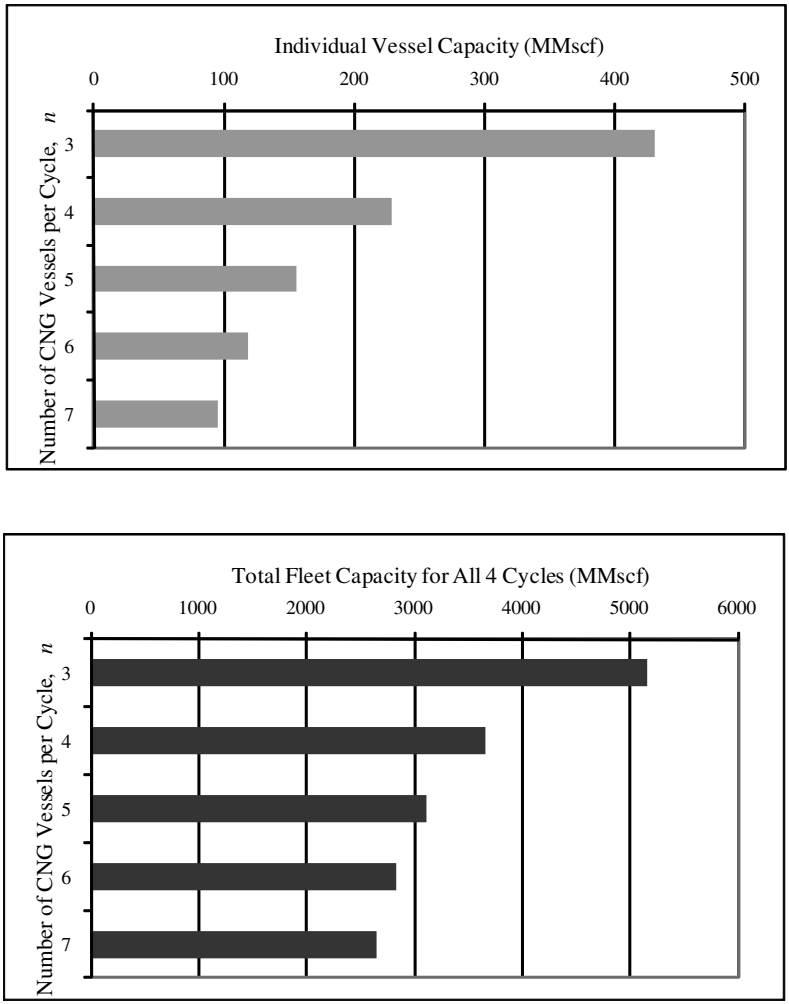

Figure 5–20 *Dependence of vessel capacity and total fleet capacity on the number of vessels, n, for Example 5–4*

Note that the total fleet capacity would be reduced significantly (by about 30%, from 5,160 to 3,653 MMscf) if 4 vessels per cycle were used, as can be visualized in Figure 5–20. Increasing the number of vessels even more would reduce the fleet size, but not significantly, and the theoretical lower limit, Eq. (5.26), would be quickly approached. Of course, operating costs would increase as the number of vessels increases, but given that the fixed cost for CNG (mainly ves-

sels) is quite high, there is an incentive to balance fixed and operating costs using medium size fleets and relatively *small* vessels.

This conclusion is arrived at by the quantitative analysis presented above, and is contrary to the wrong intuition that might opt for *large* vessels, hoping to realize economies of scale.

Example 5–5 Sensitivity evaluation of hub-and-spoke CNG transportation scheme

If the assumed consumption of 500 MMscf/d in Example 5–4 is an overestimate of the true consumption by 25%, what is the excess capacity built in a CNG fleet?

Solution

For a 25% overestimate of 500 MMscf/d, true consumption must be $q_c = 400$ MMscf/d. For this level of consumption and $q_{offload,max} =$ 150 MMscf/d, there is a need for at least

$$q_c / q_{offload,max} = 400 / 150 = 2.7 , \tag{5.31}$$

i.e. 3 cycles. Each cycle should deliver $q_{offload,max} = 400/3 = 133$ MMscf/d. Using Eq. (5.24), the smallest number of vessels needed for each cycle must be greater than or equal to

$$n \geq 1 + \frac{133}{150 \times (1 - 0.04)} = 1.92 , \tag{5.32}$$

or greater than or equal to 2. Consequently, using Eq. (5.22), the capacity of the total fleet for all 3 cycles, would be

$$G_{total,all\ cycles} = 3n \frac{4 \times 1(\text{hr}) + 2 \times \dfrac{600(\text{nm})}{14(\text{nm/hr})}}{\dfrac{(n-1)(1-0.04)}{133(\text{MMscf/d})} - \dfrac{1}{150(\text{MMscf/d})}} \frac{1(\text{d})}{24(\text{hr})} , \tag{5.33}$$

and from Eq. (5.21), the capacity of each vessel, would be

$$G_n = \frac{4 \times 1(\text{hr}) + 2 \times \dfrac{600(\text{nm})}{14(\text{nm/hr})}}{\dfrac{(n-1)(1-0.04)}{133(\text{MMscf/d})} - \dfrac{1}{150(\text{MMscf/d})}} \frac{1(\text{d})}{24(\text{hr})} . \tag{5.34}$$

The above two equations can be used to visualize the dependence of the total fleet capacity and vessel capacity on the number of vessels, n, used per cycle, and are presented in Figure 5–21. Compared to the results in Example 5–4, shown in Figure 5–20, there is a clear reduction (by 25% of the reduced values) in the total fleet volume that would be required to service consumption at the actual (lower) capacity. However, the vessel sizes required are approximately the same.

These results suggest that servicing a consumption market with CNG using a hub-and-spoke scheme is flexible, in that a fleet may be built and subsequently augmented with similar vessels if demand increases, without excessive capital costs.

Milk-Run CNG Distribution Pattern

A Milk-run pattern is shown in Figure 5–13. Consider N natural gas receiving sites (terminals $T_1,\ldots,T_N$), each consuming gas at a rate $q_{c,i}$, $i = 1,\ldots,N$. Gas is to be provided to each of these points successively by n CNG vessels, each of capacity (volume) V_n. Each vessel will deliver a gas load $G_{load,i,}$ $i = 1,\ldots,N$ to each receiving site per visit. Each receiving site has local gas storage capacity $G_{storage,i}$, $i = 1,\ldots,N$. All vessels can *load* and *offload* gas at a rate $q_{load} >> q_{c,i}$ and travel at speed v.

A gas delivery schedule for each vessel involves gas loading at the source, travel, offloading to each destination T_i, $i = 1,\ldots,N$ successively, and return to the source, to repeat the cycle, as shown in Figure 5–22. The cyclical route, shown in Figure 5–13, is the minimum closed path from the source through the delivery points and back. While finding this minimum path through numerical optimization is a challenging problem for large values of N, it is not difficult for small values of N (order of 10). Probabilistic methods, such as simulated annealing or genetic algorithms can be used.

The gas delivery schedule must be such that each gas receiving site $T_1,\ldots T_N$ is visited by a vessel on time, gets a corresponding gas load offloaded (while passing a fraction of that load to the market for consumption), and has enough gas left in storage to last until the next vessel arrives. Figure 5–22 indicates that n similar vessels visit each of the N receiving sites successively and deliver gas, a fraction of which is stored in order to last until the next vessels in the cycle starts delivery. Here the narrow black bars indicate the time needed to connect or disconnect a vessel to a station.

From the analysis done by Nikolaou (2008), the capacity of each vessel, G_n, in a fleet of n similar vessels is

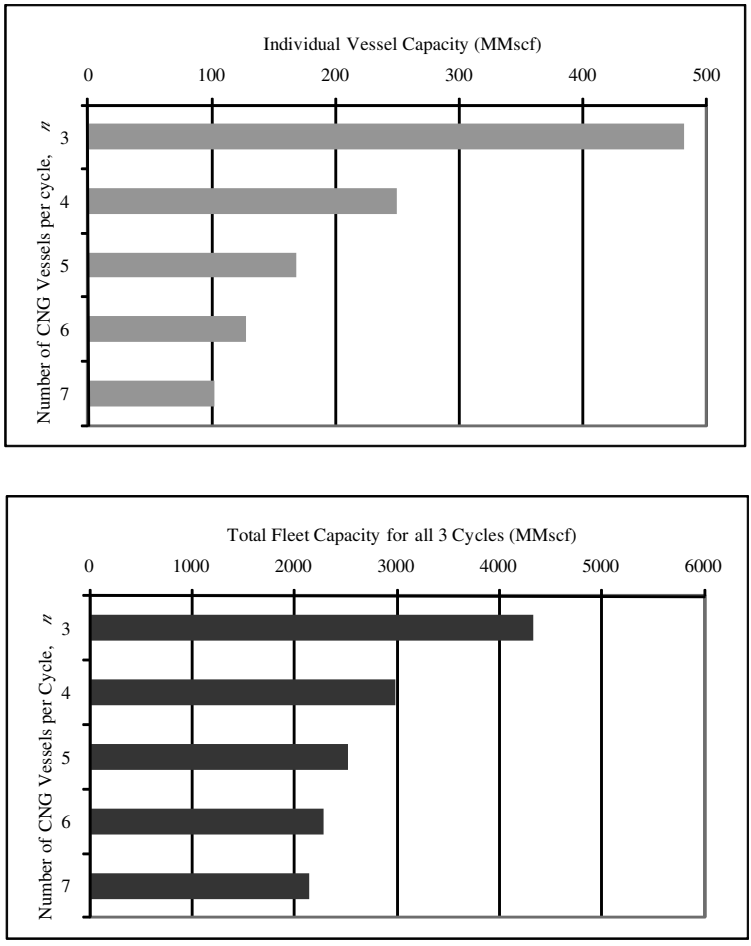

Figure 5–21 *Dependence of vessel capacity and total fleet capacity on the number of vessels, n, for Example 5–5*

$$G_n = \frac{(N+1)2t_{connect} + t_{travel}}{(1-f)\left(\dfrac{n}{q_{c,1} + \ldots + q_{c,n}} - \dfrac{2}{q_{load}}\right)}, \tag{5.35}$$

the total capacity of the fleet is

$$G_{total,n} = nG_n = \frac{(N+1)2t_{connect} + t_{travel}}{(1-f)\left(\dfrac{1}{q_{c,1} + \ldots + q_{c,N}} - \dfrac{2}{nq_{load}}\right)}, \tag{5.36}$$

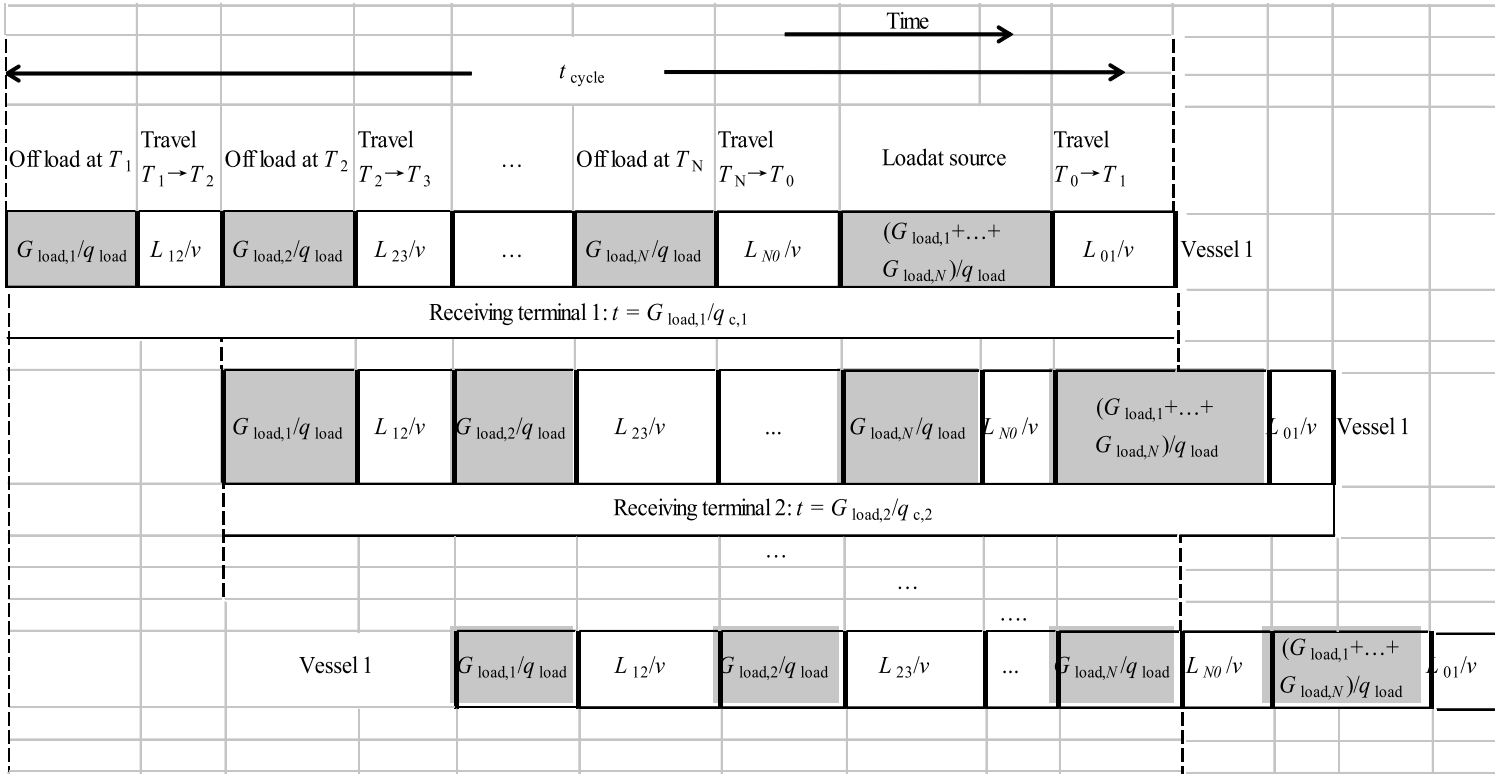

Figure 5–22 *Schedule development for CNG distribution by n similar vessels to N receiving sites serviced successively on a cyclical path as shown in Figure 5–13*

the cycle time for a vessel is

$$t_{cycle} = \frac{(N+1)2t_{connect} + t_{travel}}{1 - 2\dfrac{q_{c,1} + \ldots + q_{c,N}}{nq_{load}}}, \tag{5.37}$$

the amount of gas to be delivered to each receiving site per visit is

$$G_{load,k} = \frac{(N+1)2t_{connect} + t_{travel}}{n - 2\dfrac{q_{c,1} + \ldots + q_{c,N}}{nq_{load}}} q_{c,k}, \tag{5.38}$$

and the amount of gas to be stored at each receiving site is

$$G_{storage,k} = G_{load,k} - q_{c,k}\frac{G_{load,k}}{q_{load}} = \frac{(N+1)2t_{connect} + t_{travel}}{n - 2\dfrac{q_{c,1} + \ldots + q_{c,N}}{q_{load}}} q_{c,k}(1 - \frac{q_{c,k}}{q_{load}}) \cdot \tag{5.39}$$

Eq. (5.35) and Eq. (5.36) suggest that the required capacity of a vessel or a fleet is influenced primarily by points in the delivery path, along with the distances from each other, contributing to the term *L/v*. In fact, the effect of including or excluding a destination from the service plan depends more on the additional travel time, rather than the additional amount of gas this destination requires.

Eq. (5.36) implies that for very large fleets ($n \to \infty$), i.e., approximation of a pipeline by a fleet, the total fleet capacity is

$$G_{total,\infty} = \lim_{n\to\infty} nG_n = \frac{((N+1)2t_{connect} + t_{travel})(q_{c,1} + \ldots + q_{c,N})}{1 - f}, \tag{5.40}$$

and the total cycle time is

$$\lim_{n\to\infty} t_{cycle} = (N+1)2t_{connect} + t_{travel}, \tag{5.41}$$

as expected.

Since the capacity V_n of a vessel must be positive, Eq. (5.35) implies that for a given maximum loading/offloading rate q_{load} and

given total consumption rate $q_{c,1}$ +…+ $q_{c,N}$, the number of vessels, n, is bounded as

$$n > \frac{2(q_{c,1} + \ldots + q_{c,N})}{q_{load}} \cdot \tag{5.42}$$

Example 5–6 Optimization of milk-run CNG transportation scheme for a given market

Natural gas must be delivered as CNG to three destinations with corresponding consumption rates $q_{c,1}$ = 18, $q_{c,2}$ = 13, and $q_{c,3}$ = 5 MMscf/d. The minimum milk-run path to these destinations is shown in Figure 5–23. Assume a maximum loading rate q_{load} = 150 MMscf/d, sailing speed v = 14 knots (nm/hr), and 4% of CNG is spent as fuel.

Application of Eq. (5.29) for the first destination yields

$$G_n = \frac{4 \times 1(\text{hr}) + 2 \times \dfrac{120(\text{nm})}{14(\text{nm/hr})}}{\dfrac{(n-1)(1-0.04)}{18(\text{MMscf/d})} - \dfrac{1}{150(\text{MMscf/d})}} \frac{1(\text{d})}{24(\text{hr})}, \tag{5.43}$$

which yields a vessel capacity G_2 = 18.7MMscf, if two vessels are used in a single cycle. Vessel capacity would be even smaller if more vessels were used (n > 2). Calculations for vessel capacities for the other two destinations give G_1 = 24.6 and G_3 = 14.4 MMscf. Such capacities would be below the smallest practical capacity of a CNG ship or even a barge (see Table 5–2). Therefore, a milk-run scheme must be considered.

Application of Eqs. (5.35 to 5.42) yields the results seen in Table 5–3.

The three consumption markets can be serviced by a single vessel (n = 1) completing the milk-run cycle in 5.2 days. Significant local storage has to be provided in this case. Increasing the number of vessels decreases the fleet size, $G_{total,n}$, as well as the required storage $G_{storage,1}$, $G_{storage,2}$, and $G_{storage,3}$. However, using five vessels or more would require vessels (barges) that would be far too small to be practical. Therefore, a balance between fixed and operating costs would be found using from one to four vessels (barges).

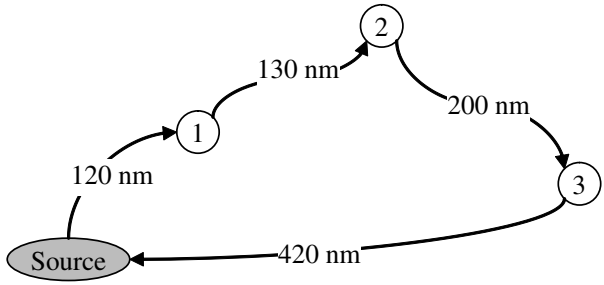

Figure 5–23 *Destinations for CNG delivery using Milk-Run scheme*

Table 5–3 Results from Example 5–6

n	G_n (MMscf)	$G_{total,\,n}$ (MMscf)	t_{cycle} (days)	$G_{load,1}$ (MMscf)	$G_{load,2}$ (MMscf)	$G_{load,3}$ (MMscf)	$G_{storage,1}$ (MMscf)	$G_{storage,2}$ (MMscf)	$G_{storage,3}$ (MMscf)
1	193.6	193.6	5.2	92.9	67.1	25.8	81.8	61.3	25
2	66.2	132.5	3.5	31.8	23	8.8	28	21	8.5
3	39.9	119.8	3.2	19.2	13.8	5.3	16.9	12.6	5.1
4	28.6	114.4	3.1	13.7	9.9	3.8	12.1	9.1	3.7
5	22.3	111.4	3	10.7	7.7	3	9.4	7.1	2.9

5.4 References

Brown, G.G. 1945. A series of enthalpy-entropy charts for natural gases. *Trans. AIME* 160: 65. Also published in *Petrol. Eng.* 1945. 16: 215.

Broeker, R.J. 1969. CNG & MLG-new natural gas transportation processes. *American Gas Journal* (July).

Dunlop, J P. and C.N. White. 2003. CNG Transport Technology is Delivering on Promises. *SPE* 84254.

Economides, M.J., A.D. Hill, and C.A. Ehlig-Economides. 1994. *Petroleum Production Systems*. New York: Prentice Hall.

Edmister, W.C. and R.J. McGarry. 1949. Gas Compressor Design. *Chem. Eng. Progress* 45: 421.

EIA. 2007. Natural gas compressor stations on the interstate pipeline network: Development since 1996. EIA, Office of Oil and Gas.

EIA. 2008. Natural gas pipeline: Transporting natural gas in the United States.

Guo, B. and A. Ghalambor. 2005. *Natural Gas Engineering Handbook*. Houston, TX: Gulf Publishing Company.

Joffe, J. 1951. Gas compressors. *Chem. Eng. Prog* 47: 80.

Katz, D.L., D. Cornell, R. Kobayashi, F.H. Poettmann, J.A. Vary, J.R. Ellenbaas, and C.F. Weinang. 1959. *Handbook of Natural Gas Engineering*. New York: McGraw-Hill.

Marongiu-Porcu, M., X. Wang, and M.J. Economides. 2008. The economics of compressed natural gas sea transport. Paper SPE 115310.

Moody, L. F. 1944. Friction factors for pipe flow. *Trans. ASME* 66: 67.

Nikolaou, M. 2008. Estimates on fleet, land storage facilities, and delivery schedules required for CNG distribution. Internal Report, XGas, Houston, TX.

Nikolaou, M., M.J. Economides, X. Wang, and M. Marongiu-Porcu. 2009. Distributed compressed natural gas sea transport. Paper OTC 19738.

Patel, H.N., P. Rynn, and G. Magadi. 2008. Compressed natural gas carrier (CNG) technology overview and regulatory update. ABS Technical Seminar: Current Technologies in Gas Carriers.

Speight, J.G. 2007. *Natural Gas: A Basic Handbook*. Houston, TX: Gulf Publishing Company.

Stenning, D.G. and J.A. Cran. 2008. Coselle CNG: Economics and opportunities. *Gastech* (November).

Wang, X. and M. Marongiu-Porcu. 2008. The potential of compressed natural gas transport in Asia. Paper IPTC 12078.

Wood, D., S. Mokhatab, and M.J. Economides. 2008. Technology options for securing markets for remote gas. Proceeding of the 87th Annual Convention, GPA.

CHAPTER 6

Liquefied Natural Gas (LNG)

6.1 Introduction[1]

Most natural gas is transported from the wellhead to a processing plant, and thereafter, to consumers in high pressure gas transmission pipelines. We dealt with this in Chapter 5. At remote locations, separated by large bodies of water from the market, liquefying the natural gas for transport has been a major industrial operation for decades and is likely to increase further. The much lower physical volume of liquefied natural gas (LNG) relative to gaseous natural gas can reduce transportation costs by allowing delivery using cargo ships or transport trucks instead of pipelines (Hudson et al., 2003). The properties of LNG (one volume unit of LNG yields 600 units of standard gas volume) allow for its long distance transport by ships across oceans to markets and for its local distribution by truck onshore. Occasionally, liquefaction of natural gas also provides the opportunity to store the fuel for use during high consumption periods close to demand centers, as well as in areas where geologic conditions are not suitable for developing underground storage facilities (which will be discussed in Chapter 8). The refrigeration and liquefaction process is the key element of an LNG project, and for most estimates it can consume about 35% of the capital expenditure, and up to 50% of the subsequent operating costs. There are several different licensed processes available with varying degrees of application and experience. In this chapter, processes are identified with their trade names and the

1. General information on LNG processes was published in Mokhatab, S, and Economides, M.J.: "Onshore LNG Production Process Selection," Paper SPE 102160, 2006.

companies that have introduced them, and are widely known in the industry; however, the analysis is strictly technical and no preference to any is given. In fact, the appropriate process selection is a complicated result of local conditions, feed makeup, and especially, the size of the LNG plant.

From the late 1990s, there has been a clear trend towards larger capacity liquefaction plants. LNG "trains" are designed for capacities up to 8 million tons per annum (MTPA) equivalent to about 1.2 Bcf/d. (Note: one metric ton of LNG contains 54.6 Mscf of gas, thus one MTPA contains 5.46×10^7 Mscf/yr or 1.5×10^5 Mscf/d or 0.15 Bcf/d.)

6.2 The LNG Process

An example of a LNG plant overall flow diagram and the main process units are shown in Figure 6–1. Typically, the feed gas is delivered at high pressure (for example, up to 1,300 psi) from upstream gas fields via trunklines and any associated condensate will be removed. The gas is metered and is pressure controlled to the design operating pressure of the plant. The gas is first pretreated (as discussed in Chapter 4) to remove any impurities that interfere with processing or are undesirable in the final products. These include nonhydrocarbon gases and water. Heavier hydrocarbons are also removed from the dry sweet natural gas using high level refrigerant to provide the cooling needed to condense the liquids, and the residual gas is then liquefied using high level and low level refrigerant. The remaining gas is made up mainly of methane and contains less than 0.1 mol% of pentane and heavier hydrocarbons. It is further cooled in the cryogenic section to approximately –160°C and is completely liquefied. Mildly pressurized LNG is further subcooled in one or more stages to facilitate storage at pressures slightly above atmospheric. Flashed vapors and boil off gas are recycled within the process (Qualls et al., 2005).

LNG is returned to a gaseous state in a regasification facility at a receiving terminal. The quality specification of the resulting gas is set by pipeline transmission companies and end users, and the gas is distributed by conventional gas pipelines. Most LNG contracts specify a range of acceptable heating values for the LNG sold into a particular market. In most cases, this requires that a certain fraction of the heavier hydrocarbon components found in the natural gas be removed prior to liquefaction, so that the LNG does not exceed the upper limit on heating value. Some natural gases also require removal of the heavy ends to prevent operating problems in the liquefaction cycle, such as freezing of aromatic hydrocarbons at low temperatures (Hudson et al., 2003).

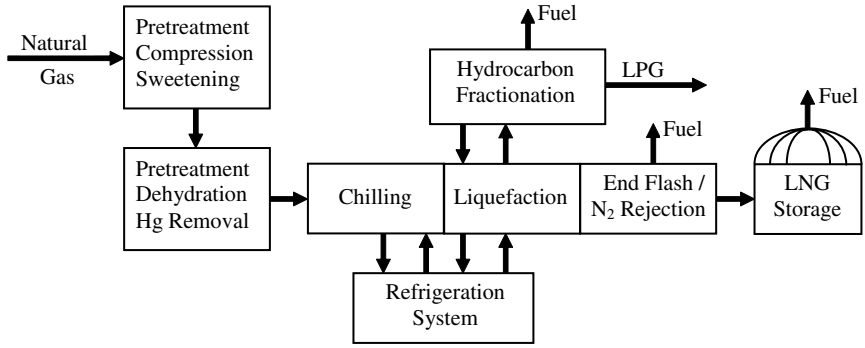

Figure 6–1 *Typical LNG plant block flow diagram* (Barclay, 2005)

Table 6–1 Typical LNG Compositions at Different Terminal Locations *(Yang et al., 2003)*

Component, mole%	Das Island, Abu Dhabi	Whitnell Bay, Australia	Bintulu, Malaysia	Arun, Indonesia	Lumut, Brunei	Bontang, Indonesia	Ras Laffan, Qatar (Ras Gas)
Methane	87.10	87.80	91.20	89.20	89.40	90.60	89.60
Ethane	11.40	8.30	4.28	8.58	6.30	6.00	6.25
Propane	1.27	2.98	2.87	1.67	2.80	2.48	2.19
Butane	0.141	0.875	1.36	0.511	1.30	0.82	1.07
Pentane	0.001	—	0.01	0.02	—	0.01	0.04

Table 6–1 shows typical LNG compositions at different well known terminals. If an LNG terminal requires C_2 or C_3 for fuel, it will need to process LNG with a component extraction unit. Although these additional facilities increase capital costs, they can create an opportunity for competitive pricing because the plant can meet export specifications, while feeding LNG from many different suppliers. LNG buyers have different requirements; therefore, reducing C_2 and C_3 at the baseload LNG plant is not always indicated or done because of: (1) less LNG produced, (2) additional compression equipment required, and (3) the desire to operate all LNG trains at the same conditions, using different source gas (Yang et al., 2003).

The composition of the liquid stream from the liquids recovery section can be matched to the circumstances of a particular LNG project by selecting the appropriate processing scheme. In locations

that have a market for ethane, an ethane product can be produced from the liquids recovery section to feed ethylene plants, etc. If there is no market for ethane, an LPG (Liquefied Petroleum Gas) product can be produced instead to supply the local chemical, heating, or fuels markets. Or, if the only need is to control the heating value of the LNG, a condensate product for the local liquid fuels market can be produced. Also, for locations where future development may create a market for lighter liquids, or where demand for products fluctuates, processes suitable for variable liquid coproduct production can be selected. In all cases, the liquid product is controlled to meet the appropriate specification for hydrocarbon liquid streams (Hudson et al., 2003).

6.3 LNG Liquefaction

The liquefaction process is the key element of the LNG plant. Liquefaction is based on a refrigeration cycle, where a refrigerant by means of successive expansion and compression, transports heat from the process side to where the natural gas is. LNG plants often consist of a number of parallel units, called trains, which treat and liquefy natural gas and then send the LNG to several storage tanks. The capacity of a liquefaction train is primarily determined by the liquefaction process, the refrigerant used, the largest available size of the compressor/driver combination that drives the cycle, and the heat exchangers that cool the natural gas (Smaal, 2003).

The basic principles for cooling and liquefying the gas using refrigerants, involve matching as closely as possible the cooling/heating curves of the process gas and the refrigerant. These principles result in a more efficient thermodynamic process, requiring less power per unit of LNG produced, and they apply to all liquefaction processes. Typical cooling curves are shown in Figure 6–2. Observing the cooling curve of a typical gas liquefaction process, three zones can be noted in the process of the gas being liquefied. A precooling zone, followed by a liquefaction zone, and completed by a subcooling zone. All of these zones are characterized by having different curve slopes, or specific heats, along the process. All of the LNG processes are designed to closely approach the cooling curve of the gas being liquefied, by using specially mixed multicomponent refrigerants that will match the cooling curve at the different zones/stages of the liquefaction process, to achieve high refrigeration efficiency, and reduce energy consumption.

The liquefaction process typically accounts for almost 45% of the capital cost of the overall LNG plant (Knott, 2001), which in turn

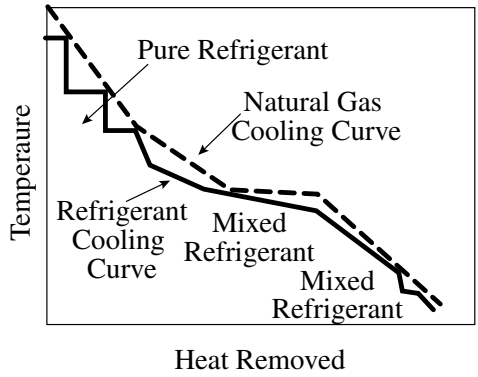

Figure 6–2 *Typical natural gas/refrigerant cooling curves* (Mokhatab and Economides, 2006)

accounts for 25% to 35% of total project costs, when including the regasification facility and the dedicated vessels for transport. Key equipment items include the compressors, used to circulate the refrigerants, the compressor drivers, and the heat exchangers, used to cool and liquefy the gas, and exchange heat between refrigerants. For recent baseload LNG plants, this equipment is among the biggest of its type, and at the leading edge of technology (Shukri, 2004).

Since LNG liquefaction requires a significant amount of refrigeration, the refrigeration system represents a large portion of a LNG facility. A number of liquefaction processes have been developed with the differences mainly residing on the type of refrigeration cycles employed. The most commonly utilized LNG technologies are described below, starting in Section 6.3.2 "Propane Precooled Mixed Refrigerant (PPMR™)/C3 MR Process". There are other processes developed or in development for baseload LNG applications, which can be, or are being, considered in feasibility studies or for future projects, but are not discussed here.

As with most process designs, there is a tradeoff between efficiency and capital cost. In addition, considerations such as ease of start-up, ability to handle feedstock composition changes, and maintenance costs play a role. Below the thermodynamic efficiency of LNG processes is explored.

6.3.1 Thermodynamic Analysis of LNG Processes

In the simplest sense, liquefaction of natural gas could be accomplished in a single stage cooler/condenser. Since natural gas contains a mixture of gases, in a real process and as mentioned earlier, the

NGL's are removed and can be marketed or used separately. Any non-condensable gases, such as N_2 and $H_{2,}$ as well as any CO_2, H_2S, and water vapor present are also removed. These processes were described in detail in Chapter 4.

For the sake of simplicity, in the analysis below, "natural gas" is assumed to be pure methane. A narrative example is used here under realistic conditions to demonstrate important thermodynamic and heat transfer issues. The results can be scaled up or down depending on the size of the natural gas stream to be liquefied. Metric units are used because almost all of the published chemical engineering literature is now in these units.

The raw feed will be taken as 25°C and 40 bar, and the product LNG (liquid methane) at 4 bar and −150°C. It is important, when comparing performance indicators, to note particularly the inlet and outlet specifications. For sizing purposes, one 8-MTPA process in two parallel 4-MTPA trains is considered.

There are two process modes which can be considered for liquefaction. In self liquefaction, cooling is accomplished by compressing the process stream (methane), cooling it to near ambient conditions, then flashing it across a throttling valve to achieve partial liquefaction. Alternatively, using process stream, methane can simply be cooled in a condenser using refrigerants to produce liquid methane.

Ideal Cooling Process

For an ideal cooling process, the cooling load can be written as a basic material and energy balance,

$$Q_{cool} = m_{out}h_{out} - m_{in}h_{in} \ . \tag{6.1}$$

Since mass in equals mass out, the terms m_{in} and m_{out} can be replaced with m, and Eq. (6.1) can be rewritten as

$$\hat{Q}_{cool} = \frac{Q_{cool}}{m}, \tag{6.2}$$

where $\hat{Q}$ is heat per unit mass, kJ/kg.

Heat transfer is given by

$$\dot{Q} = \frac{Q}{\Delta t} = UA\Delta T \ , \tag{6.3}$$

where U is the overall heat transfer coefficient, in W/m^2-s-K. Solving for area

$$A = \frac{\hat{Q}}{U\Delta t\Delta T}. \tag{6.4}$$

The coefficient of performance (COP) for a refrigeration cycle is equal to $Q_{cooling}/W_{actual}$. Classical thermodynamics indicates that the maximum COP can be calculated in terms of the temperature differences alone as

$$COP = \frac{Q_c}{W} = \frac{1}{T_o / T - 1}. \tag{6.5}$$

Example 6–1 Assessment of a simple cooling

A simple cooling process is presented in Figure 6–3. Methane enters the system at 25°C and 40 bar. It is cooled and condensed in one step to –150°C and 4 bar. Table 6–2 provides some convenient values for the enthalpy of methane at relevant conditions. Basis is 1 kg.

Table 6–2 Selected Values of Enthalpy and Entropy of Methane

Temperature(°C)	Pressure (bar)	Enthalpy (kJ/kg)	Entropy (kJ/kg-K)
25	40	870.93	4.673
–75	4	688.76	5.065
–100	4	634.39	4.772
–150	4	40.90	0.342

Solution

Using Eq. (6.2), and getting the values from Table 6–2 for the outlet and inlet conditions, respectively,

$$\hat{Q}_{cool} = \frac{40.9 - 870.93}{1} = -830.2 \text{ kJ/kg}.$$

Although actual conditions will vary with specific heat exchanger design; here, if assuming the refrigerant side of the cooler were operated as an evaporator at –150°C, and the process side is at an average

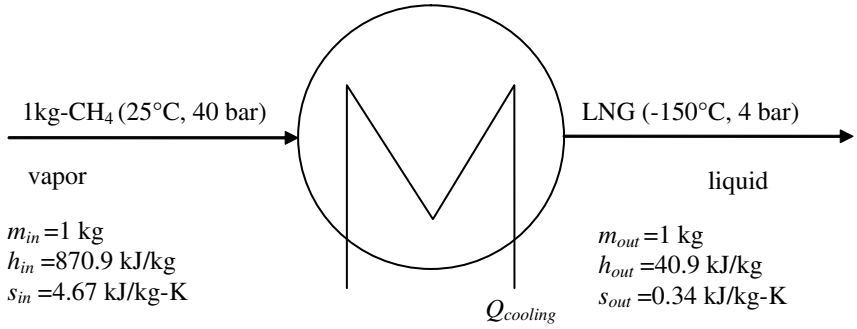

Figure 6–3 *Simple cooler/condenser*

temperature of (–150 + 25)/2 = 67.5°C, the average temperature difference in the exchanger would be approximately 82.5°C. A reasonable overall heat transfer coefficient might be 500 W/m^2-K or 0.500 kJ/s- m^2-K.

Using Eq. (6.4) and solving for the area,

$$A = \frac{830.2(\text{kJ/kg})}{0.500(\text{kJ/s} - \text{m}^2 - \text{K}) \times 82.5\text{K}} = 20.1\ \text{m}^2/(\text{kg/s}).$$

For the base case of 8 MTPA, the rate is 253.7 kg/s. Thus, the heat transfer area required for this size unit would be 253.7 kg/s × 20.1m^2/(kg/s) = 5,100 m^2.

Here, emphasis is given on the required work for the refrigeration cycle, instead of the total heat transfer. The refrigeration cycle can be modeled with a Carnot refrigerator, operating between the –150°C (123 K) process side, and an assumed 25°C (298 K) ambient temperature. For this case, with Eq. (6.5),

$$COP = 1/(298/123 - 1) = 0.703.$$

Thus, the required cooling is 830.2 kJ/kg, the minimum work is Q_c/COP = 830.2/0.703 = 1.18 MJ/kg. For the flowrate of 253.7 kg/s, this becomes 299 MW.

The analysis above assumes that all heat transfer takes place at –150°C, the final LNG temperature. In reality, a process can be constructed in temperature steps to minimize the discrete temperature difference, and thus minimize entropy degradation or "lost work." Below the highest efficiency attainable is explored.

Example 6–2 Calculation of the maximum efficiency

To demonstrate the increase in efficiency from a multistage cooling process, consider a three-stage process as described in Figure 6–4 and as presented by Kanoglu (2002). The interstage temperatures were selected arbitrarily.

Solution

Using Eq. (6.2),

$$\hat{Q}_{c1} = h(-75°C, 4 \text{ bar}) - h(25°C, 40 \text{ bar})$$

$$= 688.76 - 870.93 = -182.2 \text{ kJ/kg},$$

$$\hat{Q}_{c2} = h(-100°C, 4 \text{ bar}) - h(-75°C, 4 \text{ bar})$$

$$= 634.39 - 688.76 = -54.37 \text{ kJ/kg},$$

$$\hat{Q}_{c3} = h(-150°C, 4 \text{ bar}) - h(-100°C, 4 \text{ bar})$$

$$= 40.90 - 634.39 = -593.6 \text{ kJ/kg}.$$

Since $W_{min} = Q_c/COP$,

$$\hat{W}_{min,1} = 182.2/4.960 = 36.7 \text{ kJ/kg},$$

$$\hat{W}_{min,2} = 54.37/1.649 = 33.0 \text{ kJ/kg},$$

$$\hat{W}_{min,3} = 593.6/0.987 = 601.6 \text{ kJ/kg}.$$

Thus, the total

$$\hat{W}_{min} = \hat{W}_{min,1} + \hat{W}_{min,2} + \hat{W}_{min,3}$$

$$= 671.3 \text{ kJ/kg or } 0.671 \text{ MJ/kg}.$$

This concept can be extended to an infinite number of steps in theory, though of course not in practice. To define the ultimate limit, exergy analysis is used as presented by Kanoglu (2002).

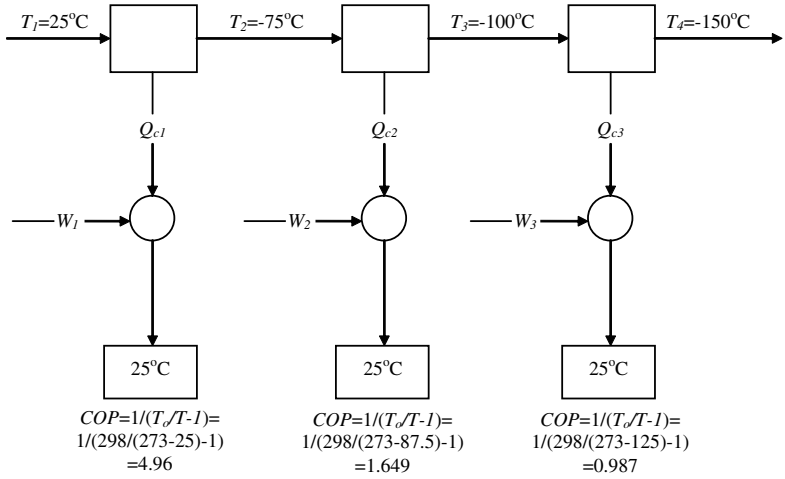

Figure 6–4 *Three-stage process for liquefaction*

For a process, exergy is defined as

$$e = h - h_o - T_o(s - s_o)\ , \tag{6.6}$$

where T_o is the temperature of the surroundings, and h_o and s_o represent enthalpy and entropy at a convenient basis, respectively. Exergy analysis provides a means to quantify reversible work, and thus the "efficiency" of real processes. For a transition from State 1 to State 2,

$$e_2 - e_1 = h_2 - h_1 - T_o(s_2 - s_1)\ . \tag{6.7}$$

This represents the minimum work for the transition. For the process analyzed here, the minimum work can be calculated as,

$$\hat{W} = W / m = e_2 - e_1 = h_{out} - h_{in} - T_o(s_{out} - s_{in})\ . \tag{6.8}$$

Inserting the values for enthalpies and entropies from Table 6–2,

$$W_{min} = (40.91 - 870.93) - 298 \times (0.3424 - 4.633) = 460.5 \text{ kJ/kg}\ .$$

The actual amount of work required in real processes is reported by Finn et al. (1999), as 1,188 kJ/kg, reflecting additional losses in a plant.

Real Cooling Processes

Real processes are less efficient than the ideal reversible processes described above. The primary sources of inefficiency are friction in the compressors, finite temperature differences in the heat exchangers, irreversible flashes across throttling valves, and heat loss to the surroundings. A simple flash condensation process and a modified Linde process, examples of self liquefaction processes, are examined below, before turning to the real industrial processes.

Example 6–3 Calculation of simple flash condensation

A stream of methane at 210 K and 100 bar flashed adiabatically will yield about 24% liquid methane at 4 bar 131.4 K. A simple process can be built around this principle as shown in Figure 6–5.

Solution

For a basis of 1 kg methane liquefied, a feed of 4.188 kg is required (for 24% to be liquefied). The work for compression can be calculated from the enthalpy difference as $W = m(h_o - h_{in}) = 4.188 \times (1{,}034.6 - 870.93) =$ 685 kJ/kg LNG. However, since the product gas from the compressor must be cooled down to –63°C, prior to the flash, some additional work would be required in a refrigeration cycle. The total heat load in the exchanger is $Q = m(h_{out} - h_{in}) = 4.188 \times (416.67 - 1{,}034.6) = 2{,}587$ kJ. The cooling portion below the ambient temperature of 25°C is 62%. Thus, the refrigeration requirement is $0.62 \times 2587 = 1{,}604$ kJ. At an average temperature of –19°C, the *COP* for a Carnot refrigerator would be $(273 - 19)/(25 - (-19)) = 5.772$. Since the $COP = Q_c/W$, the minimum work can be calculated as $W = Q_c/COP = 1{,}604/5.772 = 184.3$ kJ. Thus, the total work is 685 + 184.3 = 869.3 kJ/kg. For a 4 MTPA LNG unit this is 110 MW.

Example 6–4 Calculation for the Linde process

One obvious drawback for the process in Example 6–3 is the fact that only 24% of the methane is liquefied. The Linde process attempts to address this by recycling the vapor back into the compression cycle, giving only LNG as the product. A simplified schematic and process results are shown in Figure 6–6.

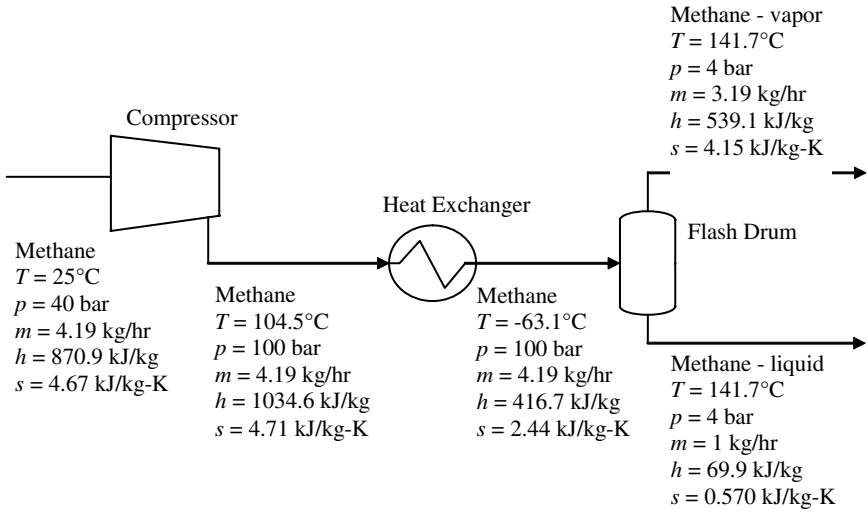

Figure 6–5 *Simple flash condensation process*

Solution

For 1 kg of LNG, the total work requirement is 666 kJ/kg, a significant improvement over the simple flash condensation. In the flash unit, 42% of the methane is liquefied. The remaining vapor is recycled and must be recompressed to combine with the 40-bar feed stream. Since natural gas contains many other compounds than methane, self liquefaction processes can become quite complicated, and are not employed in general for large scale processes.

Almost all of the industrial processes in current use are "cold box" processes in which the process stream is cooled by a series of refrigerants, either pure or mixed. A number of these processes are described below. A major goal of these processes is to bring the temperature approaches to an optimum value in the heat exchangers, to lower the rate of entropy creation, and thus lost work.

Above is the limiting case for this type of process. Below is a thermodynamic analysis of the APCI process as discussed by Ravavarapu (1996).

The APCI process (Figure 6–7) is by far the most common LNG process in current use. The major improvement in the ACPI process is a cold box cooler which uses a mixed refrigerant to provide relatively close temperature approaches, thus minimizing thermodynamic losses. Below is a demonstration of the cold box industrial processes in the APCI process.

A simulation of a real process, using a modern process simulator, with nonideal compressors, gives a total compressor workload of

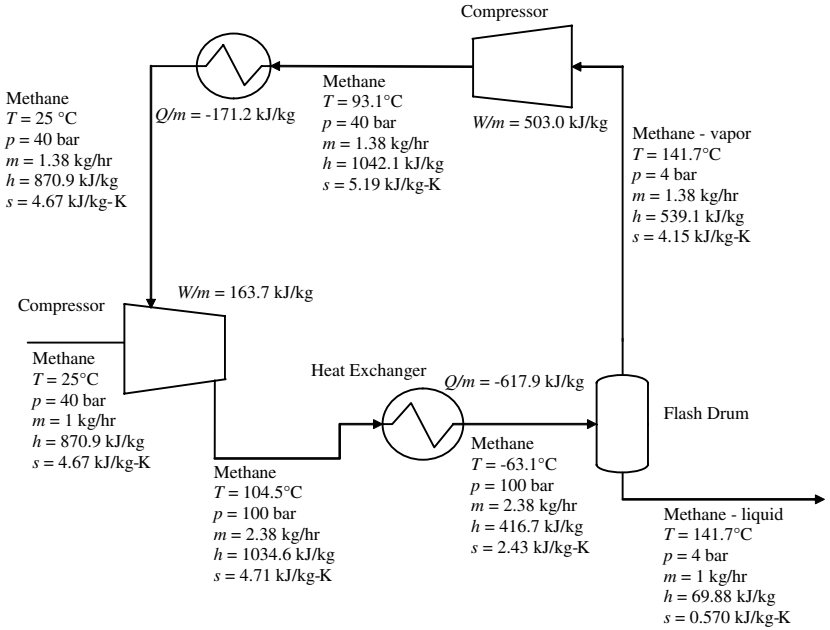

Figure 6–6 *Simplified schematic of Linde process*

approximately 1.18 MJ/kg and a total process efficiency of 40%. For a 4 million ton/annum process this is 155 MW of compressor power. The fuel requirement as a % of LNG is 8% (Ravavarapu, 1996).

Description

E12	1st Stage C3 evaporator	800 kPa, 20°C
E24	2nd Stage C3 evaporator	430 kPa, 0°C
E36	3rd Stage C3 evaporator	130 kPa, –34°C
E86	1st MR Cooler	430 kPa, 0°C
E88	2nd MR Cooler	130 kPa, –34°C

E66, E104, E106 are all cooling water coolers (30°C)

Compressors

K60	1st stage propane	130 kPa → 430 kPa
K62	2nd stage propane	430 kPa → 1.2 MPa
K100	1st stage MR	350 kPa → 2 MPa
K102	2nd stage MR	2 MPa → 4.2 MPa

Main Exchanger

MR enters separately as liquid and vapor from separator D110 at –34°C and 4.2 MPa.

It cools to –112°C in the bottom section and this condenses the vapor. The liquid flashes (V116) to 330 kPa to –121°C. The vapor stream from D110 is subcooled to –163°C in top and flashes to 350 kPa and –168°C, then re-enters the exchanger.

The MR is 10%, 40%, 35%, and 15% nitrogen, methane, ethane, and propane, respectively.

Methane

Methane passes through the process with draw offs for water and condensable hydrocarbons (C_2+).

Natural gas is cooled at 5 MPa to 2°C, 0°C, and –34°C successively in three propane precooler/evaporators E12, E24, and E36. In the bottom of the LNG/MR exchanger it is cooled to –112°C, fully condensing at 5 MPa. In the top half the LNG is supercooled to –163°C. It then leaves the exchanger and is flashed as a liquid to 0.45 MPa and –161°C. No vapor is formed.

Entropy Analysis of the APCI Process

Continuing with the analysis presented by Ravavarapu et al. (1996), ideal work can be calculated by (Smith and Van Ness, 1975)

$$\hat{W}_{ideal} = \Delta h - T_o \Delta s \ , \tag{6.9}$$

where Δs is the entropy change for the system.

Lost work is the difference between the actual work for a process and the ideal work for a reversible process,

$$\hat{W}_{lost} = T_o \Delta s_{total} = T_o \Delta s - \hat{Q} \ , \tag{6.10}$$

where Δs_{total} is total entropy change of the system and surroundings. $\hat{Q}$ is heat transfer to the system per unit mass.

It is immediately evident that the ultimate efficiency of any LNG process will be dependent on the temperature of the surroundings, T_o, available for process cooling.

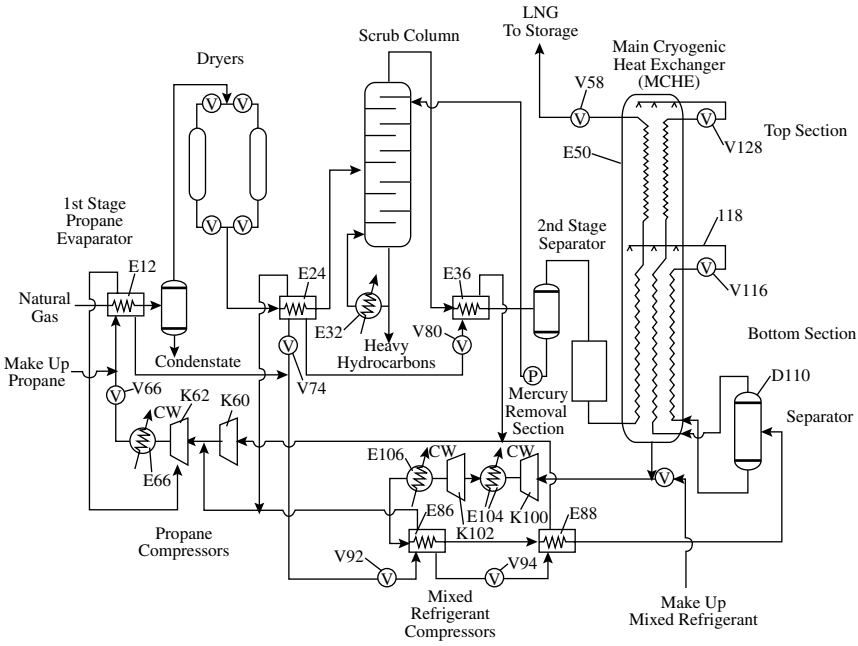

Figure 6–7 *APCI process* (Ravavarapu et al., 1996)

A pressure-enthalpy (p-H) diagram for methane is presented in Figure 6–8, which identifies the path for the LNG stream. Similar diagrams would be helpful in analyzing the propane refrigeration cycle.

Ravavarapu et al. (1996) considered the entropy changes in terms of various balance envelopes as outlined in Table 6–3.

It can be seen that the compressors are responsible for 49% of the entropy increase. Compressor efficiency is beyond the scope of this discussion, but it is not considered likely that there will be major increases in compressor efficiency. The primary area which can be addressed by process design is the 38% loss in the exchangers. This loss is primarily due to finite temperature differences in the exchangers. If these are decreased by use of mixed refrigerants in increased numbers of refrigeration cycles, and/or improvements in the internal design of exchangers, this becomes an area for potential process improvement. Such improvement would come at a cost of increased heat exchange area as the required area is proportional to the temperature difference. The addition of refrigeration cycles increases process complexity and capital cost as well.

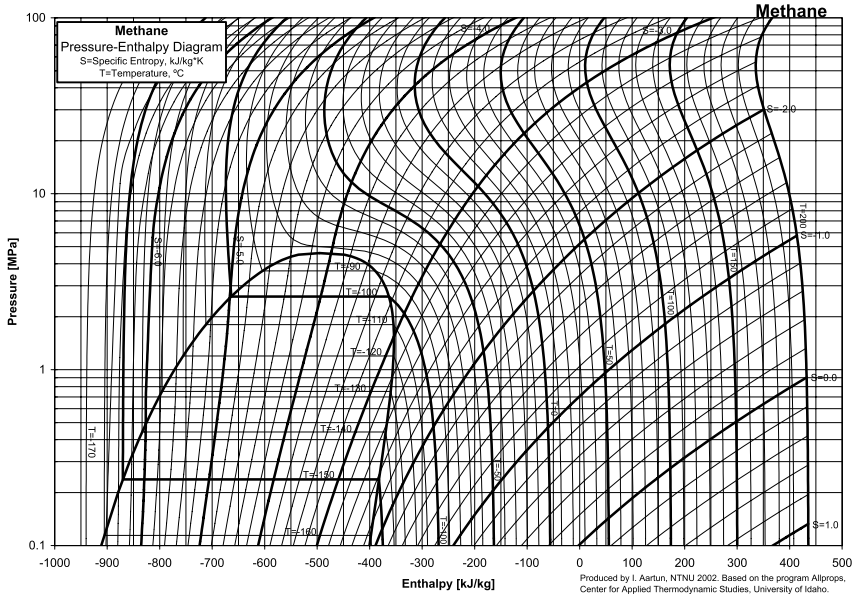

Figure 6–8 *p-H diagram for methane*

Table 6–3 Contributions to Entropy Creation

Equipment Envelope	% of Δs
Main Exchanger	23.15
Propane Evaporator	14.96
Compressors	
Propane	15.71
MR	23.31
Water Coolers	
Propane	7.57
MR	11.92

Exergy Analysis

Exergy analysis provides a simple method to assess process efficiency. Consider the simplified APCI flowsheet presented in Figure 6–9.

Ravavarapu et al. (1996) performed a simulation of the APCI process to determine the work and cooling requirements. For convenience, their results have been converted to a basis of 1 kg LNG and are presented with enthalpy and entropy data in Figure 6–9. Note the similarity of Figure 6–9 with Figure 6–4 in which the efficiency of a hypothetical one-stage process was presented. Typically, any of the commercial processes can be represented in this form, though there may be more refrigeration cycles and steps to consider. The three-stage propane evaporator cooling cycle has been combined into a single stage, as has the two-step LNG exchanger.

The total work requirement is 391.9 + 783.7 = 1175.6 kJ/kg. This is essentially the same number reported by Finn et al. (1999) as typical of industrial processes. The minimum requirement from an energy balance can be assessed. Recall from Eq. (6.8) and using the data here that

$$\hat{W}_{reversible} = 2.016 - 860.08 - 298 \times (0.01506 - 4.5316) = 487.3 \text{kJ/kg}.$$

The total cooling requirement for the LNG stream is, similarly, 858.6 kJ/kg.

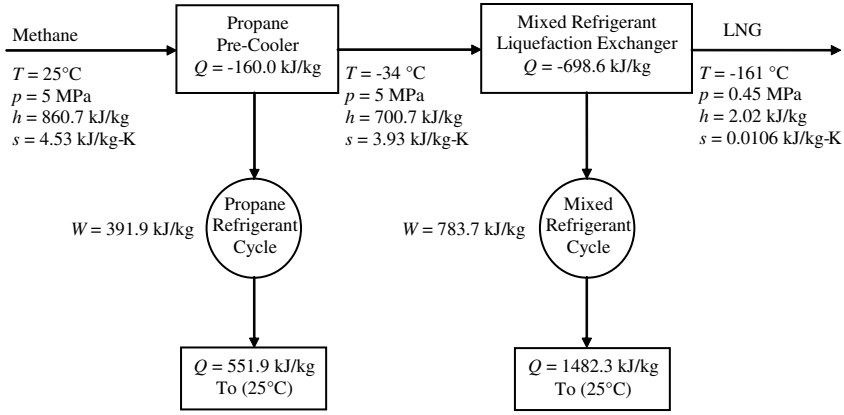

Figure 6–9 *Simplified APCI process schematic*

A *COP* can be calculated as

$$COP_{\text{actual}} = Q_{\text{cooling}} / W_{\text{actual}} = 858.6/1{,}175.6 = 0.730.$$

The ideal *COP* is then

$$COP_{\text{ideal}} = Q_{\text{cooling}} / W_{\text{reversible}} = 858.6/487.3 = 1.760.$$

Efficiency can be defined as

$$\eta = COP_{\text{actual}}/COP_{\text{ideal}} \tag{6.11}$$

and thus, $\eta = 0.730/1.760 = 0.42$.

(This value differs slightly from the 0.41 reported by Ravavarapu et al., (1996), due to rounding in the scaling process.)

A closer analysis reveals that the individual cycle efficiencies for the propane and MR cycles are 38% and 54%, respectively.

The analysis above shows that the APCI process, the most common by far in installed capacity, has an efficiency of only 42%. This leaves room for improvement. The entropy analysis also shows that nearly half of the inefficiency can be attributed to compressors. As mentioned earlier, little improvements can be envisioned in compressor design. The bulk of the remaining inefficiency is due to the finite temperature difference in the heat exchangers. In theory, it is possible to reduce the temperature differences by employing more refrigerant cycles.

Employing more refrigerant cycles will increase the heat exchanger area. For example, a change in temperature approach from 20°C to 2°C, though it would improve process efficiency, would require a ten-fold increase in heat exchanger area, which is already quite large.

A reasonable overall heat exchange coefficient for a system such as this might be 550 W/m^2-K. Using Eq. (6.4) with the appropriate values for an 8 MTPA process (254 kg/s) and a ΔT of 10°C,

$$A = \frac{254(\text{kg/s}) \times 858.6(\text{kJ/kg})}{(550\text{J/s} - \text{m}^2 - \text{K} \times 10\text{K})} = 40{,}000\text{m}^2.$$

The total cooling requirement for LNG would be 784 GJ/h and the total compressor work load, 1,073 GJ/h or 357 MW.

If two trains were employed, each exchanger would be 20,000 m^2. Nominally, a 20,000 m^2 exchanger might be configured with an internal length of 20 m and a cross-sectional area of 20 m^2.

6.3.2 Propane Precooled Mixed Refrigerant (PPMR™)/C3 MR Process

The Propane Precooled Mixed Refrigerant process—developed by Air Products & Chemicals Int. started to dominate the industry from the late 1970s on. This process accounts for a very significant proportion of the world baseload LNG production capacity. Train capacities of up to 4.5 MTPA have been built (Shukri, 2004).

The PPMR process, as shown in Figure 6–10, utilizes a mixed refrigerant (MR), which has a lower molecular weight and is composed of nitrogen, methane, ethane, and propane. The natural gas feed is initially cooled by a separate propane chiller to an intermediate temperature, approximately –35°C (–31°F), at which the heavier components in the feed gas condense out and are sent to fractionation. The natural gas is then sent to the main cryogenic heat exchanger, which is composed of a large number of small diameter spiral wound tube bundles, which permit very close temperature approaches between the condensing and boiling streams. The MR refrigerant is partially condensed by the propane chiller before entering the cold box. The separate liquid and vapor streams are then chilled further, before being flashed across Joule-Thomson valves that provide the cooling for the final gas liquefaction.

A recent modification of the process, for large LNG capacity plants (>6 MTPA), adds a third refrigerant cycle (nitrogen expander) to conduct LNG subcooling duties outside the main cryogenic heat exchanger (Roberts et al., 2002). The addition of the nitrogen cycle reduces the load on the limiting mixed refrigerant service to about 60%, hence making capacities of up to 8 MTPA possible (Avidan et al., 2003).

6.3.3 Optimized Cascade LNG Process

Phillips Petroleum developed the original Cascade LNG process in the 1960s and was constructed first in Alaska. Figure 6–11 provides an overall schematic of a typical Phillips Optimized Cascade LNG Process (POCLP). Using this process, some 3 MTPA of LNG is produced by Atlantic LNG Train 1 in Trinidad, although larger capacities of up to 5 MTPA have been designed (Knott, 2001). This process uses two pure refrigerants—propane and ethylene circuits and a methane flash circuit

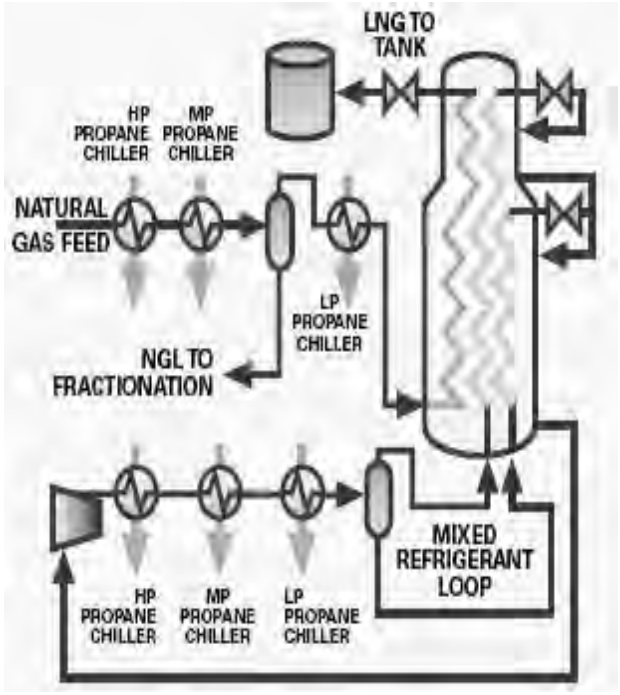

Figure 6–10 *Typical propane precooled mixed refrigerant process* (Bronfenbrenner, 1996)

cascaded to provide maximum LNG production by utilizing the horsepower available from gas turbines. Each circuit uses two 50% compressors with common process equipment. Brazed Aluminum Heat Exchangers and Core-in-Kettle Exchangers are used for the feed gas, propane, ethylene, and methane circuits. All of these heat exchangers, with the exception of the propane chillers, are housed in two "Cold Boxes." The LNG from the last stage flash drum is sent to the LNG tanks.

The POCLP is able to provide designs with high thermal efficiency and achieve a design that is optimized for project economics. The process utilized proven technology and equipment and has a wide range of operational flexibility.

6.3.4 Single Mixed Refrigerant Loop Process

The large and expensive LNG projects are often based on processes which require multiple refrigeration systems. The PPMR Process requires two sequential refrigeration systems to accomplish the LNG production task. The best way to reduce the amount of process equip-

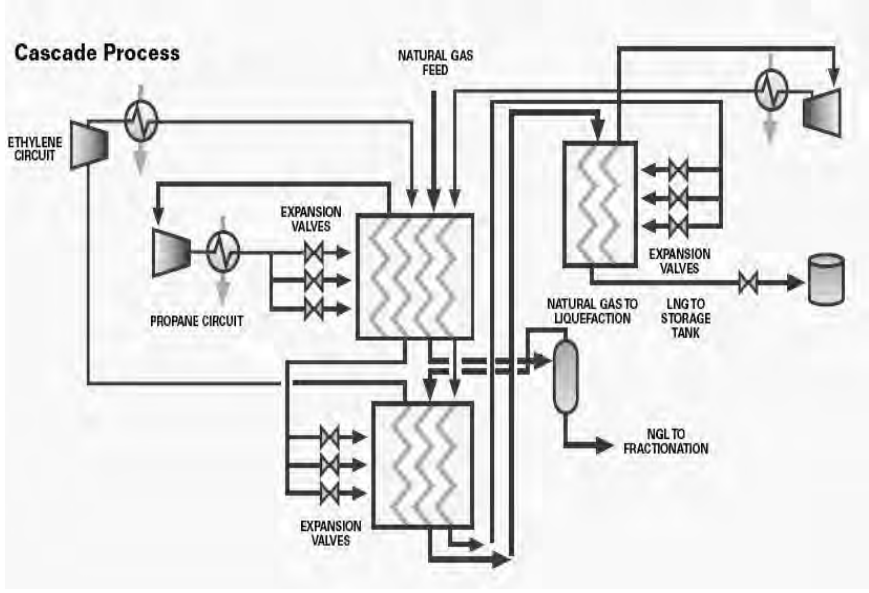

Figure 6–11 *Optimized cascade process* (Houser and Krusen, 1996)

ment is the utilization of a single refrigeration system. Black & Veatch Pritchard has developed a mixed refrigerant process, (PRICO®), which has been successfully used. This is a single mixed refrigerant loop and a single refrigeration compression system. It is illustrated in Figure 6–12. The mixed refrigerant is made up of nitrogen, methane, ethane, propane, and iso-pentane. The component ratio is chosen to closely match its boiling curve with the cooling curve of the natural gas feed. The closer the curves match, the more efficient the process is. The mixed refrigerant is compressed and partially condensed prior to entering the insulated enclosure for the highly efficient platefin heat exchangers, collectively known as the "cold box." The cold box contains a number of platefin heat exchanger cores, which allow multiple streams to be heated/cooled to extremely close temperature differences. The MR is then fully condensed before it is flashed across an expansion valve, which causes a dramatic reduction in temperature. This vaporizing liquid is used to condense the MR stream, as well as the natural gas feed stream. The warmed low pressure MR vapor is then sent to the compressor for recompression. The natural gas feed stream enters the cold box and is initially cooled to about –35°C (–31°F) with a propane chiller. The gas is then sent to a separator to remove the heavier components, which are sent to the fractionation

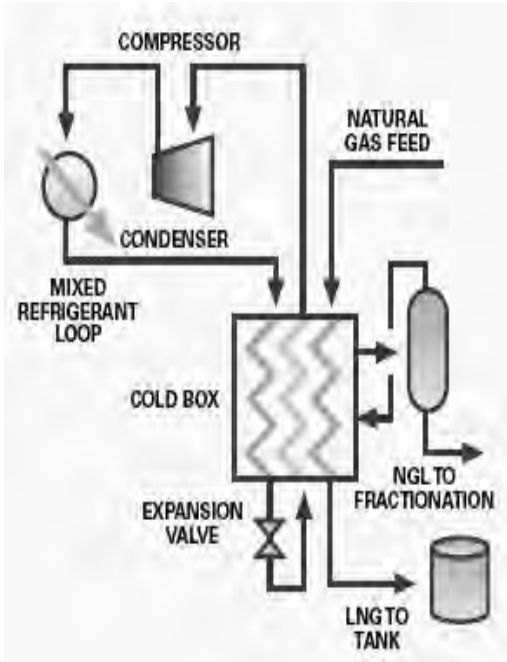

Figure 6–12 *Single mixed refrigerant loop* (Black & Veatch Pritchard PRICO process, Swenson, 1977)

plant. The expanded MR then cools the light components, primarily methane, to the liquefaction temperature (Swenson, 1977).

Use of a single refrigeration system eliminates all the equipment necessary to link the sequential refrigeration systems in other LNG processes. The single refrigeration loop greatly simplifies the piping, controls, and equipment for the liquefaction unit that translates into capital cost savings of up to 30 percent.

Since the system uses a single mixed refrigerant, there are further simplification steps which are important to decrease the investment cost. With a single mixed system, refrigerant makeup can come from storage, import, or can be made up from the feed gas. Only a small skid mounted fractionator is required to produce refrigerant makeup streams from the feed gas. The system is quite small since it is only for occasional makeup, and high purity streams are not required. This simplification eliminates many large pieces of equipment. Thus, the simplification resulting from the single mixed refrigerant makeup philosophy saves capital, versus either the propane precooled or cascade system (Price et al., 2000). However, the single cycle process is not as efficient as a multiple cycle process, as it is very unlikely that it

will ever be used in large baseload LNG plants. It is mainly used for peak shaving applications, due to its lower capital cost compared to multiple cycle processes.

6.3.5 Mixed Fluid Cascade Process

The Mixed Fluid Cascade Process (MFCP) developed by Statoil/Linde is shown in Figure 6–13. The purified natural gas is precooled, liquefied, and subcooled by means of three separate mixed refrigerant cycles. The cold of the precooling cycle is transferred to the natural gas via two plate fin heat exchangers, whereas the cold of the liquefaction and subcooling cycle is transferred via two spiral wound heat exchangers by the other two refrigerants (Bach, 2000). The refrigerants are made up of components selected from methane, ethane, propane, and nitrogen. The three refrigerant compression systems can have separate drivers or integrated to have two strings of compression. The process has been designed for large LNG trains (>4 MTPA).

The MFCP is a classic cascade process, with the important difference that mixed component refrigerant cycles replace single component refrigerant cycles, thereby improving the thermodynamic efficiency and operational flexibility.

6.3.6 Liquefin™ Process

IFP and Axens have developed the Liquefin™ process with the aim of producing LNG cheaper than with any other process, at good conditions of reliability, safety, and friendlier to the environment. With this process very high capacities can be reached with a simple scheme and standard compressors (Martin et al., 2003). It is a two mixed refrigerant process designed for LNG base load projects of train sizes up to 6 MTPA.

The process operates according to the basic flow scheme presented in Figure 6–14. All cooling and liquefaction is conducted in Plate Fin Heat Exchangers (PFHE) arranged in cold boxes. The PFHE arrangement is at the heart of the liquefaction technology. The refrigerants are made up of components from methane, ethane, propane, butane, and nitrogen. The first mixed refrigerant is used at three different pressure levels, to precool the process gas, and precool and liquefy the second mixed refrigerant. The second mixed refrigerant is used to liquefy and subcool the process gas. Using a mixed refrigerant for the precooling stage, the temperature is decreased down to a range of –50°C to –80°C depending on refrigerant composition. At these temperatures, the cryogenic mixed refrigerant can be completely

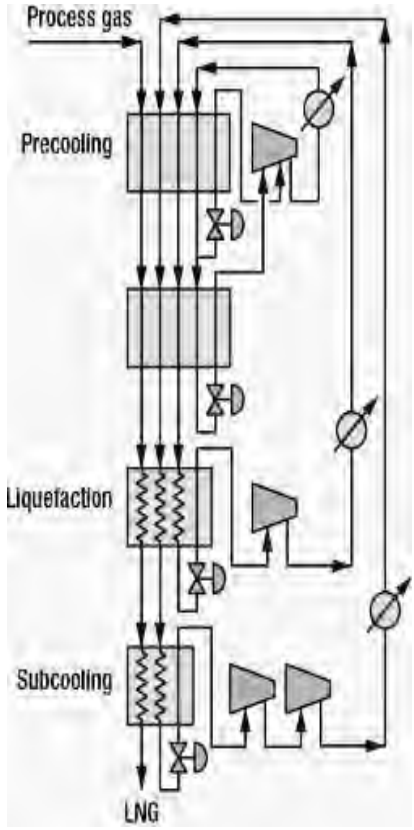

Figure 6–13 *Mixed fluid cascade process (MFCP)* (Heiersted et al., 2001)

condensed, no phase separation is necessary, and moreover, the quantity of cryogenic refrigerant is substantially reduced. The weight ratio between the cryogenic mixed refrigerant and LNG can be lower than unity. The overall necessary power is decreased, as the quantity of cryogenic mixed refrigerant is lower; and a good part of the energy necessary to condense it is shifted from the cryogenic cycle to the pre-refrigeration cycle. Moreover, this shifting of energy allows a better repartition of the exchange loads; and the same number of cores in parallel can be used between the ambient and cryogenic temperature, allowing a very compact design for the heat exchange line.

A very significant advantage of this new scheme is the possibility to adjust the power balance between the two cycles, making it possible to use the full power provided by two identical gas drivers (Fisher and Boutelant, 2002). This process was initially developed to obtain a 50%–50% sharing of power between the liquefaction refrig-

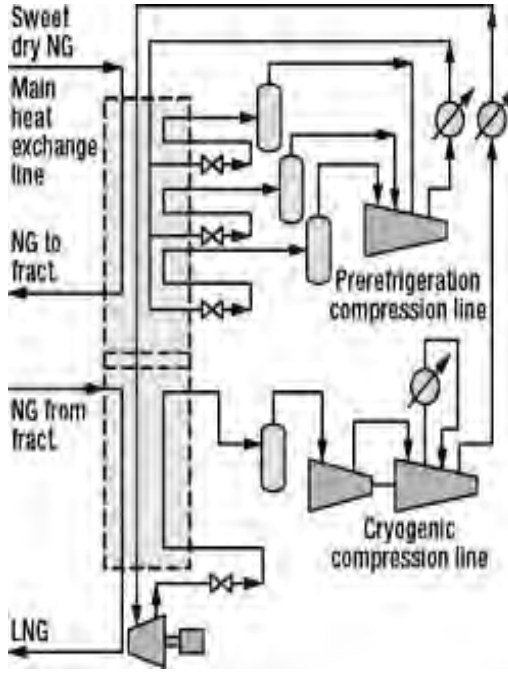

Figure 6–14 *IFP/Axens Liquefin™ process* (Fisher and Boutelant, 2002)

erant cycle and the precooling refrigerant cycle (Burin de Roziers and Fischer, 1999). The advantages of this process are in the use of a single quality of liquefaction refrigerant and a simplified PFHE type liquefier (Paradowski and Hagyard, 2000).

The Liquefin™ process is flexible, and offers more than one possibility to reach large and highly competitive capacities; either by using very large gas turbines (combined cycle) to produce electricity, and using large electrical motors (up to 70 MW) in parallel on each cycle, or by using larger gas turbines. With Liquefin, this would allow capacities of 7 to 8 MTPA with only two main drivers.

The process represents a real breakthrough, as the plant capacity can be chosen considering mainly the economics and the marketing possibilities, without being bothered by technical hindrances. A total cost reduction per ton LNG is reported to be 20% compared to other processes. The cost reductions drive from: (1) increasing the plant capacity, (2) reducing the heat exchanger costs, (3) all over plate fin heat exchangers, (4) compact plot area, and (5) multi sourcing of all equipment, including heat exchangers (Mølnvik, 2003).

The Liquefin™ process uses two mixed refrigerant circuits and PFHE cold boxes designed to match very accurately the cooling curve

of natural gas. The refrigerant cycle is about 6–7% more efficient than the other alternatives. If we add to this the effectiveness of the plate fin heat exchangers, which have a high surface-to-volume ratio, lower pressure drop than conventional units, and efficient heat transfer, the overall process is around 15% more efficient than the established competitors (Knott, 2001).

The Liquefin™ process is particularly well adapted to the range of 4 to 8 MTPA per train (greater than any current process and providing the all important economy of scale); with many open options for designing and erecting a plant fully responding to the projects needs (Martin et al., 2003).

6.3.7 Dual Mixed Refrigerant (DMR) Process

Shell developed a Dual Mixed Refrigerant (DMR) process for liquefaction, as shown in Figure 6–15, with two separate mixed refrigerant cooling cycles, one for precooling of the gas to approximately –50°C (PMR cycle) and one for final cooling and liquefaction of the gas (MR cycle). This concept allows the designer to choose the load on each cycle. It also uses proven equipment, e.g. spiral wound heat exchangers (SWHEs), throughout the process. The DMR process is the basis of the Sakhalin LNG plant, with a capacity of 4.8 MTPA per train (Smaal, 2003).

Process configuration is similar to the Propane Precooled Mixed Refrigerant (PPMR) process, but with the precooling conducted by a mixed refrigerant (made up mainly of ethane and propane) rather than pure propane. PPMR vapor from the precool exchangers is routed via knockout vessels to a two stage centrifugal PPMR compressor. Desuperheating, condensation, and subcooling of the PPMR is achieved by using induced draft air coolers. The PPMR compressor is driven by a single gas turbine. Another main difference is that the precooling is carried out in SWHEs rather than kettles. The cooling duty for liquefaction of the natural gas is provided by a second mixed refrigerant cooling cycle (MR cycle). The refrigerant of this cycle consists of a mixture of nitrogen, methane, ethane, and propane. Mixed refrigerant vapor from the shell side of the main cryogenic heat exchanger is compressed in an axial compressor followed by a two stage centrifugal compressor. Intercooling and initial desuperheating is achieved by air cooling. Further desuperheating and partial condensation is achieved by the PMR precooling cycle. The mixed refrigerant vapor and liquid are separated and further cooled in the main cryogenic heat exchanger, except for a small slipstream of vapor MR, which is routed to the end flash exchanger (Dam and Ho, 2001).

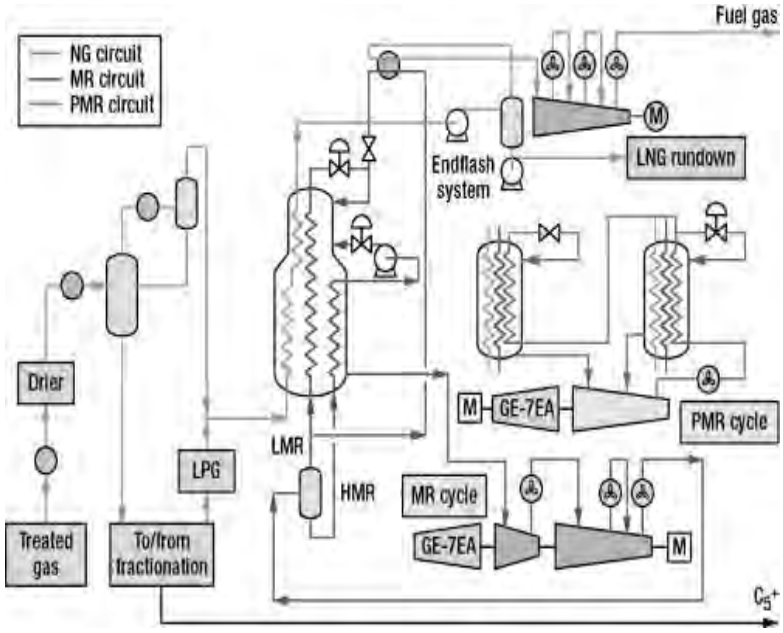

Figure 6–15 *Schematic overview of the DMR refrigeration cycles* (Dam and Ho, 2001)

The DMR process has also employed double casing instead of single casing equipment. This is a reliable method to bring the propane-MR process closer to a capacity of 5 MTPA. With a single precooling cycle and two parallel mixed refrigerant cycles, the capacity can also be boosted up to 8 MTPA. The process can either use propane or an MR in precooling. Proven refrigerant cycles can be used without step changes in technology. The capacity can be increased further with different (larger) drivers. Another possibility for the propane-MR process is to transfer power from the propane cycle to the mixed refrigerant cycle. The closer coupling between the two cycles, by mechanical interlinking of compressors, is an operational challenge.

6.4 LNG Carriers

Very large vessels capable of carrying cryogenic liquids have been constructed to transport LNG across the seas. These vessels grew considerably in size, from less than 30,000 cubic meters in the mid 1960s, to over 250,000 cubic meters in 2009. Figure 6–16 shows the evolution of vessel capacities with time.

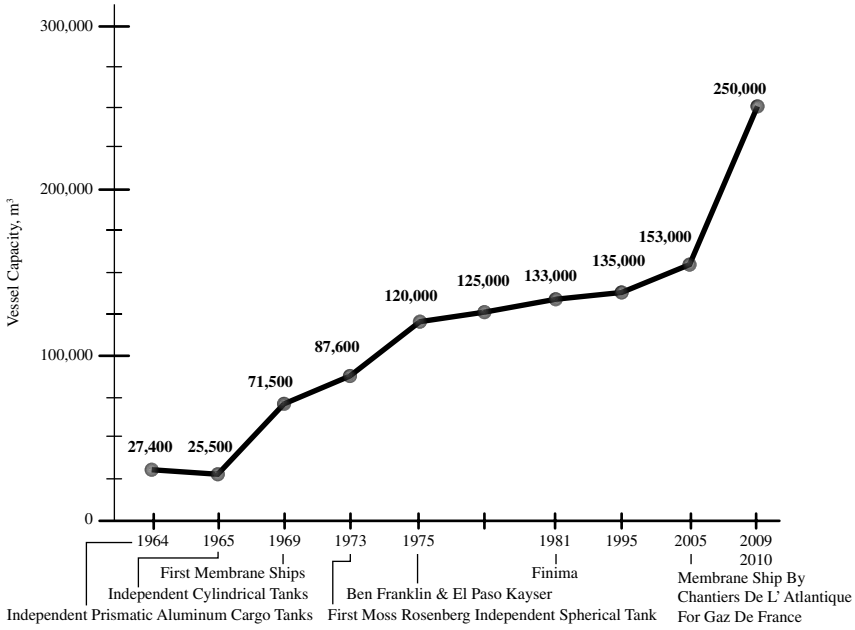

Figure 6–16 *LNG carrier size progression* (Courtesy ABS, 2009)

There are four containment systems, two self-supporting, solid type structures and two membrane type designs. The solid types are the Moss tanks, which are spherical and the patents are owned by Moss Maritime of Norway. Figure 6–17 is a photograph of a Moss-type tanker. Ishikawajima-Harima Heavy Industries (IHI) of Japan has developed the self supporting prismatic (SPB) tank. The two membrane patents are owned by Gaz Transport and Technigaz (GT&T). Figure 6–18 is a photograph of one of the largest LNG tankers that employs membrane technology. In the last several years there has been a clear move towards membrane type carriers, because their configuration uses the hull of the vessel more efficiently than self supporting structures. The LNG tanks are made of two thin membranes of the material Invar and the insulation is made of plywood structures containing perlite.

At the time of writing there were about 300 LNG carriers in service. Table 6–4 contains some representative tankers, their type, their dimensions, speed, and discharge rate. LNG carriers, smaller than 170,000 m^3 are single screw vessels with steam propulsion. The 170,000 m^3 and larger tankers generally have twin screw diesel electric propulsion with dual fuel medium speed diesel engines. The cargo

Figure 6–17 *Moss type LNG tanker*

Figure 6–18 *Membrane type LNG tanker*

Table 6–4 Capacity, Dimensions, Speed and Discharge Rate of Selected LNG Tankers

Capacity (m^3)	Tank Material/Type/ Number of Tanks	Principal Dimensions LOA × B × draft (m)	Design Speed (knots)	Discharge Time (hr)
40,000	Al / Prismatic type A / 4	207 × 29.2 × 9.17	18	12
71,500	Invar / Gaz Transport NO 82 /6	243.5 × 33.99 × 9.5	16.5	12
87,500	Al / SPB /4	230 × 34 × 9.5	17.5	12
126,000	Al / Moss/ 5	285 × 43.83 × 11.3	20	12
138,000	Invar / GTT No 96 /4	277 × 43.4 × 11.3	19.5	12
138,000	SS/ GTT MK III /4	278.6 × 42.6 × 11.3	20.5	12
137,000	Al / Moss / 4	288.6 × 48 × 11.25	19.5	12
145,000	SS/ GTT MK III /4	283 × 43.4 × 11.4	19.5	12
170,000	SS/ GTT MK III /4	290 × 45 × 12.5	19.75	12
210,000	Invar / GTT No 96 /5	315 × 50 × 12	19.5	12.5
267,000	SS/ GTT MK III /4	345 × 55 × 12.2	19.5	16

pumps on most all LNG carriers except the very largest are sized to discharge the cargo in 12 hours (ABS: Personal communication, 2009).

The design natural boil off rate is about 0.15% per day for vessels built since 1993. Prior to that time, the standard boil off rate was 0.25%. The reduction was accomplished with better insulation systems and other design improvements.

The density of LNG is 26.5 lb/ft^3 or 425 kg/m^3. Thus, 1 metric ton of LNG occupies 2.35 m^3. The capacity of the largest vessel built by 2009 of 267,000 m^3 translates to about 113,000 metric tons. One metric ton contains 54.6 Mscf of natural gas. This means that the largest ship contains, fully loaded, almost 6.2 Bscf of gas.

Example 6–5 LNG transport

Suppose that a natural gas field ten times the one described in Example 4–1 is used as the feed for an LNG train. After conversion it

will be loaded in an 87,000 m^3, 4-Moss LNG tanker. Assume the LNG conversion consumes 25 percent per day of the incoming gas and the boil off rate en route is 0.25 percent per day. Using the data in Table 6–4, calculate how many days it would take for a tanker to complete a cycle of loading, traveling a 4,000 mile distance, unloading, and then returning to the LNG facility. How much of the original field gas is actually delivered after regasification? Assume the regasification process takes an extra 3 percent of gas.

Solution

From Example 4–1 of the 1,210 MMscf/d, 5 percent is removed at the separator, and the remaining 25 percent is consumed in the liquefaction process. This leaves

$$1{,}210 \times 0.95 \times 0.75 = 862 \text{ MMscf/d},$$

converted to LNG. Dividing by 54.6 Mscf per ton the stream results into 15,790 metric tons. Multiplying by 2.35 m^3 per metric ton results in 37,110 m^3. The 87,500 m^3 vessel would take 2 days and 9 hours to load.

The distance of 4,000 miles, multiplied by 1.15 translates to 4,600 nautical miles, and from Table 6–4 at a speed of 17.5 knots per-hour, the voyage will take 263 hours. Adding 12 hours to unload and then 263 hours to return, the total is 538 hours, or 22 days and 10 hours. Thus the total of loading, voyages, and unloading amounts to 24 days and 19 hours.

The boil off during the voyage en route is $0.25 \times 263/ 24 = 2.7\%$. Coupled with 3% spent in regasification, the remaining gas to sales is

$$862 \times 0.973 \times 0.97 = 813 \text{ MMscf}.$$

This represents 813/1,210 = 0.67 of the wellhead gas production rate.

6.5 References

Avidan, A., F. Richardson, K. Anderson, and B. Woodard. 2001. LNG plant scaleup could cut costs further. *Fundamentals of the Global LNG Industry* 128–132.

Avidan, A., W. Varnell, B. Martinez. 2003. Study evaluates design considerations of larger, more efficient liquefaction plants. *Oil & Gas Journal* (August 18) 101: 32.

Bach, W.A. 2000. Developments in the mixed fluid cascade process (MFCP) for LNG baseload plants. Paper presented at the World LNG Conference, London, England, September 2000.

Barclay, M. 2005. Natural gas liquefaction process selection for emerging markets. Paper presented at 5th Doha Conference on Natural Gas, Doha, Qatar, March 2, 2005.

Bronfenbrenner, J.C. 1996. The air products propane precooled/mixed refrigerant LNG process. *LNG Journal* (November/December): 25–27.

Burin de Roziers, Th., and B. Fischer. 1999. New trends in LNG process design. Paper presented at the GPA Europe Meeting, London, England, February 19.

Dam, W. and S-M Ho. 2001. Engineering design challenges for the Sakhalin LNG project. Paper presented at the GPSA Conference, San Antonio, TX, March 2001.

Finn, A.J., G.L. Johnson, T.R. Tomlinson. 1999. Developments in natural gas processing. *Hydrocarbon Processing* (April): 78.

Fisher, B., and P. Boutelant. February 2002. A new LNG process is now available. Paper presented at the GPA Europe Technical Meeting, London, England.

Heiersted, R.S., R.E. Jensen, R.H. Pettersen, and S. Lillesund. 2001. Capacity and technology for the Snøhvit LNG plant. Paper presented at the LNG 13 Conference, Seoul.

Houser, C.G., and L.C. Krusen. 1996. Phillips optimized cascade LNG process. Paper presented at Gastech 96, 17th International LNG/LPG Conference, Vienna, Austria, Dec. 3–6, 1996.

Hudson, H.M., J.D. Wilkinson, K.T. Cuellar, and M.C. Pierce. 2003. Integrated liquids recovery technology improves LNG production efficiency. Paper presented at the 82nd GPA Annual Convention, San Antonio, TX.

Kanoglu, M. 2002. Exergy analysis of multistage cascade refrigeration cycle used for natural gas liquefaction. *International Journal of Energy Research* 26:763–774.

Knott, T. 2001. Cool future for gas. *Frontiers* (December) 10–16.

Martin, P-Y., J. Pigourier, and P. Boutelant. 2003. Liquefin™: An innovative process to reduce LNG costs. Paper presented at the 22nd World Gas Conference, Tokyo, Japan.

Mokhatab, S. and M.J. Economides. 2006. Process selection is critical to onshore LNG economics. *World Oil* 227 (February) 95–99.

Mølnvik, M.J. 2003. LNG technologies—State of the art. Paper presented at Statoil—NTNU Global Watch Seminar: Gas Technology, Norway, August 29.

Paradowski, H., and P. Hagyard. 2000. An LNG train capacity of 1 BSCFD is a realistic objective. Paper presented at the GPA Europe Annual Meeting, Barcelona, Spain, Sept. 27–29.

Price, B.C., R. Winkler, and S. Hoffart. 2000. Developments in the Design of Compact LNG Facilities. Paper presented at the 79th GPA Annual Convention, Atlanta, GA, March 13–15.

Qualls, W.R., et al. 2005. Benefits of integrating NGL extraction and LNG liquefaction technology. Paper presented at 2005 AIChE Spring, National Meeting, 5th Topical Conference on Natural Gas, Atlanta, GA, April 10–14.

Ravavarapu, V.N., J.H. Oakley, and C.C. White. 1996. Thermodynamic analysis of a baseload LNG plant. Proceedings of the Chemeca 96: Excellence in Chemical Engineering; 24th Australian and New Zealand Chemical Engineering Conference and Exhibition: 143–148.

Roberts, M., J. Petrowski, Y-N. Liu, and J. Bronfenbrenner. 2002. Large capacity single train AP-X™ Hybrid LNG process. Paper presented at the Gastech 2002 Conference, Doha, Qatar, October 2002.

Shukri, T. 2004. LNG technology selection. *Hydrocarbon Engineering* 9, (February): 71–74.

Smaal, A. 2003. Liquefaction plants: Development of technology and innovation. Paper presented at the 22nd World Gas Conference, Tokyo, Japan.

Smith, J.M. and H.C. Van Ness. 1975 *Introduction to Chemical Engineering Thermodynamics*. 3rd ed. McGraw-Hill.

Swenson, L.K. 1977. Single mixed refrigerant closed loop process for liquefying natural gas. U.S. Patent 4,033,735, (July 5, 1977).

Yang, C.C., A. Kaplan, and Z Huang. 2003. Cost-effective design reduces C_2 and C_3 at LNG receiving terminals. Paper presented at the 2003 AIChE Spring National Meeting, New Orleans, LA, March 30–April 3.

CHAPTER 7

Gas-To-Liquids (GTL)

7.1 Introduction

Natural gas is likely to capture a larger market share of the world's energy mix, and its transportation, using pipelines, CNG, and LNG, has been covered in Chapters 5 and 6. However, inroads of natural gas as a fuel into the motor vehicle sector are not easy, and the two methods that often come to mind are through the use of CNG, or indirectly, through the production of electricity, and ultimately, electric vehicles. Some of the latter issues will be covered in Chapter 9.

Because liquid fuels will be required for decades and for certain applications, such as aircrafts, there is nothing realistic in the horizon, even for the longest possible term. Gas-to-liquids (GTL) allows the conversion of natural gas into liquid hydrocarbons and oxygenates through chemical reactions. These hydrocarbons are compatible with fuels and chemicals produced in the gasoline and middle distillate range of an oil refinery. They include naphtha, diesel, kerosene, lubricants, and waxes. GTL products may include other chemicals such as ammonia, methanol, or methyl tert-butyl ether (MTBE), a major motor gasoline additive.

While interest in GTL was driven by political (e.g., South Africa during apartheid) rather than economic factors for decades, recent technical advances have made GTL more competitive. In 2009 there were still relatively few facilities in commercial operation (e.g., by Sasol in South Africa and Shell in Malaysia); however, a number of commercial scale facilities were seriously considered, and GTL activity may grow in the future as a result of both private business initiatives and strategic investments by governments of nations with significant natural gas reserves.

This chapter outlines potential benefits from GTL conversion, basic GTL methods and their history, scientific and engineering principles of GTL, and the most important technologies and implementations.

7.2 Why GTL?

The chemical conversion of natural gas to liquids allows an alternative source of liquids to the traditional refinery products deriving from crude oil. There are obvious benefits to this activity, such as energy security for nations that have little or difficult access to oil but better access to natural gas. In addition, GTL facilitates the transportation of natural gas from remote production sources to consumption destinations if alternative methods, such as pipeline or LNG, are not economically or technically attractive. Since liquid fuels are easier to transport and distribute by ship, rail, or car, and to store at the destination, natural gas conversion to GTL offers superior flexibility in comparison to pipeline and LNG. GTL is not an alternative for places where CNG is attractive because the capital investment for GTL and the operating costs would not be suitable for the size of resources that would fit CNG applications.

A number of additional benefits, all subjected to both local and international economics, may result from the use of GTL technologies. The following list illustrates these benefits:

- *Stranded natural gas monetization from large but difficult places.* Even though global reserves of natural gas are abundant and are expected to last longer than oil, most of these reserves (1/2 to 2/3 in the Former Soviet Union and Middle East) are not just separated by bodies of water, but may be significantly inland and in very hostile environments, such as the Arctic. This is a very difficult form of "stranded" gas. In the absence of pipelines, for efficient gas transportation from sources to destinations, GTL may provide a technically and economically viable transportation alternative. While GTL products may not always be competitive economically against conventional oil products, they may be the only alternative for monetizing stranded natural gas of low opportunity value.

  Key factors affecting GTL competitiveness are the cost of capital, operating costs, plant scale, and degree of facilities utilization. Thus, on many occasions, GTL could bring natural gas to markets that might otherwise be inaccessible, and make

producible significant quantities of natural gas that would not ordinarily be extracted from the ground.

- *Exploitation of associated gas*. Historically, natural gas associated with petroleum production in offshore or remote fields has been a nuisance. In the past, associated gas was usually flared or reinjected into the reservoir in the absence of means for gas transportation to markets. It is now environmentally unacceptable or economically wasteful to follow these practices. GTL may convert associated gas into "synthetic" crude (syncrude) and then use the existing liquid pipelines or liquid transport vessels. GTL plants for associated gas conversion have a small enviromental footprint, are safe, and are well integrated with production sites, particularly offshore.

- *Synthesis of environmentally friendly fuels*. The main products of GTL are fuels, such as diesel, and because of the way these fuels are produced they can offer higher performance and lower pollution. For example, GTL diesel fuel has a higher cetane number (greater than 70 versus 45–50 for conventional diesel) ensuring better thermodynamic efficiency of combustion, and practically no particulates, such as sulfur (less than 1 ppm versus more than 50 ppm) or aromatics (0.45% volume versus 1.4%). GTL fuels can be easily blended with conventional fuels to meet environmental specifications. The recent use of GTL diesel fuel to power sports cars in endurance racing highlighted the high performance of these fuels.

- *Life extension of pipelines*. Pipelines built for oil transportation are of little value if there is no more oil for them to transport from fields that have been depleted. A typical case is the Trans-Alaska pipeline, built in 1977 to transport oil from Prudhoe Bay to Valdez. It is estimated that liquids from GTL conversion of natural gas available in the North Slope area could be transported through the same pipeline, thus extending its useful life by at least 20 years (Khataniar et al., 1997).

7.3 GTL Processes[1]

Conversion of pipeline quality natural gas (essentially methane) to liquids is a polymerization process. Hydrogen is removed and methane

1. Some of the information in this chapter is derived from lectures by Prof. James Richardson, University of Houston.

molecules are polymerized to longer chain hydrocarbon or related molecules, similar to molecules found in crude oil fractions. Such fractions include diesel fuel, naphtha, wax, and other liquid petroleum or specialty products.

There are two basic GTL technologies: direct conversion of natural gas to liquid fuels and indirect conversion via synthesis gas (syngas). The direct conversion avoids the production of synthesis gas, but is difficult to control, has low selectivity (<20%), and low conversion (<40%). Several direct conversion processes have been developed, but none has been economically viable so far.

By contrast, indirect conversion relies on three basic steps:

1. Reforming (catalytic conversion) of natural gas to synthesis gas (mainly a mixture of carbon monoxide and hydrogen at varying proportions).

2. Fischer-Tropsch synthesis (named after Franz Fischer and Hans Tropsch who pioneered the process in Germany in the early 1920s) for catalytic conversion of synthesis gas to liquid hydrocarbons or oxygenates.

3. Upgrading of products via a number of standard refinery processes, such as hydrocracking, isomerization, or catalytic reforming (Figure 7–1).

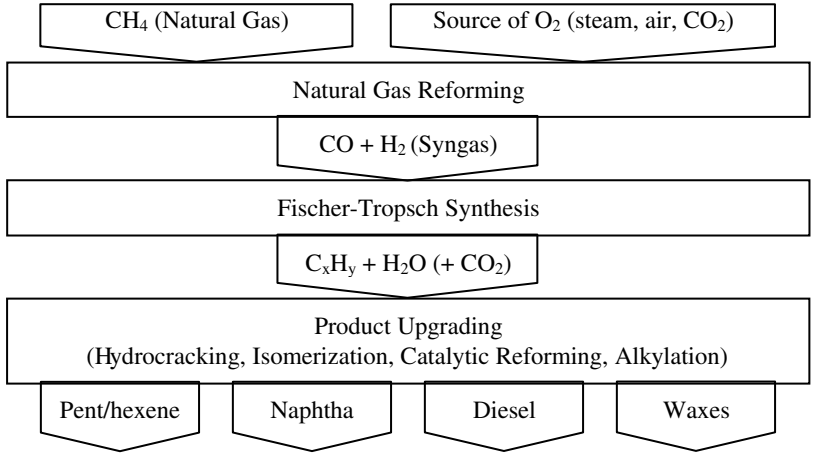

Figure 7–1 *Basic flowchart of indirect conversion of natural gas to liquids through syngas and Fischer-Tropsch synthesis*

Although complicated, the indirect synthesis approach has a long history of development, and forms the foundation for production by the petrochemical industry for a variety of chemicals using natural gas as the main feedstock. It should also be mentioned that Fischer-Tropsch synthesis may be used to produce liquids from syngas coming from other sources, such as coal or biomass.

The fundamentals of both direct and indirect GTL methods are discussed below. Since the indirect conversion method is commercially more important, it will occupy most of the following discussion.

7.4 GTL Based on Direct Conversion of Natural Gas

Direct conversion of methane to higher hydrocarbons may result from a number of reactions: (Note: In this chapter both equations and reactions are numbered sequentially.)

Dehydrogenative self interaction

$$2CH_4 \leftrightarrows C_2H_6 + H_2, \quad \Delta G°(500°C) = +35.6 \text{ kJ/mol.} \tag{7.1}$$

Oxidative coupling

$$2CH_4 + O_2 \leftrightarrows C_2H_4 + 2H_2O, \quad \Delta G°(500°C) = -374.2 \text{ kJ/mol.} \tag{7.2}$$

$$2CH_4 + 0.5O_2 \leftrightarrows C_2H_6 + H_2O, \quad \Delta G°(500°C) = -169.3 \text{ kJ/mol.} \tag{7.3}$$

Partial oxidation

$$CH_4 + 0.5O_2 \leftrightarrows CH_3OH, \quad \Delta G°(500°C) = -86.1 \text{ kJ/mol.} \tag{7.4}$$

$$CH_4 + 0.5O_2 \leftrightarrows CH_2O + H_2, \quad \Delta G°(500°C) = -83.7 \text{ kJ/mol.} \tag{7.5}$$

Oxydehydrochlorination

$$CH_4 + 0.5O_2 + HCl \leftrightarrows CH_3Cl + H_2O, \quad \Delta G°(500°C) = -119.9 \text{ kJ/mol.} \tag{7.6}$$

Complete oxidation

$$CH_4 + 2O_2 \leftrightarrows CO_2 + 2H_2O, \quad \Delta G°(500°C) = -792.9 \text{ kJ/mol.} \tag{7.7}$$

In Reaction (7.1), hydrogen is removed from two molecules of methane that are assembled to produce ethane thermally. It is the most direct reaction, but unfortunately its free energy is so positive, that the reaction is not feasible at reasonable temperatures. The use of oxygen makes the removal of hydrogen from methane and successive coupling of C–C bonds easier, as in Reactions (7.2) through (7.6).

However, Reaction (7.7) inadvertently dominates when oxygen is used, producing undesirable products. Selective acceleration of Reactions (7.2) through (7.6) has been achieved using various catalysts (e.g. 1 wt% Sr/La_2O_3, $Mn/Na_2WO_3/SiO_2$, and 2 mol%Ba/MgO) at high temperatures. These are compounds and are known as such, e.g., Barium/Magnesium Oxide (Ba/MgO). The others are Strontium (Sr), Lanthanium (La), Manganese (Mn), Tungsten (W), etc. As a result, selectivity (i.e., percentage of useful products in the product mix) up to 20% has been achieved at 40% conversion. While this is an improvement over past selectivities, it is still not industrially viable. Future development of better (more selective) catalysts might make direct conversion more attractive given its relative simplicity.

Example 7–1 Methanol production via direct conversion GTL

Calculate the mass of methanol (in lb) that can be produced from 4 Bcf of natural gas. Assume that it is all methane. How many pounds of oxygen would be required?

Solution

The stoichiometric relationship is given by Reaction (7.4). The standard molar volume of natural gas, calculated from ideal gas law with $p_{sc} = 14.7$ psi, $T_{sc} = 60°F = 520$ R, and $Z_{sc} = 1$, is $10.73 \times 520/14.7 = 380$ scf/lbmole. Thus, 4 Bcf correspond to $4 \times 10^9/380 = 1.05 \times 10^7$ lb mole. Based on Reaction (7.4), this would require 5.3×10^6 lb-mole of oxygen and produce 1.06×10^7 lb-mole of methanol. Therefore, the mass of methanol produced is

$$(32) \times (1.06 \times 10^7) = 3.4 \times 10^8 \text{ lb},$$

and the mass of oxygen required is

$$(32) \times (5.3 \times 10^6) = 1.7 \times 10^8 \text{ lb}.$$

7.5 GTL Based on Indirect Conversion of Natural Gas

7.5.1 Basics

As shown in Figure 7–1, the indirect conversion of natural gas to liquid fuels goes through two main steps (reforming and Fischer-Tropsch) and may be followed by a third step (upgrading).

The first step is natural gas reforming. The main reaction in the reforming step can be loosely described as

$$CH_4 + \text{oxygen source} \leftrightarrows CO + H_2, \tag{7.8}$$

where the oxygen source can be steam, CO_2, or air. Depending on the source of oxygen, different technologies have been developed, and are discussed below. The product resulting from reforming is composed predominantly of CO and H_2. It is called synthesis gas (*syngas*) because it is used to synthesize products without the need for additional reactants.

The next step is Fischer-Tropsch synthesis. The main reactions in this step can be summarized as

$$a\text{CO} + b\text{H}_2 \leftrightarrows \{\text{C}_x\text{H}_y\} + \{\text{H}_2\text{O and/or CO}_2\}, \tag{7.9}$$

where $\{C_xH_y\}$ refers to a mixture of liquid straight-chain hydrocarbons that include alkanes (paraffins) and alkenes (olefins) with x ranging from 1 to more than 40, depending on process conditions, catalyst, and syngas composition (ratio *a:b*). These hydrocarbons result from polymerization of $=CH_2$ groups. The ratio *a:b* determines whether H_2O (hydrogen in excess) or CO_2 will be formed.

The final step is product upgrading, and usually involves operations such as hydrocracking, isomerization, catalytic reforming, or alkylation. Standard refinery technology can be used in this step. For example, waxes (C_{18+}) are converted into naphtha (C_5–C_{11}) and diesel (C_{12}–C_{18}) in a hydrocracker.

Of the above steps, generation of synthesis gas is the most capital intensive, accounting for more than half of the fixed cost of an entire GTL process. However, the performance of Fischer-Tropsch synthesis is the most critical for the overall performance of GTL, because it is in this step that the composition of GTL liquids is determined. Critical for Fischer-Tropsch synthesis is the development of catalysts that selectively accelerate reactions resulting in desirable products, as well as the design of corresponding reactors.

Natural gas reforming and Fischer-Tropsch synthesis play a central role in GTL, and are discussed in more detail below.

Example 7–2 Volume reduction resulting from GTL

What volume reduction does GTL accomplish for natural gas? How is that compared to volume reductions achieved by LNG or CNG?

Assume the final product of GTL is a mixture of hydrocarbons of the form C_xH_y. A typical composition may be 75% diesel (C_{12}–C_{18}) and 25% gasoline (C_5–C_{11}).

The density of CH_4 is 0.68 kg/m^3 at 15°C (59°F) and atmospheric pressure. The density of gasoline is about 750 kg/m^3 and the density of diesel fuel is about 850 kg/m^3 at normal conditions.

Solution

The density of typical GTL fuel is

$$0.75 \times 850 + 0.25 \times 750 = 825 \text{kg/m}^3. \tag{7.10}$$

To find the volume reduction ratio, a carbon balance is needed to find the mass of GTL fuel produced from a corresponding amount of natural gas. Carbon balance across Figure 7–1 (further detailed by the simplified reactions of reforming, Reaction (7.8), Fischer-Tropsch synthesis, Reaction (7.9), and product upgrading, presented in Sections 7.5.2, 7.5.3, and 7.5.4, respectively) yields that *x* moles of CH_4 are required for one mole of the long-chain hydrocarbon. The average chemical formulas for diesel fuel and gasoline are $C_{12}H_{23}$ and C_8H_{18}, respectively. The stoichiometry of carbon for producing a mixture of 75% diesel and 25% gasoline is

$$44CH_4 + \ldots \rightarrow 3C_{12}H_{23} + C_8H_{18} + \ldots . \tag{7.11}$$

Therefore the mass of GTL fuel produced per unit mass of methane is

$$\frac{3 \times (12 \times 12 + 23) + (8 \times 12 + 18)}{44 \times (12 + 4)} = 0.874 \,\text{kg GTL fuel/kg methane.} \tag{7.12}$$

It follows that the volume reduction ratio is

$$(1 / 0.68) / (0.874 / 825) \approx 1{,}400. \tag{7.13}$$

The result for the part of the methane that actually gets converted compares quite favorably with LNG and CNG, for which typical volume reduction ratios are about 600 and 200, respectively. The penalty, however, for this volume reduction is the high fixed and operating cost (in capital and energy) of GTL conversion.

7.5.2 Natural Gas Reforming and Synthesis Gas

Syngas was first commercialized in the second half of the nineteenth century, as a result of the coal gasification process; even though the main reaction (passing steam over incandescent carbon) was known in the eighteenth century. In fact, it was in part the importance of liquid fuels produced from coal derived syngas that prompted the development of the Fischer-Tropsch process in Germany and its intensive use during World War II. The production of syngas from natural gas became important in the twentieth century, as inexpensive natural gas became widely available. In addition to forming the basis for liquid fuels, syngas provides hydrogen for use in the chemical industry (mainly for ammonia synthesis) or as a fuel. It could also serve as feed to fuel cells in the future.

Syngas can be produced from natural gas using steam, dry (CO_2), or oxy reforming. An important difference between these approaches is the composition (proportion of H_2 to CO) of the syngas produced, as summarized in Table 7–1. This composition is important for the subsequent steps in GTL, namely Fischer-Tropsch synthesis.

Steam Reforming

Steam reforming is the dominant gas reforming technology. It has a long history of development and has served as a source of syngas and hydrogen for years. In addition to its refinery use, steam reforming is now the preferred method of producing hydrogen for ammonia synthesis.

Table 7–1 H_2/CO Ratio for Gas Reforming Processes (% volume)

Steam Reforming	Dry Reforming	Partial Oxidation	Autothermal Reforming
3	1	>2	2

The main reaction in steam reforming is syngas production as

$$CH_4 + H_2O \leftrightarrows CO + 3H_2, \quad \Delta H°(1{,}000°C) = +226.1 \text{ kJ/mol.} \qquad (7.14)$$

Additional hydrogen is generated by the water-gas shift reaction

$$CO + H_2O \leftrightarrows CO_2 + H_2, \quad \Delta H°(1{,}000°C) = -41 \text{ kJ/mol.} \qquad (7.15)$$

Since Reaction (7.14) is reversible and highly endothermic, high temperatures (e.g., 1,000°C) are necessary to achieve significant conversions. Reaction (7.15) is slightly exothermic, and therefore favored at low temperatures. Combined, Reactions (7.14) and (7.15) yield thermodynamic equilibrium compositions that depend on temperature, pressure, and relative amounts of methane and steam. The equilibrium moves toward product formation at higher temperatures and lower pressures. Excess steam results in higher production of hydrogen as shown in Figure 7–3.

The equilibrium constants of the above two reactions depend on temperature as

$$K_{syngas} = \exp\left[30.53 - \frac{4.85\times10^4}{T} + \frac{2.42\times10^6}{T^2} + \frac{2.49\times10^9}{T^3}\right], \qquad (7.16)$$

$$K_{WaterGasShift} = \exp\left[-2.93 + \frac{3.61\times10^3}{T} + \frac{5.04\times10^6}{T^2} + \frac{1.82\times10^9}{T^3}\right], \qquad (7.17)$$

where the temperature T is expressed in degrees F (Rase, 1977). Plotting the relative values of these equilibrium constants (Figure 7–2) quantifies that the synthesis gas in Reaction (7.14) becomes practically not feasible as temperature is lowered from 1,000°C to 700°C. However, the opposite is true for the water gas shift in Reaction (7.15).

Example 7–3 Steam reforming equilibrium as a function of feed composition

A steam reformer feed of 85% mole steam and 15% mole methane achieves 95% methane conversion through the syngas and shift (Reactions (7.14) and (7.15)). The hydrogen produced is 75% mole pure when dry (i.e., with all water removed). Both reactions are

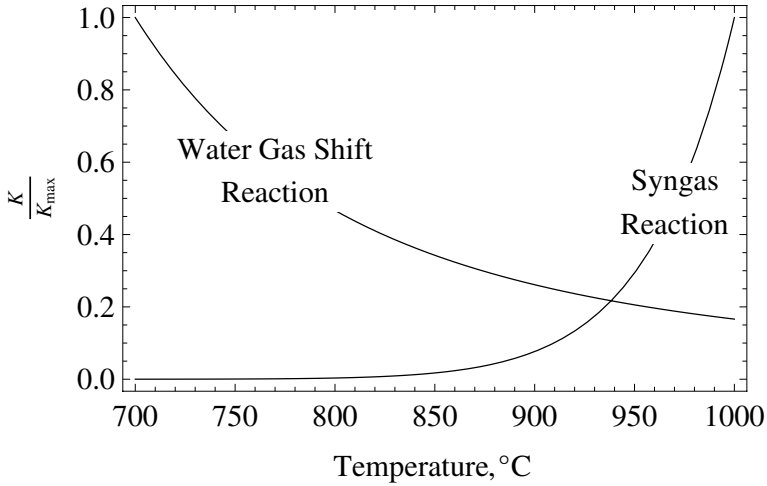

Figure 7–2 *Relative values of equilibrium constants for steam reforming and water gas shift Reactions (7.14) and (7.15), respectively*

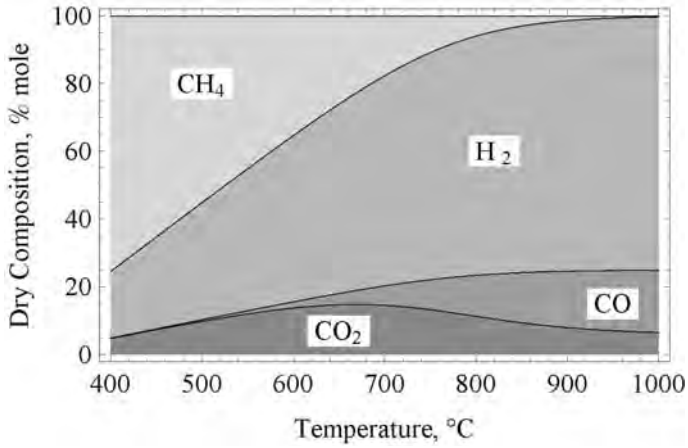

Figure 7–3 *Equilibrium compositions for steam reforming at 20 atm and stoichiometry $H_2O/CH_4 = 3$. Methane conversion is complete at about 1,000 °C. The production of CO_2 from the water gas shift reaction is maximum around 700 °C*

assumed to reach thermodynamic equilibrium: (a) What is the resulting ratio H_2/CO? (b) What should be the feed composition to make the H_2/CO ratio equal to 3.2 at the same temperature and pressure? (c) What range of values is expected for H_2/CO when the molar ratio of steam to methane spans the range 1 to 9?

Solution

(a) Assume a feed of 100 moles, of which 85 are steam and 15 are methane. Then denote the number of moles of steam reacting in Reactions (7.14) and (7.15) by x and y, respectively. The corresponding equilibrium compositions of all species are shown in Table 7–2.

Since methane undergoes 95% conversion, then $x = 0.95 \times 15 = 14.25$ mol.

The concentration of hydrogen in the products is

$$\frac{3x + y}{15 - x + 3x + y + x - y + y} = 0.75 ,$$

from which $y = 2.25$. Therefore, equilibrium composition per 128.5 mole is

$$(H_2O, CH_4, H_2, CO, CO_2) = (68.5, 0.75, 45, 12, 2.25), \qquad (7.18)$$

and the ratio H_2/CO is 45/12 = 3.75.

(b) To select the feed composition that will result in $H_2/CO = 3.2$, consider again 100 moles, of which w are steam and $100 - w$ are methane. Then the equilibrium compositions are as shown in Table 7–3, where x', y' have new values that have to be calculated along with w. The calculation will be based on the desired ratio H_2/CO and the two equilibrium conditions.

Table 7–2 Feed and Equilibrium Compositions for Steam Reformer, Example 7–3

Species	% mole in feed	% mole at equilibrium
H_2O	85	$85 - x - y$
CH_4	15	$15 - x$
H_2	0	$3x + y$
CO	0	x – y
CO_2	0	y
Total	100	$100 + 2x$

Table 7–3 Modified Feed and Equilibrium Compositions for Example 7–3

Species	% mole in feed	% mole at equilibrium
H_2O	w	w – x' – y'
CH_4	$100 - w$	$100 - w - x'$
H_2	0	$3x' + y'$
CO	0	x' – y'
CO_2	0	y'
Total	100	$100 + 2x'$

The equilibrium constants for both Reactions (7.14) and (7.15) can be computed from the results of part (a):

$$K_1 = \frac{c_{H_2}^3 c_{CO}}{c_{CH_4} c_{H_2O}} = \frac{\left(\frac{H_2}{\text{Total}}\right)^3 \left(\frac{CO}{\text{Total}}\right)}{\left(\frac{CH_4}{\text{Total}}\right)\left(\frac{H_2O}{\text{Total}}\right)} = 1.29\ , \tag{7.19}$$

$$K_2 = \frac{c_{CO_2} c_{H_2}}{c_{CO} c_{H_2O}} = \frac{\left(\frac{CO_2}{\text{Total}}\right)\left(\frac{H_2}{\text{Total}}\right)}{\left(\frac{CO}{\text{Total}}\right)\left(\frac{H_2O}{\text{Total}}\right)} = 0.123\ . \tag{7.20}$$

The equilibrium equations must also be satisfied for the new feed composition:

$$\frac{\left(\frac{H_2}{\text{Total}}\right)^3 \left(\frac{CO}{\text{Total}}\right)}{\left(\frac{CH_4}{\text{Total}}\right)\left(\frac{H_2O}{\text{Total}}\right)} = \frac{\left(\frac{3x' + y'}{100 + 2x'}\right)^3 \left(\frac{x' - y'}{100 + 2x'}\right)}{\left(\frac{100 - w - x'}{100 + 2x'}\right)\left(\frac{w - x' - y'}{100 + 2x'}\right)} = 1.29\ , \tag{7.21}$$

$$\frac{\left(\frac{CO_2}{\text{Total}}\right)\left(\frac{H_2}{\text{Total}}\right)}{\left(\frac{CO}{\text{Total}}\right)\left(\frac{H_2O}{\text{Total}}\right)} = \frac{\left(\frac{y'}{100 + 2x'}\right)\left(\frac{3x' + y'}{100 + 2x'}\right)}{\left(\frac{x' - y'}{100 + 2x'}\right)\left(\frac{w - x' - y'}{100 + 2x'}\right)} = 0.123\ . \tag{7.22}$$

In addition, the H_2/CO ratio must be

$$\frac{H_2}{CO} = \frac{3x' + y'}{x' - y'} = 3.2 \ . \tag{7.23}$$

Eliminating denominators from Eqs. (7.21, 7.22, and 7.23) and solving

$$\{w, x', y'\} = \{60.3, 26.4, 1.26\} \ . \tag{7.24}$$

For a H_2/CO product ratio equal to 3.2 at the same temperature and pressure, the feed composition should be

$$CH_4 : \frac{100 - w}{100} \times 100\% = 39.7\% \text{ and } H_2O: \ \frac{w}{100} = 60.3\% \ . \tag{7.25}$$

(c) If the molar ratio of steam to methane spans the range 1 to 9, then

$$1 < \frac{w}{100 - w} < 9,$$

$$\text{or } 50 < w < 90.$$

The corresponding values of the ratio H_2/CO are calculated as

$$\frac{H_2}{CO} = \frac{3x' + y'}{x' - y'} \ , \tag{7.26}$$

where x', y' are the solutions of Eqs. (7.21 and 7.22) for w ranging from 50 to 90. The results of numerical solution of the above equations are shown graphically in Figure 7–4.

Catalysts (Appendix) are commonly used to accelerate Reaction (7.14) preferentially to Reaction (7.15) in order to improve selectivity. The most commonly used catalyst is Ni because of low cost; although higher steam reforming and lower gas shift activity can be achieved with Rh or Ru catalysts, but at a higher cost. Commercial steam

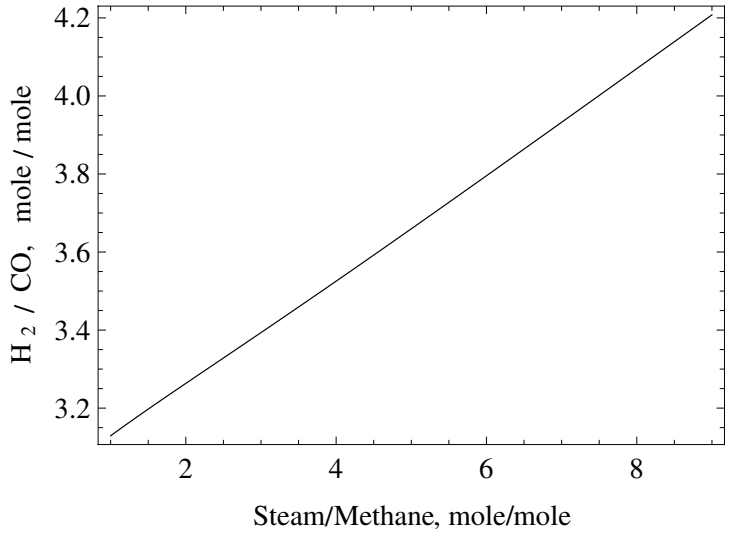

Figure 7–4 *The ratio of H_2/CO as a function of the ratio of steam/methane for Example 7–3*

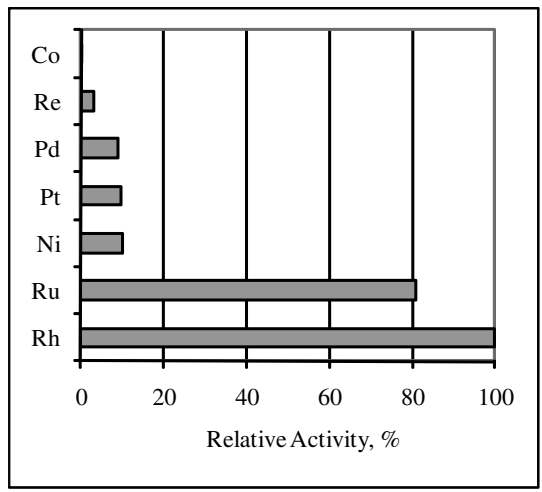

Figure 7–5 *Relative activity of transition metal catalysts for steam reforming*

reforming catalysts typically contain 15–25 wt% Ni on α–Al_2O_3, $CaAl_2O_4$, MgO, or $CaAl_2O_4$ supports. Figure 7–5 provides the relative activity of various commonly used catalysts for steam reforming.

A significant problem with steam reforming is carbon formation (coking). Carbon can be deposited on the reactor walls, creating heat

transfer problems, or on the catalyst, resulting in its deactivation. Carbon can be formed as a result of the following reactions:

Methane cracking

$$CH_4 \leftrightarrows C + 2H_2. \tag{7.27}$$

Boudouard reaction

$$2CO \leftrightarrows C + CO_2. \tag{7.28}$$

Methane cracking, Reaction (7.27), is endothermic and consequently creates coking problems at higher temperatures. The Boudouard Reaction (7.28) is exothermic, and therefore favored at lower temperatures. As a result, it does not create problems at ordinary steam reforming temperatures (700–1,000°C) except for cases where temperature is locally lower due to poor heat transfer. Coking in steam reformers using Ni catalysts results in carbon deposition on the surface of the catalyst, and subsequent polymerization until a significant part of the catalyst surface is covered and its activity decreases. Carbon atoms may also diffuse through the Ni bulk to the catalyst/support interface, where they form carbon "whiskers" with detrimental effects (rupturing of catalyst pellets and plugging of the reactor).

In addition to lowering yield, catalyst deactivation creates overheating problems, because the lower rate of the endothermic reforming reaction results in lower absorption of the heat provided to the reactor (via hot gases or any other mechanism). This may lead to hot spots in the reactor wall that may eventually rupture with potentially catastrophic consequences. To prevent catalyst deactivation by coking, most commercial Ni catalysts contain promoters, such as alkalis or alkaline earth oxides (Appendix), that accelerate the removal of carbon via the reaction

$$C + H_2O \leftrightarrows CO + H_2. \tag{7.29}$$

To promote this reaction, a large surplus of steam is usually required in the feed.

The design of reactors for steam reforming is guided by the need for effective (high rate and uniform) heat transfer to the endothermic Reaction (7.14), while keeping reactor footprint low, and maintaining reactor and catalyst integrity at high reaction temperatures. Typical designs rely on bundles of long, narrow tubes with thick walls (up to 2 cm) made from high alloy steel, as shown in Figure 7–6. The tubes

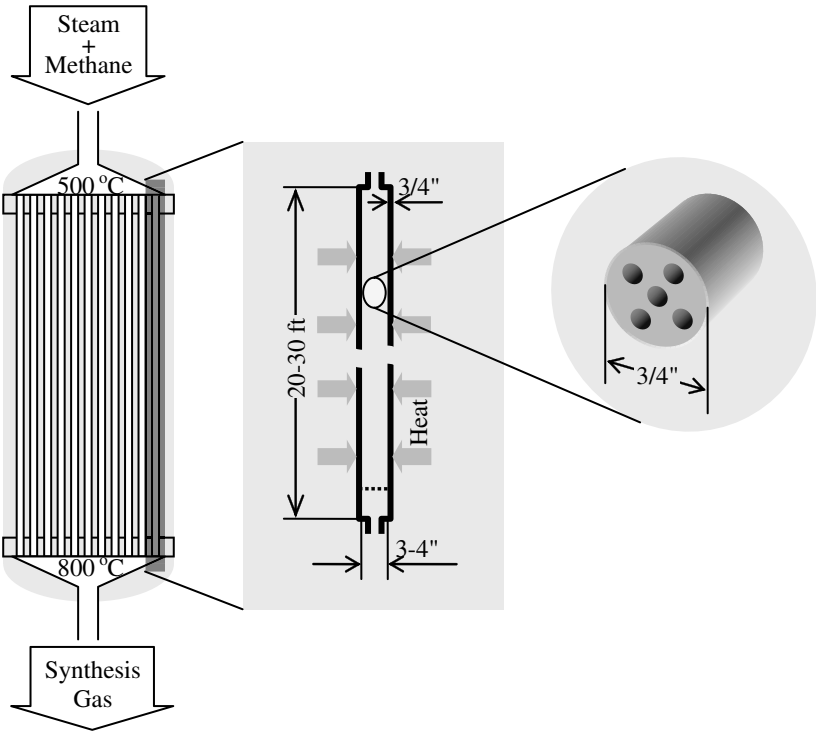

Figure 7–6 *Configuration of a steam reforming reactor at multiple levels of detail: (a) tube bundle in furnace, (b) reactor tube, and (c) catalyst pellet. Heat can be provided to the long tubes in a number of ways, not shown*

are packed with catalyst. Such designs enhance heat transfer and can withstand the high temperatures of the reaction. Various configurations of such reactors have appeared over the years. In older designs, heat was provided by radiation from natural gas flames between the tubes, and such reactors are quite bulky. Since they use only 50–60% of the energy in the fuel for the reaction (the rest exiting with the still hot flame gases), they require heat integration to avoid waste through feed effluent heat exchange. Newer designs are more compact and accomplish efficient heat transfer.

Several new designs rely on convective heating with hot gas. The hot gas is usually provided by a smaller partial unit that combusts part of the methane feed (increasing its temperature), then passes over the tubes, and enters the primary reformer as the feed at about 500°C. The gas exits the reactor at the other end with the equilibrium composition corresponding to the exit temperature and pressure.

The catalyst can be shaped in a number of forms, usually as large pellets. Pellet designs aim to keep pressure drop low, increase heat transfer, and increase the surface-to-volume ratio, to provide as much area for catalytic reaction as possible (i.e., increase the effectiveness factor). Since the diffusion rate of the reactants into such pellets is low compared to the reaction rate, only a small fraction of the catalyst mass (about 5%) is actually used in the reaction.

CO_2 or "Dry" Reforming

Dry reforming relies on the reaction

$$CH_4 + CO_2 \leftrightarrows 2CO + 2H_2, \quad \Delta H°(1{,}000°C) = +258.9 \text{ kJ/mol}. \qquad (7.30)$$

Dry reforming is less common than steam reforming, and its main use is for processes that require high proportion of CO in the synthesis gas. The thermodynamics of dry reforming is similar to steam reforming. The main operational difference of dry reforming from steam reforming is its tendency for coking, made more severe by the lack of steam to remove carbon according to Reaction (7.29). In some applications, such as in mixed reforming (combination of steam and dry reforming), steam is added for effective containment of coking problems. Since coking quickly deactivates Ni catalysts, Rh and Ru catalysts are used in most dry reforming applications.

Oxy Reforming or Partial Oxidation and Autothermal Reforming

Partial oxidation (POX) is another proven method for production of syngas. In partial oxidation, natural gas reacts with pure oxygen at a temperature above 1,000°C. The overall reaction is noncatalytic and slightly exothermic

$$CH_4 + 0.5O_2 \leftrightarrows CO + 2H_2, \quad \Delta H° \ (1{,}000°C) = -35.67 \text{ kJ/mol}. \qquad (7.31)$$

As Reaction (7.31) suggests, the resulting ratio of H_2/CO for POX is ideally equal to 2, which is in the middle of the desired range for Fischer-Tropsch synthesis (1.8–2.3). However, this ratio is difficult to achieve due to the reverse water gas shift Reaction (7.15), which consumes H_2 to produce CO, thus lowering the ratio of H_2/CO below 2. To avoid the consumption of H_2 and formation of CO via the reverse Reaction (7.15), steam is added to the feed, in a process known as *autothermal reforming*.

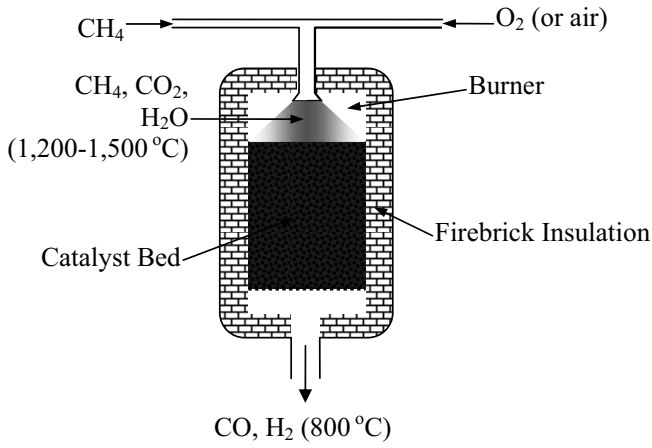

Figure 7–7 *Autothermal reforming reactor*

As Figure 7–7 shows, in autothermal reforming, a mixture of methane and oxygen (or air) enters the burner, where part of the methane is combusted, according to the exothermic reaction:

$$CH_4 + 2O_2 \rightarrow CO_2 + 2H_2O. \tag{7.32}$$

The hot mixture of combustion gases and unburned methane passes through a packed catalyst bed (usually Ni), where it undergoes mixed reforming, namely steam (endothermic Reaction (7.14)) and dry reforming (endothermic Reaction (7.30)). Combining Reactions (7.14) and (7.30) with Reaction (7.32) yields the overall Reaction (7.31).

Autothermal reactors are adiabatic. Since heat is provided by partial combustion of methane, no external source of heating is needed, which simplifies reactor design and operation. Combustion consumes about 1/4 of the feed methane, and is either homogeneous in the burner (as shown in Figure 7–7) or catalytic at the top of the bed. The temperature of the combustion gases rises to about 1,000–1,500°C, and subsequently drop as the gases undergo the endothermic mixed reforming reactions in the catalyst bed, to exit as syngas at a lower temperature. If the H_2/CO ratio of the syngas is not as desired, steam may be added to the feed.

Autothermal reformers face the same carbon forming challenges as other reforming reactors. Advantages of autothermal reformers include simple design (no heat transfer concerns), small size, and easy

control of H_2/CO ratios. Their main disadvantage is the need for an oxygen plant, justified economically only for fairly large units.

To avoid the disadvantage of requiring an expensive oxygen plant, a new reactor design (Figure 7–8) based on ceramic membranes has been proposed for small reforming plants. *Ceramic membrane reactors* perform both air separation and reaction in a single unit and do not require external energy to support the oxidation reaction. The critical component for these reactors is a dense ceramic membrane that can separate oxygen from air, thus making oxygen available for reaction with methane. The thin membrane (about 50–100 μm thick) sits on the outside of a porous ceramic and is composed of a dense ionic conducting mixed oxide, such as $La_{1-x}Sr_xCo_{1-y}O_{3-z}$.

The mechanism of separation of oxygen from air relies on the dissociation of oxygen molecules as they pass through the inner tube to form O^{2-} ions. These ions, in turn, diffuse through the thin outer layer and meet CH_4 in the annulus, where they recombine to form O_2 and react to form syngas according to Reactions (7.32) and (7.30). Features of membrane reactors that need to be addressed include low oxygen permeation rates, membrane stability, and fabrication and sealing of ceramic tubes.

Prereforming

Even though natural gas contains mostly methane, in some instances it may contain large amounts of higher hydrocarbons (e.g., 10% C_2–C_4). This would require large reforming reactors and would exacerbate carbon problems. In such instances, a prereforming process step may be added to a gas reforming process. The main reaction in prereforming is

$$2C_xH_y + 2zH_2O \leftrightarrows 2(x - z)CH_4 + 2zCO + (6z + y - 4x)H_2, \qquad (7.33)$$

where $y, x \geq 2$. Prereforming units are adiabatic with the feed entering around 300°C and subsequently reacting on a catalyst comprised of 70 wt% Ni on γ–Al_2O_3 substrate, to produce gas at 550°C. Methane in this gas is then converted to syngas in a downstream reforming unit that is smaller than would be required if the prereformed gas was fed directly at 550°C.

7.5.3 Fischer-Tropsch synthesis

The terms "Fischer-Tropsch synthesis" or "Fischer-Tropsch chemistry" refer to a wide variety of similar processes relying on catalytic chem-

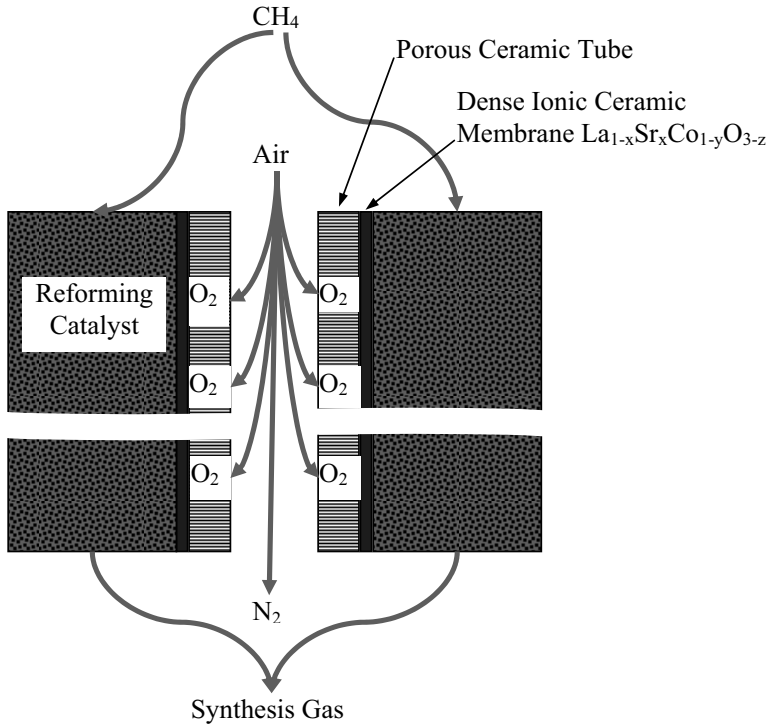

Figure 7–8 *Configuration of ceramic membrane partial oxidation reactor (not drawn to scale)*

ical reactions that produce liquid hydrocarbons from syngas. It was Franz Fischer and Hans Tropsch who made (and patented) significant advances associated with both the chemistry and engineering of corresponding processes, to deserve lending their names to the process. The timeline of Fischer-Tropsch synthesis is summarized in Figure 7–9.

Resulting from R&D at the Kaiser Wilhelm-Institut für Kohlenforschung (Coal Research) in the 1920s, the Fischer-Tropsch process allowed Germany to produce liquid fuels domestically from its abundant *coal* reserves and address its lack of petroleum resources. With major petroleum resources around the world controlled by the Allies, Fischer-Tropsch technology was used extensively by Germany and Japan to produce *ersatz* (substitute) fuels during World War II. Germany's industrial capacity was decimated towards the end of the war, as a result of Allied bombing. After World War II, US and British companies started using the Fischer-Tropsch process to produce synthetic

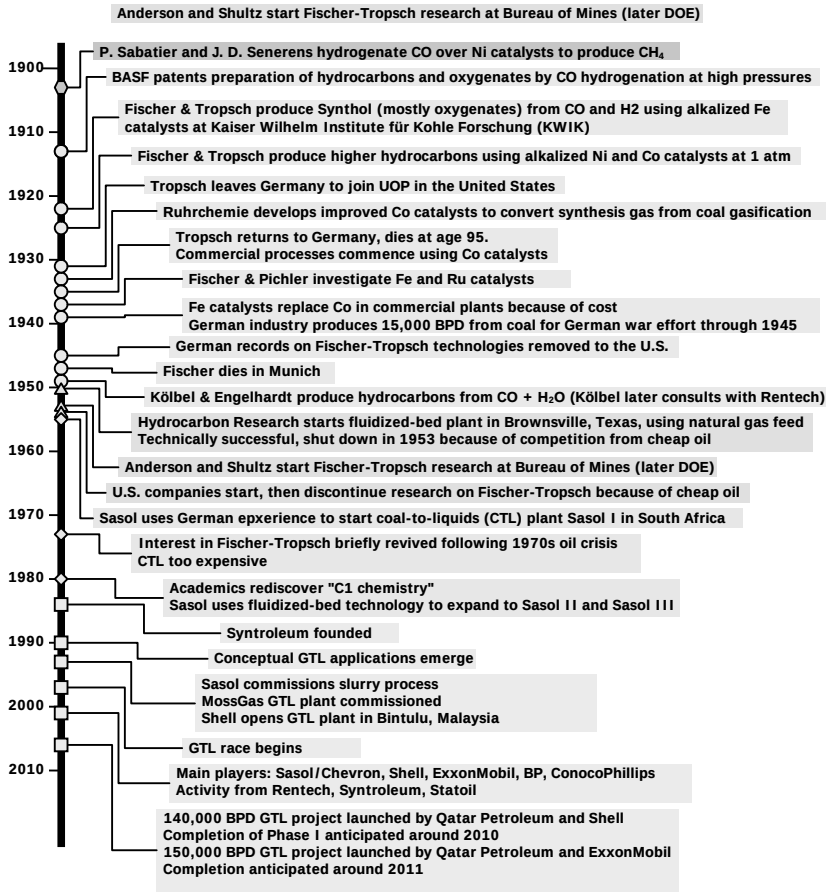

Figure 7–9 *Timeline of Fischer-Tropsch synthesis.* ⬡ *= The Beginning,* ○ *= The German Era,* △ *= The Post-War Era,* ◇ *= The South-African Era,* □ *= The Modern Era*

fuels. However, high capital and operating costs, environmental concerns, and most importantly, widely available cheap oil prompted all such efforts to falter.

Interest in Fischer-Tropsch was rekindled during the energy crisis of the 1970s, but especially in South Africa during its isolation under the Apartheid regime. Years of Fischer-Tropsch development have resulted in better catalysts and better engineering. Although the technology is now fairly well developed, there are currently only a handful of companies that are running commercial installations. Most notable is Sasol in South Africa, which uses syngas from coal and natural gas to produce a variety of synthetic petroleum products,

including most of South Africa's diesel fuel. However, a number of GTL projects involving Fischer-Tropsch are on the horizon, mainly in the Middle East.

In the following sections the basic Fischer-Tropsch chemistry, catalysts, reactor configurations, and industrial processes are examined.

Fischer-Tropsch chemistry

Fischer-Tropsch synthesis of hydrocarbons involves a vast number of reactions that can be summarized in the general form

$$n\mathrm{CO} + m\mathrm{H_2} \rightarrow \begin{Bmatrix} \mathrm{C_1 - C_{40+}\,alkanes} \\ \mathrm{C_1 - C_{40+}\,alkenes} \end{Bmatrix} + \begin{Bmatrix} \mathrm{H_2O} \\ \mathrm{CO_2} \end{Bmatrix}. \tag{7.34}$$

For example, the following general reactions may occur:

$$n\mathrm{CO} + (2n+1)\mathrm{H_2} \rightarrow \mathrm{C_nH_{2n+2}} + n\mathrm{H_2O}\ \text{(n-paraffins)}, \tag{7.35}$$

$$n\mathrm{CO} + 2n\mathrm{H_2} \rightarrow \mathrm{C_nH_{2n}} + n\mathrm{H_2O}\ \text{(olefins)}, \tag{7.36}$$

$$(6+n)\mathrm{CO} + (2n+9)\mathrm{H_2} \rightarrow \mathrm{C_{6+n}H_{6+2n}} + (6+n)\mathrm{H_2O}\ \text{(aromatics)}. \tag{7.37}$$

Alcohols or other oxygenates may also be formed, as

$$n\mathrm{CO} + 2n\mathrm{H_2} \rightarrow \mathrm{C_nH_{2n+2}O} + (n-1)\mathrm{H_2O}\ \text{(alcohols or other oxygenates)}, \tag{7.38}$$

but they are in very small amounts and are usually neglected. It is of historical interest that the original Fischer-Tropsch synthesis actually concentrated on oxygenates.

Whether the products of Reaction (7.34) contain alkanes or alkenes (with anywhere from one to 40+ carbon atoms) and H_2O or CO_2 depends primarily on:

- Ratio H_2/CO.
- Catalyst.
- Type of reactor.
- Process conditions.

Alkanes formed in Reaction (7.34) are mainly straight-chain and alkenes are mostly tertiary. In general, H_2O is formed if H_2 is in excess, otherwise CO_2 is formed. For syngas generated from natural gas (as part of a GTL process), the ratio H_2/CO is in the range 1.8–2.3 depending on the reforming method (see Section 7.5.2 "Natural Gas Reforming and Synthesis Gas"), and it is this ratio that Fischer-Tropsch is compatible with GTL. The preferred products for GTL are alkanes and H_2O.

Fischer-Tropsch synthesis may be used with syngas from other sources, such as coke, coal, and residue (H_2/CO = 0.6–0.8) and fuel oil or low Btu gas (H_2/CO = 0.9–1.1). Products other than alkanes may be pursued, such as alkenes (desirable for subsequent production of chemicals) or oxygenates (such as alcohols, ketones, and aldehydes) but these products are minimized when Fischer-Tropsch is part of a GTL scheme.

The precise mechanisms of Fischer-Tropsch reactions are quite complicated and details are still debated. Nonetheless, a simplified mechanism in place of thousands of reactions is useful, in that it can be used to explain the formation of observed products in terms of a single parameter, α, as will be explained below.

Fischer-Tropsch starts with the formation of the building block $–CH_2–$ through the reaction

$$CO + 2H_2 \rightarrow [–CH_2–] + H_2O, \quad \Delta H^\circ\ (25^\circ C) = –167.4\ \text{kJ/mol (CO)}, \tag{7.39}$$

or

$$CO + 2H_2 \rightarrow [–CH_2–] + CO_2. \tag{7.40}$$

The $–CH_2–$ blocks subsequently polymerize to yield final products. The composition of the final products depends on both the thermodynamics and kinetics of corresponding reactions. In general, the free energy of reaction increases with temperature for a product with a given number of carbon atoms, n, making this product less likely to form as temperature increases (Figure 7–10). At a given temperature, a product becomes thermodynamically less likely to form as n increases. In Figure 7–10 the shaded area represents the thermodynamically feasible area. (At a given temperature, increasing n would increase ΔG° and decrease ΔH°, corresponding to less favorable conversion and more heat released.) In the commercial temperature range of 200–350°C, all desired reactions are thermodynamically favorable. The significantly negative enthalpy of reaction makes it necessary to remove considerable amounts of heat.

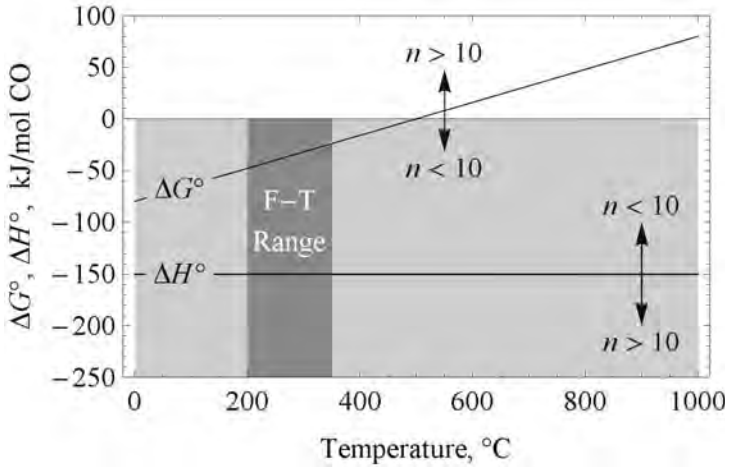

Figure 7–10 *Thermodynamics of the Fischer-Tropsch synthesis of decane (n = 10) via the reaction* $10CO + 20H_2 \rightarrow C_{10}H_{20} + 10H_2O$

Why is Fischer-Tropsch synthesis considered feasible at the range of temperatures shown in Figure 7–10? Because the equilibrium constant, *K,* of a reaction $\alpha A + \beta B... \rightarrow \sigma S + \tau T...$ is defined as

$$K = \frac{\{S\}^{\sigma}\{T\}^{\tau}...}{\{A\}^{\alpha}\{B\}^{\beta}...}, \tag{7.41}$$

where $\{S\}$ is the activity of species *S*, a dimensionless quantity that can be thought of as the mole fraction. According to reaction thermodynamics, the equilibrium constant *K*, of a reaction is related to the reaction free energy $\Delta G°$ by

$$K = \exp\left[-\frac{\Delta G^{\circ}}{RT}\right]. \tag{7.42}$$

From Eq. (7.42) it is clear that $K < 1$ when $\Delta G° > 0$, generally favoring higher mole fractions for the reactants rather than for the products. Conversely, $K > 1$ when $\Delta G° < 0$, generally favoring higher mole fractions for the products of the reaction. As Figure 7–10 indicates, $\Delta G° < 0$ for the range of products of interest in Fischer-Tropsch synthesis.

How exactly Reaction (7.39) (or (7.40)) occurs on the surface of a metal catalyst and how the subsequent polymerization proceeds can

be represented in terms of the following simplified polymerization scheme that involves three major steps:

1. **Chain initiation**—As shown in Figure 7–11, surface sites M on the catalyst readily chemisorb and dissociate H_2. CO is also chemisorbed initially in a bridged mode (involving two M sites) and equilibrates with a linear mode (only one M site). This is the point at which oxygen is removed, in this case by H_2 as H_2O. Two main paths are possible: (1) adsorbed CO dissociates into surface O (which reacts with H_2 to H_2O) and surface C (which hydrogenates to surface CH_2), and (2) adsorbed CO reacts with surface H to form a surface enol group (which hydrogenates to surface CH_2, liberating H_2O and forms surface CH_2). In either case, the resulting surface CH_2 is the chain carrier that builds the hydrocarbon molecule. There is evidence that option (1) is favored at higher temperatures and leads to excessive CH_4 formation via a parallel reaction. Option (2) prevails at lower temperatures, where the enol group can react further to produce oxygenated products.

2. **Chain growth**—Surface CH_2 (Figure 7–11) is polymerized, leading to adsorbed chains $–HC–(CH_2)_{n–2}–CH_3$ (Figure 7–12) where n takes a number of values.

3. **Chain termination**—Polymerization terminates when the adsorbed chains $–HC–(CH_2)_{n–2}–CH_3$ are released from the catalyst surface after combining with surface adsorbed CH_3 or H (yielding alkanes), or with an empty surface site (yielding alkenes (Figure 7–13)).

Secondary reactions, such as dehydrogenation of alkanes to alkenes, isomerization of n-alkanes to iso-alkanes, and hydrogenolysis to lighter alkanes may also occur after a hydrocarbon molecule is released from the catalyst surface, and readsorbed to follow other reaction paths.

It is evident from the above discussion that Fischer-Tropsch reactions are not selective towards a single product or an arbitrarily specific range of products; the only exception being methane, which can be produced with very high selectivity. Instead a distribution of products is obtained (Stenger and Askonas, 1986). Remarkably enough, the distribution of products as a function of the number of carbon atoms n in the chain of a product can be approximated in terms of a single parameter, the chain growth probability, α, defined as

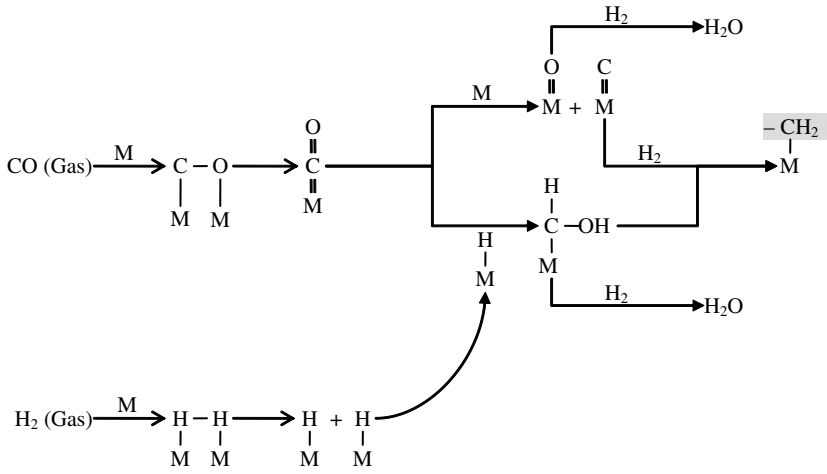

Figure 7–11 *Initiation step of Fischer-Tropsch reactions*

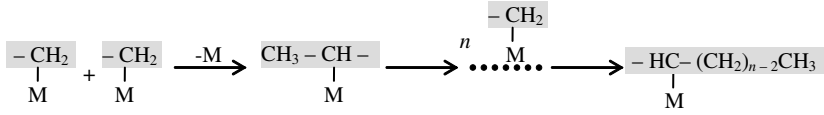

Figure 7–12 *Chain growth step of Fischer-Tropsch reactions*

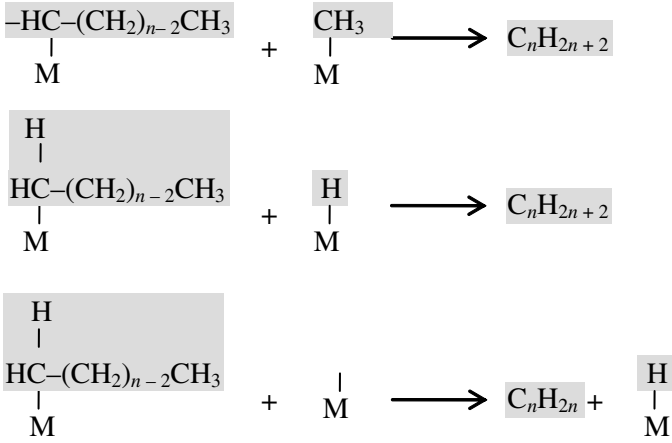

Figure 7–13 *Chain termination step of Fischer-Tropsch reactions resulting in alkanes (first two) or alkenes (third)*

$$\alpha = \frac{r_G}{r_G + r_T} , \tag{7.43}$$

where r_G and r_T are the reaction rates of chain growth (Figure 7–12) and termination (Figure 7–13). Application of classical polymerization concepts leads to the celebrated Anderson-Flory-Schultz (AFS) distribution function

$$W_n = n(1-\alpha)^2 \alpha^{n-1} , \tag{7.44}$$

where W_n, n = 1, 2,…, is the mass fraction of a product molecule with n carbon atoms in its chain. Eq. (7.44) can be visualized in Figure 7–14, which shows the theoretical dependence of mass fraction W_n of Fischer-Tropsch products of various lengths on the chain growth probability, α, according to the AFS Eq. (7.44).

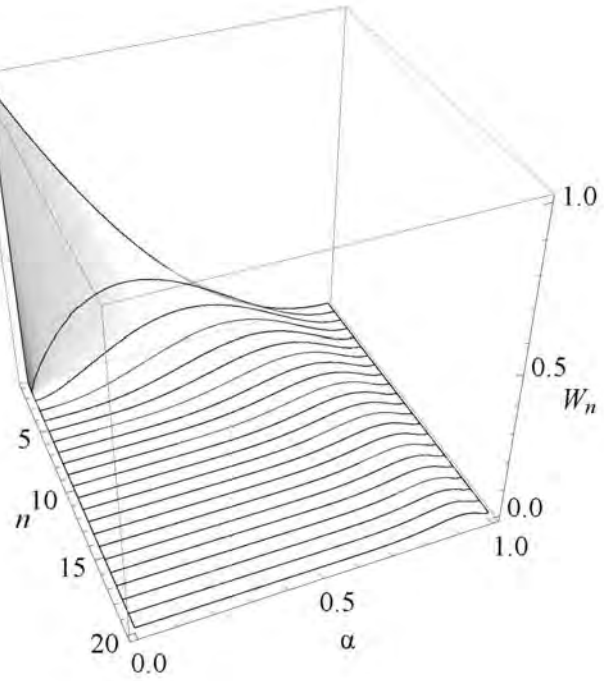

Figure 7–14 *Theoretical dependence of mass fraction W_n of Fischer-Tropsch products C_1–C_{20} on the chain growth probability, α, according to the AFS Eq. (7.44)*

Figures 7–15 and 7–16 show the theoretical distribution and cumulative distribution of Fischer-Tropsch products according to the AFS Eq. (7.44), for different values of the growth probability, α. It is clear that even though no arbitrary product compositions can be achieved, product distributions can be influenced by appropriately selecting the value of α, as shown in Figure 7–17. In Figure 7–17 fuel gas is C_1 and C_2, LPG is C_3 and C_4, gasoline is C_5 to C_{11}, diesel is C_{12} to C_{18}, and wax is C_{18+}. In addition to catalysts used, the main factors affecting α are process conditions, as shown in Table 7–9. For GTL plants, values of $\alpha > 0.95$ are desired to achieve almost complete conversion to liquids.

Note the increasing prevalence of low number hydrocarbons as α decreases. Note also that for $\alpha = 0$ (zero probability of chain growth) methane is the only product theoretically expected by AFS, according to Figure 7–14. In fact, measured values of methane and ethane mass fractions W_1 and W_2 always appear to deviate from the theoretical values predicted by AFS, as shown in Figure 7–15. The higher experimental selectivity of methane is due to parallel methanation reactions, and the lower selectivity of ethane results from readsorption and incorporation into growing chains. Long chains usually show higher selectivity than predicted by AFS.

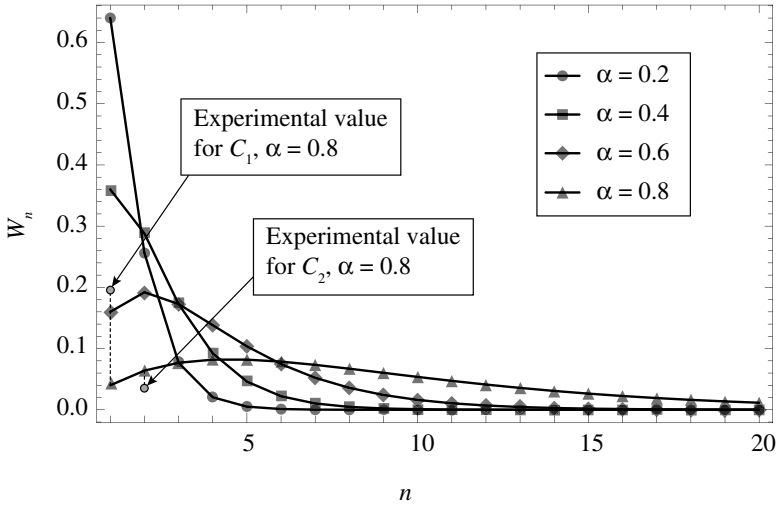

Figure 7–15 *Theoretical cumulative distribution* ($W_{k\le n} = \sum_{k=1}^{n} W_k$) *of Fischer-Tropsch products according to the AFS Eq. (7.44), for different values of growth probability, α*

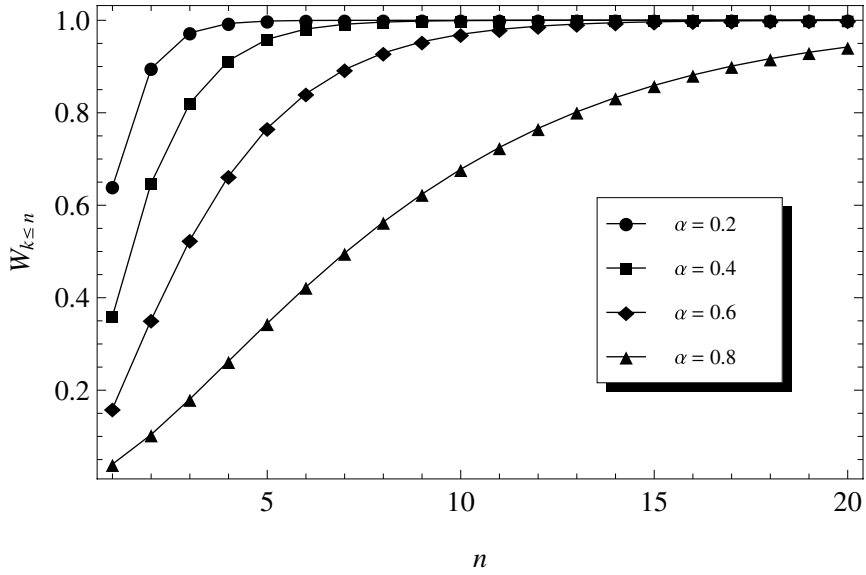

Figure 7–16 *Theoretical cumulative distribution of Fischer-Tropsch products according to the AFS Eq. (7.44), for different values of the growth probability, α*

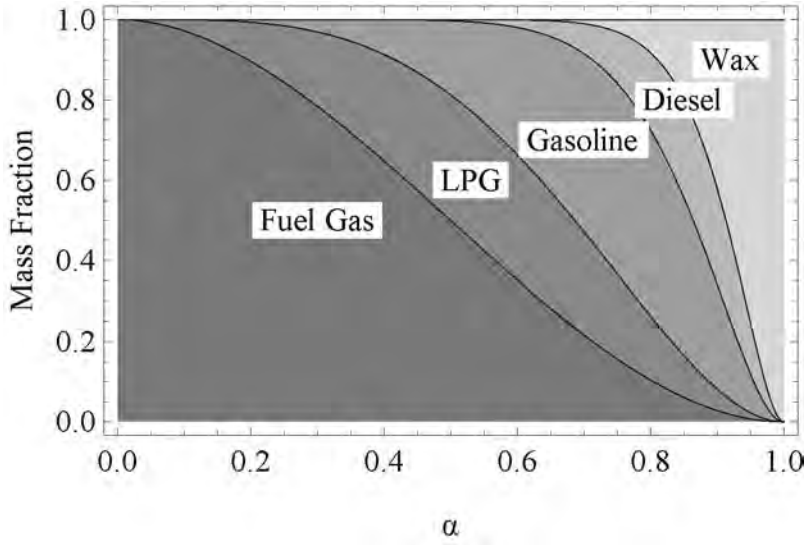

Figure 7–17 *Theoretical composition of fuel product from Fischer-Tropsch synthesis according to the AFS Eq. (7.44), for different values of the growth probability, α*

Table 7–4 Effect of Process Conditions on Chain Growth Probability, α

Process variable	Effect on α
Temperature	–
Pressure	–
H_2/CO	–
Residence time in reactor	+

Example 7–4 Maximum weight fractions of Fischer-Tropsch products

What is the maximum mass fraction for gas fuel, LPG, gasoline, diesel, and wax as well as the corresponding values of α predicted by the AFS equations?

Solution

These numbers can be computed by solving the equation:

$$\frac{d}{d\alpha}\sum_{n=n_{\min}}^{n_{\max}} n(1-\alpha)^2\alpha^{n-1} = \sum_{n=n_{\min}}^{n_{\max}} n(1-\alpha)\alpha^{n-2}(n-1-\alpha-n\alpha) = 0 \,, \qquad (7.45)$$

for α. The values of ($n_{\min}$, $n_{\max}$) are (1, 2) for fuel gas, (3, 4) for LPG, (5, 11) for gasoline, (12, 18) for diesel, and (19, ∞) for wax. For wax, the probability calculation identity

$$\sum_{n=1}^{\infty} n(1-\alpha)^2\alpha^{n-1} = 1 \,, \qquad (7.46)$$

yields

$$\sum_{n=1}^{\infty} n(1-\alpha)^2\alpha^{n-1} = 1 - \sum_{n=1}^{18} n(1-\alpha)^2\alpha^{n-1} \,,$$

which can be used to compute

$$\frac{d}{d\alpha}\sum_{n=19}^{n_{\max}} n(1-\alpha)^2\alpha^{n-1} \quad \text{as} \quad -\frac{d}{d\alpha}\sum_{n=1}^{18} n(1-\alpha)^2\alpha^{n-1} \,.$$

Numerical solution of Eq. (7.45) yields the results in Table 7–5. The same results can be visualized in Figure 7–18, where the peaks of corresponding weight fraction curves can be observed.

Example 7–5 Operating envelop for Fischer-Tropsch to produce desired products

Assume that operating conditions and a catalyst have been selected to result in the value of α required for production of diesel fuel at its maximum mass fraction, as calculated in Example 7–4. What can be expected if the resulting value of α is within ±10% of its optimal value?

Solution

According to Table 7–5, the value of α for maximum diesel production is $\alpha_{\text{diesel}} = 0.87$. Fluctuations of that value by ±10% yield $\alpha_{\text{low}} = 0.78$ and $\alpha_{\text{high}} = 0.96$ for which the corresponding diesel fractions

$$W_{diesel} = \sum_{n=12}^{18} n(1-\alpha)^2 \alpha^{n-1}$$

are 17% and 9.3%, respectively (see Figure 7–18), i.e., quite lower than the optimum value of 25%.

It should also be noted that the mass fraction of wax

$$W_{wax} = \sum_{n=19}^{\infty} n(1-\alpha)^2 \alpha^{n-1}$$

at $\alpha_{\text{high}} = 0.96$ is 83%. This might create operating problems, given that waxes become solid at lower temperatures.

Example 7–6 Average mass fraction of Fischer-Tropsch products for varying α.

Assume again that operating conditions and a catalyst have been selected to result in the value of α required for production of diesel fuel at its maximum mass fraction, as calculated in Example 7–4. What is the average mass fraction of diesel if the resulting value of α fluctuates uniformly within ±10% of its optimal value?

Table 7–5 Maximum Mass Fractions of Fischer-Tropsch Products

Fraction	Maximum % mass	α
Fuel gas	100	0
LPG	32	0.55
Gasoline	48	0.76
Diesel	25	0.87
Wax	100	1

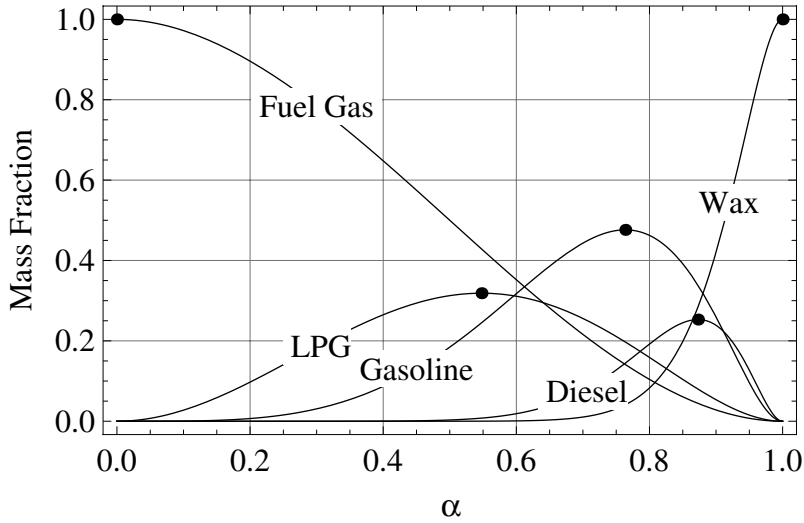

Figure 7–18 *Theoretical composition of fuel products from Fischer-Tropsch synthesis according to the AFS Eq. (7.44), for different values of the growth probability, α*

Solution

The average mass fraction for diesel can be calculated as

$$\frac{1}{0.96-0.78}\sum_{n=12}^{18}\int_{0.78}^{0.96} n(1-\alpha)^2\alpha^{n-1}d\alpha = \alpha^{12} - \frac{11\alpha^{13}}{13} - \alpha^{19} + \frac{9\alpha^{20}}{10}\Bigg|_{0.78}^{0.96} = 21\% \ .$$

Fischer-Tropsch catalysts

Appropriate catalyst selection can influence the reactions outlined in the basic mechanism of Fischer-Tropsch reactions, thus affecting the distribution of products. Table 7–6 outlines basic activities that Fischer-Tropsch catalysts should exhibit, along with the most important candidates. This table explains the catalyst selections made by the pioneers shown in Figure 7–9. Catalyst selection affects the value of the chain growth probability α, thus affecting product distribution. Table 7–7 summarizes the effect on α of basic variables related to catalyst composition and preparation.

Table 7–6 Effect of Catalyst Metal Selection on Desired Fischer-Tropsch Activity

Desired activity	Candidate catalyst (in order of activity)
High CO activation rate	Ru > **Fe** > Ni > **Co** > Rh > Pd > Pt
Low hydrogenolysis	**Fe** < Pd < Pt < **Co** < Rh < Ni < Ru
Low shift activity at high H_2/CO	Rh < Pd < **Co** < Pt < Ni < Ru < Fe
High shift activity at low H_2/CO	**Fe** > Ru > Ni > Pt > Co > Pd > Rh
High hydrogenation activity (when alkanes are preferred)	Rh > Ru > Pd > Pt > Ni > **Co** > **Fe**

Table 7–7 Effect of Catalyst Variables on Chain Growth Probability, α

Catalyst variable	Effect on α
Metal	Co > Ru > Fe
Support	$TiO_2 > Al_2O_3 > SiO_2$
Promoter (K_2O, rare earth oxides, V_2O_5, ZrO_2, TiO_2, Cr_2O_3)	+
Crystallite size	+
Metal concentration	+
Pellet size	–

Modern technologies focus completely on Fe and Co, with Co preferred for GTL. Ni and Ru may also be used, but they cause excessive hydrogenolysis leading to the formation of methane and are expensive. Due to their industrial importance, basic facts about Fe and Co catalysts are discussed next. In summary, Fe is more flexible, less delicate, and cheaper than Co; whereas Co is more chemically straight forward, and more susceptible to promotion that improves selectivity and lifetime.

Iron catalysts for Fischer-Tropsch synthesis generally consist of precipitated or fused Fe and need no support because of its low cost. A number of promoters for higher activity and selectivity (such as K and Cu) and structural stabilizers (such as Al_2O_3 or SiO_2) may be added (see Table 7–8). The active phase is Fe carbides ($Fe \rightarrow Fe_3C \rightarrow Fe_5C_2$). The presence of steam in the gases oxidizes the catalyst ($Fe_5C_2 \rightarrow Fe_3O_4$). Iron catalysts can work in a wide range of conditions, but are sensitive to S in the feed gas. They do not last long (order of weeks), are not worth regenerating, and are easy to dispose of. They can be used with syngas of H_2/CO ratios 0.7–2, but result in low yields. They tend to lower the value of the chain growth probability α, favor the production of light olefins (alkenes) with low selectivity towards CH_4, lower the production of heavy waxes, and form CO_2 (cf. Reaction (7.34)).

Cobalt catalysts consist of precipitated Co on an inexpensive support, such as TiO_2, Al_2O_3, SiO_2, C, or MgO acting as promoters, in decreasing order of activity (Table 7–10). The active phase is metallic Co. Steam has practically no effect on Co catalysts. Cobalt catalysts can work in a limited range of conditions (without shift reactions), and are even more sensitive to S in the feed gas than Fe catalysts. They can last for years, can be regenerated, but are difficult to dispose of because of environmental concerns (necessity to reclaim Co as heavy metal). They can be used with syngas of H_2/CO ratio 2, but result in high yields. They tend to increase the value of the chain growth probability α, form mostly paraffinic products (alkanes), and favor the production of heavier hydrocarbons because they can easily readsorb and induce further polymerization of intermediate products. The main oxygen containing byproduct is H_2O (see Reaction (7.34)).

Fischer-Tropsch reactors

Reactor design for Fischer-Tropsch synthesis has significant effects on product composition (by influencing the chain growth probability α), operability, safety, and economics. Although different designs are provided by various companies, the following three reactor categories can be identified, namely fixed-bed, circulating and entrained fluidized-bed, and slurry reactors (Figure 7–19).

Table 7–8 Promoters of Fe Catalysts

Promoter	Effect	Reason
K_2O	Increases α	Donates electrons to Fe
	Decreases CH_4	Increases CO adsorption
	Increases olefins	Decreases H_2 dissociation
MnO_2, V_2O_5	Increases light paraffins	Increases surface concentration of H, CO
TiO_2	Increases light paraffins	Increases CO dissociation at metal/interface; lowers reducibility of mixe oxide
La_2O_3	Increases rate	Decorates metal surface
Y_2O_3	Increases rate	Increases CO adsorption
ThO_2	Increases rate	Lowers support acidity
Cu	Increases reduction rate	Dissociates H_2

Table 7–9 Effect of Process Conditions on Chain Growth Probability, α

Process variable	Effect on α
Temperature	–
Pressure	–
H_2/CO	–
Residence time in reactor	+

Fixed-bed reactors

Fixed-bed reactors consist of a bundle of a few thousand long narrow tubes sitting vertically inside a vessel. Each tube contains catalyst particles (about 2–3 mm in diameter). The vessel also acts as heat exchanger to remove the Fischer-Tropsch reaction heat by generating steam on the outer side of the tubes.

Table 7–10 Promoters of Co Catalysts

Promoter	Effect	Reason
K_2O	Increases α	Donates electrons to Fe
	Decreases CH_4	Increases CO adsorption
	Increases olefins	Decreases H_2 dissociation
ZrO_2, V_2O_5	Increases α	Increases surface concentration of H, CO
TiO_2, Cr_2O_3, La_2O_3	Increases light paraffins	Increases CO dissociation at metal/interface; lowers reducibility of mixed oxide
Ru	Increases activity	Decreases carbon poisoning
Fe, Re, Au	Less attrition	Increases active sites

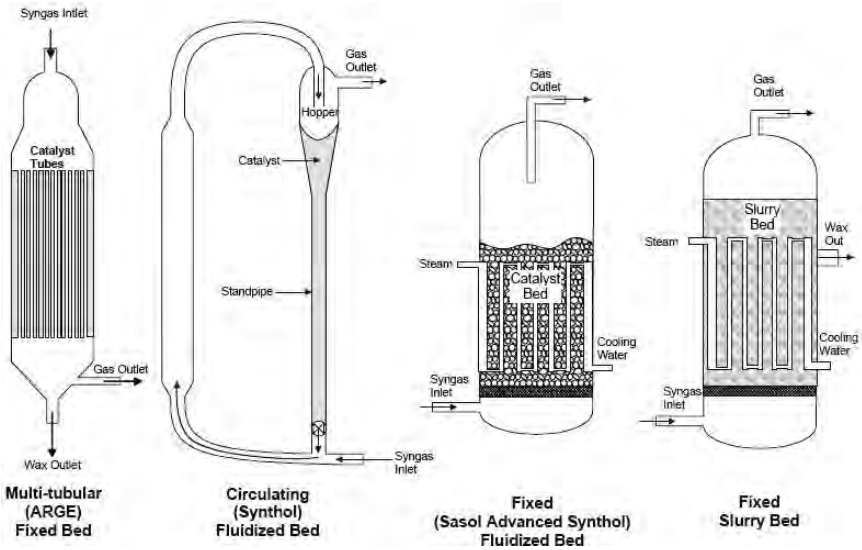

Figure 7–19 *Types of Fischer-Tropsch reactors* (Spath and Dayton, 2003)

Fixed-bed reactors are simple, flexible, and easy to scale up. However, they have a number of disadvantages:

- High cost.
- Multiple reactors in parallel are required for larger plants.

- To avoid high pressure drop in the reactor tubes, large catalyst particles are needed resulting in low effectiveness factor (low catalyst activity per unit mass, resulting from difficulty of reactants to diffuse into the core of a catalyst particle).

- Low heat transfer from the catalyst bed and temperature variation in the tubes. This results in (a) difficulty in controlling product composition due to variability of the chain growth probability α; (b) hot spots in the catalyst bed that may lead to catalyst sintering and reactor instability; and (c) low conversion (35–40%) necessary to avoid excessive temperatures (in this case, unreacted feed may be recycled).

Packed-bed reactors were originally used by Fischer and Tropsch and by Sasol. They remain an option for relatively small GTL plants.

Circulating and entrained fluidized-bed reactors

Circulating fluidized-bed reactors address the heat removal problems that affect fixed-bed reactors. Heat is removed through internal cooling coils that make steam in the reaction section (in Figure 7–19), where small catalyst particles (100 μm) circulate with the feed. The products of the reaction and the catalyst circulate from the reaction section to the separation section (right) where products are removed.

Fluidized-bed reactors have a number of advantages:

- Better heat removal results in isothermal operation with better product control.

- Smaller catalyst particles result in higher effectiveness factor.

- Small unit size.

- Because of circulation, fresh catalyst can be added and deactivated catalyst removed.

However, fluidized-bed reactors also have a number of disadvantages:

- Complex design and difficult scale-up. More recent designs using an entrained fluidized-bed have resulted in increased capacity, and lower complexity, size, cost, and catalyst consumption.

- Catalyst agglomeration caused by liquid product sticking to the particles. To avoid this, the operating temperature can be maintained above the dew points of the products, which may

inadvertently force the value of α to be low (with products only suitable for gasoline and chemicals markets).

A comparison of fixed-bed and circulating-bed reactors is shown in Table 7–11.

Slurry reactors

Another way to alleviate the poor heat transfer problem of packed-bed reactors is the use of slurry reactors. The slurry is a mix of catalyst particles (10–200 μm) and product oil at about 35% in a reactor (in Figure 7–19). Reaction heat is removed by internal cooling coils that generate steam. Part of the slurry is taken out of the reactor where the oil is removed at a filter, and catalyst particles are separated and recycled.

Slurry reactors have the following advantages:

- They are suitable for large-scale designs.
- Temperature control is effective, resulting in high conversion and high values for α (0.95–0.98).
- Pressure drop is low.
- Catalyst can be replenished after separation at the filter.
- Units are compact, easy to scale up, and less expensive than packed-bed designs.

Slurry reactors have the following disadvantages, which will be likely overcome in the future:

- High viscosity of slurries.
- Catalyst particle settling and attrition.
- Low mass transfer in the liquid.
- Filtration difficulties.

7.5.4 Product upgrading

Product upgrading uses standard processes from petroleum refining to make GTL products more desirable.

Since Fischer-Tropsch units are operated at high values of α to avoid gases in the products (Figure 7–17), they produce large percentages of heavy linear waxes. These waxes are converted to more

Table 7–11 Comparison of Fixed and Circulating-Bed Selectivities

Process variable	Fixed bed	Circulating bed
Temperature, °C	180–250	330–350
α	0.95	0.85
Product	Selectivities (% carbon basis)	
CH_4	4	7
C_2–C_4 alkenes	4	24
C_2–C_4 alkanes	4	6
Gasoline (naphtha)	18	36
Middle distillate (diesel)	19	12
Waxes	48	9

valuable hydrocarbons in the middle distillate range (diesel and naphtha) through the process of *hydrocracking*. Hydrocracking is a mature catalytic process developed in petroleum refining, where it serves the same purpose. There are many reactor designs, using different types of catalysts to perform both cracking with acidic sites and hydrogenation with metal sites. Examples are Pt incorporated into zeolites and Co, Ni, Mo, and W supported on SiO_2–Al_2O_3 or zeolites. Since Fischer-Tropsch products contain no sulfur or nitrogen compounds and no aromatics, they are cleaner than petroleum feeds, making GTL streams much easier to hydrocrack than petroleum.

Adiabatic fixed-bed reactors are used with extruded catalysts. Inlet temperatures range from 300 to 350°C and pressures from 30 to 45 atm. The linear alkanes are cracked almost completely in half, so that only the C_{20+} Fischer-Tropsch products are treated. Alkenes are hydrogenated to alkanes and oxygenates converted through hydrogenolysis. An excess of hydrogen of two to three times the amount needed for hydrotreating is used to control coking. Hydrogen is produced by steam reforming of the light ends from the Fischer-Tropsch unit. Typical compositions of products before and after hydrocracking are shown in Figure 7–20.

There are other upgrading processes, such as isomerization and catalytic reforming, which convert Fischer-Tropsch products into gasoline and chemicals. These are the same as practiced in petroleum

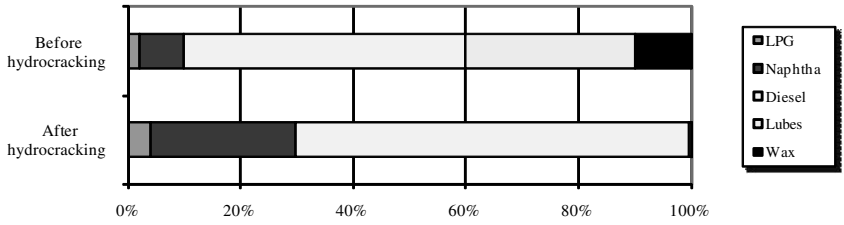

Figure 7–20 *Typical compositions of Fischer-Tropsch products before and after hydrocracking*

refining, and are not discussed here since the main objective of GTL is to convert natural gas into transportable liquids.

7.6 GTL economics and outlook

Making an accurate economic feasibility analysis of GTL projects is difficult, given the fluctuation of oil and gas prices, as well as the continuous evolution of GTL technology and cost of GTL plants. Nevertheless, there are cost/benefit drivers that dominate GTL processes (Seddon, 2004). In this section, the most basic drivers of GTL economics are outlined, with a full understanding that these drivers evolve with time.

In general, GTL is expected to cover a small part of the global demand for fuels in the foreseeable future. Rather than producing fuels economically, GTL's main claim (in addition to facilitating natural gas transportation) is the quality and environmental friendliness of produced fuels. As such, GTL fuels can be blended with refinery fuels, to improve quality. For example, GTL diesel is sold in small quantities as blendstock in a number of locations.

GTL processes are both capital and energy intensive. However, fixed costs have been steadily going down as a result of technological improvements. From a value of about $120,000 of investment per barrel of fuel produced in the 1950s, the cost has decreased to less than $50,000/bbl, and recent claims place that value below $35,000/bbl. The target is to reach below $20,000/bbl. This may become feasible in the future, if scientific (catalysis) and technological advances can improve efficiency of GTL processes. By comparison, the corresponding value for crude oil refining is a little over $10,000/bbl.

The dominant step in a GTL process is the production of syngas through reforming. Reforming accounts for more that half of the capital cost and about 20–30% of the total energy losses of a GTL process

(Seddon, 2004). The fixed and operating costs of Fischer-Tropsch synthesis are roughly half of those of reforming. Product upgrading accounts for the remaining costs.

Several efforts are underway to reduce GTL costs. In general, these efforts strive to balance fixed and operating costs. As an example to contain fixed costs, compact reforming processes have been developed to reduce cost by eliminating the need for large and expensive oxygen plants. Optimization of operating costs is more complicated. Economic optimization is based on efficient conversion of natural gas to high value products, without excessive fixed cost requirements. When producing GTL fuels, the key issue is how to economically maximize the production of liquids, particularly middle distillates (such as diesel) in the Fischer-Tropsch and upgrading steps. As Example 7–4 illustrates, the products of Fischer-Tropsch synthesis cannot contain more than 25% diesel fuel. At that optimum, there will be significant amounts of both light hydrocarbons and waxes, which are not of high value. Upgrading would then be necessary. To avoid having to upgrade both light hydrocarbons and wax, Fischer-Tropsch synthesis conditions are adjusted so that either light hydrocarbons or wax are not produced (see Figure 7–17). If light hydrocarbons are avoided, then significant amounts of wax will be produced. Wax is then upgraded (cracked) to produce liquid fuels. Alternatively, the fraction of light hydrocarbons produced by Fischer-Tropsch synthesis can be increased and the amount of wax minimized. Light hydrocarbons can be made rich in olefins (by dehydrogenation of paraffins produced). The olefins can then be oligomerized, to produce liquids, which can be further hydrogenated to produce diesel fuel. As another example of operating cost optimization, high value chemicals rather than fuels may be produced. However, this approach may introduce operational complexity.

7.7 References

Bartholomew, C.H. and R. J. Farrauto. 2005. *Fundamentals of Industrial Catalytic Processes*. 2nd ed. New York: John Wiley & Sons.

Khataniar, S., G.A. Chukwu, S.L. Patil, and A.Y. Dandekar. 2004. Technical and economic issues in transportation of GTL products from Alaskan North Slope to markets. Paper SPE 86931.

Khataniar, S., G.A. Chuwku, S.L. Patil, and A.Y. Dandekar. 1997. Technical and economic issues in transportation of GTL products from Alaskan North Slope to markets. Synopsis published in the *JPT*, April 2004.

Rase, H.F. 1977. *Chemical Reactor Design for Process Plants*. Vols. 1 and 2. New York: John Wiley & Sons.

Seddon, D. 2004. Why is GTL so expensive? Paper SPE 88632.

Spath, P.L., and D.C. Dayton. 2003. Preliminary screening-technical and economic assessment of synthesis gas to fuels and chemicals with emphasis on the potential for biomass-derived syngas. NREL/TP-510-34929.

Stenger, H.G., and C.F. Askonas. 1986. Thermodynamic product distributions for the Fischer-Tropsch Synthesis. *Ind. Eng. Chem. Fundam.* 25: 410–413.

Steynberg, A. and M. Dry (Eds.) 2004. *Fischer-Tropsch Technology*. Burlington, MA: Elsevier.

7.8 Appendix—Catalysis *(Bartholomew and Farrauto, 2005)*

Catalysis is a technique that *accelerates* (or sometimes decelerates) *a chemical reaction* towards equilibrium. The acceleration is accomplished by a *catalyst*, namely a substance that facilitates the reaction, without itself being altered or consumed by the reaction. The degree to which a reaction is accelerated is termed catalyst *activity*, and can reach several orders of magnitude. Since a catalyst may selectively accelerate a chemical reaction from a set of competing possible reactions, it can steer a system of reactants towards rapid production of desirable products, thus improving the *selectivity* of the system. Catalysis is both a naturally occurring phenomenon and a human-made technology—with very long history. Life itself relies on catalysis, as thousands of enzymes (biological catalysts) continuously steer biological reactions towards highly specialized directions in living organisms. As a technology, catalysis is ubiquitous in shaping many aspects of modern life. Catalytic converters have made modern cars much less polluting. Fluid catalytic cracking (FCC), a process discovered serendipitously in the 1940s, accounts for more than half of the global production of gasoline. Of course, catalysis is of paramount importance for GTL technologies.

Industrial catalysts are usually solids, catalyzing reactions involving gases or liquids. They are shaped as pellets or powders. An industrial catalyst works by providing a *catalytic surface* with active sites or centers, on which reactants are chemisorbed and are thus facilitated (by having to overcome lower energy barriers) to react with neighboring molecules that are also adsorbed on the surface. Selectivity results from the catalyst surface steering adsorbed reactants

towards specific products. For example, synthesis gas (CO and H_2) can be steered to react towards production of mostly methane, methanol, or hydrocarbons if Ni, Cu, or Fe catalysts are used.

Since catalytic activity is available at the surface of the catalyst, solid catalysts, such as metals, oxides, sulfides, or alumino-silicates, are prepared as small crystallites to make as much surface area as possible available to reactants. These classes of main components of catalysts function in different ways. Metals and oxides initiate redox-type reactions, such as hydrogenation, oxidation, and hydrogenolysis. Metals have more activity, but oxides exhibit better selectivity because of their complex structures. Alumino-silicate materials are solid acids and induce carbonium-type reactions, such as cracking, isomerization, and polymerization. An industrially important class of alumino-silicate catalysts is *zeolites*, which are molecular cages that allow shape selective reactions, in which the size of the openings into zeolite cages restricts reaction of molecules because of their size.

Catalyst activity or selectivity may decrease as a result of sintering or poisoning. *Sintering* refers to the growth of crystallites with time and it accelerates with time. *Poisoning* results from chemisorption of feed impurities, such as sulfur, on active sites, which then become deactivated. It is catalytic converter deactivation problems (in addition to public health concerns) that have prompted the elimination of lead based additives for octane number boosting from gasoline. Catalyst deactivation may also result by carbon deposition on active sites as a result of a number of coking reactions (carbon formation from hydrocarbon decomposition at high temperature), all of which are undesirable. Coking may be so severe, that continuous catalyst regeneration may be required, as in the case of fluidized catalytic cracking (FCC) reactors.

In addition to the preparation of the main component, catalytic activity and stability can be optimized by appropriate choice of catalyst *support* and *promoters*. The most important function of catalyst support is to ensure that the active component is dispersed enough to provide the largest possible number of active sites on the catalyst surface. To accomplish this, the crystallites of the active material are spread over an inert surface to avoid interactions. The support material is made of materials with high melting points, such as α–Al_2O_3 γ–Al_2O_3, MgO, or ZrO_2, to avoid sintering. Support materials often have acidic activity, which leads to inadvertent carbon deposition. Another important role of catalyst support is to impart desired properties (e.g. size, shape, hardness) to catalyst pellets or powders, suitable for a variety of reactors. The role of a catalyst promoter is to affect the performance of either the active component or the support.

Promoters are added in small amounts to a catalyst. For example, small (<3 wt%) amounts of K_2O added to γ–Al_2O_3 neutralize inherent acid sites and prevent excessive coking. Metals are promoted by alloying with a second metal that changes either the activity or selectivity of the host metal.

The development of catalysts remains a combination of solid science and art. Catalyst designers rely on a vast database of known catalysts, high performance computations that purport to predict the most promising candidates for a certain kind of catalytic activity, and experiments. The performance of a catalyst depends critically on a number of factors besides composition, such as method of preparation and pretreatment before use. Finding the best recipe for making a catalyst is an iterative process, involving trial and error. Elements of this process are carefully guarded industrial secrets.

Catalysis is prevalent in GTL technologies, particularly in Fischer-Tropsch synthesis, where the design of a successful catalyst is often the deciding factor for the success of a proposed process.

CHAPTER 8

Underground Natural Gas Storage

8.1 Introduction

In the United States and a few other countries, the underground storage of natural gas has become increasingly important after World War II. The obvious reason for storage is that, traditionally, natural gas usage has been changing with seasons. The demand has been higher in the winter, prompted by residential heating. Thus, the "base load" and the "peak load" natural gas, not just in different seasons, but also different days within a season, can be quite different. This situation could create an imbalance between the receipts and deliveries of a pipeline network. To avoid supply disruptions, underground storage can be used to provide pipelines, local distribution companies, producers, and pipeline shippers with an inventory management tool, seasonal supply backup, and access to natural gas as needed (EIA, 2008). In addition, natural gas storage is also used by industry participants for commercial purposes: to store gas when gas price is low and withdraw and sell gas when the price is high (Speight, 2007).

Currently, most of the natural gas storage facilities are in the United States, with very few in Japan and Europe. By the end of 2007, there were about 400 underground storage reservoirs in the United States with working gas capacity of ~4,100 Bcf and deliverability rate potential of ~89 Bcf/d (EIA, 2008). There are other ways to store natural gas (such as in liquid form in above-ground tanks as LNG, discussed in Chapter 6). In this chapter, we will only focus on underground natural gas storage. The impact of LNG on gas storage will be briefly discussed at the end of the chapter.

8.2 Types of Underground Storage

There are primarily three types of underground storage facilities, and the descriptions below, widely acceptable in the industry, are taken mostly from the EIA (2004):

- **Depleted oil or gas reservoirs**—The advantage of converting a field from production to storage duty is that one can use the existing wells, gathering systems, and pipeline connections. It is usually close to consumption centers. This type of underground storage sites, as shown in Figure 8–1, is widely used in the United States (about 326 sites, accounting for 82 percent of the total at the beginning of 2008, EIA, 2008).

- **Aquifers**—An aquifer is suitable for gas storage if the water bearing sedimentary rock formation is overlain with an impermeable cap rock. Storage is created by injecting gas and displacing the water. Therefore, the water movement and cap rock quality should be taken into account when selecting and designing the storage (Katz and Tek, 1981). This type of storage usually requires more base (or cushion) gas (for definition see Section 8.3 "Storage Measures") and greater monitoring of withdrawal and injection performance. With the presence of an active water drive, the deliverability rates may be enhanced.

- **Salt caverns**—Salt caverns provide very high withdrawal and injection rates relative to their working gas capacity. Base gas requirements are relatively low. As shown in Figure 8–1, the large majority of salt cavern storage facilities have been developed in salt dome formations located in the US Gulf Coast States. Salt caverns have also been leached from bedded salt formations in the Northeastern, Midwestern, and Southwestern United States to take advantage of the high injection/withdrawal rates and flexible operations possible with a cavern facility. Cavern construction is more costly than depleted field conversions when measured on the basis of dollars per thousand cubic feet of working gas capacity, but the ability to perform several withdrawal and injection cycles each year reduces the per unit cost of each thousand cubic feet of gas injected and withdrawn.

Some reconditioned mine caverns have been in use as well. Hard rock caverns can also be good candidates of gas storage (Heath et al., 1998).

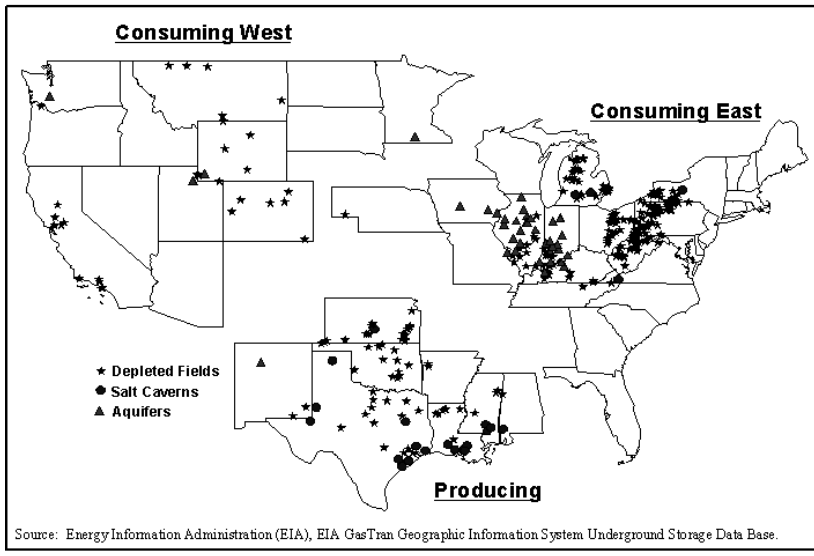

Figure 8–1 *U.S. Underground natural gas storage facilities in the lower 48 states* (EIA 2004)

To determine a field's suitability as a natural-gas -storage, its physical characteristics such as porosity, permeability, and retention capability should be examined along with the site preparation costs, deliverability rates and cycling capability. The good underground storage reservoir is obviously the one that has high capability to hold natural gas for future use and high deliverability rate at which gas inventory can be withdrawn.

8.3 Storage Measures

It is necessary to introduce some of the concepts used in storage calculation before we go to the detailed calculation of the storage capacity. For consistency, here we use the same definitions as they are used by EIA (2004):

- **Total gas storage capacity—**the maximum volume of gas that can be stored in an underground storage facility by design. It is determined by the physical characteristics of the reservoir and installed equipment.

- **Total gas volume in storage—**the volume of storage in the underground facility at a particular time.

- **Base gas or cushion gas—**the volume of gas intended as permanent inventory in a storage reservoir to maintain adequate pressure and deliverability rates throughout the withdrawal season. It contains two elements (Tureyen et al., 2000):

  - *Recoverable base gas*—the portion of the gas that can be withdrawn with current technology, but it is left in the reservoir to maintain the pressure.

  - *Non-recoverable base gas*—the portion of the gas that cannot be withdrawn with the existing facilities both technically and economically.

  The relationship among the total gas storage capacity, total gas volume in storage, and base gas is illustrated in Figure 8–2.

- **Working gas capacity**—the total gas storage capacity minus base gas, i.e., the volume of gas in the reservoir above the level of base gas. So, for a given storage capacity, the higher the base gas is, the lower the working gas will be, the less efficient the storage will be.

- **Injection volume**—the volume of gas injected into storage fields during a given period.

- **Deliverability or deliverability rate, withdrawal rate, withdrawal capacity**—a measure of the amount of gas that can be delivered or withdrawn from a storage facility on a daily basis with the unit of MMscf/d, same as that for production rate. Occasionally, it is expressed in terms of equivalent heat content of the gas withdrawn from the facility such as dekatherms per day. A therm is roughly equivalent to 100 scf of natural gas; a dekatherm is about 1 Mscf. In general, a facility's deliverability rate varies directly with the total amount of gas in the reservoir; it is at its highest when the reservoir is most full and declines as working gas is withdrawn.

- **Injection capacity or rate**—the amount of gas that can be injected into a storage facility on a daily basis. As with deliverability, injection capacity is usually expressed in MMscf per day, although dekatherms per day is also used. By contrast, the injection rate varies inversely with the total amount of gas in storage; it is at its lowest when the reservoir is most full and increases as working gas is withdrawn.

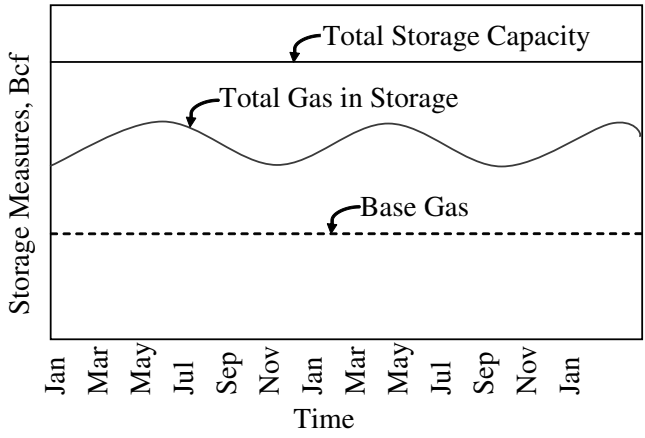

Figure 8–2 *Storage measures*

These measures for any given storage facility are not necessarily absolute and are subject to change or interpretation. In the following sections, natural gas storage is viewed in terms of a depleting or increasing pressure in a closed reservoir without active water drive. If the reservoir pressure is supported by active water movement, equations have to be modified (Katz and Tek, 1981; Mayfield, 1981).

8.3.1 Total Gas Volume and Injected Gas Volume in Storage

The injected gas volume in a depleted gas reservoir can be calculated by using a similar approach as discussed in Section 1.6.4 "Gas Formation Volume Factor" of Chapter 1 for the initial gas-in-place calculation of a producing field (Eq. (1.13)). Assume the reservoir pore volume is constant, the initial gas-in-place in the depleted gas reservoir in standard conditions is G_i, and the total gas volume in storage facility is G, then the cumulative injected gas volume, G_s is

$$G_s = G - G_i, \tag{8.1}$$

or, by employing the formation volume factors at initial and final conditions

$$G = G_i \frac{B_{gi}}{B_g} - G_i = G_i \left(\frac{B_{gi}}{B_g} - 1 \right). \tag{8.2}$$

Note: the G_i is the residual gas in a depleted gas reservoir that will be used for storage, or the initial gas in a storage field after the seasonal withdrawal and at the beginning of the resumption of injection. It can be calculated by using Eq. (1.13). Substituting Eq. (1.12) into Eq. (8.2) and assuming the temperature is constant, Eq. (8.2) becomes

$$G_s = G_i\left(\frac{p/Z}{p_i/Z_i} - 1\right) = \frac{G_i}{p_i/Z_i}\left(\frac{p}{Z} - \frac{p_i}{Z_i}\right). \tag{8.3}$$

In Eqs. (8.1 to 8.3), the subscript *i* stands for the initial conditions of the gas storage. The pressures are measured when the storage is at its maximum and minimum capacities. The pressures measured are then near the maximum and minimum pressures. Eq. (8.3) is valid when there is no active water drive.

Example 8–1 Calculation of total gas volume

A depleted gas reservoir is converted to natural gas storage. The reservoir data and conditions are given in Table 8–1. Calculate the total gas volume in the reservoir and the total injected gas volume at p = 6,000 psi. For convenience, Z is given as 1.07 (otherwise it can be calculated by using the correlations given in Chapter 1 with γ_g = 0.6). Assume the temperature will be the same as the initial temperature.

Table 8–1 Input Parameters for Example 8–1

Variable	Quantity	Unit
A	200	acre
h	50	ft
ϕ	0.25	
S_w	0.25	
γ_g	0.6	
T_i	150	°F
p_i	1,000	psi
Z_i	0.91	

Solution

Use Eq. (1.12) for the calculation of the formation volume factors

$$B_{gi} = 0.0283 \times \frac{0.91 \times (150 + 460)}{1{,}000} = 0.0157 \text{ res ft}^3/\text{scf},$$

$$B_g = 0.0283 \times \frac{1.07 \times (150 + 460)}{6{,}000} = 0.0031 \text{ res ft}^3/\text{scf}.$$

Use Eq. (1.13), at 1,000 psi

$$G_i = 43{,}560 \times \frac{200 \times 50 \times 0.25 \times (1 - 0.25)}{0.0157 \times 1{,}000{,}000} = 5{,}202 \text{ MMscf}.$$

Total gas volume in storage at 6,000 psi can be calculated as

$$G = 5{,}202 \times \frac{0.0157}{0.0031} = 26{,}346 \text{ MMscf}.$$

The cumulative gas volume injected can be obtained from Eq. (8.1)

$$G_s = 26{,}346 - 5{,}202 = 21{,}144 \text{ MMscf},$$

or by using Eq. (8.2)

$$G_s = 5{,}202 \times \left(\frac{0.0157}{0.0031} - 1 \right) = 21{,}144 \text{ MMscf}.$$

This is an important exercise as, in reality, the initial gas-in-place for a given storage is often not known. By recording the cumulative injected gas volume at given conditions (p and T) and assuming the temperature is constant at all time (a reasonable assumption), then p/Z versus G_s can be plotted. If there is no aquifer support, this line should be straight, as demonstrated in Figure 8–3, and the slope can be determined. Rearranging Eq. (8.3) gives

$$\frac{p}{Z} = \frac{G_s(p_i / Z_i)}{G_i} + \frac{p_i}{Z_i}. \tag{8.4}$$

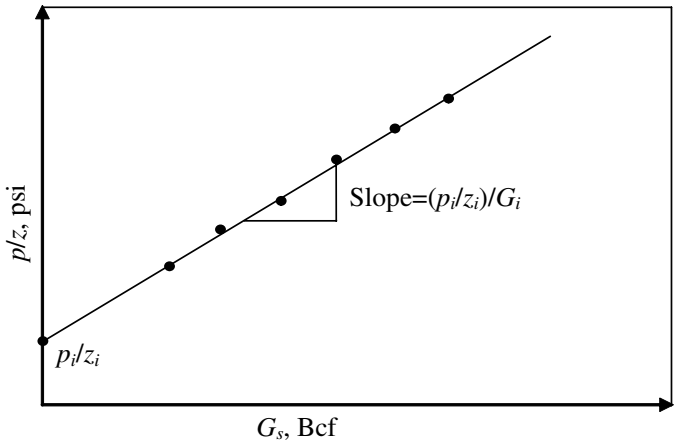

Figure 8–3 *p/Z curve vs cumulative gas storage*

A plot of p/Z versus G_s should yield a straight line and the slope should be $(p_i/Z_i)/G_i$. Therefore the initial gas-in-place can be obtained by

$$G_i = (p_i/Z_i) / \text{slope}. \tag{8.5}$$

p_i/Z_i can be determined by measuring the pressure at initial conditions through a pressure buildup test.

Example 8–2 Calculation of initial gas-in-place

Determine the initial gas-in-place for a shallow, low pressure gas storage reservoir. The injected gas over time and the p/Z data are given in Table 8–2.

Table 8–2 Input Data for Example 8–2

Year	Season	G_s, Bcf	p/Z, psia
Year *i*	Spring	13.5	365
	Fall	17.6	470
Year *i* + 1	Spring	14.5	389
	Fall	17.5	465

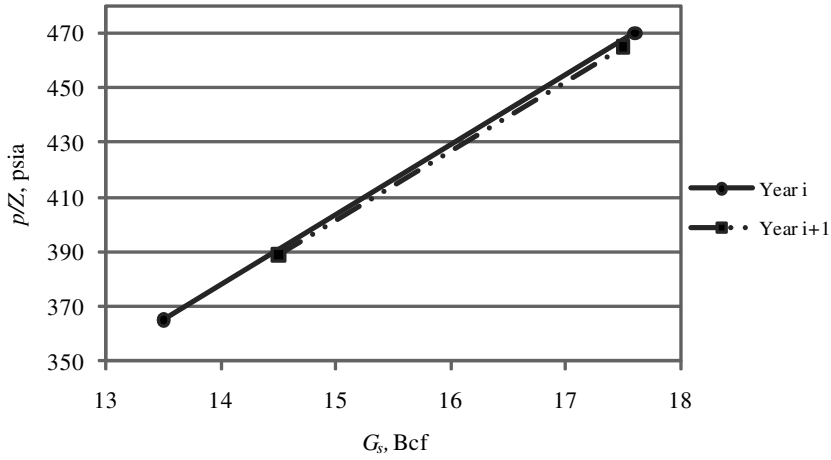

Figure 8–4 *p/Z vs gas storage for Example 8–2*

Solution

Plot p/Z versus G_s (see Figure 8–4) by using the data provided in Table 8–2. Obviously this is an ideal case as it shows the slopes from both Year i and Year $i + 1$ are pretty much the same and is about 25.5 psia/Bcf. Extrapolate the line and intercept it with the vertical axis. This gives $p_i/Z_i = 21.0$ psia (at $G_s = 0$). Use Eq. (8.5), the initial gas-in-place for this given gas storage is

$$G_i = 21.0 / 25.5 = 0.824 \text{ Bcf}.$$

This is also a good tool to evaluate the gas losses in storage, which is one of the critical issues in gas storage that should be addressed.

8.3.2 Losses in Gas Storage[1]

Gas loss in gas storage is a very serious issue. It happens when the cap rock does not seal well, cement around the wellbore is flawed, or there is a communication between the storage and other reservoirs. Once gas loss is happening, the storage deliverability or withdrawal rate will decline from year to year, and the operator will have to bear with high cost or even the risk of not meeting the peak demand. A

1. Some of the material in this section is contributed by Phil Lewis, 2009.

report (Neukarn, 2008) showed that the annual losses can be up to 0.5 Bcf. If the gas price is $4/Mscf that means this storage is losing $2 million per year, which is a significant loss. Therefore, gas storage must be monitored properly to determine the magnitude of such loss, the root cause, and remedy it as soon as it is detected.

For gas storage that is converted from depleted gas reservoir with no water drive, the gas flows to the wells primarily by gas expansion. Then a procedure can be used to determine the gas loss (Mayfield, 1981).

There are several ways to determine the reservoir pressure. One way is to conduct regular (e.g., semiannual) pressure build-up tests similar to pressure surveys done in gas production fields. Another way is to monitor the bottomhole pressure in observation wells. Ordinarily, these pressure surveys are conducted in the fall and spring when reservoir pressure is near maximum and minimum for total gas volume calculation (as discussed in Section 8.3.1 "Total Gas Volume and Injected Gas Volume in Storage"). The preferred observation well is the one at the location with the highest permeability. The plot is usually smoother and more reliable for the injection season as the injection rate is usually constant. During the withdrawal season, fluctuation can happen as the demands from pipeline systems can be different (Mayfield, 1981).

The total gas in storage or gas-in-place can be plotted along with the determined p/Z. If there is no gas loss, all data points should fall on the same line after repeated cycles of injection and withdrawl. If the slope of the line becomes smaller, this is likely to mean that the storage increases because of gas migration or leakage.

When there is gas loss, parallel lines would appear from year to year and are shifted towards a larger gas volume at a given p/Z. The difference between these lines is gas loss. This can be seen in Example 8–3.

Example 8–3 Calculation of gas loss

Assume this is the same storage reservoir as that shown in Example 8–2. After a few years, well deliveries started declining. The bottomhole pressure over Z and gas injected in Year $i + 2$ are collected and summarized in Table 8–3.

Solution

Plot p/Z versus G_s for different years in Figure 8–5. Results show that the line from Year i is overlain with that from Year $i + 1$. The line from Year $i + 2$ is parallel with those from Year i and Year $i + 1$ but shifted towards a larger G_s. This implies that the storage is losing gas.

Table 8–3 Data for Example 8–3

Year	Season	G_s, Bcf	p/Z, psia
Year i	Spring	13.5	365
	Fall	17.6	470
Year $i + 1$	Spring	14.5	389
	Fall	17.5	465
Year $i + 2$	Spring	15.1	395
	Fall	17.7	460

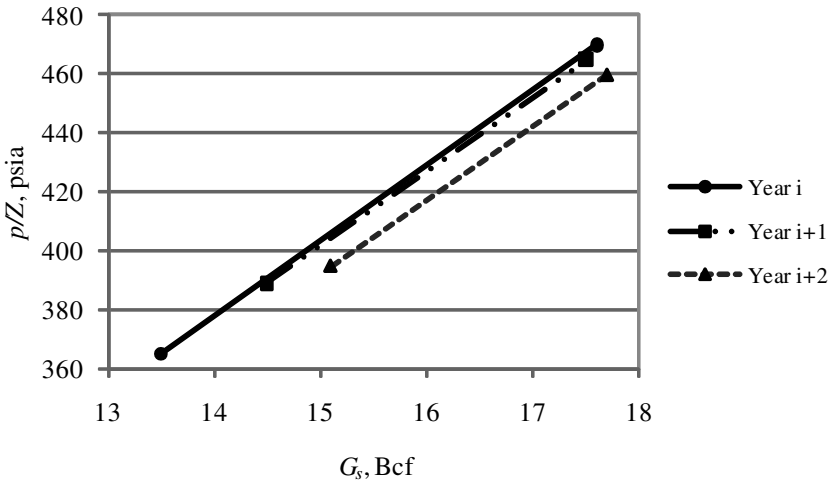

Figure 8–5 *p/Z versus G_s plot for Example 8–3*

From the data set of Year i and Year $i + 1$, Eq. (8.4) yields

$$\left(\frac{p}{Z}\right)_{i+1} = 25.5\left(G_s\right)_{i+1} + 21.0.$$

Similarly, from the data set of Year $i + 2$, Eq. (8.4) yields

$$\left(\frac{p}{Z}\right)_{i+2} = 25.2\left(G_s\right)_{i+2} + 4.4.$$

Choose p/Z = 465 psia, then $(G_s)_{i+1}$ = 17.4 Bcf, and $(G_s)_{i+2}$ = 17.9 Bcf. So the gas loss = $(G_s)_{i+2} - (G_s)_i$ = 0.5 Bcf.

Gas loss can also be determined by plotting $G_s/(p/Z)$ versus time (year). If $G_s/(p/Z)$ does not change with time, it is an indication that the storage facility is secure. If the values are increased with time, that will be an indication that either the storage is losing gas or the effective size of the storage is increased. The amount of gas lost can be determined by using the procedure outlined above.

8.3.3 Injectivity in Gas Storage Well

The expression for injectivity of a gas storage well can be inferred from the expressions for the productivity of a gas well, remembering that in storage, gas is injected into a closed system (unless there is a leak). So steady state is not applicable in injectivity evaluation of gas storage wells. Under pseudosteady state, the injectivity can be calculated by

$$q_{inj} = \frac{kh(p_{inj}^2 - \bar{p}^2)}{1,424\bar{\mu}\bar{Z}T[\ln(\frac{0.472r_e}{r_w}) + s]} . \tag{8.6}$$

For transient flow, in terms of real gas pseudopressure,

$$q_{inj} = \frac{kh[m(p_{inj}) - m(p_i)]}{1,638T}\left[\log t + \log\frac{k}{\phi(\mu c_t)_i r_w^2} - 3.23 + 0.87s\right]^{-1}, \tag{8.7}$$

or, in terms of pressure squared difference,

$$q_{inj} = \frac{kh[p_{inj}{}^2 - p_i{}^2]}{1,638\bar{\mu}\bar{Z}T}\left[\log t + \log\frac{k}{\phi(\mu c_t)_i r_w^2} - 3.23 + 0.87s\right]^{-1} . \tag{8.8}$$

In Eq. (8.7), the *m(p)* is defined in Eq. (3.19).

In Chapter 3, we presented a comprehensive method of combining material balance (p/Z versus G_p) along with well deliverability, and showed how to establish a forecast of well performance. The production rate decreases as the reservoir pressure decreases. In storage, the injection rate may also decrease as the reservoir pressure

increases, therefore the driving pressure difference decreases for a constant injection pressure.

Example 8–4 Calculate the injection rate of a well in a given gas storage

Given: the well bottomhole injection pressure is 3,000 psi. The reservoir pressure at the time and the temperature are 1,500 psi and 200°F, respectively. r_e = 660 ft, r_w = 0.359 ft, k = 1 md, and h = 45 ft. The average Z-factor and viscosity are 0.897 and 0.0175, respectively. Repeat the calculation when the reservoir pressure is 2,000 psi. (The average Z-factor and viscosity are 0.890 and 0.0181 cp, respectively).

Solution

Use Eq. (8.6),

$$q_{inj} = \frac{1 \times 45 \times (3{,}000^2 - 1{,}500^2)}{1{,}424 \times 0.0175 \times 0.897 \times (200 + 460) \times [\ln(\frac{0.472 \times 660}{0.359}) + 0]}$$

$$= 3{,}040 \text{ Mscf/d.}$$

Repeating the above calculation for average storage pressure equal to 2,000 psi, the injection rate is 2,200 Mscf/d, showing the impact of the pressurization of the reservoir on well injectivity.

8.4 Discussion

The emergence of LNG as a major contributor to natural gas supply in the United States will most certainly alter traditional storage patterns and their seasonality. While the calculations presented in this chapter will still be valid, in practice, there will probably be a lot fewer large cycles, such as one in the summer and one in the winter, of storage injection and production as has been the case in the past. Instead cycles may be a lot smaller and repeated several times in a year; reflecting weather induced high and low demand of heating or air conditioning loads. Management of gas storage, with its ability to inject and withdraw relatively quickly in conjunction with a steady or discreet supply of LNG, becomes an important new dimension in natural gas use.

8.5 References

EIA. 2004. The basics of underground natural gas storage. Natural Gas Division.

EIA. 2008. Underground natural gas storage.

Heath, S.M., R.C. Hodrien, E. Kostakis, J.P. Harrison. 1998. Underground storage of natural gas in unlined hard rock caverns. Paper SPE 47221.

Katz, D.L. and M.R. Tek. 1981. Overview on underground storage of natural gas. *JPT* 33 (6).

Mayfield, J.F. 1981. Inventory verification of gas storage fields. *JPT* 33 (9).

Neukarn, J. "Response to Federal Energy Regulatory Commission's Data Requests," Southern Star Central Gas Pipeline, Inc., Docket No CP08-4-000. Dated February 8, 2008.

Speight, J.G. 2007. *Natural Gas: A Basic Handbook*. Houston: Gulf Publishing Company.

Tureyen, O.I., H. Karaalioglu, and A. Satman. 2000. Effect of the wellbore conditions on the performance of underground gas-storage reservoir. Paper SPE 59737.

CHAPTER 9

Natural Gas Supply, Alternative Energy Sources, and the Environment

Natural gas is the cleanest and most hydrogen rich of all hydrocarbon energy sources, and it has high energy conversion efficiencies for power generation. Of more significance is that gas resources discovered but as yet untapped remain plentiful. The sector is poised for considerable growth over the next two decades, and some believe that it may even overtake oil as the prime fuel between 2020 and 2030 (Economides and Wood, 2009; Economides et al., 2001).

The trend towards natural gas becoming the premium fuel of the world economy is not now easily reversible. The key and the challenge for the energy industry is how the transition is to be managed. In this chapter, sources of natural gas, their limitations, and potential are examined. The technological and commercial challenges to be overcome in taking the world through the transition are identified. Finally alternatives to natural gas in both utilization and environmental concerns are addressed.

9.1 Introduction

In 2009 natural gas accounted for about 23% of the world energy demand (EIA, 2009). Large capital investments in infrastructure to enable increased gas consumption were made on both the demand and supply sides. Several gas producing countries embarked upon very ambitious plans for markedly increased gas output. Many new LNG facilities were built. Other gas conversion technologies, such as GTL (see Chapter 7) and CNG (see Chapter 5) have been attracting more serious attention, but energy efficiency, cost, and cost inflation continued to hinder the evolution and development of these promising alternatives.

As the cost of carbon emissions has a bigger impact around the world, natural gas have the potential to increase its share of the power generation market significantly over the coming decade. A rapid growth opportunity exists for natural gas in its potential contribution to transportation either directly or by electrifying the sector. Real and imagined environmental concerns and restricted access for OECD (Organization for Economic Co-operation and Development) nations to long term oil reserves are expected to accelerate the emergence of hydrogen fuel cells. Currently available technologies dictate that the most commercially viable source of hydrogen in large quantities is natural gas, particularly methane through the reforming processes that yield synthesis gas (i.e., carbon monoxide and hydrogen, see Chapter 7). Technologies, investments, and consumption trends suggest that natural gas will be at the center of a worldwide transformation. This will result in a greatly expanded market share of gas in the energy mix for power generation, space heating, petrochemical feedstocks, and transportation fuels (e.g., natural gas vehicles are on the agenda for both energy efficiency and lower emissions reasons).

9.2 The Great Energy Dilemma

An adequate energy supply is vital to economic development and well being. There is an unambiguous relationship between per capita energy consumption and wealth for all nations.

The commercial advantages associated with energy consumption are one reason why governments struggle to search for energy sources, and in the face of potential shortages or geopolitical challenges, to change regional primary energy mixes. The most commercially attractive energy sources usually prevail in most markets, which suggest that initiatives to promote renewable energy sources around the world on environmental grounds alone remain likely to fail. For such alternatives to be adopted in the longer term, they need to demonstrate that they have commercial advantages to consumers, either on a level playing field or through artificially imposed carbon pricing.

Coal was the fuel of choice in the nineteenth and early twentieth centuries, but was gradually superseded by oil right after World War II. Since the 1970s natural gas has slowly but progressively increased its share of the energy mix. These three fossil fuels account for more than 85% of the world's primary energy, and this has not changed over time (see Figure 9–1). Other energy sources (nuclear, hydro and renewables) play a far smaller role by comparison.

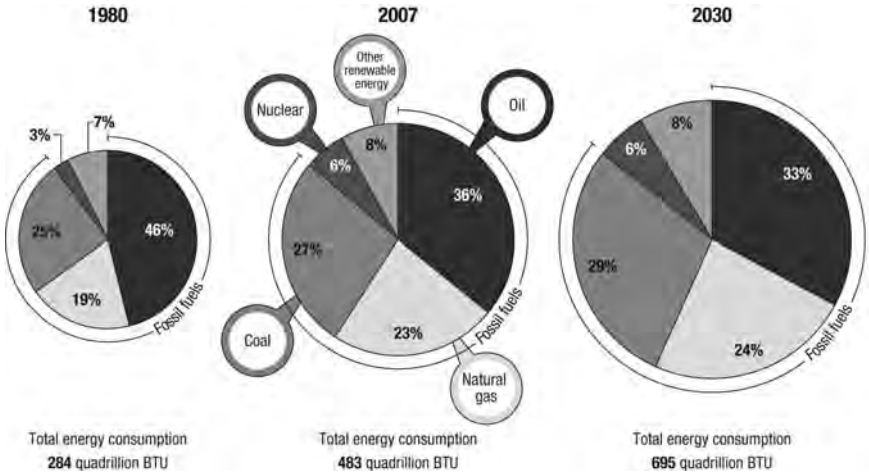

Figure 9–1 *The world energy mix, past, present, and future* (raw data source: US Energy Information Administration, EIA, 2009)

Thirty years before the time of the writing of this book, when worldwide energy demand was 60% of current levels, fossil fuels were the source of nearly 90% of the world's energy supply. According to most forecasts, this is not likely to change much in the foreseeable future, with 86.5% of the total energy mix coming from fossil fuels in 2030 despite—or perhaps because of—an expected increase in total energy demand of 62% by then. However, many question whether such growth and energy mix is sustainable both in environmental terms and with the remaining fossil fuel reserves much beyond 2030 (Wood et al., 2007).

In spite of programs going back more than 30 years that have subsidized alternative forms of energy at substantial costs to consumers, fossil fuels still represent more than 85% of the world's primary energy mix. Why is it proving to be so difficult to reduce this dependency? One first must consider fossil fuels' advantages.

9.3 Advantages of Fossil Fuels

Fossil fuels have advantageous properties enabling them to store and deliver large quantities of energy more effectively and consistently than current alternative energies. Of course, it is recognized that the recent push towards reducing green house gas emissions, especially carbon dioxide, has led to many initiatives to promote less commercially viable and less efficient renewable energy substitutes for fossil fuels.

One advantage of fossil fuels is their abundance. Coal is one of the most abundant energy resources, with supplies capable of meeting electricity needs for more than 250 years. Yet despite some claims based upon misunderstandings of proven reserves (i.e., the relatively small components of conventional oil and gas currently commercialized) versus available resources (i.e., the much larger volumes of conventional and unconventional oil and gas resources both discovered and undiscovered) oil and gas is available in quantities sufficient for it to dominate global primary energy supply for many decades to come. In fact, it is geopolitical factors, including production quotas, civil disturbances, lack of investment among some major petroleum exporting countries, and supply bottlenecks in the supply chains that have placed constraints on the availability of oil and gas to consuming nations for the last several decades. These constraints on supply fed the oil price spike of 2004 to 2008 in conjunction with sustained demand growth in the developing world. Yet another factor in the inequality of fuels is that they are not easily interchangeable.

9.4 Energy Interchangeability versus Inflexibility

Fossil fuels such as oil, natural gas, and coal can be used interchangeably, although with reduced levels of efficiency depending on the use. Coal in the past has been best used for electricity production as it is cheapest, but also the most polluting. New coal plants are likely to incur an additional carbon cost burden through cap-and-trade mechanisms or of carbon capture and sequestration (CCS). However coal can be gasified, at an additional cost, to produce natural gas for lower emissions consumption by various energy end-users. Natural gas can provide space heating at various scales, drive combined-cycle turbines for efficient electricity generation, and, with additional infrastructure costs, provide fuel for road vehicles. It can be reformed from a gas to release its hydrogen and to produce longer hydrocarbon liquid fuel molecules through a variety of GTL (see Chapter 7) conversion processes to fuel motor vehicles. Oil can be refined to yield large fractions of gasoline, diesel, aviation fuel, and fuel oil for transportation. Crude oil, distillates, and fuel oil can also be burned directly to produce electricity, or cracked to produce lighter liquids and gases. In the US and Europe, because coal and natural gas are both cheaper and more readily available, they are the fuels for power generation plants, while oil and oil products are now mainly used as backup fuels. However, much distillate and fuel oil are consumed for power generation in other regions of the world as gas supply chains have yet to be extensively developed.

Alternative sources of energy such as solar, wind, geothermal, and nuclear can provide electricity, in most cases at considerably higher costs, but cannot provide liquid fuels for transportation. Their use for transportation would require motor vehicles equipped with battery packs that, in spite of much investment in improved battery technologies, lead to increased costs and lower efficiencies. To replace current road transportation fuels with electricity, it would require a substantial boost in electricity production, for which the lowest cost and most easily built plants would use coal, nuclear, and natural gas.

It is precisely because of these reasons that many in developed nations interested in achieving "energy independence" with reduced fossil fuel use are backing the biofuel initiatives, such as ethanol, for transportation. But in pursuing biofuels, proponents are ignoring the many shortcomings that make them inadequate and potentially economically and environmentally hazardous if used as anything more than a supplement, or minor blend stock to existing gasoline stocks.

There is an undeniable gap between what is being expected, and in some cases claimed, for the future role of alternative energies. For example, if the U.S. turned all of its corn into ethanol, it would only supply about 20% of the gasoline motorists consume (US Department of Agriculture, 2007).

The decarbonization of fuels is a historical imperative, motivated not only by the real and perceived environmental concerns, but also to improve energy consumption efficiencies. This will require development of new technologies, which initially will be costly. This situation is similar to the passing of the steam engine era. There is no doubt that today's technology could build a steam engine far superior to those of the nineteenth century, but on energy efficiency grounds there is no point in doing so.

Natural gas is the only hydrocarbon source of energy that could easily and at manageable cost lead to further reductions in global carbon intensity through reduction in carbon dioxide emissions. Furthermore, natural gas could provide an ultimate bridge to carbon free energy sources, particularly in the form of hydrogen extracted from the vast available natural gas and methane hydrate (clathrates) resources (Mokhatab and Wood, 2007).

Transitions in energy are revolutionary by nature. For example, how does one circumvent trillions of dollars in existing infrastructure designed to handle oil, petroleum products, and coal? More prosaic is how to convert transportation currently more than 99% dependent on oil to something different such as natural gas directly (e.g., CNG and other natural gas vehicles—NGVs) or by electrifying the entire sector. While such approaches are plausible, their actual implementation

would be costly (trillions of dollars worldwide), take time to achieve, and be commercially difficult for both large and small energy consumers. Certainly nothing will happen overnight. This is a several decades-long process required to achieve such changes, even if such policies were to be globally embraced (Economides et al., 2001; Oligney and Economides, 2002).

9.5 Regional Gas Supply Potential

Since the early 1970s, world reserves of natural gas have been increasing steadily, at an annual rate of about 5%. Similarly, the number of countries with known reserves has also increased from around 40 in 1960 to about 85 in 2005. The distribution among those regions dominating the global proved reserves of natural gas is identified in Figure 9–2. As can be seen, the world's ratio of proven natural gas reserves to production at current levels is about 60 years. This represents the time that remaining reserves would last if the present levels of production were maintained. (Note: For petroleum reservoir engineers this statement is easily understood. For others, a clarification is in order because such statements have caused confusion in the past.)

The term "reserves" does not mean natural gas in place or resources available and yet to produce. The concept of reserves as generally adopted refers only to that portion of the global gas resources so far discovered that can be produced with currently available technology, infrastructure, and within the bounds of commercial constraints. In fact, it is conceivable that through further exploration success, changing market conditions, investment in infrastructure, and new technology that gas reserves over time could increase even though globally we continue to produce and consume more and more of it.

Most explorationists accept that it is easier to find more gas resources than oil resources, making a similar claim for oil less credible. It is quite possible that 60 years from today, the reserves-to-production ratio may still be 60 years or more. Figure 9–2 is a brief overview of strategically important natural gas reserves holdings on a geographic basis.

9.6 Alternatives to Natural Gas Fired Electricity

In 2009 the only meaningful comparison of alternatives to natural gas is for the generation of electric power. In this section, first the potential options are described, and then the technical dimensions and constraints, as well as rudimentary economics for electricity generation are presented.

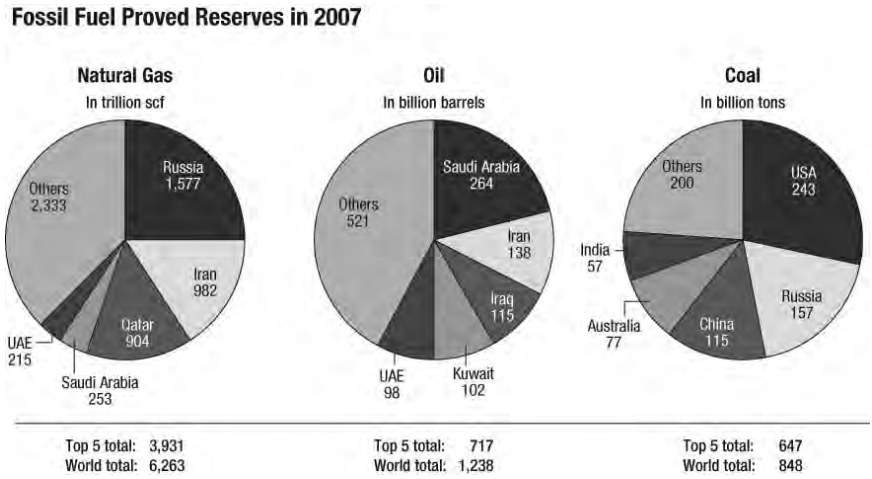

Figure 9–2 *World's main natural gas proven reserves holders compared to oil and coal (UAE means United Arab Emirates)*

9.6.1 Coal

Coal has had a very long history as an energy source. Anecdotal historical evidence suggests that it has been used as a fuel for thousands of years. Its use became pronounced during the 19th century and it is clear that coal fueled the industrial revolution. Eventually it was used for transportation, in railways and steamships, for lighting as coal gas, and for iron and steel production (Boyle et al., 2003).

Coal has played a vital role in electricity generation in the United States since the first electrical power plant in the 1880s. Its abundance, easy handling, and low cost, compared to other energy sources, have made it the preferred fuel for electricity. Coal continued to power the industrialized world through the Second World War, even with the discovery of oil and natural gas. However, health and environmental problems have plagued coal use. As late as the 1950s, combustion of coal was blamed for the deaths of about 4,000 people in London because of respiratory and cardiovascular complications (Kemp, 2004).

The situation led to the enactment of pollutant regulations ("clean air" acts) in many nations and a move towards other sources of energy. However, coal is still very much used in the world's power sector. Currently, about 80% of the coal produced in the US is consumed in coal fired power plants.

9.6.2 Nuclear

Peaceful use of nuclear energy was established in the mid-20th century. It started with experiments performed by physicist Enrico Fermi (awarded the Nobel Prize in Physics in 1938 for his work on induced radioactivity) to show that neutrons could split many kinds of atoms. When he bombarded uranium with neutrons, contrary to his expectation, the resulting elements were lighter than uranium. This suggested that some mass must have been changed to energy. This discovery led to the possibility of a self-sustaining chain reaction in which a large amount of energy is released when an atom is split.

Earlier research on nuclear energy was focused on using it as a weapon during World War II. After the war, investors began seeking a means of using nuclear energy in electricity generation. The first commercial electricity nuclear power plant was a Light Weight Reactor (LWR) located at Shipping Port, Pennsylvania in 1957. The majority of today's nuclear reactors are LWRs and most of them are Pressurized Water Reactors (Boyle et al., 2003).

The nuclear industry for power generation has yet to live down the legacy of two major industrial accidents: the Three Mile Island, Pennsylvania accident in 1979, and the even more serious disaster in Chernobyl, Ukraine in 1986. In the United States, 30 years have elapsed between the time that a new nuclear power plant was initiated and the time of the writing of this book. One of the striking issues involves concerns on how to treat nuclear wastes from spent fuel. About 90% of the fuel (enriched uranium) used in a nuclear cycle is unspent. A method called reprocessing is used to separate the spent fuel into uranium, plutonium, and wastes thereby reducing the total wastes generated and making more uranium available for reuse. However, the process produces plutonium which can be used as a nuclear weapon. There is concern that employing this technique could lead to arms proliferation. The United States does not reprocess spent fuel; instead it is stored in concrete vaults onsite.

9.6.3 Wind

Wind energy has been one of the most touted alternatives to fossil fuels, ideologically compatible with certain groups' perceptions of environmental propriety, or even to prevent future environmental catastrophes. As early as the end of the nineteenth century, wind mills were used to generate electricity in remote areas (US Department of Energy, 2009).

Industrialization brought about more efficient ways to generate electricity and a shift in population to the cities. This led to a gradual

decline in the use of wind mills. In more modern eras, the use of larger wind mills called wind turbines started leading to far larger plant capacities. However, the use of wind turbines for electricity generation has been affected by the prevailing price of fossil fuels. The price of fossil fuels became cheaper after World War II and interest in using wind turbines to generate electricity declined.

Primarily because of politically motivated government subsidies, wind turbines are poised to become more prevalent in electricity generation. However, it is important to note that in 2009 actual wind generated electricity accounted for about 0.1 percent of the total.

There are two problems with wind energy. The first is that in many parts of the world, there is not enough wind to turn the turbine blades. The second is the intermittent nature of the wind. When it does not blow, something reliable such as natural gas must kick in. Figure 9–3 is a map that shows the wind resource potential in various locations in the United States. Entire parts of the country with very large populated areas are not appropriate for wind power development.

9.6.4 Solar

The earth receives a huge amount of radiant energy from the sun daily, and mankind has always used this energy both actively and passively. People from ancient times in northern latitudes have instinctively built their cities in such a way that the houses look towards the south and solar radiation warmed them during the winter (Southface, 2008). Solar radiation was used actively to heat water early in the twentieth century. Water collectors containing insulators were placed on top of the buildings to trap the energy from the sun during the day for use both day and night (Boyle, 2003).

However space and water heating, even in places with lots of sunshine, is a far cry from electric power generation. William Grylls Adams discovered that when light was shined upon selenium, its conductivity rose to as much as a thousand fold and shed electrons. The shed electrons could be used to create electricity; this is known as the Photovoltaic (PV) effect (Southface, 2008).

The price of electricity generated by PV cells has been orders of magnitude more expensive compared to electricity generated by fossil fuels. During the oil embargo of the 1970s, interests in PV cells rekindled with the belief that with research and the manufacture of more PV cells, the price of solar electricity would reduce. Such a situation is still way off, if ever.

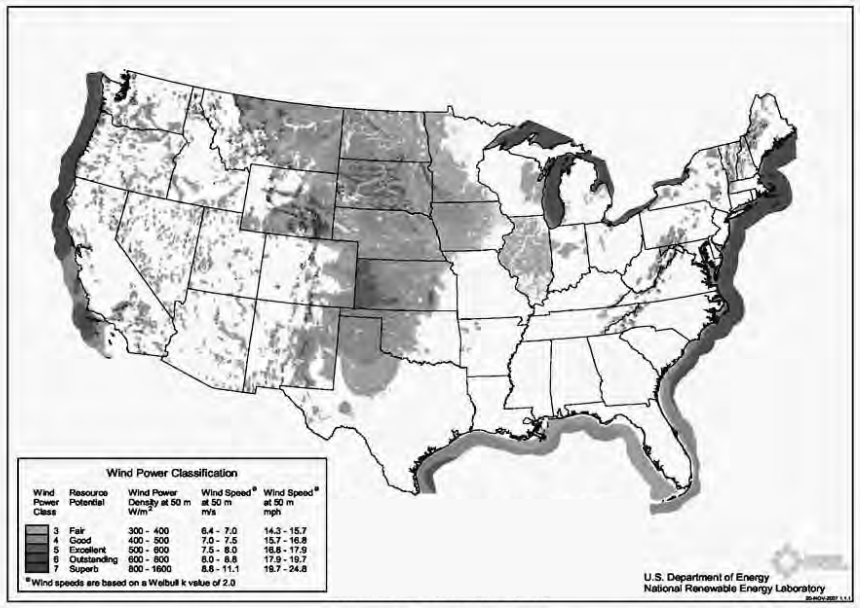

Figure 9–3 *The Wind potential of the United States at 50 land and offshore* (EIA, 2009)

9.7 Fundamentals of Electricity Generation from Alternative Energy Sources

This section contains the basic fundamentals of electric power generation from the four alternatives to natural gas energy sources, using state of the art technologies. Examples of economic calculations are also included to show comparison of the relative attractiveness.

9.7.1 Coal

The basis is 1 megawatt (MW) of electricity production *capacity*. To make this calculation, it is necessary to know the capacity (load) factor of the power plant, the efficiency of the power plant, and the heat content of the coal used in electric utilities. The capacity factor of a power plant is the ratio of the average actual output to its available output (rated capacity). Contemporary coal fired power plants have a capacity factor of 75% and a conversion efficiency of about 32%. Table 9–1 contains the relevant calculations leading to the conclusion that about 3,450 short tons of coal are needed annually to generate 1 MW of electricity. Table 9–2 contains actual reported speci-

Table 9–1 Coal Needed to Generate 1 MW of Electricity

(a) Capacity	1 MW (1,000kW)
(b) Capacity factor	0.75
(c) Annual hours	8,760 h
(d) Annual electricity generation (a×b×c)	6,570,000 kW-h
(e) Conversion factor, 1 kW-h	3,413 Btu
(f) Annual electricity generation (in Btu)	22,423 MMBtu
(g) Power plant efficiency	0.32
(h) Total output (f/g)	70,073 MMBtu
(i) Coal heat rate	20,411,000 Btu/short ton
(j) Amount of coal needed (h/i)	3,433 short tons

fications for three commercial power plants using three different technologies (Zhao et al., 2008).

9.7.2 Wind

The amount of energy generated by a wind turbine depends on the wind velocity of that location. Wind energy systems are classified with respect to locations with strong or weak wind performance (General Electric, 2008). A strong wind performance increases the capacity factor of a wind turbine and therefore the amount of generated electricity. To calculate the amount of wind required to generate 1 MW of electricity, the specific air mass ρ must be considered. It changes depending on temperature and pressure. Other variables include the swept area A, the wind velocity v, and the power coefficient c_p which describes energy losses in power conversion by the wind turbine.

The relationship is

$$P = 0.5\rho c_p A v^3 , \tag{9.1}$$

where P is in Watt, ρ in kg/m^3, A in m^2, and v in m/s.

Table 9–2 Technical Performance Summary for Three Coal Electricity Generation Technologies *(Zhao et al., 2008)*

	Pulverized Fuel Coal (PFC)	Circulating Fluidized Bed (CFB)	Integrated Gasification Combined Cycle (IGGC)
Gross power (MW)	1,200	600	251.2
Total auxiliary losses (%)	6	7	15.5
Net power (MW)	1128	558	212.3
Coal consumption rate for power supply (g/kW-h)	348.4	366.8	340.7
Standard coal consumption rate for power supply (g/kW-h)	310.7	327.2	303.9
Net design efficiency (%)	39.6	37.6	40.5

Example 9–1 Calculation of the average wind velocity to generate 1 MW of power

Assuming a power coefficient c_p = 0.4, a rotor diameter 54 m, and $\rho \approx 1.2$ kg/m^3.

Solution

First, $A = \pi \dfrac{d^2}{4} = 2{,}290 \text{ m}^2$.

Then by re-arranging Eq. (9.1)

$$v = \sqrt[3]{\frac{1{,}000{,}000}{0.5 \times 1.2 \times 0.4 \times 2{,}290}} = 12.2 \text{ m/s}.$$

Thus, the average wind speed to generate 1 MW of electricity using a rotor diameter of 54 m and a capacity factor of 0.4 is 12.2 m/s.

Table 9–3 shows the technical data for GE's 1.5 MW wind turbine, which is one of the most widely used wind turbines in the world.

Table 9–3 Technical Specifications of Commercial Wind Turbines *(General Electric, 2008)*

Model	1.5sle	1.5xle
Rated Capacity	1,500 kW	1,500 kW
Temperature Range: Operation	–30°C to +40°C	–30°C to +40°C
Survival (with Cold Weather Extreme Package)	–40°C to +50°C	–40°C to +50°C
Cut-in Wind Speed	3.5 m/s	3.5m/s
Cut-out Wind Speed (10 min avg.)	25 m/s	20 m/s
Rated Wind Speed	14 m/s	12.5 m/s
Electrical Interface		
Frequency	50/60 Hz	50/60 Hz
Voltage	690V	690V
Rotor		
Rotor Diameter	77 m	82.5 m
Swept Area	4,657 m^2	5,346 m^2
Tower		
Hub Heights	65/80 m	80 m
Power Control	Active Blade Pitch Control	Active Blade Pitch Control

9.7.3 Nuclear

In a nuclear power plant, energy is created when a heavy nucleus undergoes nuclear fission. Each fission process of each molecule creates about 200 million electron-volts (MeV) of energy but about 10 MeV is lost per fission (Edem, 1981). Therefore, the usable energy which is converted to heat in the reactor core is about 190 MeV.

Some basic fundamentals are presented here. The number of atoms or molecules in a substance is known as its Avogadro' number

and has a constant value of 6.02×10^{23} particles/mole. The number of moles equals mass/molar mass. For example, 1 g of U-235 contains 1/235 g-mol of uranium. Therefore the number of atoms in 1 g of U-235 is $6.02 \times 10^{23}/235 = 2.56 \times 10^{21}$ atoms.

The complete fission of 1 gram of U-235 would provide $2.56 \times 10^{21} \times 190$ MeV. Considering that 1 MeV equals 1.6×10^{-13} J, the energy provided by a complete fission of 1g of U-235 is $2.56 \times 10^{21} \times 190 \times 1.6 \times 10^{-13}$ J = 7.78 x 10^{10} J ≈ 78 GJ.

Since 1 J = 2.78×10^{-10} MW-h, then the 78 GJ = 21.6 MW-h, and therefore 0.046 g of U-235 are needed to generate 1 MW-h of energy.

In conventional nuclear power plants, the heat released by the fission of the heavy metal (uranium) is used to heat water, the water is turned into steam, and the steam is used to turn a turbine to generate electricity. About two-thirds of the energy used to generate electricity is lost in the form of waste heat, so only 7.2 MW-h of electricity is generated from 1 g of U-235.

In the above calculation it was assumed that pure Uranium 235 fuels the reactor. However, natural Uranium occurs in the isotopic ratio: 99.27% U-238, 0.72% U-235, and 0.005% U-234 (Boyle et al., 2003). The proportion of U-235 isotope is increased by a process called Uranium enrichment to about 5% for use in power generation.

The actual amount of fuel used in a reactor is measured by its burnup, which is the amount of energy created per mass of fuel. The burnup of a fuel will depend on the amount of U-235 contained in the fuel, i.e., how enriched the fuel is.

Table 9–4 contains technical parameters of a commercial nuclear power plant.

Example 9–2 Determination of the annual uranium use for electricity production

Let's consider a light weight reactor (LWR) with a plant capacity of 1 MW, what will be the annual uranium use for electricity production if the capacity factor is 0.9 and the fuel burnup is 792,000 MWh per ton? Assume that two-thirds of the energy is lost as waste energy, i.e., 1 MW(e) LWR reactor will require a thermal output of 3 MW(t), which means that 33 percent of the thermal energy output is converted into electricity.

Solution

Annual thermal energy required = 3 × 0.9 × 8,760 (MW-h) = 23,652 MW-h.

Thus, annual uranium per 1 MW of electricity production would be 23,652/792,000 = 0.03 tons of uranium.

Table 9–4 Technical Parameters for a Nuclear Power Plant *(Javys, 2009)*

Paramerter	Value
Number of reactor units	2
Reactor's electric output	440 MW
Type of reactor	WWER 440 / V 230
Reactor's thermal output	1,375 MW(t)
Coolant and Moderator	Demineralized water
Turbo generator	
Nominal output	220 MW
Revolutions	3,000 rev/min
Output voltage	15.75 kV

9.7.4 Solar

The energy delivered by a photovoltaic system depends on the average solar radiation, overall PV system efficiency, and PV system capacity factor among other factors. The electricity produced (E) in kW-h/d by a PV array is given by

$$E = H_t A \eta \, . \tag{9.2}$$

where H_t is the hourly irradiance in the plane of the PV array, A is the PV array area, and η is the efficiency of the PV array. The hourly irradiance is given by

$$H_t = H_b R_b + H_d \left(\frac{1+\cos\beta}{2} \right) + H\rho \left(\frac{1-\cos\beta}{2} \right), \tag{9.3}$$

where ρ is the diffuse reflectance of the ground, β is the slope of the PV array, R_b is the ratio of beam radiation on the PV array to that of the horizontal, H is global horizontal irradiance, H_b is the beam component of H, and H_d is the diffuse component of H.

Example 9–3 Calculation of the amount of energy delivered annually by a 1 MW PV array. For example, as applied for by Houston, Texas.

The following data are given:

PV module rating = 150W,
Number of PV modules= 6,670
(i.e., nominal PV array power = 1,000.5 kW),

Frame area = 1.26 m^2
(i.e., PV array area = 6,670 × 1.26 = 8,404.2 m^2).

Solution

Software by RETScreen International is used to calculate the monthly average daily radiation, H_t, in plane of PV array for Houston, Texas, using Eq. (9.3), and the values are shown in Table 9–5. Using the calculated area of 8,404.2 m^2 and an efficiency of 0.096 (BP, 2007), the average daily electricity production, using Eq. (9.2), is also shown in Table 9–5.

Annual energy production = 3,780 (kW-h/d) × 365 days = 1,380 MW-h.

Thus, a 1 MW coal fired power plant with a 0.75 capacity factor requires 3,433 short tons of coal annually to generate 6,570 MW-h of electricity. Therefore a 2,000 MW coal fired power plant with the same capacity factor will require 6.9 million short tons of coal and will generate 13,140 GWh of electricity annually. To generate the same amount of electricity, it will require a 2,000 MW capacity nuclear power plant operating at a capacity factor of 0.9 and 556.9 tons of uranium annually. For wind to match that capacity, it will require 829 wind turbines each with a 1,000 kW rated capacity that will cover at least 1.9 million m^2 of space. Finally, it will require 12,000,000 PV modules, each with a rated capacity of 80 W and it will cover 7.8 million m^2 of space.

9.8 Economics of Electricity Generation from Different Energy Sources

The methods used to evaluate the cost of electricity production from different energy sources differ a great deal, and often depend

Table 9–5 Monthly Average Daily Radiation and Energy Production of 1 MW Solar Power Plant

Month	Monthly average daily radiation in plane of PV array (kW-h/m^2/d)	Monthly average daily energy production (kW-h/d)
Jan	3.51	2,833
Feb	4.09	3,301
Mar	4.64	3,745
Apr	4.98	4,019
May	5.2	4,197
Jun	5.37	4,334
Jul	5.39	4,350
Aug	5.41	4,367
Sep	5.15	4,157
Oct	5	4,036
Nov	4.04	32,601
Dec	3.42	2,760
Average monthly energy production		3,780

on a person's perspectives, social, economic, and environmental interests (Kammen and Pacca, 2004). In this chapter, a method for a comparative economic calculation is presented, along with a rather lengthy and comprehensive example. The levelised lifetime cost approach was used to calculate the cost of electricity generation. The parameters that are taken into consideration are the plant capacity (for the example, common for all, 2,000 MW), capacity factor, capital cost, operation and maintenance cost, economic life time (for the example, 25 years), and discount rates (for the example, 10%). The electricity generation cost calculated is the busbar cost, at the station and does not include other costs like the transmission cost and carbon emission cost (Nuclear Energy Agency, 2005).

The formula to calculate the average lifetime levelised electricity generation cost, C_{EG} is

$$C_{EG} = \frac{\sum \frac{(I_t + M_t + F_t)}{(1+r)^t}}{\sum \frac{E_t}{(1+r)^t}}, \tag{9.4}$$

where I_t is the investment expenditures in year t, M_t are operations and maintenance (O&M) expenditures in year t, F_t are fuel expenditures in year t, E_t is electricity generation in year t, and r is the discount rate.

Example 9–4 Cost evaluation for power generation from: natural gas, coal, nuclear, wind, and solar

The study assumes that investment costs are made in the first year, while the O&M cost and the fuel costs are constant throughout the life of the plant (i.e., not including inflation, price volatility etc.). The study also assumes that the alternative electric power plants (coal, nuclear, wind, solar, natural gas) all have a 2,000 MW plant capacity. It should be noted that this is just an ideal case as wind and solar do not have such plant capacity at the time of this study.

Solution

General assumptions for natural gas are summarized in Table 9–6. This will be the base case. Because of the volatility in the price of natural gas experienced in 2008–2009, and the economic crisis at the time, yearly average price of natural gas was used as the fuel cost ($6.8/MMBtu) rather than the cost at the time of this writing ($3.63/MMBtu). The cost of electricity is about $41/MW-h.

The electricity generation cost for a coal fired power plant is calculated next and presented in Table 9–7. Coal fired plants have a capacity factor that ranges from 70% to 80%. A mean capacity factor of 75% is chosen for this case. The fuel cost data are collected from the EIA website.

Table 9–8 contains the results of the calculation for a nuclear power plant.

The amount of electricity generated by a wind turbine in any location depends on the wind power density (WPD), which indicates the amount of energy available for conversion at the site. The capacity

Table 9–6 Natural Gas Fired Electricity: Assumptions for Base Case

Nameplate capacity, MW	2,000
Capacity factor	60%
Operating Time, hr/day	24
Annual electricity generated, MW-h	10,512,000
Fuel cost, $/MMBtu	6.8
Operation and maintenance cost*, $/kW/yr	13
Investment cost†, $/kW-h	800
Discount rate, %	10%
Plant life	25
C_{EG}, $/MW-h	40.92

* http://www.nwcouncil.org/energy/powerplan/grac/052202/gassimple.htm
† Nuclear Energy Agency, International Energy Agency and Organization for Economic Co-Operation and Development: "Projected costs of generating electricity," 2005.

Table 9–7 Coal Fired Electricity: General Assumptions

Nameplate capacity, MW	2,000
Capacity factor	75%
Operating Time, hr/day	24
Annual electricity generated, MW-h	13,140,000
Fuel cost*, $/MMBtu,	1.77
Operation and maintenance cost†, $/kW/yr	25
Investment cost‡, $/kW-h	1,500
Discount rate, %	10%
Plant life	25
C_{EG}, $/MW-h	32.71

* Energy Information Administration/Electric Power Annual, 2007.
† http://www.nwcouncil.org/energy/powerplan/grac/052202/coalfireplants.htm
‡ Same as the second reference in Table 9–6.

Table 9–8 Nuclear Electricity: General Assumptions

Nameplate capacity, MW	2,000
Capacity factor	90%
Operating Time, hr/day	24
Annual electricity generated, MW-h	14,191,200
Fuel cost[*], cents/kW-h	0.47
Operation and maintenance cost[†], cents/kW-h	1.29
Investment cost[‡], $/kW-h	2,000
Discount rate, %	10%
Plant life	25
C_{EG}, $/MW-h	44.87

[*] Nuclear Energy Institute: Resources and Stats, 2009. http://www.nei.org/resourcesandstats/nuclear_statistics/costs/

[†] Nuclear Energy Institute: Resources and Stats, 2009. http://www.nei.org/resourcesandstats/nuclear_statistics/costs/

[‡] Same as the second reference in Table 9–6.

factor chosen in this study (30%) is achievable at locations with wind power class 5. This corresponds to a WPD of 250–300 W/m^2, a wind speed of 6.0–6.4 m/s measured at a height of 10 m or a WPD of 500–600 W/m^2, or a wind speed of 7.5–8.0 m/s measured at a height of 50 m. Table 9–9 contains the results of this study.

To calculate the electricity generated by a solar (PV) power plant, a location with sufficient annual solar radiation (Phoenix, Arizona) was selected for this study. The annual solar radiation data was generated by RETScreen; however, it could be easily gathered from popular sources. The PV module chosen is the GEPV-100-M, which is a mono silicon PV module with 100W rated capacity per module. The capacity factor for the overall system is 20.6%. Table 9–10 contains the results of this calculation.

In this Example, the lifetime levelised electricity generation costs are calculated. Results show that, for plants with nameplate plant capacity of 2,000 MW, coal powered electricity is the cheapest ($33.91/MW-h); while solar powered electricity is by far the most expensive, almost ten times larger ($349.3/MW-h), even if the most

Table 9–9 Wind Electricity: General Assumptions

Nameplate capacity, MW	2,000
Capacity factor	30%
Operating Time, hr/day	24
Annual electricity generated, MW-h	5,256,000
Operation and maintenance cost*, cents/kW-h	0.65
Investment cost†, $/kW-h	2,000
Discount rate, %	10%
Plant life	25
C_{EG}, $/MW-h	82.72

* http://www.awea.org/faq/cost.html
† Same as the second reference in Table 9–6.

Table 9–10 Solar Electricity: General Assumptions

Nameplate capacity, MW	2,000
Annual solar radiation, MW-h/m^2	2.32
Specific yield, kW-h/m^2	187.5
Overall PV system efficiency, %	8.10%
Capacity factor	20.60%
PV array area, m^2	19,230,770
Annual electricity generated, MW-h	3,606,708
Operation and maintenance cost*, cents/kW-h	3
Investment cost†, $/kW-h	5,750
Discount rate, %	10%
Plant life	25
C_{EG}, $/MW-h	349.3

* http://www.truthaboutenergy.com/Solar.htm
† http://solarcellsinfo.com

ideal geographical conditions were used. Natural gas and nuclear power plants come close second and third to coal. Wind without government subsidies is about two to three times as expensive as the coal, natural gas, and nuclear.

Environmental issues, government approvals, and government subsidies have muddled the economic issues. Environmental concerns will be addressed in the next section. Table 9–11 contains the breakdown of electricity generating capacity from different energy sources as it was in 2007.

Nameplate installed capacity does not mean a proportional actual electric power output. This affects wind but also natural gas. While in Table 9–11 there is a 50% larger nameplate capacity of natural gas generators compared to coal, the latter provides more than twice the actual generated electricity as shown in Figure 9–4.

It is worth noting that wind power and solar power electricity generation varies from location to location, depending on the wind power density and the average daily radiation, respectively. A city with a high wind speed such as Cold Bay, Alaska would generate electricity at a cheaper rate compared to a city with low wind speed such as Houston, TX as shown in Figure 9–5, along with an arbitrarily chosen city, Great Falls, MT. The price of wind electricity from Houston, TX is more than three times that from Alaska's Cold Bay. (This of course assumes that construction and operating costs are the same, which is a very simplistic assumption.)

Likewise, a high daily solar radiation increases the capacity factor of a PV system, thereby increasing the amount of electricity generated. Phoenix, AZ has one of the highest annual solar radiations in the United States, and electricity generation would be better than Sacramento, CA and far better than Houston, TX, as shown in Figure 9–6. However in all cases, both wind and solar generating electricity is far more expensive than natural gas.

9.9 Environmental Impact of Fossil Fuels and Renewable Energy Sources

Fossil fuels and renewable energy sources have been associated with varying environmental concerns. Because of some real, and even at times some not so real but perceived, and controversial environmental issues, the resulting public and government attitudes have caused, and will cause in the future, additional costs. These costs may

Table 9–11 Electricity Capacity by Energy Source, 2007 MW *(www.eia.doe.gov)*

Energy Source	Number of Generators	Generator Nameplate Capacity	Net Summer Capacity	Net Winter Capacity
Coal	1,470	336,040	312,738	314,944
Petroleum	3,743	62,394	56,068	60,528
Natural Gas	5,439	449,389	392,876	422,184
Other Gases	105	2,663	2,313	2,292
Nuclear	104	105,764	100,266	101,765
Hydroelectric Conventional	3,992	77,644	77,885	77,369
Wind	389	16,596	16,515	16,541
Solar Thermal and Photovoltaic	38	503	502	422
Wood and Wood Derived Fuels	346	7,510	6,704	6,745
Geothermal	224	3,233	2,214	2,362
Other Biomass	1,299	4,834	4,134	4,214
Pumped Storage	151	20,355	21,886	21,799
Other	42	866	788	814
Total	17,342	1,087,791	994,888	1,031,978

tilt the balance and the relative attractiveness of the various forms of energy.

There are real and direct environmental problems such as contamination of water bodies, suspension of particulates in the atmosphere, and local air quality. But there are others that are more controversial and long term that are purported to affect life in profound ways. Central is global climate change and the degree to which it is anthropogenic (man-made). The latter affects all fossil fuels. It is beyond the scope of this book to address global climate change, the economic, political, and social implications that are connected with it. Clearly however, voices that have been raised, questioning the very

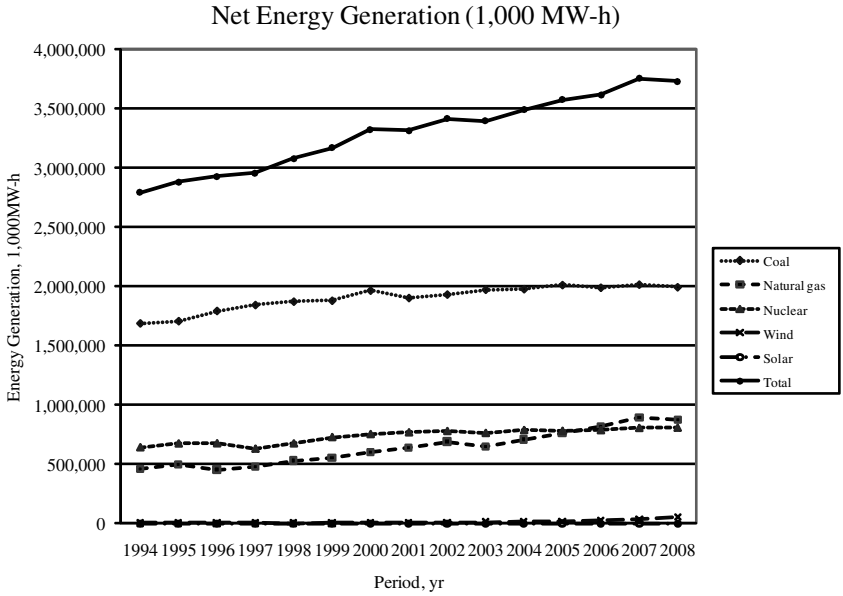

Figure 9–4 *Net electricity generation by energy source* (www.eia.doe.gov)

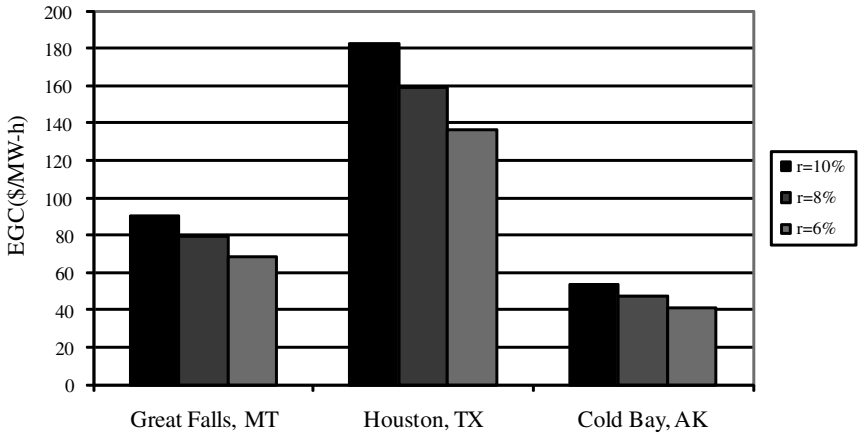

Figure 9–5 *Wind electricity generation cost for three US cities at discount rates (6%, 8%, and 10%)*

use of energy in the modern world to alleviate environmental concerns, are inappropriate.

More elementary environmental issues with fossil fuels relate to their exploration, extraction, processing, and combustion. On the other hand, renewable energy sources often suggested, in spite of

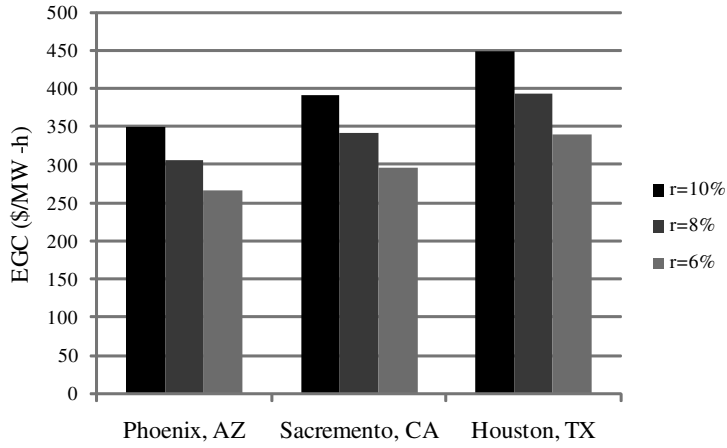

Figure 9–6 *Solar electricity generation cost for three US cities at discount rates (6%, 8%, and 10%)*

their costs, as the solution to the environmental problems of fossil fuels, have other environmental issues of their own, relating to their construction, visual impact, and disturbance.

9.9.1 Environmental Impact of Coal

Coal has been formed from organic sediments that have been deposited several hundred million years ago. It is extracted from the ground by mining. The two major ways in which coal is extracted is by surface mining and underground mining. Surface or "strip" mining involves the removal of the top soil and the hard strata over the coal seam, and it affects the local landscape. In deep mining, the geologic medium is enclosed and coal is extracted from underground and brought to the surface through shafts that have been created. Deep mining causes land subsidence and wastes. The latter, piled on the surface, can leak dangerous chemicals into the ground and also present other dangers.

Coal combustion emissions include carbon dioxide, nitrous oxide, sulfuric oxide, fly ash (particulates), and trace elements such as mercury and arsenic. Fly ash consists of particulates that contaminate the atmosphere and can damage the lungs. It may also contain poisonous impurities that can pollute groundwater with sulfuric acid and arsenic. "Clean coal" technologies are intended to remedy the situation, but they also add to the cost of coal as an energy source.

Coal has a high carbon-to-hydrogen ratio. Therefore the combustion of coal results in large quantities of carbon dioxide emitted into

the atmosphere. Coal combustion produces more than twice the amount of CO_2 for the same useful energy compared to natural gas (Boyle et al., 2003). Figure 9–7 shows the historical CO_2 emissions from the US electric power sector using coal and natural gas.

A point of comparison: In 2007, the U.S CO_2 emission from coal from the electric power sector energy consumption was 1,979.7 million metric tons of CO_2 compared to 376.4 million metric tons of CO_2 for natural gas. Therefore, the amount of CO_2 emitted per kW-h of electricity consumed was 2.164 lb CO_2/kW-h for coal compared to 0.925 lb CO_2/kW-h for natural gas.

9.9.2 Environmental Impact of Nuclear Power Plants

Unlike fossil fuel based power plants, nuclear power plants do not produce greenhouse gases during normal operation. The environment concerns of nuclear energy are mostly related to the nuclear fuel cycle which involves mining, milling, plant construction, and waste management. The waste generated in the mining, milling, and chemical processing of uranium ore contain radionuclides, and equipment used for the processing of the ore are disposed off in a landfill specially created for disposal of radioactive wastes. Improper disposal could lead to a release of radioactive materials into the environment and groundwater (http://www.world-nuclear.org/sym/1998/frost.htm).

Currently, spent nuclear fuels are stored onsite, either in steel lined concrete vaults, or in steel and concrete containers with steel inner canisters each weighing more than 100 tons (Boyle, 2004). About 400,000 cubic yards of concrete and 66,000 tons of steel are required in the construction of a new nuclear power plant. Therefore, although not emitting during electricity generation, a lot of carbon dioxide is emitted during the construction of a nuclear power plant and the processing of its fuel compared with other electricity generating technologies.

9.9.3 Environmental Impact of Wind Turbines

Wind energy is a renewable form of energy and therefore does not emit CO_2 or other forms of green house gases during energy production. However, CO_2 is emitted during construction and installation. Also, wind turbines have environmental concerns relating to noise disturbance, electromagnetic interference, and visual impact.

During installation of a wind turbine, a sizeable amount of land is dug to provide a foundation base and filled with concrete and rein-

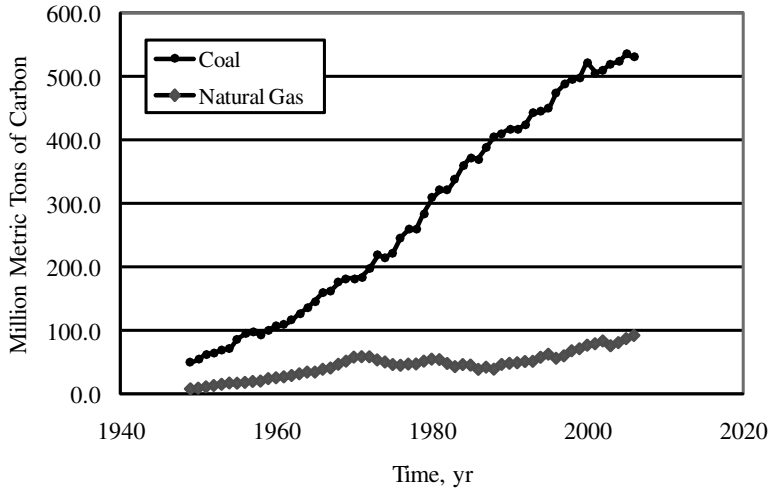

Figure 9–7 *Historical CO_2 emissions from electric power sector* (www.eia.doe.gov)

forced steel. About 1,200 tons of concrete is used for the foundation of a wind turbine.

There have been several complaints of noise disturbance from the swishing sound caused by the interaction of airflow with the blades and the tower, and also mechanical noise from the gearbox (Boyle, 2004). During winter or icing conditions, there is ice buildup on the rotor blades and other exposed parts of the wind turbine. Depending on the prevailing wind speed and the hub height of the turbine, the ice on the rotor blade could be cast a long distance away from the turbine. Wind turbines also cause avian deaths. It is said to have an effect on migrating birds and other sea creatures if installed offshore.

Depending on the height, color, and array of wind turbines installed in a location, the landscape changes and some have complained. The installation of a wind turbine between a television, microwave, or radio transmitter may cause electromagnetic interference. The extent of interference depends on the materials used to make the rotor blades and the shape of the tower (Boyle, 2004).

9.9.4 Environmental Impact of PV Systems

PV systems are relatively safe and do not emit gases during normal operation. They have the least environmental concerns among renewable energy systems. Most PV modules are made of silicon, which is harmless, but some modules contain chemicals like cadmium which

could leak into the environment in cases of fires. There is also a risk of electric shock in large PV systems (Boyle, 2004).

In summary, other forms of energy that have been proposed in recent times as alternatives to natural gas, do not seem to have the capability to do so without extraordinary, very expensive, and highly disruptive government interference. The market share of natural gas has been creeping up and it is certain that it will play an even bigger role in the future.

9.10 References

Boyle, G. 2004. *Renewable Energy: Power for a Sustainable Future*. New York: Oxford Press.

Boyle, G., B. Everett, and J. Ramage. 2003. *Energy Systems and Sustainability: Power for a Sustainable Future*. New York: Oxford Press.

BP, 2007 http://www.bp.com/liveassets/bp_internet/solar/bp_solar_usa/STAGING/local_assets/downloads_pdfs/3200_Data_Sheet.pdf

Economides, M.J., R.E. Oligney, and A.S. Demarchos. 2001. Natural gas: The revolution is coming. *JPT* (May): 102–109.

Economides M.J. and D. Wood. 2009. The state of natural gas. *JNGSE* 1 (July).

Eden, R.J. 1981. *Energy Economics: Growth, Resources, and Policies*. Cambridge: CUP Archive.

Energy Information Administration. 2009. www.eia.doe.gov

General Electric. 2008. 1.5 MW Wind Turbine, http://gepower.com/prod_serv/products/wind_turbines/en/downloads/ge_15_brochure.pdf

Javys, 2009, http://www.javys.sk/en/index.php?page=popup/jadrova-elektraren-v1/technicky-popis-je-v1/technicke-parametre-je-v1

Kammen, D.M. and S. Pacca. 2004. Assessing the costs of electricity. *Annual Review of Environment & Resources* 29: 301–344.

Kemp, D.D. 2004. *Exploring Environmental Issues: An Integrated Approach*. New York: Routledge.

Mokhatab, S., and D.A. Wood. 2007. Why consider exploiting stranded gas. *Petroleum Science & Technology* 25 (3): 411–413.

Nuclear Energy Agency, International Energy Agency and Organization for Economic Co-Operation and Development. 2005. Projected costs of generating electricity.

Oligney, R.E. and M.J. Economides. 2002. Natural gas: The excruciating transition. Paper SPE 77371.

Southface: A Brief History of Solar Energy, 2008, http://www.southface.org/solar/solar-roadmap/solar_how-to/history-of-solar.htm

U.S. Department of Agriculture, Agricultural Projections to 2016, February 2007, at www.ers.usda.gov/publications/oce071/oce20071.pdf

U.S. Department of Energy: The History of Nuclear Energy, 2009, http://nuclear.gov/pdfFiles/History.pdf

U.S. Department of Energy: The History of Wind Energy, 2009, http://www1.eere.energy.gov/windandhydro/wind_history.html

Wood, D.A., J.P.N. Giri, and S. Mokhatab. 2007. Energy balances and climate change—hard choices for Asia. *Hydrocarbon Processing* 86 (May):107–122.

World Coal Institute. 2004. *The Coal Resource. A Comprehensive Overview of Coal*. London.

Zhao, L., Y. Xiao, K.S. Gallagher, B. Wang, and X. Xu. 2008. Technical, environmental, and economic assessment of deploying advanced coal power technologies in the Chinese context. *Energy Policy* 36 (7): 2709–2718.

Nomenclature

A	reservoir area, acre (Chapter 3)
A	vertical vessel cross-sectional area, ft^2 (Chapter 4)
A	area, m^2 (Chapter 6)
A_H	vertical vessel cross-sectional area occupied by heavy liquid, ft^2 (Chapter 4)
A_D	downcomer cross-sectional area, ft^2 (Chapter 4)
A_{HL}	cross-sectional area of the heavy liquid, ft^2 (Chapter 4)
A_L	baffle plate area, ft^2 (Chapter 4)
A_{LL}	cross-sectional area of the light liquid, ft^2 (Chapter 4)
A_{LLL}	cross sectional area for low liquid level, ft^2 (Chapter 4)
A_{NLL}	area of the normal liquid level, ft^2 (Chapter 4)
A_T	total cross-sectional area (horizontal vessel), ft^2 (Chapter 4)
A_V	cross-sectional area of the vapor, ft^2 (Chapter 4)

B	formation volume factor, res bbl/stb
B_g	gas formation volume factor, res ft^3/scf
$\overline{B_g}$	average gas formation volume factor, res ft^3/scf (Chapter 3)
B_{gi}	initial formation volume factor, res ft^3/scf
C_D	drag coefficient, dimensionless (Chapter 4)
C_{EG}	cost of electricity generation, $/kWh (Chapter 9)
C_{fD}	dimensionless fracture conductivity (Chapter 3)
C_{fDopt}	optimal dimensionless fracture conductivity (Chapter 3)
C_G	gravity correction factor (Chapter 4)
C_g	correction factors for gas gravity (Chapter 4)
C_p	ideal-gas specific heats at constant pressure (Chapter 5)
$\overline{C_p}$	specific heat under constant operating pressure and average temperature of the interstage cooler (Chapter 5)
C_S	salinity correction factor (Chapter 4)
C_t	correction factors for operating temperature (Chapter 4)
C_v	ideal-gas specific heats at constant volume (Chapter 5)
c_g	gas compressibility, 1/psi (Chapter 3)
c_p	wind power coefficient (Chapter 9)
c_t	total compressibility, 1/psi (Chapter 3)

c'	shape constant (Chapter 3)
D	turbulence coefficient, $(Mscf/d)^{-1}$ (Chapter 3)
D	vessel diameter, ft or in. (Chapter 4)
D_i	vessel internal diameter, ft or in. (Chapter 4)
D_V	vertical vessel internal diameter, ft or in. (Chapter 4)
d_N	inlet or outlet nozzle diameter, ft or in. (Chapter 4)
d_P	droplet diameter, ft (Chapter 4)
E	elastic modulus, Pa (Chapter 2)
E	joint efficiency, dimensionless (Chapter 4)
E	combination of the compression and mechanical efficiencies (Chapter 5)
E	electricity produced, kWh/d (Chapter 9)
E_t	electricity generation in year t (Chapter 9)
e	exergy, kJ/kg (Chapter 6)
F_D	drag force, lb_f (Chapter 4)
F_G	gravity force, lb_f (Chapter 4)
F_t	fuel expenditures in year t (Chapter 9)
f	fraction of gas load used as fuel for transportation (Chapter 5)
f_f	Fanning fraction factor
G	baffle liquid load, gph/ft^2 (Chapter 4)

G	total gas volume in storage facility, MMscf or Bcf (Chapter 8)
G_i	initial gas-in-place, scf, MMscf or Bcf
$G_{load,k}$	natural gas load delivered by a vessel to site k, MMscf (Chapter 5)
G_n	natural gas capacity of a vessel in a fleet of n vessels, MMscf (Chapter 5)
G°	reaction free energy, kJ/mol (Chapter 6)
G_p	cumulative production from gas reservoir, MMscf (Chapter 5)
G_s	cumulative injected gas volume, MMscf or Bcf (Chapter 8)
$G_{storage,k}$	local natural gas storage capacity at site k, MMscf (Chapter 5)
G_{total}	total capacity, MMscf (Chapter 5)
$G_{total,min}$	minimum total capacity, MMscf (Chapter 5)
$G_{total,max}$	maximum total capacity, MMscf (Chapter 5)
g	gravitational constant, 32.17 ft/s^2 (Chapter 4)
g_c	dimension proportionality constant, lb_f/lb_m-ft/s^2 (Chapter 4)
H	height, ft
H	global horizontal irradiance (Chapter 9)
H_A	liquid level above baffle, in. or ft (Chapter 4)
H_a	barrier depth, ft (Chapter 2)
H_{BN}	liquid height from above baffle to feed nozzle, ft (Chapter 4)

H_b	depth below the barrier, ft (Chapter 2)
H_b	beam component of H, kWh/d-m^2 (Chapter 9)
H_D	disengagement height, ft (Chapter 4)
H_d	diffuse component of H, kWh/d-m^2 (Chapter 9)
H_H	holdup height, ft (Chapter 4)
H_{HL}	height of the heavy liquid, ft (Chapter 4)
H_{HLL}	high liquid level height, ft (Chapter 4)
H_L	height from liquid interface to light liquid nozzle, ft (Chapter 4)
H_{LIN}	high liquid level to inlet nozzle centerline height, ft (Chapter 4)
H_{LL}	height of the light liquid, ft (Chapter 4)
H_{LLL}	low liquid level height, ft (Chapter 4)
H_{ME}	mist eliminator to top tank height, ft (Chapter 4)
H_{NLL}	height of the normal liquid level, ft (Chapter 4)
H^o	heat of reaction, kJ/mol (Chapter 6)
H_R	height from light liquid nozzle to baffle, ft (Chapter 4)
H_S	surge height, ft (Chapter 4)
H_T	total vertical separator height, ft (Chapter 4)
H_t	hourly solar irradiance, kWh/d-m^2 (Chapter 9)
H_V	vapor space height, ft (Chapter 4)

H_W	weir height, ft (Chapter 4)
HETP	height equivalent to a theoretical plate (Chapter 4)
h	net reservoir thickness, ft (Chapter 3)
h	actual packing height, ft (Chapter 4)
h	Enthalpy, kJ/kg (Chapter 6)
h_{in}	Enthalpy in, kJ/kg (Chapter 6)
h_{out}	Enthalpy out, kJ/kg (Chapter 6)
h_o	enthalpy at a convenient basis, kJ/kg (Chapter 6)
h_{perf}	perforated section length, ft (Chapter 3)
I_{APT}	index of aqueous phase trap (Chapter 2)
I_{ani}	index of permeability anisotropy (Chapter 3)
I_{IPA}	the invasion profile adjustment factor (Chapter 2)
I_{PA}	reservoir pressure adjustment factor (Chapter 2)
I_{RPA}	relative permeability adjustment factor (Chapter 2)
I_t	investment expenditures in year *t*, $ (Chapter 9)
I_x	penetration ratio (Chapter 3)
J_D	dimensionless productivity index (Chapter 3)
$J_{D,max}$	maximum dimensionless productivity index (Chapter 3)

J_{DV}	the $J_{D,max}$ of the fractured vertical well (Chapter 3)
J_{DTH}	dimensionless productivity index of each transverse fracture (Chapter 3)
K	terminal velocity constant, ft/s (Chapter 4)
K	equilibrium constant (Chapter 6)
k	reservoir permeability, md
k_a	formation absolute permeability to air, md (Chapter 2)
k_f	proppant pack permeability, md (Chapter 3)
$k_{f,e}$	effective proppant pack permeability, md or m^2 (Chapter 3)
$k_{f,n}$	nominal proppant pack permeability (under Darcy flow conditions), md or m^2 (Chapter 3)
k_g	effective permeability to gas, md
k_H	horizontal permeability, md (Chapter 3)
k_S	Stoke's law terminal velocity constant, (in./min)(cP)/(lb/ft^3) (Chapter 4)
k_s	near wellbore permeability, md (Chapter 3)
k_x	x-axis permeability, md (Chapter 3)
k_y	y-axis permeability, md (Chapter 3)
k_z	z-axis permeability, md (Chapter 3)
L	horizontal well length, ft (Chapter 3)
L	vessel length, ft (Chapter 4)

L	distance from natural gas source to receiving site, km (Chapter 5)
L_{jk}	distance from site j to site k, km (Chapter 5)
M_P	droplet mass, lb_f (Chapter 4)
M_t	operations and maintenance (O&M) expenditures in year t, $ (Chapter 9)
MW_i	molecular weights of individual component in the gas mixture (Chapter 3)
m	mass, kg (Chapter 6)
m_{in}	mass in, kg (Chapter 6)
m_{out}	mass out, kg (Chapter 6)
N	the number of theoretical stage (Chapter 4)
N	number of natural gas receiving sites (terminals $T_1,\ldots, T_N$) (Chapter 5)
N_{prop}	Proppant number (Chapter 3)
N_{Re}	Reynolds number
n	number of moles of the gas
n	number of vessels in a CNG fleet (Chapter 5)
P	power, W (Chapter 9)
p	pressure, psi or Mpa
p	operating pressure, psig or psia (Chapter 4)
p_{ci}	critical pressures of individual component, psi (Chapter 3)
$p_{dp,I}$	initial shut-in pressure in the drill pipe, psi (Chapter 2)

p_e	outer boundary pressure, psi (Chapter 3)
p_{inj}	injection pressure of a well, psi (Chapter 8)
p_o	arbitrary reference pressure (usually zero) (Chapter 3)
p_{pc}	pseudocritical pressure, psi
p'_{pc}	corrected (for sour gas) pseudocritical pressure, psi
p_{pr}	pseudoreduced pressure
p_r	reduced pressure (Chapter 3)
p_{sc}	pressure at standard conditions, psi (Chapter 3)
p_{wf}	flowing bottomhole pressure, psi (Chapter 3)
$\overline{p}$	average reservoir pressure, psi
Q	heat load, kJ (Chapter 6)
$\hat{Q}$	heat per unit mass, kJ/kg (Chapter 6)
$\dot{Q}$	heat rate, kJ/s (Chapter 6)
Q_g	the gas flow rate, MMscf/d (Chapter 4)
Q_g	vapor volumetric flow, ft^3/s or ft^3/min (Chapter 4)
Q_{Hl}	heavy liquid volumetric flow rate, ft^3/min (Chapter 4)
Q_{Ll}	light liquid volumetric flow rate, ft^3/min (Chapter 4)
Q_l	liquid volumetric flow rate, ft^3/min (Chapter 4)

Q_m	inlet mixture volumetric flow, ft^3/s or ft^3/min (Chapter 4)
Q_o	gas capacities of the absorber at the operating condition, MMscf/d (Chapter 4)
Q_s	gas capacities of the absorber at $\gamma_g = 0.7$ at 100°F (at operating pressure), MMscf/d (Chapter 4)
q	flow rate, Stb/d or Mscf/d
q_c	gas consumption rate, MMscf/d (Chapter 5)
q_{load}	gas loading rate, MMscf/d (Chapter 5)
q_{gc}	gas critical flow rate, MMscf/d (Chapter 2)
q_{inj}	injection rate of a well, Mscf/d (Chapter 8)
$q_{offload}$	offloading rate, MMscf/d (Chapter 5)
$q_{offload,max}$	maximum offloading rate, MMscf/d (Chapter 5)
$q_{offload,min}$	minimum offloading rate, MMscf/d (Chapter 5)
R	universal gas constant and equals to 10.73 psi ft^3/lb-mol-R
R_b	ratio of beam radiation on the PV array to that of the horizontal (Chapter 9)
R_c	reflection coefficient (Chapter 2)
R_c	compression ratio (Chapter 5)
R_o	overall compression ratio (Chapter 5)
r	discount rate (Chapter 9)
r_e	outer boundary radius, ft

r_{eH}	drainage radius in the horizontal wells, ft (Chapter 3)
r_G	reaction rate of chain growth, mol/s (Chapter 7)
r_p	fluid invasion, cm (Chapter 2)
r_T	reaction rate of termination, mol/s (Chapter 7)
r_w	wellbore radius, ft
r_{wH}	effective wellbore radius of the horizontal well, ft
S	allowable stress, psi (Chapter 4)
S_{cc}	critical condensate saturation
S_g	gas saturation
S_{wi}	initial water saturation (Chapter 2)
s	skin factor
s	entropy, kJ/kg-K (Chapter 6)
s_c	skin factor caused by combination of flows (Chapter 3)
s_{CA}	shape related skin (Chapter 3)
s_m	mechanical (damage) skin (Chapter 3)
s_o	entropy at convenient basis, kJ/kg-K (Chapter 6)
Δs	entropy change of the system, kJ/kg-K (Chapter 6)
T	temperature, °C (Chapter 6)

T	absolute temperature, R
T	operating temperature, °F (Chapter 4)
T_1	gas suction temperature, °F or R (Chapter 5)
T_2	gas discharge temperature, °F or R (Chapter 5)
T_{ci}	critical temperatures of individual component, R or K (Chapter 3)
T_{pc}	pseudocritical temperature, R or K
T'_{pc}	corrected (for sour gas) pseudocritical temperature, R or K
T_{sc}	temperature at standard condition, R
T_{pr}	pseudoreduced temperature (Chapter 3)
T_r	reduced temperature (Chapter 3)
t	time, s
t	time between arrivals of two successive CNG ships at a receiving site, days or hours (Chapter 5)
t_H	holdup time, min (Chapter 4)
$t_{connect}$	time needed to connect or disconnect a vessel to a supply (source) or distribution line, days or hours (Chapter 5)
t_{cycle}	cycle time for a vessel, days or hours (Chapter 5)
t_{pss}	time to pseudosteady state, hr
t_S	surge time, min (Chapter 4)
$t_{s,Hl}$	settling time for heavy liquid droplets out of light liquid, min (Chapter 4)

$t_{s,Ll}$	settling time for light liquid droplets out of heavy liquid, min (Chapter 4)
t_{travel}	time needed for a vessel to complete a gas distribution cycle from source to receiving sites and back, days or hours (Chapter 5)
$t_{r,Hl}$	residence time of each phase based on the volumes occupied by the heavy liquid phase, min (Chapter 4)
$t_{r,Ll}$	residence time of each phase based on the volumes occupied by the light liquid phase, min (Chapter 4)
U	Overall heat transfer coefficient, W/m^2-K or kJ/s- m^2-K
V	gas volume, ft^3
V_f	volume of one propped wing, ft^3 (Chapter 3)
V_H	holdup volume, ft^3 (Chapter 4)
V_p	volume of the proppant in the pay zone, ft^3 (Chapter 3)
V_r	reservoir drainage volume, ft^3 (Chapter 3)
V_S	surge volume, ft^3 (Chapter 4)
V_{sc}	volume at standard condition, ft^3 (Chapter 3)
v	fluid velocity at reservoir conditions in the fracture, m/s (Chapter 4)
v	vessel velocity of sea travel, knots (Chapter 5)
v	velocity, m/s (Chapter 6)
v_{Hl}	settling velocity of heavy liquid out of light liquid, in./min (Chapter 4)

v_{Ll}	rising velocity of light liquid out of heavy liquid, in./min (Chapter 4)
v_T	terminal velocity, ft/s or in./min (Chapter 4)
v_V	vertical velocity, ft/s (Chapter 4)
v_{VA}	actual vapor velocity, ft/s (Chapter 4)
v_c	velocity of compressional wave, ft/s (Chapter 2)
v_g	gas velocity, m/s (Chapter 2)
v_{gc}	gas critical velocity, ft/s (Chapter 2)
v_s	velocity of shear wave, ft/s (Chapter 2)
W	water content in pure component, lb/MMscf (Chapter 4)
W	work, kJ
W_D	downcomer chord width, in. (Chapter 4)
W_g	gas (vapor) mass flow rate area, lb/h (Chapter 4)
W_{Hl}	heavy liquid mass flow rate, lb/h (Chapter 4)
W_i	water contents of the inlet gas, lb H_2O/MMcf (Chapter 4)
$\hat{W}_{ideal}$	ideal work, kJ (Chapter 6)
W_{Ll}	light liquid mass flow rate, lb/h (Chapter 4)
$\hat{W}_{lost}$	lost work, kJ (Chapter 6)
W_n	AFS distribution function (Chapter 7)
W_o	water contents of the outlet gas, lb H2O/MMcf (Chapter 4)

W_r	the water removed, lbm/h (Chapter 4)
W_{sweet}	saturated water content of the sweet gas at given temperature, pressure and gas gravity, lb/MMcf (Chapter 4)
W_{sour}	saturated water content of the sour gas at given temperature, pressure and gas gravity, lb/MMcf (Chapter 4)
w	fracture width, ft (Chapter 3)
w	vessel thickness, in. (Chapter 4)
w_H	head thickness, in. (Chapter 4)
w_{opt}	optimal fracture width, ft (Chapter 3)
w_S	shell thickness, in (Chapter 4)
x	shape factor of the relative permeability curve (Chapter 2)
x_f	fracture length, ft (Chapter 3)
x_{fopt}	optimal fracture length, ft (Chapter 3)
y_{H_2S}	mole fraction of hydrogen sulfide (Chapter 3)
y_i	mole fraction of individual component in the gas mixture (Chapter 3)
Z	gas deviation factor or "*Z*-factor"
Z_{sc}	*Z*-factor at standard conditions, (Chapter 1)
α	Chain growth probability (Chapter 7)
β	non-Darcy coefficient, 1/m (Chapter 3)
β	slope of the PV array (Chapter 9)

β_g	effective non-Darcy coefficient to gas, 1/m (Chapter 3)
γ_g	gas specific gravity
ε	relative pipe roughness (Chapter 3)
ε_3	correction factor (Chapter 3)
η	Efficiency (Chapter 9)
μ	viscosity, cp or Pa·s
μ	rigidity (Chapter 2)
μ_g	the gas viscosity, cp
μ_{gi}	viscosity of the individual component in the gas mixture, cp (Chapter 3)
μ_{Hl}	heavy liquid viscosity, cp (Chapter 4)
μ_{Ll}	light liquid viscosity, cp (Chapter 4)
ρ	density, lb/ft^3
ρ	diffuse reflectance of the ground (Chapter 9)
ρ_f	density of the formation rock, lb/ft^3 (Chapter 2)
ρ_g	gas density, lb/ft^3 or kg/m^3
ρ_{Hl}	heavy liquid density, lb/ft^3 (Chapter 4)
ρ_{Ll}	light liquid density, lb/ft^3 (Chapter 4)
ρ_l	liquid density, lb/ft^3
ρ_m	mixture density, lb/ft^3 (Chapter 4)
$\rho_{o,g}$	densities of oil or gas, lb/ft^3(Chapter 2)

σ	surface tension, dynes/cm, g-cm/s^2 or lbm-ft/s^2 (Chapter 2)
ϕ	reservoir porosity

INDEX

B

C

G

I

O

W